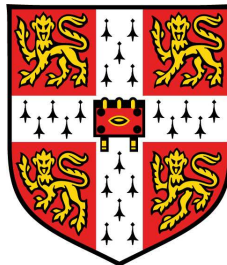


University of Cambridge
Cavendish Laboratory

Experimental Study of Stress Transmission Through Particulate Matter

Jasna Brujić
Gonville and Caius College



February 2004

A Dissertation
submitted for the degree of Doctor of Philosophy
at the University of Cambridge

This, as a whole, just hazily foreseen,
never in any joy or suffering,
collected for a firm accomplishment;
and yet, as though, from far off, with scattered Things,
a serious true work were being planned.

Rainer Maria Rilke,
Self-Portrait 1906
New Poems

I hereby declare that this dissertation is the result of my own work and includes nothing which is the outcome of work done in collaboration, except where the work of others is cited, either explicitly or via the list of references.

This dissertation is submitted for the degree of Doctor of Philosophy at the University of Cambridge. No part of this work has been submitted for a degree or diploma or other qualification at any other University. The thesis contains less than 60 000 words.

Parts of this work have been presented in the following publications:

1. *3D bulk measurements of the force distribution in a compressed emulsion*,
J. Brujić, S. F. Edwards, D.V. Grinev, I. Hopkinson, D. Brujić and H. A. Makse,
Faraday Disc. **123**, 207 (2003).
2. *Measuring the distribution of interdroplet forces in a compressed emulsion*,
J. Brujić, S.F. Edwards, I. Hopkinson and H.A. Makse,
Physica A **327**, 201 (2003).
3. *Jammed systems in slow flow need a new statistical mechanics*,
J. Brujić, S. F. Edwards and D. Grinev,
Phil. Trans. R. Soc. Lond. A **361**, 741 (2003).
4. *Fundamental problems in statistical physics of jammed packings*,
S. F. Edwards, D. V. Grinev and J. Brujić,
Physica A **330**, 61 (2003).

Jasna Brujić
Cambridge, January 2004

Acknowledgements

It is owing to the many exceptional people whom I met during this PhD degree study that my time in Cambridge will be captured by the fondest of memories in years to come. I have been very lucky in terms of the people I have had a chance to interact and collaborate with. It is only through constant communication and collective participation that we have managed to piece this puzzle together:

Discussions with Sir Sam Edwards gave meaning, inspiration and even joy to my work, and in return provided Sir Sam with a mere confirmation of what he already knew to be true (but needed experimental evidence to persuade the sceptics). Even more importantly, I thank him for being truly great and teaching me much more than I could ever have hoped for. I will certainly miss him.

I thank Ian Hopkinson for being the “intellectual driving force” throughout this project, providing help and guidance despite his departure from Cambridge. Stuart Clarke, who has been the ideal ‘stand-in’ supervisor, particularly helped by making sure I finish the Thesis sooner rather than later.

Collaborating with Hernán Makse throughout this project has been a pleasure. It was not easy getting acquainted with granular theories and their mathematical content. I thank Dmitri Grinev and Andrew Tolley for clarifying much of my tasks. I also thank Rafi Blumenfeld and Sebastian Courty for their collaboration in exploring the parallels between granular packings and foam structures. The colloidal (PMMA) particles were kindly provided by Arturo Moncho, which has led to very interesting advances. This Thesis would not have been as neatly laid out and as grammatically sound had it not been for Pietro Cicuta’s invaluable help.

Several visits to the E.S.P.C.I. in Paris provided me with insight about emulsion synthesis as well as hands-on experience, for which I am grateful to Jerome Bibette and Jacques Fattacioli. Last summer, I had the great opportunity to work in Schlumberger Doll Research in Ridgefield, Connecticut, performing experiments on granular rheology. I thank Olivier Sindt and Dave Johnson for making my time there most enjoyable.

Many people have participated in broadening my knowledge in the field and

providing me with useful advice and enthusiastic comments about my research. I am grateful to David Pine, John Melrose, David Weitz, Mike Cates, and from the P&C group, Eugene Terentjev and Cait McPhee.

The P&C group provided the ideal working environment, giving me liberties to shape my own research. It has been fun to work alongside such a friendly and helpful bunch of ‘scientists’. Special thanks to Pietro, Loucas Petridis, Beth Bromley, Laurent Costier, Rosi Rizzieri, Brad Thiel and Debbie Stokes, for keeping a sane level of humour during all ‘working’ hours. Since the list is too long, thanks to *everybody* in the group for making these three years an enjoyable time. I am particularly indebted to Suresh Mistry who has looked after me, also chemically speaking, Frank Baker for helping with the magnetic field design, and Pete Bone for a perfectly sealed sample cell.

I wish to thank Athene Donald for offering me a place within the group and keeping me financially provided during the patient wait for the contract with Unilever. Thank you is not enough to express my gratitude to Meg Staff for accommodating my last minute habits, organising money, travel, visas, equipment - you name it, at the drop of a hat. Also, I thank Vicky and Sarah for their support. I thank Unilever, and particularly Matt Reed, for the industrial participation.

There are a few people who deserve a special mention, without whom my life in Cambridge would have been bare and empty. Ferry path has been a great home to me, together with my second family, Neil and Trolley, Dan and Helen. Little did I know how important my friendship with Christophe would become. Without the care of Alex and Bruno, les fous, I would have gone mad. And where would I spend my ‘free’ time without my beloved Greeks: Loucas, Panos, Zoe and Jorgos? I also thank my longstanding friends, Marc and Becky, for being there for me. I thank a certain someone for everything else.

Finally, I do not thank my parents for all their love and support, instead, I learn to appreciate them each day more.

To my dedicated parents.

Contents

Summary	xii
Structure of the Thesis	xii
1 Introduction to the Concept of Jamming	1
1.1 Jamming in Glassy Systems	3
1.2 Jamming in Particulate Systems	5
1.2.1 Applications of the Jamming Condition	7
1.2.2 Achieving the Jammed State	8
1.3 Unifying Concepts in Granular Matter and Glasses	10
1.4 Thesis Aims and Objectives	12
1.4.1 A Model System	12
1.4.2 Characterisation of Jammed States	14
1.4.3 Physical Properties Measured by Experiment	15
2 New Statistical Mechanics for Granular Matter	18
2.1 Introduction	18
2.2 Classical Statistical Mechanics	19
2.3 Statistical Mechanics for Jammed Matter	20
2.3.1 Volume Function, \mathcal{W}	21
2.3.2 Entropy and Compactivity	23
2.3.3 Remarks	26
2.4 The Classical Boltzmann Equation	27
2.5 ‘Boltzmann Approach’ to Granular Matter	30
3 Emulsions as a Model System	34
3.1 Introduction	34
3.2 Background	36
3.2.1 Applications of Emulsions	37
3.3 Emulsion Properties	38
3.3.1 Kinetic Stability	38

3.3.2	Interdroplet Potential	39
3.3.3	Emulsion Elasticity	42
3.4	Emulsion Preparation	44
3.4.1	Fluorescent Labeling	45
3.4.2	Continuous Phase	46
3.4.3	Emulsification: Crude Mixing	46
3.4.4	Refractive Index Matching	47
3.5	Tayloring Droplet Size	48
3.5.1	Size Segregation	51
3.5.2	Narrow Gap Shearing	51
3.5.3	Dropwise Emulsification	53
3.6	Characterisation of the Emulsion	53
3.6.1	Influence of Glycerol on the Water Phase	54
3.6.2	Measurement of the CMC	54
3.6.3	Surface Tension Measurement	56
3.7	Emulsion Component Selection	56
3.8	Preliminary Experiments	57
3.8.1	Mixing Surfactants	57
3.8.2	Addition of Salt	58
3.8.3	Dodecane Model Emulsion	61
3.9	Summary	62
4	Fluorescence Techniques	63
4.1	Introduction	63
4.2	What is Confocal Microscopy?	64
4.3	Principles of Fluorescence	64
4.4	Microscope Set-up	67
4.5	Optics	67
4.5.1	Objective Lenses	68
4.5.2	Image Degradation	69
4.5.3	Image Resolution	72
4.6	Image Acquisition	74
4.7	Experimental Methods	76
4.7.1	Emulsion Compression	76
4.7.2	Centrifugal Forces	77
4.7.3	Sample Cell	78
4.8	Fluorescence in the Confocal Images	80
4.8.1	Multichannel Detection of Fluorescence	81

4.8.2	Effects of the PSF on Experimental Data	83
4.9	UV-Visible Fluorescence Experiments	84
4.9.1	Properties of Nile Red	84
4.9.2	Amphiphilic Behaviour of Nile Red	85
4.9.3	Environment-Sensitive Fluorescence Spectra	87
4.9.4	Interface Fluorescence	87
4.9.5	Semi-Quantitative Analysis	91
4.9.6	Postulated Mechanism of Dye Insertion	94
4.9.7	Limit of the Fluorescence Method	95
4.10	Summary	96
5	Characterisation of Compressed Emulsions	97
5.1	Introduction	97
5.2	3D Image Processing Methods	99
5.2.1	Image Segmentation	100
5.2.2	Removal of Outliers and Noise	100
5.2.3	Intensity Histogram Equalisation	101
5.3	Droplet Reconstruction	103
5.3.1	Sphere Matching Method (SMM)	104
5.3.2	Mathematical Basis for Using SMM	104
5.3.3	Implementation of SMM	107
5.3.4	Peak Location	112
5.3.5	Computation Requirements	117
5.4	Method Assessment	117
5.5	Test for the Validity of Snell's Law	118
5.6	Computation of Forces	120
5.6.1	Eliminating Edge Effects	120
5.6.2	Geometrical Sphere Overlaps	120
5.6.3	Areas of Deformation-‘Patches’	121
5.7	Summary	127
6	Statistical Mechanics of Jammed Matter	129
6.1	Introduction	129
6.2	Probability Distribution of Forces, $P(f)$	130
6.2.1	Experimental Measurement of $P(f)$	132
6.2.2	Limit of the Force Measurement	135
6.2.3	Simulations of Compressed Emulsions	137
6.2.4	Theory of Force Distributions	140
6.3	Coordination Number, Z	143

6.3.1	Determination of the Coordination Number	145
6.4	Structure and Force Correlations	150
6.5	Spatial Distribution of Forces	154
6.6	Experimental Validation of the Force Model	158
6.7	Aging in Emulsions	160
6.8	Summary	162
6.9	Probability Distribution of Configurations, $P(W)$	164
6.9.1	Partitioning into volumes W_i	164
6.9.2	Calculation of the Entropy	166
6.9.3	Coordination Shell Approximation	168
7	Conclusions	172
7.1	Experimental Method	172
7.1.1	Development of a Model System	172
7.1.2	Environment-Sensitive Fluorescence of Nile Red	173
7.1.3	Novel Image Analysis Technique in 3D	174
7.2	Physics of Jammed Matter	174
7.2.1	Force Distributions, $P(f)$	174
7.2.2	Microstructure	175
7.2.3	Configuration Distributions, $P(W)$	175
7.3	Final Conclusion	176
7.4	Future Work	177
	Bibliography	178

Summary

This Thesis reports experimental investigations of particulate systems experiencing structural arrest and their response to external pressure. Their mechanical properties provide insight into the thermodynamic framework describing ‘jammed’ systems out-of-equilibrium in general and are of interest to technological processes in a range of industries spanning from oil drilling and recovery to the manufacture of food and personal care products.

The mechanism of transmission of stress through the dense particulate medium is investigated in terms of the distribution of forces, $P(f)$. As a granular pile is experimentally impenetrable, it is difficult to investigate $P(f)$ other than at the sample walls, where boundary effects cannot be eliminated. Therefore, a novel model system suitable for optical observation in 3D by confocal microscopy, is developed by refractive index matching a stable emulsion. The droplets can be regarded as deformable, frictionless spheres with well-defined elastic properties. The emulsion is compressed by an external pressure and a force network develops within the system in response to the applied stress. The forces are indirectly measured using a novel methodology based on the fluorescence enhancement in the area of droplet deformation, proportional to the force. Consequently, the direct imaging of the 3D particulate ensemble forms the basis of the *first* experimental study capable of spatially resolving the forces and testing the isotropy of stress transmission. The obtained distribution represents an exponential decay at forces above the mean value - a result that can be described by the functional form of $P(f)$ derived from a theoretical model and is in agreement with previous experiments on grains. The packing configuration is further investigated in terms of the coordination number, testing the isostatic limit for frictionless spheres.

Finally, a new statistical mechanics approach to particulate materials is investigated by partitioning the ensemble into volume elements, the statistics of which leads to the measurement of macroscopic properties, such as the ‘compactivity’ and entropy. The path from micromechanics to thermodynamics provides an experimental foundation for the use of statistical mechanics in jammed matter.

Structure of the Thesis

Chapter 1 introduces the concept of ‘jamming’ as a state that occurs in a wide range of materials, implying there should exist a unifying theory. Experimental objectives of the Thesis, to characterise a jammed state, are also set out.

Chapter 2 presents the concepts of statistical mechanics which have been successfully applied to describe the properties of granular materials. These concepts provided a framework for the experiments and some of them were later explicitly used in the analysis of the results.

Chapter 3 describes the design and preparation of the model emulsion system, appropriate for use in the confocal microscope. The successful system is characterised in terms of the properties necessary to mimic granular behaviour.

Chapter 4 discusses the intriguing fluorescence of Nile red dye, used to emphasise contrast between the emulsion regions in the confocal microscope images. This original method enabled the measurement of interdroplet forces. The fluorescence mechanism is then further investigated using UV-Visible spectrophotometry to determine the different fluorescent species.

Chapter 5 explains the 3D image analysis methods necessary for the characterisation of the emulsion in terms of the particle features. We present a novel technique through which we are able to reconstruct the original image with subvoxel accuracy, thus facilitating a thorough investigation of the particulate packing.

In Chapter 6, the major results of the Thesis are presented in terms of the physics of jammed matter. We provide the statistical analysis of the force fluctuations within the particulate medium, and the effect of theoretically important quantities such as the coordination number and the structural features on the force distribution. The particulate packing is also investigated in terms of geometrical configurations, according to the ideas presented in Chapter 2. The notion of compactness and entropy in jammed matter is then put to the test, thus completing the statistical analysis of the model system.

Chapter 7 summarizes the most important results, leading to conclusions in support of the universality of the physics of jammed matter and suggesting directions for further research.

Chapter 1

Introduction to the Concept of Jamming

“Jamming” is a recently acquired scientific term and therefore requires clarification in the context of this research. The act of jamming or the condition of being jammed stems from the following layman meaning:

‘a crowd or congestion of people or things in a limited space, e.g. a traffic jam’.

The scientific translation defines “jamming” as a state which emerges when a many-body system is blocked in a static configuration far from equilibrium, from which it takes too long a time to relax for the time scale to be a measurable quantity. Jamming is emerging as a fundamental feature of many diverse systems (Liu and Nagel, 2001), such as

- Granular materials: sand, sugar, marbles, dry powders
- Emulsions: mayonnaise, custard, milk
- Colloidal suspensions: paints, muds
- Structural glasses: polymer melts, silica glass
- Spin glasses: (model system).

These distinct disordered systems are but a few examples of out of equilibrium systems, which are united by their behaviour at the point of structural arrest. Whereas one can think of liquids or suspensions as consisting of particles which move very slowly compared to gases, a state may occur where all particles are in close contact with one another and therefore experience jamming. The process of

jamming is specific to the system in question due to their different microscopic properties. The following examples illustrate this. While it suffices to pour a granular material into a closed container and shake it to jam up the particles, the emulsion droplets require a large ‘squeezing’ force usually implemented by centrifugation. On the other hand, the interaction between colloidal particles can be tuned such that the interparticle attraction induces a jammed configuration even at low densities of the material (Pusey and van Meegen, 1986). Furthermore, glassy materials can be cooled down to very low temperatures at which the molecules can no longer diffuse, thus trapping the system into jammed configurations. Hence, through very different jamming mechanisms, we arrive at the jammed state for a variety of systems.

All these systems belong to a class of materials known as ‘soft’ matter, referring to their complex mechanical properties which are neither fluid nor solid-like. This behaviour is directly linked to the material’s capability to support a mechanical disturbance once it has reached a jammed state. While the concepts of crowding and the subsequent mechanical response unite these materials, the details of their constitutive particles introduce important differences.

For instance, in a polymer melt, it is the physical chemistry of the individual strands which will govern the ensemble, whereas it is the interactions between the colloidal particles, rather than their constituent molecules, which will determine the system behaviour in suspensions. Moreover, particles of sizes up to $1\mu\text{m}$ are governed by the laws of statistical mechanics since their dynamics is due to thermal (Brownian) motion. Above that threshold size (e.g. grains), the gravitational energy exceeds $k_B T$, where T is the room temperature and k_B the Boltzmann constant, thus prohibiting motion. The colloidal regime is therefore defined for sizes between 1nm and $1\mu\text{m}$, such that thermal averaging is present. It applies to glasses, colloids, surfactants and microemulsions, or in other words, to ‘complex fluids’. Most of the fundamental physics research has been performed on thermal systems until present, and many of the unifying concepts have arisen through the comparison of systems within this category.

In the next two sections we first describe the structural arrest in thermal systems, where the classical statistical mechanics tools are applicable, and then proceed to athermal systems, such as granular materials and compressed emulsions, in which new situations suitable for a statistical analysis are introduced.

1.1 Jamming in Glassy Systems

In a fluid at thermal equilibrium the particle dynamics is too fast to capture the detail of the underlying potential energy landscape, thus it appears flat. Decreasing the temperature slows down the Brownian dynamics, implying a limiting temperature below which the system can no longer be equilibrated in this way. Hence, the thermal system falls out of equilibrium on the time scale of the experiment and thus undergoes a *glass transition* (Debenedetti and Stillinger, 2001).

The motion of each particle is no longer thermally activated and only the vibration inside the cage formed by its surrounding neighbours persists. However, even below the glass transition temperature, T_g , the particles continue to relax, but the nature of the relaxation is very different to that in equilibrium. This phenomenon of a structural evolution beyond the glassy state is known as “aging”.

The dynamics becomes dominated by the multidimensional potential energy surface which the system can explore as a function of the degrees of freedom of the particles, depicted in Fig. 1.1. In order to describe this landscape Stillinger and coworkers (Stillinger and Weber, 1984), based on ideas introduced by Goldstein (Goldstein, 1969), developed the concept of inherent structures which are defined as the potential energy minima. The trajectory of a system aging at temperature T can be mapped onto the successive potential basins that the system explores.

Computational methods are the only available technique for investigating this behaviour, in which the inherent structures are found via steepest-descent quenching of the system configurations to the basins of the wells. The entropy of the system can be shown to be separable into contributions from the available configurations and the vibrational modes around each minimum. There have been many studies which have embarked on an investigation of aging through the exploration of the configurational space (Sastry et al., 1998; Kob et al., 2000; Coluzzi et al., 2000).

The importance of the inherent structure formalism is in enabling the comparison of jamming in particulate systems with glasses (Fierro et al., 2002). The entropy arising from the inherent configurations of the glass at very low temperatures and the exploration of these configurations due to the vibrational modes of the particles could be viewed as analogous to the configurational changes in particulate packings under slow tapping or shear. However, in granular materials there is an added effect of friction, which dissipates the analogous vibrations at once.

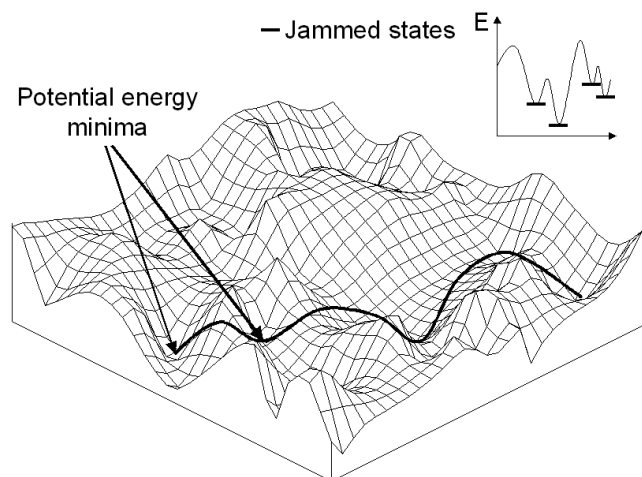


Figure 1.1: The multidimensional energy landscape dominates the dynamics below the glass transition, as the system explores the inherent structures defined as the potential energy minima. A trajectory through the landscape is shown and the analogy between these inherent structures and the jammed states in granular materials is examined.

Unlike granular materials, a thermal system is never permanently trapped in the bottom of a valley, but escapes in other accessible unstable directions through intrinsic thermal vibrations. At any finite temperature the system will not resemble the granular system in that it continuously evolves toward a maximum density state. Thus, the only true analogous situation between glasses and granular materials is valid at zero temperature. However, there are characteristic features of the glassy relaxation at a finite T which act as useful tools for the description of granular systems by exploiting the analogy between the relaxation of powders and aging in glassy systems (Struik, 1978).

For instance, theories developed during the late eighties and nineties in the field of spin glasses (Kirkpatrick and Thirumalai, 1987) have led to a better understanding of glassy systems through the generalisation of usual equilibrium relations, such as the fluctuation-dissipation relation, to situations far from equilibrium (Cugliandolo et al., 1997). This approach yielded macroscopic observable properties, such as an effective temperature for the slow modes of relaxation, which could then be compared between various glassy systems. Furthermore, the existence of an “effective temperature” with a thermodynamic meaning in glasses at very low temperature suggests an ‘ergodicity’ for the long-time behaviour of the system (Kurchan, 2001).

This ergodicity is closely related to the statistical ideas for granular systems (Huang et al., 2000; Nicodemi, 1999; Barrat et al., 2000) which we will introduce in the following sections. In support of this argument, the effective temperature in glasses is found to be an adequate concept for describing granular matter (Makse and Kurchan, 2002).

From a theoretical point of view, these systems are still only understood in terms of predictions of a general nature and many open questions remain. There is still much debate on issues such as the precise mechanisms of surfing the energy landscape, the effects of memory in the system, the slowing down of the system with time, and the discrepancies between the behaviour of different glassy systems, but they are beyond the scope of this work.

1.2 Jamming in Particulate Systems

In a sense one would imagine there is no simpler physical system than a granular assembly. After all it is just a set of packed rigid objects with no interaction energy. It is the inability to describe the system on the continuum level in any other way except according to its geometry which has led to a lack of a well established granular theory until present. Mostly due to their industrial importance, there has been a vast literature describing phenomenological observations without an encompassing theory. In the words of de Gennes, the state of granular matter can be compared to solid state physics in the 30's or critical phenomena in phase transitions before the 60's. In other words, there is a need for describing the universal features of the observed behaviour within a theoretical framework devised for these and other jammed systems.

In parallel with the extensive research on glasses, described earlier, a decade ago Edwards and collaborators postulated the existence of a statistical ensemble for granular matter, despite the lack of thermal motion and the absence of an equilibrium state (Edwards, 1991; Edwards, 1994; Edwards and Oakeshott, 1989; Mehta and Edwards, 1989; Brujić et al., 2003a; Edwards et al., 2003). His postulate was based on jamming the granular particles at a fixed total volume such that all microscopic jammed states are equally probable and become accessible to one another (ergodic hypothesis) by the application of a type of external perturbation such as tapping or shear, just as thermal systems explore their energy landscape through Brownian motion. Hence, let us consider granular jamming in more detail.

Pouring sugar into a cup is the simplest example of a fluid to solid transition which takes place solely because of a density increase. Another very visual example of the importance of density on the macroscopic mechanical properties of the material is to consider a stroll on a sandy beach. The only reason why we do not fall through the sand is its high enough density to support our weight without the constituent sand grains starting to flow and rearrange. It is also the very reason why the opposite is true when walking on quick-sand.

In terms of physics, in particulate materials such as emulsions and granular media, a jammed system results if particles are packed together so that all particles are touching their neighbours, which obviously requires a sufficiently high density. In these athermal systems there is no kinetic energy of consequence; the typical energy required to change the positions of the jammed particles is very large compared to the thermal energy at room temperature ($\sim 10^{14}$ times). As a result, the material remains arrested in a static state and is able to withstand a sufficiently small applied stress.

There is a subtle, but crucial difference, between a configuration in mechanical equilibrium and a jammed configuration, particularly in the context of this research. The mechanism of arriving at a static configuration by an increase in density, which is an intuitively obvious process, is not always sufficient to satisfy the jamming condition in our definition. This applies especially to systems which bear knowledge of the process of their creation. For instance, pouring grains into a container results in a pile at a given angle of repose. This equilibrium configuration is not jammed because in response to an external perturbation, the constituent particles will irreversibly rearrange, approaching a truly jammed configuration. The statistical mechanics which we are aiming to test implies an ergodic hypothesis, which is not valid in such history-dependent samples*.

It turns out that by allowing the system to explore its available configurational space through external mechanical perturbations, the system will rearrange such that all possible configurations (w.r.t. the perturbation) become accessible to one another. Continuing with the analogy in the real world, the gentle tapping on a table of the cup filled with sugar will initially change the unstable angle of repose of the sugar pile and flatten its top surface, and therefore its density, until it settles

*Theories attempting to describe such systems have been developed by Bouchaud et al, proposing a model for the ‘fragile’ systems, i.e. systems which rearrange under infinitesimal stresses (Bouchaud et al., 1995; Cates et al., 1998). However, this situation will not be considered here.

into a desired configuration which depends on the strength of the tap. Such a ‘settling’ of grains is a process which naturally occurs on the beach by the motion induced by the sea waves, for instance.

We can only perform a statistical analysis on the resulting static configurations which have no memory of their creation, i.e. the true jammed configurations. Thus we arrive at an Edwards’ ensemble, suitable for the application of statistical mechanics, described in Chapter 2. Since the particles can jump across the energy landscape during the tap, but then stop at once due to frictional dissipation, there is an analogy to the inherent structure formalism in glassy systems (Fierro et al., 2002). This new statistical mechanics is able to provide unifying concepts between previously unrelated media.

1.2.1 Applications of the Jamming Condition

The statistical mechanics which we are aiming to develop implies an ergodic hypothesis, which is not valid in history-dependent samples. In fact, there are many experimental situations in which the statistical mechanics cannot be applied due to the lack of ergodicity.

For instance convection cycles have been observed in granular systems under vigorous tapping (Knight et al., 2001)- an effect which is closely associated with the segregation process of different granular species. These types of closed loops in phase space cannot be described within the thermodynamic framework. Rapid granular flows observed in pouring sand in a pile, or vigorously shaken granular systems at low density are out of the scope of the present approach since the systems are exploring configurations far from the jammed states (Savage, 1984).

Kinetic theories of inelastic gases are more appropriate to treat these situations (Jenkins and Savage, 1983). The physics of the angle of repose (Herrmann et al., 1998) may not be understood under the thermodynamic framework due to the absence of the jamming condition of the pile, despite the fact that it is static. In many practical situations, heterogeneities appear which also preclude the application of a thermodynamic approach. For instance, when granular materials are sheared in a sufficiently large shear stage, shear bands appear where the strain is discontinuous (Behringer and Jenkins, 1997). Such local effects cannot be captured by the present thermodynamic approach.

On the other hand, if the application of statistical physics to jammed phenomena were to prove productive, then one could anticipate a more profound insight into the characterisation and understanding of the system as a whole. For instance, the thermodynamic hypothesis would lead to the prediction of macroscopic quan-

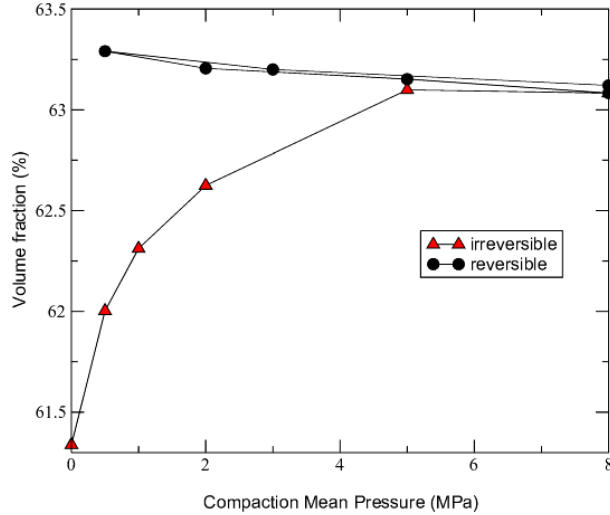


Figure 1.2: Compaction curve for a packing of glass beads under an oscillating pressure. Increasing the amplitude of oscillation initially increases the density by filling the loose voids, after which a reversible regime is achieved.

tities such as viscosity and complex shear moduli, which would in turn provide a complete rheological characterisation of the system. As a matter of theoretical interest, a statistical ensemble for jammed matter could be one of the very few generalisations of the statistical mechanics of Gibbs and Boltzmann to systems out of equilibrium.

1.2.2 Achieving the Jammed State

Experimentally, the conditions for a statistical ensemble of jammed states can be achieved by pre-treating the granular assembly by tapping or via slow shear-driving. Experiments at the University of Chicago involving the tapping of granular columns were the first to show the existence of a reversible regime in which the system configurations are independently sampled (Nowak et al., 1997). Starting with a loose packing of the grains, the tapping routine initially removes the unstable loose voids and thus eliminates the irreversible grain motion. Once all the grains are touching their neighbours, the density of the resulting configuration becomes dependent on the tapping amplitude and the number of taps; the larger the amplitude, the lower the density.

The mechanism of the *compaction* process leading to a steady-state density is extremely slow, in fact, it is logarithmic in the number of taps (Josserand et al., 2000; Brujić et al., 2003c). This dependence of the density of grains on the external perturbation of the system once the memory effects of the pile construction details have been removed, is known as the reversible branch of the ‘compaction curve’,

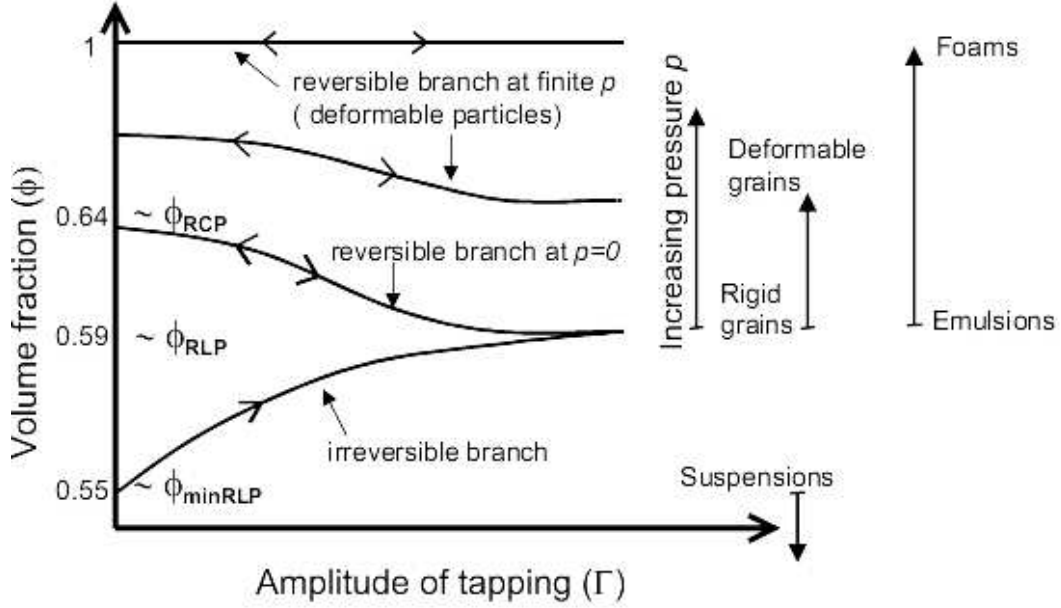


Figure 1.3: Compaction curves of volume fraction ϕ versus amplitude of oscillation A for different external confining pressures. Increasing the amplitude of oscillation initially increases the volume fraction by filling the loose voids (irreversible branch), after which a reversible regime is achieved. At “zero pressure” the minimum volume fraction along the irreversible branch is the random loose packing. The reversible branch goes from the maximum random loose packing fraction to the random close packing fraction. See section 2.3.2 for details.

see Fig. 1.3. Despite the presence of friction between grains (implying memory effects) this curve is reversible, establishing a new type of equilibrium states. It is along this curve that the thermodynamics for granular matter can be applied.

There have been several further experiments confirming these results for different system geometries, particle elasticities and compaction techniques. For example, the system can be mechanically tapped or oscillated, vibrated using a loudspeaker, slowly sheared in a couette geometry, or even allowed to relax under large pressures over long periods of time, all to the same effect (Nowak et al., 1998; Philippe and Bideau, 2002; Brujić et al., 2003c; Chakravarty et al., 2002). Here we show a new compaction regime under an oscillating pressure where the same density dependence of a packing of glass and acrylic beads is noted for varying amplitudes of the pressure oscillation. These experiments have been performed at Schlumberger-Doll Research (Brujić et al., 2003c). The resulting curve of the achieved volume fraction as a function of the amplitude of the pressure oscillation is shown in Fig. 1.2.

Moreover, experiments in the Cavendish laboratory (Chakravarty et al., 2002)

have shown how the conductivity of powdered graphite can also be a measure of the particle density as it is being vibrated, in which the direct link to the volume function is less obvious, but the qualitative results indicate the same trends. The methodology for achieving jammed configurations has also been established numerically for the purpose of rheological and thermodynamical studies.

At this point, it is important to note that we have only considered infinitely rigid, rough grains until present, in which an increase in the pressure of the system, for instance by placing a piston on top of the grains, causes no change in the shape of the grains and therefore no change in the packing density. On the other hand, real grains have a finite elastic modulus, thus the application of a sufficiently large external pressure will always result in grain deformation and therefore a density increase unrelated to the tapping. In soft particles, such as emulsions, the effect of pressure is more significant. The tapping experiment described above measured the resulting densities at atmospheric pressure, which is considered to be the zero reference pressure. The same experiment can be repeated at finite pressures giving rise to equivalent compaction curves, depicted in Fig. 1.3. Whereas hard grains, such as glass beads, require extremely large pressures ($\sim 1\text{MPa}$) to deform and the amount of deformation is limited by their yield stress, softer particles, such as rubber, are able to reach higher densities with relative ease. Droplets and bubbles, being the softest particles one can have, are capable of reaching the density of 1, corresponding to a biliquid foam and a foam, respectively, by an application of much smaller pressures ($\sim 1\text{kPa}$). They have the advantage of the whole pressure range being accessible to them. Another distinction between granular materials and emulsions is the presence of friction in the former and the smoothness of the latter. Since friction plays an important role in inducing memory into the system, its absence leads to a much easier achievement of the jammed state, described above. For instance, in the case of emulsions, allowing the particles to cream under gravity will suffice to arrive at the reversible part of the compaction curve, bypassing the irreversible branch, as it will be shown in Section 6.3.1 in Chapter 6.

1.3 Unifying Concepts in Granular Matter and Glasses

In the preceding paragraphs, it has been shown under which conditions both thermal and athermal systems explore the configurational energy landscape, which possibly results in commonalities in their behaviour. At present, new unifying theoretical descriptions for jammed matter are being sought, as well as new exper-

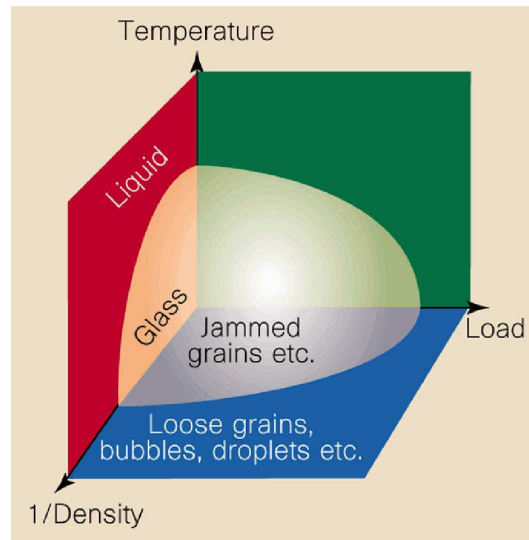


Figure 1.4: Diagram reproduced from (Liu and Nagel, 1998) shows how different systems experience “jamming” by lowering the temperature, increasing the density or decreasing the strain.

imental evidence to unify the predicted state for *all* varieties of jammed systems.

The prediction of how different systems jam with respect to the applied stress, density and temperature has led to a speculative diagram proposed by Liu and Nagel (Liu and Nagel, 1998; Trappe et al., 2001; D’Anna and Gremaud, 2001). It links the behaviour of glasses (thermal systems) and bubbles, grains, droplets (athermal systems) by the dynamics of their approach to jamming.

When the external driving force (temperature, density or load) is too small, these materials jam to form amorphous solids and develop a yield stress. If it were true that temperature, and density play a similar role in unjamming the systems according to the proposed phase diagram, one could imagine describing driven (tapped), athermal systems of different types by concepts of statistical mechanics. Recent approaches have also exploited the analogy between the jammed configurations of granular materials and the inherent structures in glasses to characterize the energy distribution in granular systems under tapping (Fierro et al., 2002).

Since the observable properties such as applied strain, temperature and density can be obtained by consideration of only the jammed configurations in a given system, the thermodynamics of jamming, discussed in Chapter 2, is intimately related to the ideas put forward in the jamming phase diagram.

1.4 Thesis Aims and Objectives

The first step in realising the grand idea of a unifying theory is to understand in detail the characteristics of a jammed configuration in particulate systems. Thus, the main aim of the Thesis is to design and perform an experiment to provide a microscopic foundation for the statistical mechanics of jammed systems. Understanding the micromechanics on the scale of the particle, together with the respective statistical measures, paves the path towards an experimental proof of the existence of such an underlying thermodynamics.

To achieve these general aims, the following specific objectives have to be met:

1. Design of an optically penetrable model particulate system.
2. Development of image analysis algorithms to allow for a complete characterisation of the system in terms of the particle positions and radii.
3. Measurement of interparticle forces facilitated by particle elasticity.
4. Statistical analysis of the forces and the configurational parameters of the packing to probe the thermodynamical measures.

The important stages in this research are given a brief introduction in the following sections.

1.4.1 A Model System

The problem with the characterisation of the jammed state in terms of its microstructure is that the condition of jamming implies an optically impenetrable particulate packing. The fact that we cannot take a look inside the bulk to infer the structural features has confined all but one three-dimensional study of packings to numerical simulations and the walls of an assembly. In the old days Mason, a postgraduate student of Bernal, took on the laborious task of shaking glass balls in a sack and ‘freezing’ the resulting configuration by pouring wax over the whole system. He would then carefully take the packing apart, ball by ball, noting the positions of contacts (ring marks left by the wax) for each particle, which was later to earn him only an acknowledgement in the much acclaimed article (Bernal, 1960). The statistical analysis of his hard-earned data led to the reconstruction of the contact network in real space and also the number of contacts of each particle satisfying mechanical equilibrium. This has been the only reference point for simulators and theoreticians to compare their results with those from the real world and it therefore deserves a particular mention.

Although there have not been any other such studies until present, alternative techniques which allow 3D observation are extensively used, primarily in biology and medical research. The available 3D techniques are scarcely applied to granular matter and include X-ray tomography (Orsi et al., 1996), Magnetic Resonance Imaging (MRI) (Porion et al., 2000) and confocal microscopy (Bromley and Hopkinson, 2002). The latter is the only technique which does not require a large amount of data per 3D image, allowing for the thorough image analysis characterisation with relative ease. In fact, X-ray tomography data has been collected and reported for granular packings under flow (Mueth et al., 2000), however, it was the velocity profile which was investigated rather than the details of the granular structure.

In search of an alternative method of investigating particulate packings, more in line with the automated nature of our times, we developed a model system suitable for optical observation in the confocal microscope. Moreover, our aim was to investigate the jammed state in a jammed medium different to rigid grains in order to probe the universality of the configurational features. Finally, one needs to solve the system geometry as well as the stresses propagating through it in order to come up with a general theory. Hence, to probe the stress propagation through the medium, rather than its configuration alone, the particles must have well-defined elastic properties. The system which could satisfy all our requirements was found in a packing of *emulsion droplets* in the following way:

Transparency. An alternative way of ‘seeing through’ the packing is to refractive index match the phases in the system - i.e. the particles and the continuous medium filling the voids. Since an emulsion is made up of two immiscible liquids (see Chapter 3), it is possible to raise the refractive index of the aqueous phase to match that of the dispersion of oil droplets. However, transparency is not the only requirement, since the particles are then dyed to allow for their optical detection (see Chapter 4).

Alternative Medium. The emulsion is made up of smooth, stable droplets in the $1 - 100\mu m$ size range, as compared to rigid, rough particles in the above described granular system. Both systems are athermal, but the length scale and the properties of the constituent particles of the system are very different.

Elasticity. Emulsion droplets are deformable, stabilised by an elastic surfactant film, which allows for the measurement of the interdroplet forces from the amount of film deformation upon contact. Moreover, the elasticity facilitates the measurement of the dependence of the contact force network on the external pressure applied to the system.

1.4.2 Characterisation of Jammed States

Having prepared a stable, transparent emulsion, to be described in Chapter 3, we use confocal microscopy for the imaging of the droplet packings under compression. The contrast is provided by the differential fluorescence of the dispersed (droplets) and continuous (aqueous) phases, investigated in Chapter 4. The resulting 3D images are then processed using sophisticated image analysis algorithms, developed in this Thesis (see Chapter 5), to yield all the structural features, described below.

Directly from the images we are able to isolate the following information in 3D for each droplet configuration, i.e. image stack:

1. Droplet centres and radii with subvoxel accuracy, \vec{x}, r
2. Distribution of droplet sizes, $P(R)$
3. Radial distribution function, $g(r)$
4. Volume fraction of droplets, ϕ
5. Geometric areas of overlap between droplets in contact, A_s [†]
6. Areas of droplet deformation from an increased fluorescence, A_p [‡]
7. Droplet contact network (centres of A_s, A_p), \vec{C}
8. Forces calculated from areas in 5 or 6, \vec{f}_s, \vec{f}_p , respectively
9. Spatial representation of the 3D network of forces, contacts etc.

As shown in the above list, using the information of droplet centres and radii alone (point 1), we are able to characterise the configuration of the packing in terms of the particle size distribution, the radial distribution function as well as the droplet volume fraction (points 2,3 and 4). Since the droplets are deformable and they exert forces on one another upon contact, these forces can be inferred from the areas of their geometrical overlap (point 5), (see Section 6.2.1 in Chapter 6). In addition, owing to an interesting fluorescence mechanism upon compression, to be described in Section 4.3, the areas of droplet deformation appear brighter than the rest of the image, allowing for a separate measurement of the same areas from a physical effect (point 6). The comparison of forces arising from the two different methods in 8 serves as a test for the validity of the technique. All the forces within the bulk can then be visualised in 3D (point 9).

[†]subscript 's' = simulated

[‡]subscript 'p' = patches

1.4.3 Physical Properties Measured by Experiment

Once each image has been characterised by all of the above parameters, important physical features and relations can be extracted from the previously unavailable data from true 3D experiments. These are summarized below.

Probability Distribution of Forces, $P(f)$

In order to investigate the micromechanics of any many-body system, the most interesting property to be considered, governing the mechanical response, is the probability distribution of forces $P(f)$. It is well known that the forces are transmitted inhomogeneously through granular materials, characterised by an exponential force distribution. This is the *first* study of the $P(f)$ in the bulk of a 3D sample, and also the first study of jamming in an emulsion system. The micromechanics of jammed systems has previously been extensively studied in terms of $P(f)$, however, the experiments were confined to 2D granular systems or the measurement of the forces exerted at the walls of a 3D granular assembly. On the other hand, numerical simulations have provided $P(f)$ for a variety of jammed systems, from structural glasses to foams and compressible particles, in 3D. Thus, our novel experimental technique can be compared with all previous studies in search of a common behaviour. In addition to the novelty of the experiment, we present a simple theoretical model, developed by our collaborators (Edwards and Grinev, 2003), to explain the exponential result.

Coordination Number, Z

The mean coordination number Z of the system is another theoretically important parameter. It is the average number of contact points per grain. It has been shown that the isostatic limit, i.e. mechanical equilibrium, is achieved (in 3D) for $Z = 4$ for frictional systems and $Z = 6$ for smooth particles. This has not been tested in the real world until present, except in the famous experiment of Bernal for rough particles, discussed in Section 1.4.1. Even there, all particles in contact were counted, whereas the theory predicts the coordination number assuming only those particles which are exerting a force. In this work we calculate the coordination number for emulsion systems as well as for colloidal poly(methyl-methacrylate) (PMMA), which are both considered frictionless due to the lubrication by the suspending medium, but have very different elastic properties.

Spatial Correlations in the Force Network

The spatial correlations provide insight into the important micromechanical features which arise in response to external pressure. For instance, the existence of force correlations, such as percolating force chains through the medium can be detected by the visualisation of the forces larger than the mean force. A preferential direction of propagation or structural inhomogeneities are clearly visible by such a method. These features have been postulated, yet there is no clear consensus on their existence in 3D at present.

Interdroplet Force Model Verification, $f \propto A^\alpha$

The area of deformation is assumed to be proportional to the force between two droplets if the deformation is small compared to the radius of the droplets. It is a surface tension effect, by which all the energy is stored in the deformation, $E = \sigma A$. This model does not take into account shape deformation (Gang et al., 1995), the nonlinear droplet response nor the collective behaviour in a droplet assembly. The validity of the crude assumptions in the model are tested by the comparison of the areas of droplet deformation which the theory predicts and those measured by the enhanced fluorescence.

Time Evolution of a 'Static' Packing - Aging

Finally, the phenomenon known as aging, which is the time evolution of a system far from equilibrium, has been reasonably well understood in thermal systems, yet there is scope to believe that spontaneous rearrangements of emulsion droplets are possible too. Since the particles are frictionless, one could imagine a frustrated particle slipping into a more favourable configuration over long times and the collective nature of the system leading to a slow relaxation into another configurational state. Diffusing wave spectroscopy experiments have presented results indicating aging for a range of materials, including compressed emulsions, and we provide a microscopic test for that hypothesis, whereby each particle position is monitored with time. Importance is given to this approach due to its possible commonality with glasses.

This completes the study of the static structures in terms of the questions related to the stress distribution in the droplet packing. Although the system seems fully characterised at this point, there are more subtle ways in which the static structure is investigated in terms of the particle configuration.

Probability Distribution of Configurations, \mathcal{W}

In our experiments, the 3D images of the particulate system also allow for the characterisation of the probability distribution of the volume function \mathcal{W} , which is basically the volume occupied by the first coordination shell of each grain in the pack. Its significance and definition will be described in detail in Section 2.3.1 of Chapter 2.

The ability to measure this function and therefore its fluctuations in a given particle ensemble, enables the calculations of the macroscopic variables. This implies that we can arrive at the thermodynamic system properties from the knowledge of the microstructure. Such a characterisation of the governing macroscopic variables, arising from the information of the microstructure, allows one to predict the system's behaviour through an equation of state. This is the first experimental study of such statistical concepts in particulate matter and opens new possibilities for testing the thermodynamic formulation for particulate matter.

Chapter 2

New Statistical Mechanics for Granular Matter

Very like indeed:
Sea and sky afar, on high,
Sand and strewn seaweed,-
Very like indeed.

Dante Gabriel Rossetti,
Even so.

2.1 Introduction

This Chapter aims to justify the use of equilibrium statistical mechanics tools in situations where the system is far from thermal equilibrium, but jammed. Its relevance to this Thesis is that it not only highlights the fundamental questions in this area of physics, but also points to the key quantities in characterising a packing of particles, accessible through our experiments. This powerful theoretical framework provides the motivation for the work, the guidance through the experiments and a deeper understanding of the results.

In what follows, we present the classical statistical mechanics theorems to an extent which facilitates an understanding of the important concepts for the development of an analogous granular theory, as well as the assumptions necessary for the belief in such a parallel approach. Thereafter, we present a theoretical framework to fully describe the exact specificities of the granular packing, and the shaking scenario which leads to the proof of the Second Law of thermodynamics in granular systems, $dS/dt \geq 0$. These very recent advances have been made by the

inventor of the statistical mechanics for granular matter, S. F. Edwards, in which the Boltzmann equation is derived for a jammed granular system.

This kind of analysis paves the path to macroscopic quantities, such as the compactivity, from the statistical analysis of the microstructural information of the packing. By characterising each static configuration obtained from our experiments, we are able to test some of the aspects of the theory presented here.

In a thermal system, the Brownian motion of the constituent particles implies that the system dynamically explores the available energy landscape, such that the notion of a statistical ensemble applies. For densely packed systems of interest in this study, in which enduring contacts between particles are important, the potential energy barrier prohibits an equivalent random motion. At first sight it seems that the thermal statistical mechanics do not apply to these systems as there is no mechanism for averaging over the configurational states. Hence, these systems are inherently out of equilibrium. On the other hand, recent theoretical and numerical work has yielded evidence for the validity of an underlying thermodynamics in particulate systems, analogous to the equilibrium case scenario. This train of ideas started more than a decade ago when S.F. Edwards and collaborators from the University of Cambridge proposed a statistical ensemble valid for dense, static and slowly moving granular materials and through it, notions of entropy, temperature and compactivity (Edwards and Oakeshott, 1989).

2.2 Classical Statistical Mechanics

In the conventional statistical mechanics of thermal systems, the different possible configurations, or microstates, of the system are given by points in phase space (Landau and Lifshitz, 1970). Explicitly, phase space is the space of all positions and momenta $\{p, q\}$ of the constituent particles, in which Liouville's theorem applies. It follows from Liouville's theorem - combined with the fact that the logarithm of the distribution must be an additive quantity - that the distribution of microstates must be expressed only in terms of the additive integrals of motion of the system. Classical mechanics shows that there are only seven independent additive integrals: the total energy of the system, the momentum and the angular momentum. If we consider a rigid system at rest the probability distribution ρ_{eqm} of the microstates must be expressed only in terms of the total energy of the system. The simplest form for a system with a Hamiltonian $\mathcal{H}(p, q)$ which satisfies Liouville's equation

is

$$\rho_{\text{eqm}}(E) \sim \delta(E - \mathcal{H}(p, q)), \quad (2.1)$$

which is the microcanonical distribution. Note that assuming that this is the true distribution of the system implies accepting the ergodic hypothesis, i.e. the trajectory of the closed system will pass arbitrarily close to any point in phase space. If the total energy, E , of the system is fixed, as implied for a microcanonical ensemble, then the number of microstates is

$$\Omega_{\text{eqm}}(E) = \int \delta(E - \mathcal{H}(p, q)) \, dp \, dq, \quad (2.2)$$

at a given volume and number of particles. Here $dp \, dq$ is the volume measure on phase space. The crucial assumption is that all microstates are equally probable. Therefore the probability of a state ν is $P_\nu = 1/\Omega_{\text{eqm}}(E)$ for the states within the ensemble and zero otherwise.

It was the remarkable step of Boltzmann to associate this ‘statistical’ concept of the number of microstates, with the thermodynamic notion of entropy through his famous formula

$$S_{\text{eqm}}(E) = k_B \log \Omega_{\text{eqm}}(E). \quad (2.3)$$

Thus, in classical statistical mechanics, the total energy of the system is sufficient to describe the probability density of states. Whereas the study of thermal systems has had the advantage of available statistical mechanics tools for the exploration of the phase space, an entirely new statistical method, unrelated to the temperature, had to be constructed for grains.

2.3 Statistical Mechanics for Jammed Matter

We now consider a jammed granular system composed of *rigid* grains, although the experiments in the Thesis are performed on deformable particles. Such a system is analogously described by a network of contacts between the constituent particles in a fixed volume, V , since there is no relevant energy E in the system. In the case of granular materials, the analogue of phase space, the space of microstates of the system, is the space of possible jammed configurations as a function of the degrees of freedom of the system $\{\zeta\}$.

Edwards conjectured that it is the volume of this system, rather than the energy, which is the key macroscopic quantity governing the behaviour of granular matter (Edwards and Oakeshott, 1989; Edwards, 1994). It is argued that if we

have N grains of specified shape which are assumed to be infinitely rigid, the system's statistics would be defined by a function $\mathcal{W}(\zeta)$, a function which gives the volume of the system in terms of the specification of the grains.

In this analogy one replaces the Hamiltonian $\mathcal{H}(p, q)$ of the system by the volume function, $\mathcal{W}(\zeta)$. The average of $\mathcal{W}(\zeta)$ over all the jammed configurations determines the volume V of the system in the same way as the average of the Hamiltonian determines the average energy E of the system.

2.3.1 Volume Function, \mathcal{W}

One of the key questions in this analogy is to establish the 'correct' \mathcal{W} function, the statistics of which is capable of fully describing the system as a whole. The idea is to partition the volume of the system into different subsystems, α with volume \mathcal{W}^α , such that the total volume of a particular configuration is

$$\mathcal{W}(\zeta) = \sum_{\alpha} \mathcal{W}^\alpha. \quad (2.4)$$

It could be that considering the volume of the first coordination shell of particles around each grain is sufficient; thus, we may identify the partition α with each grain. However, particles further away may also play a role in the collective system response due to enduring contacts, in which case \mathcal{W} should encompass further coordination shells. In reality, of course, the collective nature of the system induces contributions from grains which are indeed further away from the grain in question, but the consideration of only its nearest neighbours is a good starting point for solving the system, and is the way in which we proceed to describe the \mathcal{W} function. The significance of the appropriate definition of \mathcal{W} is best understood by the consideration of a response to an external perturbation to the system in terms of analogies with the Boltzmann equation which we will describe in Section 2.5.

Perhaps the most straightforward definition of the function \mathcal{W}^α is given in terms of the Voronoi diagram which partitions the space into a set of regions associating all grain centroids in each region to the closest grain centroid, depicted by line OP in the diagram in Fig. 2.1a. The loop formed by the perpendicular bisectors (ab) of each of the lines joining the central grain to its neighbours is the Voronoi cell, depicted in red. Even though this construction successfully tiles the system, its drawback is that there is no analytical formula for the enclosed volume of each cell. Recently Ball and Blumenfeld (Ball and Blumenfeld, 2002) have shown by an exact triangulation method that the volume defining each grain can be given in terms

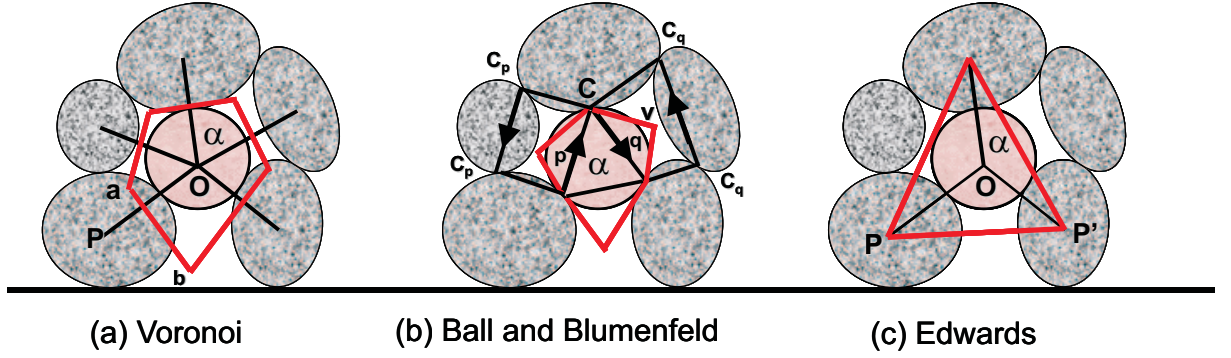


Figure 2.1: Different volume functions as discussed in the text: Voronoi (a), Ball and Blumenfeld (b) and Edwards (c) construction.

of the contact points C using vectors constructed from them (see Fig. 2.1b). The method consists in defining shortest loops of grains in contact with one another (p, q loops), thus defining the void space around the central grain. The difficulty arises in three dimensions since this construction requires the identification of void centres, v . This is not an obvious task, but is currently under consideration. The resulting volume (red) is the antisymmetric part of the fabric tensor, the significance of which is its appearance in the calculation of stress transmission through granular packings (Blumenfeld and Edwards, 2003).

A cruder version for the volume per grain, yet with a strong physical meaning, has been given by Edwards. For a pair of grains in contact, the grains are labeled α, β , the contact points between the grains (assumed to be point contacts for rough, rigid grains) are labeled $m^{\alpha\beta}$, and specify the complete geometrical information of the packing. The centroid of the contacts of grain α is

$$\vec{R}^\alpha = \frac{\sum_\beta m^{\alpha\beta}}{z^\alpha}, \quad (2.5)$$

where z^α is the number of grains in contact with grain α , and the vector from the centre of α to that of β is $\vec{R}^{\alpha\beta}$. The first step is to construct a configurational tensor based on the structural information, which is

$$\mathcal{C}_{ij}^\alpha = \sum_\beta R_i^{\alpha\beta} R_j^{\alpha\beta}. \quad (2.6)$$

Then an approximation for the area in 2D or volume in 3D encompassing the first coordination shell of the grain in question is given as

$$\mathcal{W}^\alpha = 2\sqrt{\text{Det}\mathcal{C}_{ij}^\alpha}. \quad (2.7)$$

Consider the case depicted in the Fig. 2.1c, with grain coordination number 3 in two dimensions, where Eq. (2.7) should give the area of the triangle (red) constructed by the centres of grains which are in contact. The above equation is exact if the area is considered as the determinant of the vector cross product matrix of the two sides of the triangle, but its validity for higher coordination numbers and in 3D has not been tested. However, it is the simplest approximation for the system based on a single coordination shell of a grain. We use this definition of \mathcal{W} for the analysis of our particulate configurations in Section 6.9 and test the validity of this volume per grain approximation in more complex geometries than that depicted in the figure.

2.3.2 Entropy and Compactivity

Now that we have explicitly defined \mathcal{W} it is possible to define the number of microstates of a given volume V which is measured by the volume of the surface $\mathcal{W}(\zeta) = V$ in the phase space of jammed configurations:

$$\Omega_{\text{jammed}}(V) = \int \delta(V - \mathcal{W}(\zeta)) \Theta(\zeta) d\zeta, \quad (2.8)$$

where now $d\zeta$ refers to an integral over all possible jammed configurations and $\delta(V - \mathcal{W}(\zeta))$ formally imposes the constraint to the states in the sub-space $\mathcal{W}(\zeta) = V$. $\Theta(\zeta)$ is a constraint that restricts the summation to only jammed configurations as opposed to the merely static equilibrium configurations as previously discussed. Edwards' radical step is the assumption of the ergodic hypothesis which leads to an analogous thermodynamic entropy associated with this statistical quantity:

$$S(V) = \lambda \log \Omega_{\text{jammed}}(V) = \lambda \log \int \delta(V - \mathcal{W}(\zeta)) \Theta(\zeta) d\zeta, \quad (2.9)$$

which governs the macroscopic behaviour of the system. Here λ plays the role of the Boltzmann constant. The corresponding analogue of temperature, christened by Edwards as the ‘‘compactivity’’, is defined as

$$\frac{1}{X_V} = \frac{\partial S}{\partial V}, \quad (2.10)$$

where the subscript V refers to the fact that it is the derivative of the entropy with respect to the volume.

This is a bold statement, which perhaps requires further explanation in terms of the actual role of compactivity in describing granular systems. We can think of

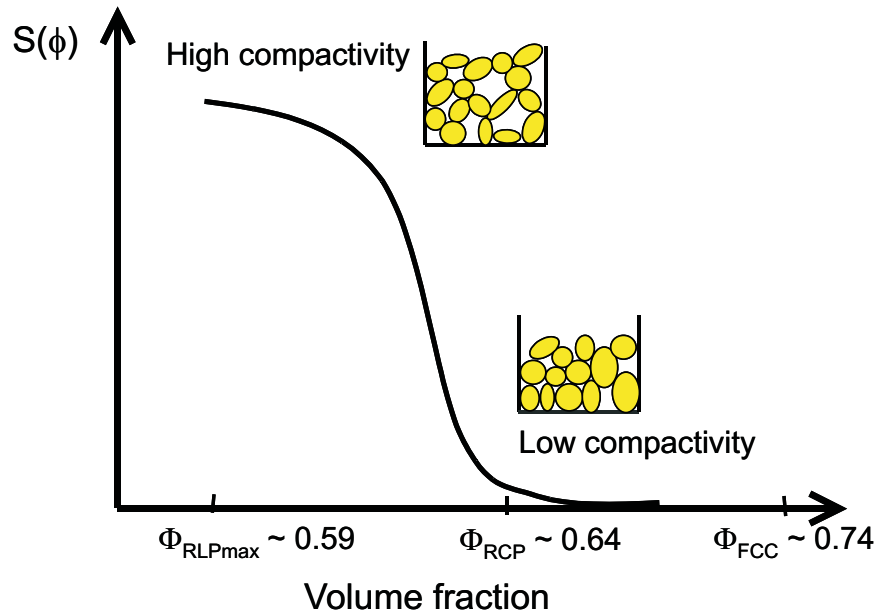


Figure 2.2: Interpretation of the compactivity and entropy in terms of different packings. See also Fig. 1.2.

the compactivity as a measure of how much more compact the system could be, i.e. a large compactivity implies a loose configuration (e.g. random loose packing, RLP) while a reduced compactivity implies a more compact structure (e.g. random close packing, RCP). In terms of the reversible branch of the compaction curve large amplitudes generate packings of high compactivities, while in the limit of the amplitude going to zero a low compactivity is achieved. In terms of the entropy, many more configurations are available at high compactivity, thus the dependence of the entropy on the volume fraction can be qualitatively described as in Fig. 2.2. In the figure, for monodisperse packings the RCP is identified at $\phi \approx 0.64$ (?), the maximum RLP fraction is identified at $\phi \approx 0.59$ (Scott, 1960), while the crystalline packing, FCC, is at $\phi = 0.74$, but cannot be reached by tapping.

At any given tapping amplitude, there exists an equilibrium volume fraction toward which the system slowly evolves. For instance, a system may find itself at a lower entropy than the equilibrium curve by the application of an internal constraint at a given volume fraction. This situation can be achieved by creating small crystalline regions within a packing configuration of a lower density, and looser regions compensating for the volume reduction such that the total volume of the system remains constant. This configuration, given that it is not jammed, will tend toward the equilibrium packing via the application of a small perturba-

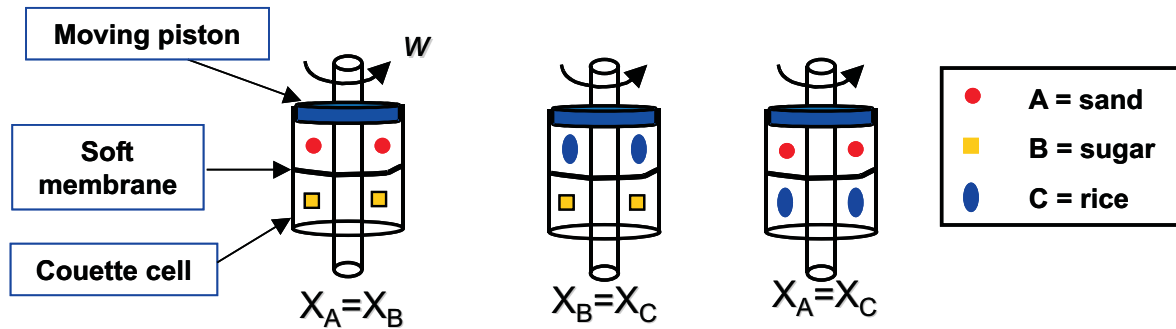


Figure 2.3: ABC experiment to test the zeroth law of granular thermodynamics.

tion by increasing its entropy. Such an example will be made more explicit in the derivation of the Boltzmann equation for granular materials. At volume fractions beyond the RCP (and at atmospheric pressure) the system is not able to explore the configurations as they can only be achieved by the partial crystallisation of the sample, where there are very few configurations available.

It becomes clear from Eq. (2.10) that the compactivity is only applicable in equilibrated jammed states. As an analogue of temperature, it should also obey the zero-th law of thermodynamics. Hence, two different powders in physical contact with one another should equilibrate at the same compactivity, given a mechanism of momentum transfer between the two systems. Indeed, we may think of an appropriate laboratory experiment which would test this hypothesis under certain conditions necessary for creating the analogous situation to heat flow.

Two powders, A and B, of different grain types are poured into a vertical couette cell as shown in Fig. 2.3. The grains must experience an equivalent tapping or shearing regime, which is achieved by the rotation of the inner cylinder of the couette cell. The species are separated by a flexible diaphragm, such that momentum transfer between the two systems is ensured. The two powders must be well separated such that there is no mixing involved, but in contact nevertheless. The grains are kept at a constant pressure by a piston which is allowed to move freely to accommodate for the changes in volume experienced by the two types of grains. Gravity may play a role in the experiment, which is avoided by density matching the particles with a suspending fluid.

The experiment consists in placing powders A and B together in the above cell and slowly shearing them at a given velocity. The powders should come to equilibrium volumes V_A and V_B , with equivalent respective compactivities,

$X_A = X_B = X$. While it is easy to measure the volumes of the two systems, the measurement of their compactivities employs more sophisticated methods, discussed in the following sections. In the absence of a compactivity scale, we use powder B as a ‘thermometer’ by placing it in contact with a third powder C. The volume B is kept at V_B and the volume of C is allowed to fluctuate until it reaches the equilibrium state. Finally, powders A and C are put together to test if they will reach the same volumes as they did in previous runs in contact with B, thus proving the zeroth law.

2.3.3 Remarks

To summarise, the granular thermodynamics is based on two postulates:

1. While in the Gibbs construction one assumes that the physical quantities are obtained as an average over all possible configurations at a given energy, the Edwards ensemble consists of only the jammed configurations at the appropriate volume.
2. As in the microcanonical equilibrium ensemble, the strong ergodic hypothesis is that all jammed configurations of a given volume can be taken to have equal statistical probabilities.

The ergodic hypothesis for granular matter was treated with skepticism, mainly because a real powder bears knowledge of its formation and the experiments are therefore history dependent (Nowak et al., 1998). Thus, any problem in soil mechanics or even a controlled pouring of a sand pile does not satisfy the condition of all jammed states being accessible to one another as ergodicity has not been achieved, and the thermodynamic picture is therefore not valid. This point has been discussed in Section 1.2.2 where the condition to achieve the true jammed state where ergodicity could be applied has been discussed in detail.

It is often noted in the literature that although the simple concept of summing over all jammed states which occupy a volume V works, there is no first principle derivation of the probability distribution of the Edwards ensemble as it is provided by Liouville’s theorem for equilibrium statistical mechanics of liquids and gases. In granular thermodynamics there is no justification for the use of the \mathcal{W} function to describe the system as Liouville’s theorem justifies the use of the energy in the microcanonical ensemble. In Section 2.5 we will provide an intuitive proof for the use of \mathcal{W} in granular thermodynamics by the analogous proof of the Boltzmann equation.

The comment was also made that there is no rigorous proof of entropy being a basis for granular statistical mechanics, and that it cannot be shown that entropy increases until the equilibrium jammed distribution is achieved. Although everyone believes that the second law of thermodynamics is universally true in thermal systems, the only accessible proof comes in the Boltzmann equation, as the ergodic theory is a difficult branch of mathematics which will not be covered in the present discussion. By investigating the assumptions and key points which led to the derivation of the Boltzmann equation in thermal systems, it is possible to draw analogies for an equivalent derivation in jammed systems. The derivation of the Boltzmann equation for jammed systems shows that this analysis can be used to produce a second law of thermodynamics, $\delta S \geq 0$. The equivalence in the approaches only becomes evident with arriving at Eq. (2.9).

It should be noted that there is an extensive literature on granular gases (Savage, 1984; Jenkins and Savage, 1983), which are observed when particles are fluidised by vigorous shaking, thus inducing continuous particle collisions. Despite a powerful literature on this topic, it is not applicable to the problem of jamming.

2.4 The Classical Boltzmann Equation

The notion of entropy is important for thermal systems because it satisfies the second law,

$$\frac{\partial S}{\partial t} \geq 0, \quad (2.11)$$

which states that there is a maximum entropy state which, according to the evolution in Eq. (2.11), any system evolves toward, and reaches at equilibrium. A ‘semi’-rigorous proof of the Second Law was provided by Boltzmann (the well-known ‘H-theorem’), by making use of the ‘classical Boltzmann equation’, as it is now known.

In order to derive this equation, Boltzmann made a number of plausible assumptions concerning the interactions of particles, without proving them rigorously. The most important of these assumptions were:

- The collision processes are dominated by two-body collisions (Fig. 2.4a). For a dilute gas, this is plausible since the system is of very low density, and the probability of there being three or more particles colliding is infinitesimal.
- Collision processes are uncorrelated, i.e. all memory of the collision is lost on completion and is not remembered in subsequent collisions: the famous

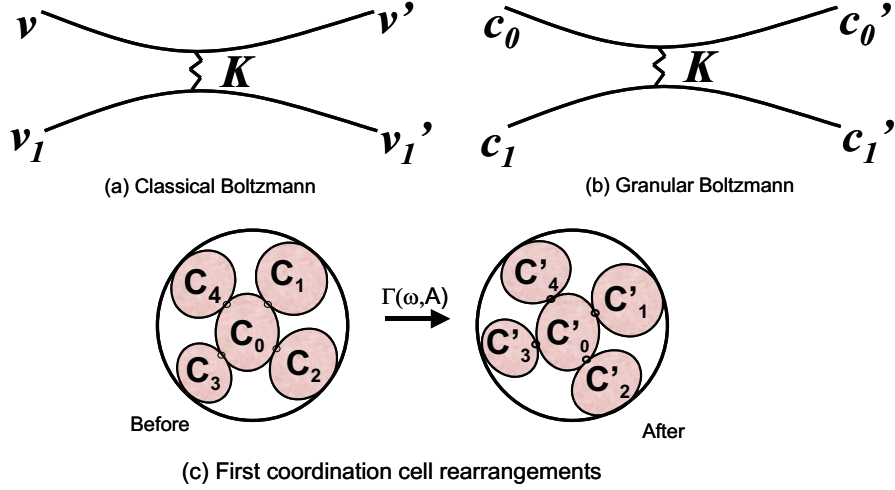


Figure 2.4: (a) Collision of two particles in a dilute gas. (b) “Collision of two configurations” given in terms of two contact points in a jammed material. (c) Rearrangements inside a pocket a under the first coordination shell approximation of grain α .

Stosszahlansatz. This is also valid only for dilute gases, but the proof is more subtle.

Thus, Boltzmann proves Eq. (2.11) for a dilute gas only, but this is a readily available situation. The remaining assumptions have to do with the kinematics of particle collisions, i.e. conservation of kinetic energy, conservation of momentum, and certain symmetry of the particle scattering cross-sections.

Let $f(v, r)$ denote the probability of a particle having a velocity v at position r . This probability changes in time by virtue of the collisions. The two particle collision is visualised in Fig. 2.4a where v and v_1 are the velocities of the particles before the collision and v' and v'_1 after the collision.

On time scales larger than the collision time, momentum and kinetic energy conservation apply:

$$\begin{aligned} mv + mv_1 &= mv' + mv'_1 \\ \frac{1}{2}mv^2 + \frac{1}{2}mv_1^2 &= \frac{1}{2}mv'^2 + \frac{1}{2}mv'^2_1. \end{aligned} \quad (2.12)$$

Then, the distribution $f(v, r)$ evolves with time according to

$$\frac{\partial f}{\partial t} + v \frac{\partial f}{\partial r} + \int \mathcal{K}(v, v'; v_1, v'_1) \left(f(v)f(v_1) - f(v')f(v'_1) \right) d^3v_1 d^3v' d^3v'_1 = 0 \quad (2.13)$$

The kernel \mathcal{K} is positive definite and contains δ functions to satisfy the conditions (2.12), the flux of particles into the collision and the differential scattering cross-section. Considering the case of homogeneous systems, i.e. $f = f(v)$, then

$$S = -k_B \int f \log f dv. \quad (2.14)$$

Defining $x = f f_1 / f' f'_1$ we obtain

$$\begin{aligned} \frac{\partial S}{\partial t} &= \int \mathcal{K} \log x (1-x) d^3 v_1 d^3 v' d^3 v'_1 \\ &\quad (1-x) f'_1 f'_2 \geq 0 \\ &\quad \mathcal{K} \geq 0. \end{aligned} \quad (2.15)$$

Hence $\partial S / \partial t \geq 0$ (Landau and Lifshitz, 1970).

It is also straightforward to establish the equilibrium distribution where $\partial S / \partial t = 0$ since it occurs when the kernel term vanishes. This occurs when the condition of detailed balance is achieved, $x = 1$:

$$f(v) f(v_1) = f(v') f(v'_1). \quad (2.16)$$

The solution of Eq. (2.16) subjected to the condition of kinetic energy conservation, i.e. $K \sim \delta(1/2mv^2 - 1/2mv'^2)$ is given by the Boltzmann distribution

$$f(v) = \left(\frac{m}{k_B T 2\pi} \right)^{3/2} e^{-\frac{1}{2}\beta m v^2} \quad (2.17)$$

where $\beta = 1/k_B T$. Equation (2.17) is a reduced distribution and valid only for a dilute gas. The Gibbs distribution represents the full distribution and is obtained by replacing the kinetic energy in (2.17) by the total energy of the state to obtain:

$$P(E) \sim e^{-\beta E}. \quad (2.18)$$

The question is whether a similar form can be obtained in a granular system in which we expect

$$P(W) \sim e^{-W/\lambda X}, \quad (2.19)$$

where X is the compactivity in analogy with $T = \partial E / \partial S$. Such an analysis is shown in the next section in an approximate manner.

2.5 ‘Boltzmann Approach’ to Granular Matter

The analogous approach to granular materials consists in the following:

- the creation of an ergodic grain pile suitable for a statistical mechanics approach via a method for the exploration of the available configurations analogous to Brownian motion,
- the definition of the discrete elements tiling the granular system via the volume function \mathcal{W} (the sum of which provides the analogous ‘Hamiltonian’ to the energy in thermal systems),
- an equivalent argument for the energy conservation expressed in terms of the system volume necessary for the construction of the Boltzmann equation.

We have already established the necessity of preparing a granular system adequate for real statistical mechanics so as to emulate ergodic conditions. The grain motion must be well-controlled, as the configurations available to the system will be dependent upon the amount of energy/power put into the system. This pre-treatment is analogous to the averaging which takes place inherently in a thermal system and is governed by temperature.

As explained, the granular system explores the configurational landscape by the external tapping introduced by the experimentalist. The tapping is characterised by a frequency and an amplitude (ω, A) which cause changes in the contact network, according to the strength of the tap. The magnitude of the forces between particles in mechanical equilibrium and their confinement determine whether each particle will move or not. The criterion of whether a particular grain in the pile will move in response to the perturbation will be the Mohr-Coulomb condition of a threshold force, above which sliding of contacts can occur and below which there can be no changes. The determination of this threshold involves many parameters, but it suffices to say that a rearrangement will occur between those grains in the pile whose configuration and neighbours produce a force which is overcome by the external disturbance.

The concept of a threshold force necessary to move the particles implies that there are regions in the sample in which the contact network changes and those which are unperturbed, shown in Fig. 2.5.

In order to present this argument pictorially, in response to a vibration of amplitude A and frequency ω the system will find a steady-state volume after some relaxation time, regions of which will be prone to rearrangements and others which will be unaffected by A, ω . Of course, since this is a description of a collective

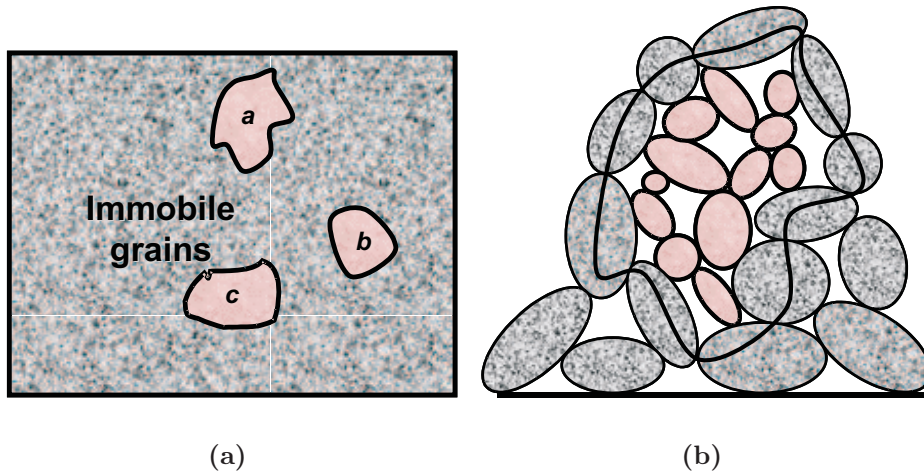


Figure 2.5: Schematic of a jammed granular system showing (a) regions of mobile grains a, b, c in a matrix of immobile grains below the Coulomb threshold. (b) Detail of a pocket of mobile grains a surrounded by immobile grains which are shaded.

motion behaviour, the region which can move may expand or contract, but the picture at any moment in time will contain pockets of motion encircled by a static matrix. Each of these pockets has a perimeter, defined by the immobile grains. It is then possible to consider the configuration before and after the disturbance inside this well-defined geometry.

The present derivation assumes the existence of these regions. It is equivalent to the assumption of a dilute gas in the classical Boltzmann equation, although the latter is readily achieved experimentally.

The energy input must be on the level of noise, such that the grains largely remain in contact with one another, but are able to explore the energy landscape over a long period of time. In the case of external vibrations, the appropriate frequency and amplitude can be determined experimentally for different grain types, by investigating the motion of the individual grains or by monitoring the changes in the overall volume fraction over time. It is important that the amplitude does not exceed the gravitational force, or else the grains are free to fly up in the air, re-introducing the problem of initial creation just as they would if they were simply poured into another container.

Thus within a region a we have a volume $\sum_{\alpha \in a} \mathcal{W}^\alpha$ and after the disturbance a volume which is now $\sum_{\alpha \in a} \mathcal{W}'^\alpha$ as seen in Fig. 2.4c. In Section 2.3.1 we have discussed how to define the volume function \mathcal{W}^α as a function of the contact network. In this case, the simplest “one grain” approximation is used as the “Hamiltonian” of the volume as defined by Eq. (2.7). In reality it is much more complicated, and although there is only one label α on the contribution of grain

α to the volume, the characteristics of its neighbours may also appear. Instead of energy being conserved, it is the total volume which is conserved while the internal rearrangements take place within the pockets described above. Hence

$$\sum_{\alpha \in a} \mathcal{W}^\alpha = \sum_{\alpha \in a} \mathcal{W}'^\alpha. \quad (2.20)$$

We now construct a Boltzmann equation. Suppose z particles are in contact with grain α_0 , as seen in Fig. 2.4c. For rough particles $z = 4$ while for smooth $z = 6$ at the isostatic limit. The probability distribution will be of the contact points which are represented by the tensor \mathcal{C}^α for each grain, where $\alpha = 0 - 4$ in this case. So the analogy of $f(v)$ for the Boltzmann gas equation becomes $f(\mathcal{C}^\alpha)$ for the granular system and represents the probability that the external disturbance causes a particular motion of the grains. We therefore wish to derive an equation

$$\frac{\partial f(\mathcal{C}^0)}{\partial t} + \int \mathcal{K}(\mathcal{C}^\alpha, \mathcal{C}'^\alpha) \left(f_0 f_1 f_2 f_3 f_4 - f'_0 f'_1 f'_2 f'_3 f'_4 \right) \prod_{\alpha \neq 0} d\mathcal{C}^\alpha d\mathcal{C}'^\alpha = 0 \quad (2.21)$$

The term \mathcal{K} contains the condition that the volume is conserved (2.20), i.e. it must contain $\delta(\sum \mathcal{W}_\alpha - \sum \mathcal{W}'_\alpha)$. The cross-section is now the compatibility of the changes in the contacts, i.e. \mathcal{C}^α must be replaced in a rearrangement by \mathcal{C}'^α (unless these grains part and make new contacts in which case a more complex analysis is called for). We therefore argue that the simplest \mathcal{K} will depend on the external disturbance A, ω and on \mathcal{C}^α and \mathcal{C}'^α , i.e.

$$\frac{\partial f(\mathcal{C}^0)}{\partial t} + \int \prod_{\alpha=0}^z \delta\left(\sum_{\alpha} \mathcal{W}^\alpha - \sum_{\alpha} \mathcal{W}'^\alpha\right) \mathcal{J}(\mathcal{C}^\alpha, \mathcal{C}'^\alpha) \left(\prod_{\alpha=0}^z f_\alpha - \prod_{\alpha=0}^z f'_\alpha \right) = 0 \quad (2.22)$$

where \mathcal{J} is the cross-section and it is positive definite. The Boltzmann argument now follows. As before

$$S = -\lambda \int f \log f, \quad x = \frac{f_0 f_1 f_2 f_3 f_4}{f'_0 f'_1 f'_2 f'_3 f'_4}, \quad (2.23)$$

and

$$\frac{\partial S}{\partial t} \geq 0, \quad (2.24)$$

the equality sign being achieved when $x = 1$ and

$$f_\alpha = \frac{e^{-\mathcal{W}^\alpha / \lambda X}}{Z}, \quad (2.25)$$

with the partition function

$$Z = \sum e^{-w^\alpha/\lambda X} \Theta, \quad (2.26)$$

and the analogue to the free energy being $Y = -\lambda X \ln Z$, and $X = \partial V/\partial S$. The detailed description of the kernel \mathcal{K} has not been derived as yet due to its complexity. Just as Boltzmann's proof does not depend on the differential scattering cross section, only on the conservation of energy, in the granular problem we consider the steady state excitation externally which conserves volume, leading to the granular distribution function, Eq. (2.25).

It is interesting to note that there is a vast and successful literature of equilibrium statistical mechanics based on $\exp(-H/k_B T)$, but a meager literature on dynamics based on attempts to generalise the Boltzmann equation or, indeed, even to solve the Boltzmann equation in situations remote from equilibrium where it is still completely valid. It means that any advancement in understanding how it applies to analogous situations is a step forward.

Chapter 3

Emulsions as a Model System

There may be complex scientific explanations behind the creation of emulsions, but all you need to make them properly is some patience and a strong mixing arm.

Heston Blumenthal,

chef of the Fat Duck in Berkshire, the Guardian

3.1 Introduction

Our approach to the study of emulsions is interdisciplinary, in that the emulsion serves as a paradigm for a wide range of systems that experience structural arrest. The aim is to present a new perspective on emulsion research within the larger field of statistical physics as a whole. The design of a model emulsion system is the crucial step in achieving this goal.

The system used in this study has the particular aim to model granular materials, and several conditions must be satisfied to facilitate this analogy. The constituent emulsion particles should be seen as soft, compressible spheres, pushing one another and deforming when their interparticle distance is smaller than the sum of their radii. We show that we have achieved the conditions under which these requirements are satisfied:

1. elasticity is governed by surface tension only,
2. there is no significant adhesion between droplets,
3. depletion attraction is avoided (i.e. purely repulsive potential),
4. emulsion is stable to coalescence and Ostwald ripening.

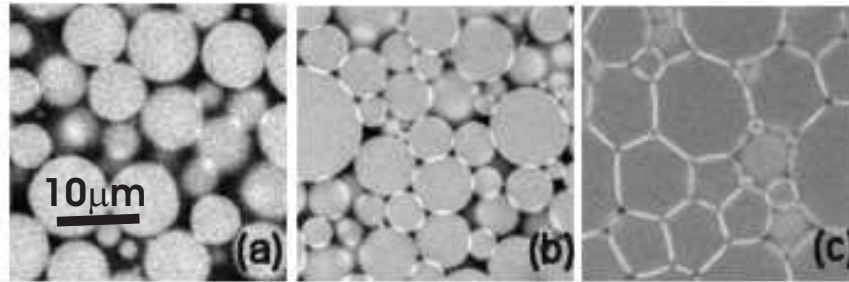


Figure 3.1: Confocal 2D fluorescent images of emulsions under varying compression rates: 1g(a), 6000g(b) and 8000g(c). All images are taken on the same scale. Contrast is provided using Nile red dye in all the fluorescent confocal microscope images shown in the Thesis.

Moreover, the experimental technique requires that the emulsion be transparent, yet fluorescently dyed to provide contrast between the phases. A narrow enough size distribution is needed for adequate statistical measures. The demands on the physical system as well as on the experimental technique are discussed in this Chapter. The areas of droplet deformation and the structural features of the particulate packing are then investigated in detail in Chapter 6.

The successful system consists of a dense packing of silicone oil droplets, with a sufficiently elastic surfactant stabilising layer to mimic solid particle behaviour, suspended in a continuous phase fluid. The refractive index of the continuous phase is raised by the addition of glycerol to make a transparent sample, without destabilising the emulsion. The size distribution of the droplets is controlled by narrow gap shearing, post-emulsification, to achieve a large statistical ensemble within a confocal 3D image.

The emulsion system is then detected in the confocal microscope by means of fluorescence. It consists of two phases, the dispersed and the continuous phase, which are distinguished in the microscope using a single dye owing to the differential solubility of the dye molecules in each phase, to be discussed in Chapter 4. The fluorescence is manipulated such that, upon compression, the deformed areas arising from the forces between the droplets exhibit a higher fluorescence intensity than the rest of the sample, as seen in Fig. 3.1.

Raising the volume fraction of the emulsion, beyond random close packing, introduces compressive forces between the droplets. The emulsion volume fraction is defined as:

$$\phi = V_d/V_{tot} \quad (3.1)$$

where $V_{tot} = V_d + V_c$, V_d is the volume of the dispersed phase and V_c is the volume

of the continuous phase. The volume fraction can be varied with relative ease: it can be increased by centrifugation or by osmosis (Mason et al., 1997b), and decreased by dilution. Moreover, the droplet deformation upon compression is fully and spontaneously reversible upon removal of the external force.

The effect of emulsion compression is depicted in the sequence of images in Fig. 3.1 showing 2D slices from the middle of the sample volume after: (a) creaming under gravity, (b) centrifugation at 6000g and (c) centrifugation at 8000g. The 3D images are analysed to provide the structural information of the droplet packing as well as the transmission of stress.

First, a brief review of emulsions is given in terms of the factors influencing their preparation, stabilisation and physical properties (Bibette et al., 1999; Bibette et al., 2002). Then, the experimental methods leading to a stable transparent emulsion of well-controlled droplet size are presented, together with the difficulties encountered in the process. Finally, the resulting emulsion system is characterised in terms of the surface tension of the droplets and the interaction potential between them, by the measurement of the critical micellar concentration (CMC) of the aqueous phase. Preliminary experiments, which lead to the selection of compatible ingredients are also presented, as they indicate the problems which may arise.

3.2 Background

Emulsions are a class of material that you can find amongst the most commonly used ingredients in the kitchen. No wonder they have been studied empirically for far longer than using the fundamental laws of physics. The true experts of emulsion rheology and connoisseurs of their thermodynamic properties are perhaps distinguished chefs and grandmothers who make unforgettable custard, mayonnaise and butter, the recipes of which have been passed down through generations to achieve the best texture, smoothness, opacity and so on. It is important to get that pecking order right, before praising distinguished physicists for their contribution in quantifying all those properties and searching for universal laws to describe and predict the required emulsion system. There is an intermediate stage which should not be overlooked and which provides the broadest literature on emulsion research. It is the industrial contribution, aiming to optimise their production and to control parameters which are likely to stimulate the taste buds of the end user (Heusch, 2002). This research, although mostly empirical, has led to important fundamental discoveries which have enabled the use of emulsions as a well-controlled model system. Before venturing into the specificities of their particular use within this

Thesis, the reader will be acquainted with emulsions through the following brief review of their properties.

3.2.1 Applications of Emulsions

Emulsions are hugely important materials for their numerous and widespread commercial applications (Becher, 1983). Most of their technological applications are based on the fact that emulsions can transport water or oil soluble active substances within the appropriate dispersed phase to the desired area and subsequently release them. For instance, this makes them ideal for surface treatments such as painting, paper-coating and lubrication, by simple evaporation of the continuous phase once the emulsion has been applied. Particularly viscous (or even solid) hydrophobic substances can be dispersed into a dilute emulsion to fluidise them, facilitating their transport and delivery (e.g. bitumen for road-surfaces).

Another property governing their usage is the dependence of their mechanical properties on the density, particularly useful in the food industry (e.g. mayonnaise) and cosmetics (e.g. creams, lotions). Rheology governs much of their exploitation in these domains because the control of texture and stiffness are important to the end user. More sophisticated emulsions, containing more than one dispersed phase (double emulsions) are used in precisely controlled ways in drug delivery, as carriers of the active agents (Dinsmore et al., 2002). The importance of emulsions in every day life has led to many empirical laws describing their behaviour and a broad literature on their properties has arisen from it. In addition, the studies of individual interdroplet forces, colloidal structures, emulsion elasticity and controlled emulsification methods have greatly improved our understanding of the basic principles.

Relatively speaking, there have been very few attempts in understanding emulsions from a fundamental point of view, that is, from laws of physics governing the droplet interactions and then passing from discrete to continuum models in order to describe their macroscopic behaviour (Princen, 1983; Mason et al., 1995). This is the first exploitation of emulsions as a model for granular matter, suitable for use as a system of a packing of frictionless spheres, for which numerous theoretical and simulation studies could be applied to and compared with (Silbert et al., 2002; Makse et al., 2000).

3.3 Emulsion Properties

Emulsions belong to a wider class of materials, colloidal systems, in that they consist of two immiscible phases, one of which is dispersed into the other. The colloidal length scale of the dispersed phase varies between a few molecular sizes up to several microns. Colloids can be separated into two distinct categories: a) thermodynamically stable species which can form spontaneously, and b) those which are metastable, requiring an energy input to form. The latter are inherently out of equilibrium, therefore necessitating specific surface chemistry to prevent the coalescence of the individual dispersed particles and an eventual macroscopic phase separation.

Emulsions belong to this metastable category of material, where both of the phases are liquids and their interface is stabilised by the presence of surface-active species. The surfactant provides a barrier to coalescence by introducing an effective repulsion between the droplets, either by electrostatics or steric hindrance, favouring the individual droplets. By definition, direct emulsions consist of droplets of oil in water, and inverse emulsions are water-in-oil.

The dispersed phase is introduced into the continuous phase by fragmentation using shear forces which influence the size distribution and range of the resulting emulsion. Emulsification methods are extremely important in industrial production, particularly in terms of controlling stability and size distributions, and recent important advances are constantly being made towards achieving that goal.

3.3.1 Kinetic Stability

Emulsion stabilisation is an area of research in itself because their stability is always achieved on a kinetic rather than a thermodynamic basis in the case of macroemulsions (Bibette et al., 1992). In other words, it is ensured that their rupture does not take place on experimentally measurable timescales.

There are two main mechanisms by which phase separation can occur, which should be eliminated when designing the emulsion system. The first, known as Ostwald ripening, is based on a slight miscibility of the two phases so that the dispersed phase can diffuse through the continuous phase from one droplet to another causing the larger droplets to grow at the expense of smaller ones and ultimately resulting in complete phase separation (see Section 3.8.2). The second process is coalescence (Deminiere et al., 1999), which involves the rupture of the film between two adjacent droplets to form one large droplet in order to reduce the interfacial tension. Both of these processes are greatly slowed down by the presence of surfactants, prolonging the emulsion life span essentially indefinitely.

The choice of surfactant is extremely important as it determines the emulsion type, stability and interdroplet potential. The property of the surfactant which predicts its stabilising power with the oil and the water phase in question is the hydrophilic-lipophilic balance, known as the HLB number. This number indicates the polarity of the molecules in an arbitrary range of 1-40, according to the balance between the hydrophilic (“water-loving”) and lipophilic (“oil-loving”) portions of the molecule. The HLB number increases with increasing hydrophilicity. For instance, HLB values lower than 7 will form water-in-oil emulsions whereas higher HLB values tend to form direct emulsions. The task of proper selection of compatible materials should not be underestimated, as many parameters must be simultaneously satisfied.

3.3.2 Interdroplet Potential

Emulsions are subject to a variety of colloidal interactions, which can be fine-tuned by the control of their surface chemistry and environment. Understanding the interdroplet forces, both short and long range, is important in understanding their collective behaviour. In the case of the model system, it is important to ensure a purely repulsive potential, as any attraction between the droplets induces structural changes, such as clustering (see Section 3.8.2), and would interfere with the measurement of interdroplet forces, to be discussed in Chapter 6. It is for that reason that the discussion of interdroplet forces below is given with reference to the specific features of the model system, presented in detail in Section 3.4.

Repulsive Forces

Repulsive interactions can be directly measured using the magnetic chaining technique (Leal-Calderon et al., 1994). This probes steric as well as electrostatic forces of the order of pN . The system used in this Thesis consists of silicone oil droplets stabilised by sodium dodecyl sulfate (SDS). This particular system has been investigated by Mondain-Monval et al. (Mondain-Monval et al., 1995) in terms of the repulsive forces between colloidal droplets as a function of the surfactant concentration. The higher the surfactant concentration, the larger the repulsion and the shorter its range, as shown in Fig. 3.2.

Even though the droplet interaction potential is governed by the electrostatic repulsion arising from the presence of anionic SDS molecules on the surface of the droplets, there is an additional ionic atmosphere surrounding the particle charge,

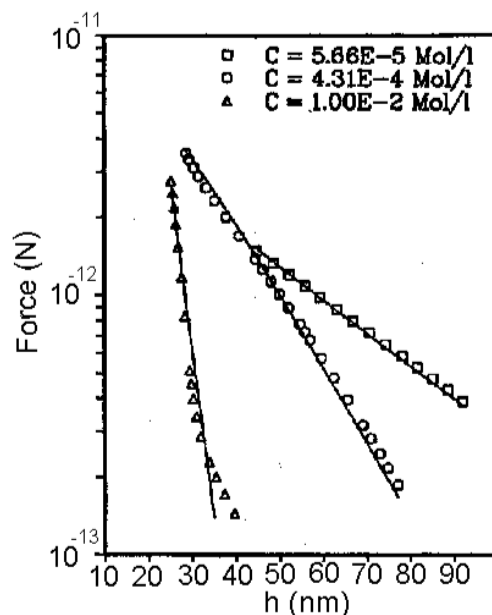


Figure 3.2: Evolution of the force with the spacing h between droplets of radius 94nm, for three surfactant (SDS) concentrations. The graph is reproduced from the literature (Mondain-Monval et al., 1995).

to satisfy electroneutrality. It forms a double layer with the surface charge and determines the range of the repulsive interaction. At the concentration comparable to that used in our experiments, i.e. 10mM SDS, a short range repulsive interaction of 30nm for droplets of radius 94nm is measured.

Our system differs from theirs in two ways:

- the presence of glycerol, which slightly alters the surfactant solubility (see Section 3.6.1),
- the larger average particle radius ($\approx 3\mu\text{m}$), which should not significantly change the interaction potential.

Since these differences should not have a profound effect on the range and strength of the repulsion, the results presented in the figure are applicable to our model system. Therefore, we can conclude that a relatively high surfactant concentration implies a large short range repulsion owing to the decrease in the Debye screening length.

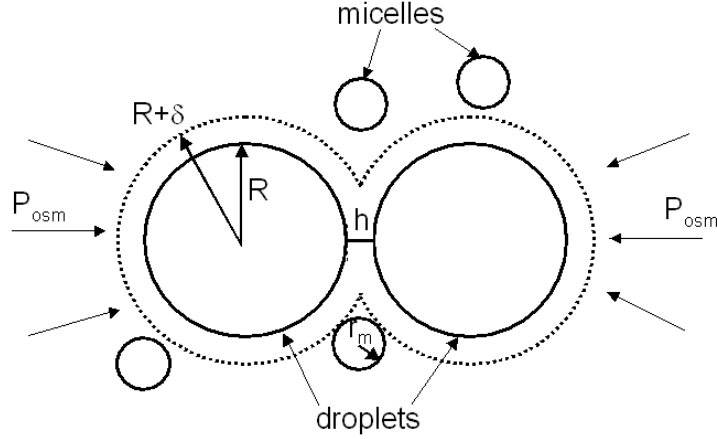


Figure 3.3: Schematic of the depletion mechanism. Micelles are excluded from the gap leading to an uncompensated pressure in the region. This gives rise to a depletion force.

Depletion Attraction

Depletion interactions may induce attraction between droplets, and this ‘soft’ potential has also been measured (Richetti and Kekicheff, 1992). If the SDS concentration is too high, the repulsive force may coexist with an attractive depletion force if there are any surfactant aggregates present in solution, as shown in Fig. 3.3. These nanometer-sized aggregates are called micelles and form above the critical micellar concentration (CMC). Hence, we measure the CMC of our system in Section 3.6.2 and perform experiments below that concentration.

On the other hand, the attraction induced by adding excess surfactant is a useful tool for the fractionation of polydisperse emulsions into more controlled size ranges (Bibette, 1991; Manoj et al., 1998). This method is applied to our system in Section 3.5.1.

The depletion attraction, entropic in origin, occurs when two large droplets approach one another, excluding the micelles from the region in between the droplets. This leads to an uncompensated osmotic pressure. This depletion interaction scales with the osmotic pressure of the micelles and the exclusion volume in between the droplets. The contact potential, given that the droplet size R is much larger than the characteristic exclusion length Δ , can be approximated by

$$u_c = -\frac{3}{2}kT\phi_m\frac{R}{\Delta} \quad (3.2)$$

where ϕ_m is the volume fraction of the micelles. Therefore, by adjusting the

concentration of surfactant above its CMC value, the volume fraction of micelles can be easily controlled, and with it the extent of attraction.

Adhesion

Upon contact emulsion droplets may also experience spontaneous adhesion when there exists a pronounced attraction, which leads to large contact angles when they adhere to one another and therefore large areas of deformation between the droplets. It is important to note that adhesion is an entirely different phenomenon to the forces exerted between droplets in response to an external pressure, studied in this work, even though this difference is not evident from the images of each source of surface deformation, as seen in the image in Fig. 3.4. Previous work has shown that droplets stabilised by SDS only exhibit adhesion in the presence of monovalent salts such as KCl and NaCl (Aronson and Princen, 1982). The larger the counter ion, the less pronounced the adhesion, such that LiCl induces very little adhesive attraction (see Section 3.8.2).

The surface film thickness of the droplets at different volume fractions above the random close packing limit has been previously measured by scattering. These measurements show 175\AA thickness at low ϕ which flattens to 50\AA for a biliquid foam. This observation is important in that it confirms that the deformed interfaces are subresolution of the confocal microscope, relevant to the image analysis described in Chapter 5.

3.3.3 Emulsion Elasticity

Depending on the volume fraction, which can vary between zero and almost one due to the compressibility of the droplets, emulsion mechanical properties show interesting changes from fluid to solid behaviour. Namely, a dilute emulsion behaves like a Newtonian fluid whereas a highly concentrated emulsion, above the random close packing limit where the particles are all touching one another, exhibits viscoelastic behaviour (Mason et al., 1995; Mason et al., 1997b; Mason et al., 1997a). Increasing the volume fraction of the dispersed phase is achieved by the application of an osmotic pressure Π on the system. This effectively squeezes out the continuous phase, causing the droplets to firstly deform and eventually form a biliquid foam in which a honeycomb cellular structure persists.

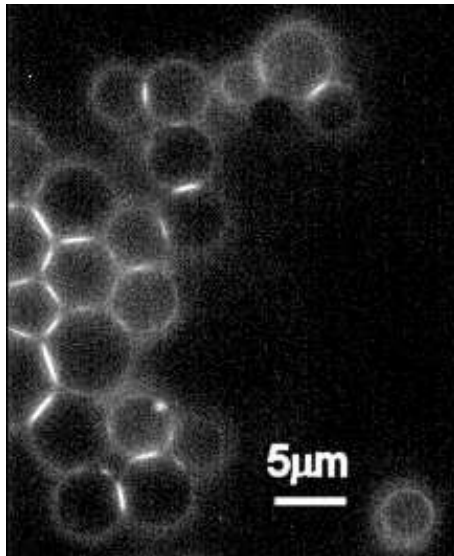


Figure 3.4: A dilute emulsion ($\phi = 10\%$) at a high surfactant concentration (10CMC), in the presence of NaCl (0.1M), experiences attraction due to both depletion flocculation and adhesion. The deformed interfaces fluoresce with a higher intensity, just as in the compressed emulsion with a repulsive potential, but the cause is crucially different.

Osmotic Pressure $\Pi(\phi)$ and Elastic Modulus $G(\phi)$

The basic physics explaining emulsion elasticity upon compression is rationalised in terms of the ability to store energy in the areas of surface deformation. Two repulsive droplets under compression will begin to deform before their interfaces actually touch. Thus, emulsion droplets minimise their free energy by reducing their repulsion at the expense of creating some additional surface area, i.e. $\partial G = \sigma \partial A$. The amount of surface deformation in the system determines the equilibrium elastic energy G stored at a given osmotic pressure. Although Π and G represent fundamentally different properties, they both depend on the degree of deformation and therefore the droplet volume fraction ϕ . Π reflects the storage of energy F as a function of the volume fraction under static conditions, i.e. $\Pi = -\partial F / \partial V$.

This relation has been investigated experimentally on polydisperse and monodisperse systems by rheology. The monodisperse emulsion system, reported by Mason et al., only differs to ours in that the continuous phase does not contain glycerol, thus their rheological results provide insight into the elasticity of our system as well. They find that an anharmonic interdroplet potential (discussed in Section 6.2.1) and disorder in the system account for the discrepancies between the theory

Component	Density $\rho(\text{g}/\text{cm}^3)$	Refractive index n (at $\lambda=488\text{nm}$)	Viscosity $\eta(\text{cS})$
Silicone oil	0.97	1.403	10
Water	1.00	1.331	0.89
Glycerol	1.261	1.474	1000

Table 3.1: Components of the successful emulsion system, stabilised by $\approx 10\text{mM}$ SDS.

and the experiments. We are able to probe the appropriate force model on the microscopic scale in Section 6.6 of Chapter 6.

The compressibility of emulsions and the ability to store energy in this way is an important emulsion property. It facilitates many of the important applications, the simplest being the spreading of butter and cosmetic creams.

3.4 Emulsion Preparation

Since the subject of emulsion preparation is not straightforward, it is most convenient to begin with a description of the successful system used throughout this study, with subsequent explanations of the issues involved in achieving the necessary stability and size range for its use. The collaboration with Jérôme Bibette led to the development of the system described here through useful discussions.

The recipe for a stable emulsion is based on a well-characterised emulsion system previously reported by (Mason et al., 1995), which is modified to raise the refractive index of the water phase to match that of the oil, producing a transparent sample suitable for confocal microscopy. A further requirement is that the emulsion remains stable to coalescence and Ostwald ripening, which is not trivial in a system where the water phase has been modified. The system consists of the components presented in Table 3.1.

The stability of the emulsion depends on numerous parameters such as the relative viscosity of the two phases, the activity of the surfactant depending on the polarity of the solvents, the ionic content of the continuous phase etc., which makes the choice of extra ingredients a difficult one. We find that glycerol is the most benign component one can add to the water phase, without significantly altering the interdroplet potential or the activity of the surfactant, discussed in Section 3.6.1.

Note that the simple addition of glycerol changes the viscosity of the water phase and therefore the rate of droplet break-up under shear. Thus, the viscosity of the silicone oil, the shear rate and the surfactant concentration during emul-

sification all had to be modified to achieve the adequate size range and stability. The emulsion remains stable 2 years since its production. The same synthesis described here has been successfully employed for both silicone oil and dodecane, although the latter experiences photobleaching upon illumination above 5% of the laser power.

The emulsion preparation consists of three crucial stages:

1. The dye incorporation into the dispersed oil phase of the emulsion,
2. The design of a continuous phase compatible with the oil phase,
3. The shearing procedure, which determines the size range and the stability of the droplets.

The next section describes each of the stages in detail.

3.4.1 Fluorescent Labeling

Silicone oil (DC 200), purchased from Dow Chemicals, is of a high viscosity ($\eta = 10\text{cS}$) with an average molecular weight of 136.2AMU, implying a very long backbone of silicone-oxygen linkages of relatively low polarity, $(\text{CH}_3)_3\text{Si} - [-\text{O} - \text{Si}(\text{CH}_3)_2]_n - \text{CH}_3$. The oil is fluorescently dyed with Nile Red (Sigma-Aldrich Chemical Co.). It is a hydrophobic dye with amphiphilic properties, to be discussed in Section 4.9. Despite the hydrophobic nature of Nile Red, it is only marginally soluble in silicone oil as it preferentially dissolves in polar organic solvents. Its dissolution is therefore described below.

An excess of Nile Red is added to a 100ml volumetric flask, then filled to the mark with the bulk oil. The dissolution of Nile Red requires heating ($T = 60^\circ\text{C}$) and magnetic stirring for several hours. In order to speed up the process it is advantageous to predissolve Nile Red in a polar organic solvent, such as acetone, and evaporate off the solvent subsequent to its addition to the silicone oil. It is important to ensure all the acetone has been eliminated by prolonged heating and stirring as acetone molecules can form stable complexes with the dye molecules, the presence of which inhibits emulsion stabilisation. An effective way of monitoring the process is to observe the colour change from the very bright fluorescent pink acetone solution to a deep yellow appearance of the solution of dye in silicone oil. The colour is also temperature dependent and is therefore compared at room temperature. The dye reaches saturation point after several hours and the remaining undissolved dye is filtered off using glass fibre filters (Millipore) of $0.5\mu\text{m}$ diameter.

Upon emulsification of the oil phase, to be described in Section 3.4.3, the dye molecules migrate from the oil inside the formed droplets to the aqueous interface until an equilibrium is reached between the concentration of molecules localised in the bulk and those at the surface. This is known as the adsorption isotherm. Furthermore, the dye partitions into the aqueous phase as well, due to the presence of surfactant molecules (see Section 4.9.2). The differential partitioning of the dye into all the regions of the sample is then investigated by confocal microscopy and fluorescence spectroscopy, to be discussed in detail in Chapter 4.

3.4.2 Continuous Phase

This section describes the components of the water phase. The crucial ingredient in emulsion stabilisation is the surfactant, which must be added at a concentration higher than the critical micellar concentration (CMC) to ensure full droplet coverage upon emulsification. Prior to emulsification, concentrations above the CMC are necessary for the fast adsorption of surfactant to the interfaces created by fragmentation, and are later diluted to ensure a repulsive interdroplet potential.

Fast surface coverage is achieved by weighing out 1.152g of SDS (Sigma Chemical Co.) into a 100ml conical flask. The flask is filled up to the mark with deionised water, resulting in a 40mM SDS solution. It is essential that the SDS is pure ($> 99\%$). The solution is left to stir for several hours such that all the SDS is fully dissolved. 5ml of glycerol (Sigma-Aldrich Chemical Co.) is then added to a 25ml beaker and mixed with 5ml of the bulk SDS solution. An equal amount of water and glycerol approaches the refractive index of the oil, such that the continuous phase will not need to be altered significantly post-emulsification. The resulting SDS concentration is 20mM and is therefore higher than the measured CMC of $13\text{mM} \pm 1\text{mM}$ (see Section 3.6.2), yet avoids the dye partitioning significantly into the aqueous phase (see Section 4.9.2).

3.4.3 Emulsification: Crude Mixing

In most cases, a crude parent emulsion was first formed by droplet fragmentation using a motor-driven stirrer, after which the size distribution was improved. The shearing stage must be reproduced exactly in order to obtain a relatively narrow particle size distribution, of approximate radius range between $\approx 1 - 15\mu\text{m}$. The standard shear set-up includes a motor (IKA, RW20) equipped with a long stirrer with rectangular cross-blades. The 25ml beaker containing the continuous phase is clamped beneath the stirrer for emulsification, so that the beaker diameter (4cm)

is comparable to the rotating blades driven by the motor.

The blades are fully immersed into the continuous phase inside the clamped beaker and the solution is stirred at 600rpm (Motor speed, type II: 7.5), or 125cm/s. There may be significant frothing of the solution due to the surfactant at this stage. The pre-dyed oil phase (10ml) is then introduced dropwise into the continuous phase using a syringe with an exit diameter of ≈ 1 mm. The syringe is clamped above the edge of the fixed beaker, such that it drips the oil phase at a fixed radial position from the centre of the beaker, ensuring a constant shear rate. For better control of particle size, instead of manually controlling the droplet influx, a syringe pump (Gilson Dilutor 401) may be used to control the extrusion rate of the oil, at say 2ml/min.

Thus, the oil phase is added in about 5 minutes, up to a volume fraction $\phi = 0.50$. The shearing is continued at the same shear rate for a further 8 minutes to homogenise the droplet size. The emulsion should be slightly opaque at this stage since the refractive indices have not been accurately matched as yet, enabling the resulting droplet size to be checked under the optical microscope. If the polydispersity is high with many large particles around $100\mu\text{m}$ diameter, it is worth applying a further 2 minutes of shear, and so on. An acceptable particle size distribution is obtained $\approx 25\%$ of the time because the factors which may affect the distribution are not very well controlled by this technique. These include:

- temperature fluctuations which alter the relative viscosity of the phases,
- shear geometry within the beaker and the entry point of the influx of oil,
- increase in local shear rates as the droplet volume fraction is increased.

The obtained parent emulsion can then be treated further to narrow down the size distribution, as discussed in Section 3.5.

3.4.4 Refractive Index Matching

Once the parent emulsion has been successfully prepared, the task of refractive index matching the droplets to the continuous phase still remains to be done. Preliminary experiments showed that a very good refractive index match ($\Delta n = 0.002$) between the continuous and dispersed phase of the emulsion is required in order to allow the acquisition of high quality images.

Index matched samples were most often determined by eye immediately prior to imaging. This is to avoid the fluctuation of the refractive indices with temper-

ature, surfactant concentration and the smallest amount of evaporation of water from the sample. The best accuracy is achieved by placing a large amount of an emulsion ($\approx 20\text{ml}$) with a high volume fraction of droplets into a well illuminated beaker equipped with a magnetic stirrer, then adding micropipette aliquots ($\approx 25\mu\text{l}$) of either water or glycerol, as necessary. A sharp edged object placed behind the beaker comes into focus at the desired concentration. Once this is achieved, the sample is transferred into the sample cell and directly observed under the microscope. It was found that the RI matching solution had a volume ratio of glycerol to water of 1 : 1.05, at room temperature. The emulsion sample which is initially at 20mM SDS concentration is diluted further by this refractive index matching procedure such that the final specimen is below the CMC, i.e. below 13mM SDS. The exact final concentration depends on the number of attempts necessary to satisfy the index match, but always ranges between 5mM and 12mM SDS. As long as the surfactant concentration does not reach below 1/3 of the CMC, full droplet coverage is ensured even for much smaller droplets (i.e. larger surface area) (Lu, 2003).

The continuous phase is a multicomponent system, in which glycerol is used to raise the refractive index of the water to match that of the silicone oil. The transparency can be monitored as a function of the amount of glycerol added to the emulsion system. A quantitative measure of transparency can be achieved by observing the laser intensity as it passes through the sample cuvette. The same experiment can be performed in the UV-Visible spectrometer by monitoring the sample scatter at a non-absorbing wavelength ($\lambda = 800\text{nm}$), in which the sample absorbing the least is the most transparent.

3.5 Tyloring Droplet Size

The mechanical mixing of emulsions induces a wide distribution of droplet sizes, depending on the mixing geometry, shear rate, the relative viscosity of the phases and so on. A large polydispersity is unfavourable to the experiments as it is difficult to achieve good statistics of the packing within the small sample volume, limited by the working distance of the objective lens in the z direction. Moreover, large polydispersity is not accounted for by the available theories as it involves very high coordination numbers of large droplets and may induce particle size segregation due to the difference in buoyancy upon creaming (see Fig. 3.11). Since polydisperse samples contain small droplets which can fit in the spaces between larger droplets without deforming, it is difficult to predict the volume fraction at which they

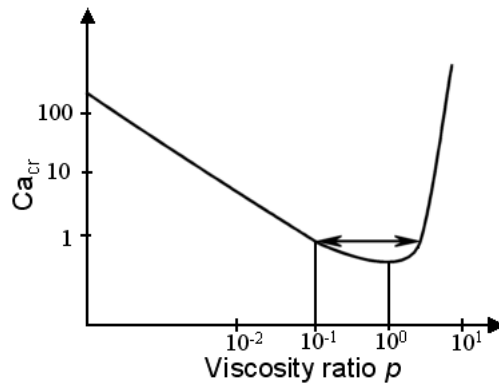


Figure 3.5: Schematic to show the critical capillary number at which droplet breakup occurs as a function of the viscosity ratio between the dispersed and the continuous phases, $p = \eta_d/\eta_c$. The region around the minimum critical capillary number (shown by the arrows) is favourable for emulsification.

will exhibit elastic behaviour, rendering the study of the pressure dependence on volume fraction very difficult to control (Princen, 1980).

The aim is to achieve a random packing of droplets, with a manageable polydispersity, sufficient to avoid crystallisation, yet easily treated by the image analysis algorithms. This is achieved at a level of polydispersity in which the standard deviation divided by the mean is $\approx 30\%$.

The fundamental understanding of droplet breakup is limited to the rupturing of a single droplet. Here, it happens when the capillary number, defined as the ratio of the shear stress, $\eta\dot{\gamma}$, to the Laplace pressure, $2\sigma/a$, is ≥ 1 . Therefore the resulting droplet radius is

$$a \approx \frac{\sigma}{\eta\dot{\gamma}} \quad (3.3)$$

where η is the viscosity of the suspending medium (Taylor, 1934). Although this model captures the essential physics of fragmentation, there are additional factors which influence the behaviour.

The capillary number at which rupture occurs is strongly dependent on the viscosity ratio between the dispersed and the continuous phase, η_d/η_c , (Hinch and Acrivos, 1980). This ratio should not exceed the value of 4, or else the emulsion will not be formed, as indicated in Fig. 3.5. In order to account for the role of an increase in the volume fraction of droplets in an emulsion under high shear, the viscosity of the medium is elevated, resulting in smaller droplet sizes (Aronson, 1989). At even higher volume fractions, when the emulsions are compressed beyond the random close packed limit, instead of rupture, the droplets deform as they begin to store elastic energy, see Section 3.3.3.

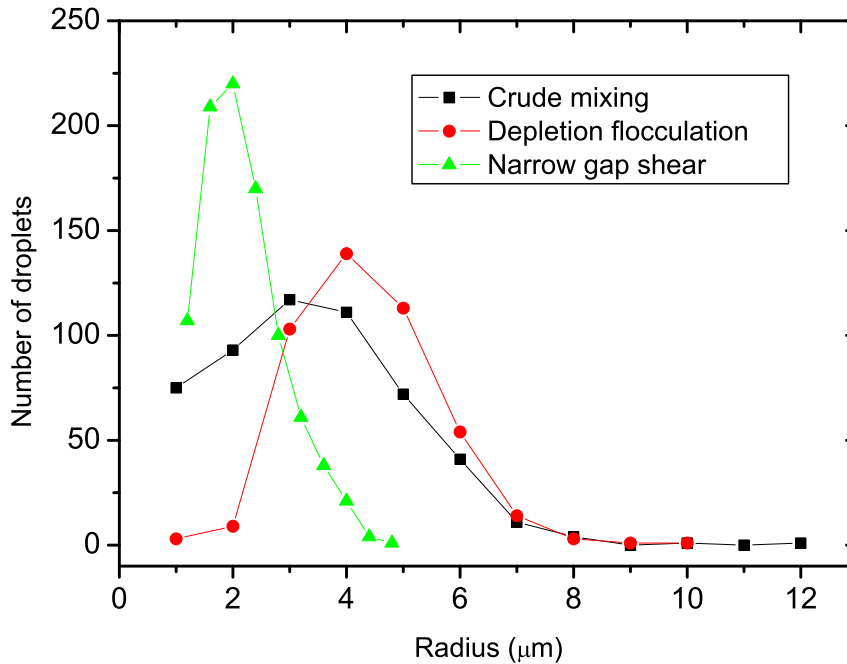


Figure 3.6: Histogram of particle radii for the same emulsion sample after emulsification by crude mixing. Small droplets were removed by fractionation crystallisation and finally high shear rates were applied. The radii are determined by 3D image analysis methods described in Chapter 5.

Controlling polydispersity has been a major goal within the industrial community and naturally many advances have been made. For example, various fractionation schemes have been developed which induce a size segregation of the polydisperse sample according to the droplet buoyancy, permitting their separation (Bibette, 1991). This process is time-consuming, but can lead to small amounts of sample with 10% polydispersity. This technique is based on depletion attraction, which has been described in Section 3.3.2. More advanced shearing techniques with precise geometries are available, which provide greater quantities but require specialised equipment (Mabille et al., 2000; Mason and Bibette, 1996). In addition, monodisperse emulsions can be made drop by drop by slowly introducing the oil phase into a continuous phase rotating at a constant velocity (Umbanhowar, 2000).

Based on the above arguments, the parent emulsion samples are treated to narrow down the size distribution to an acceptable level for the experiment. Each of the methods used is described in brief and the resulting particle size distribution at each stage is presented in Fig. 3.6.

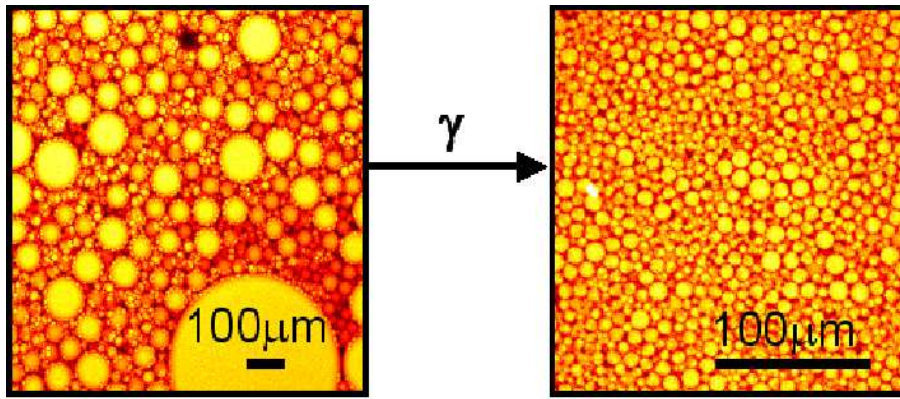


Figure 3.7: Droplet fragmentation in a parallel-plate geometry by shearing the parent emulsion at $\gamma=7000\text{s}^{-1}$ in the Linkam shear stage.

3.5.1 Size Segregation

This method is based on the depletion attraction between the droplets, the intensity of which can be varied with the micellar concentration. Above some critical radius, the depletion attraction will be larger than kT , resulting in their flocculation (Pusey et al., 1993).

The crude emulsion is first diluted to 10% droplet volume fraction. The density difference between the oil droplets and the water phase will cause the flocs to cream over a period of several hours in a tall measuring cylinder. The droplets which are smaller than the critical radius, usually considered to be satellite droplets, will remain dispersed in solution, enabling their separation and subsequent exclusion from the system using a separating funnel. Since the flocculation is reversible, lowering the surfactant concentration leads to a segregation of the remaining larger droplets further, and repeating the procedure several times leads to the production of monodisperse samples. We have only employed a one-stage procedure (at $\phi_m = 1\% \approx 50\text{mM}$) to eliminate the smallest droplets ($< 0.5\mu\text{m}$) by decanting off the continuous phase and keeping the cream layer. This technique, known as fractionation crystallisation, was not performed for all samples since it was found that the very small droplets do not play a significant role in the transmission of stress and could therefore be considered as ‘rattlers’, diffusing in between the larger droplets.

3.5.2 Narrow Gap Shearing

Placing the coarse parent emulsion under high shear rates in a well-defined geometry at a high volume fraction (but below compression) leads to the fragmentation

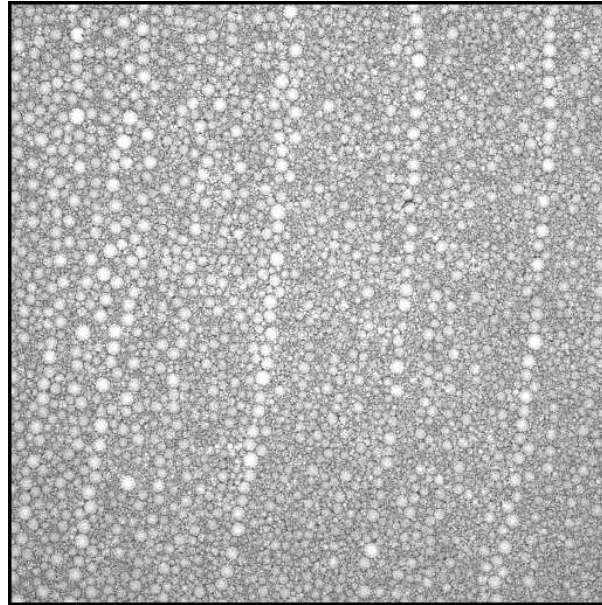


Figure 3.8: 2D image obtained using a $5\times$ lens, NA 0.3, after 6 minutes of shear at $7000s^{-1}$, showing size segregation into lines with a characteristic separation length. The field of view is very large at 1.8mm and the radial direction of shear coincides with the observed lines.

of larger droplets down to a critical size and does not alter the size of the smaller droplets (Mason and Bibette, 1996; Mabillet et al., 2003). The results of such an experiment are shown in Fig. 3.7.

A relatively narrow droplet size distribution is achieved by applying shear rates of $\gamma = 7000s^{-1}$ using a Linkam shear stage (Perrin, 2000). Such a high shear rate results from the narrow gap ($d = 30\mu\text{m}$) between the parallel rotating plates, since $\gamma = r\omega/d$, where ω is the angular velocity and r the plate radius. The polydisperse sample at $\phi \approx 0.85$ is sheared for 5 minutes, after which no further droplet breakup is observed.

This method yields an emulsion of a manageable polydispersity, shown in Fig. 3.7, relatively fast.

Shear Ordering

During the application of shear to this almost 2D coarse emulsion layer, after the droplet break-up down to the critical radius, given by Eq. (3.3), size segregation into evenly spaced lines of well-defined droplet size along the radial direction are observed, as seen in Fig. 3.8. These structures are weak and return to a disordered state under the smallest perturbations, i.e. upon the application of slowest available shear. X-ray scattering experiments on sheared emulsions have shown such structural features with a characteristic length scale (Perrin et al., 2001). The

phenomenon may be due to shear banding. This behaviour suggests a similarity between the model emulsion system and granular systems.

3.5.3 Dropwise Emulsification

A better control of the parameters influencing droplet size is necessary for the preparation of monodisperse emulsions at the emulsification stage. It is based on the controlled breakup of a stream of oil phase into fine droplets, the radius of which is determined by the flow parameters, the geometry and the properties of the liquids involved (Ganan-Calvo and Gordillo, 2001).

The dropwise emulsification set-up involves a beaker containing the continuous phase, rotating at a constant slow velocity, and a syringe pump controlling the velocity of the influx of the oil phase, through a micropipette of a specified diameter (Umbanhowar, 2000). It was reproduced in our laboratory. If the velocities of the oil flow and the continuous phase in the rotating beaker are slow enough to produce the droplets one by one, at a tip angle parallel to the flow, monodisperse droplets break-off at the tip, approximately three times the size of the micropipette tip through which they are extruded. This method is very slow, producing 1ml of emulsion every 24 hours. The slowest available syringe pump available to us extrudes the oil at the rate of $10\mu\text{l}/\text{min}$, which sets the minimum reproducible droplet size to $30\mu\text{m}$. This size is too large for the field of view of the lenses employed in our study and smaller droplets could only be obtained at the expense of monodispersity.

In conclusion, the controlled shearing of the parent emulsion yields a sufficiently narrow size distribution for use in our experiments, particularly when combined with the fractionation method for removing small droplets. If a higher level of monodispersity is required, one can further fractionate the sample, or turn to a more controlled emulsification through a micron-sized pipette. All of the above methods contributed to the control of droplet size in the model system.

3.6 Characterisation of the Emulsion

Even though SDS and silicone oil systems have been studied extensively, it was not clear what the effect of glycerol and the dye particles would be on the emulsion properties. We therefore discuss the changes invoked by the increase in continuous phase viscosity and measure the surface tension and the CMC for the exact system used in the experiments.

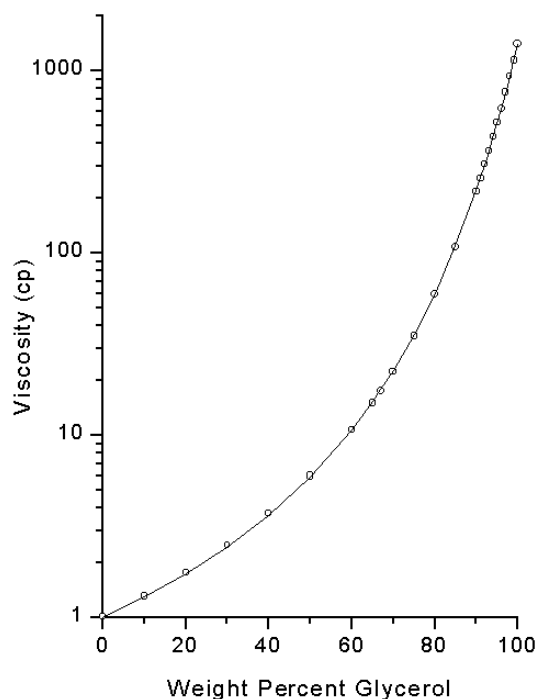


Figure 3.9: Change in viscosity as the glycerol content is increased. This graph was taken from P. Huiber's Thesis (Huibers, 1996).

3.6.1 Influence of Glycerol on the Water Phase

The effect of glycerol as an additive on the model anionic surfactant system, SDS, is investigated. When glycerol/water mixtures are used as the solvent, two competing factors influence the micellar stability. Firstly, the addition of glycerol to water drastically increases the viscosity in a nonlinear fashion, as shown in Fig. 3.9. The viscosity ratio of glycerol (1000cS) at 25°C and water (0.89cS) is large, thus the kinetics of the system are drastically slowed down. Secondly, the solvent interaction (hydrogen-bonding) is slightly weaker in glycerol than in water, as measured by a decrease in surface tension. Glycerol is a solvent similar to water in that it engages in extensive hydrogen bonding with itself, resulting in a surface tension of 63 mN/m, comparable to 72 mN/m for water, and much higher than the 20 mN/m of silicone oil.

3.6.2 Measurement of the CMC

The influence of glycerol on micellar properties has been established in terms of the CMC. We measure the conductivity of the solution, proportional to the number of free ions in solution, as a function of SDS concentration. As surfactant monomers begin to be incorporated into the micellar structures in solution the increase in conductivity is still linear, but reduced. Hence, the CMC is identified as the change in

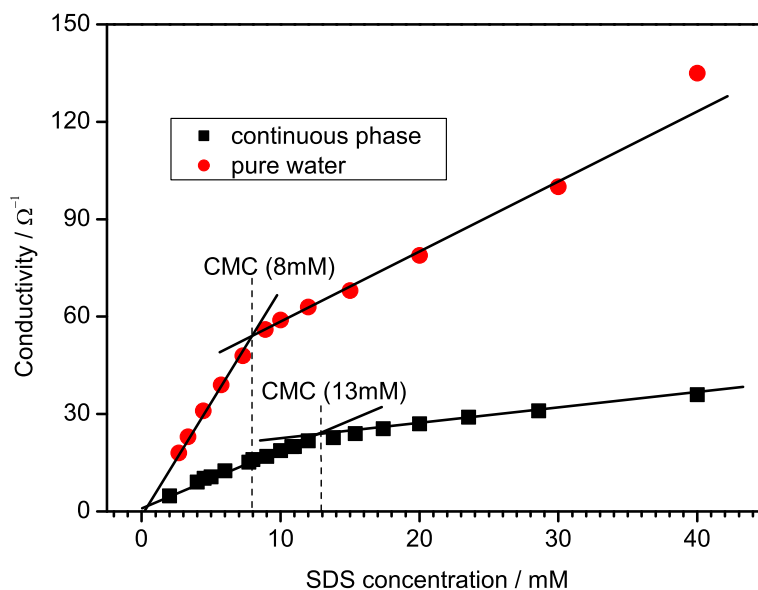


Figure 3.10: Conductivity as a function of SDS concentration in pure water and in the continuous phase glycerol/water mixture. The CMC is shifted to a higher concentration upon addition of glycerol.

slope of the conductivity dependence on the surfactant concentration. The graph in Fig. 3.10 shows the values obtained for the CMC for pure SDS in aqueous solution, as well as for the continuous phase mixture of water and glycerol (51% : 49%).

The significant increase in the CMC upon the addition of glycerol can be attributed to the change in the nature of the solvent by changing the structure of water. The measurement is in agreement with the observation that the intermolecular solvent forces are weaker than in pure water, already established by the reduced surface tension of glycerol. The solubility of the surfactant monomer increases, resulting in a higher CMC. The increased monomer solubility would also imply an increase in the conductivity, contrary to the observed result. This can be explained by a viscosity increase of the continuous phase, which slows down the transport of monomers to and from the micelles, thus causing a significant decrease in the overall conductivity. The results in the figure show that the viscosity increase must be the dominant factor.

3.6.3 Surface Tension Measurement

The interfacial tension between the continuous and the dispersed phase is reduced by the presence of surfactant. In this case both Nile red and SDS play the role of the surfactant and therefore the oil phase was dyed prior to the surface tension measurement.

The surface tension is measured using the pendant drop method. This technique deduces the surface tension from the optical observation of the shape of the oil drop being extruded into the continuous phase through a 1.6mm syringe. Since the oil is less dense than the continuous phase, the set-up must be inverted such that the drop is extruded from below upwards. Since the two phases are almost refractive index matched, a sheet of white paper should be placed behind the illuminated drop to obtain a good enough contrast in the image to determine the curvature of the drop by the equipment software. An average of 50 images measured a surface tension of $9.2\text{mN/m} \pm 0.5$, in very good agreement with the value of 9.8mN/m obtained by Mason et al. for the same emulsion without glycerol (Mason et al., 1995). Hence, glycerol and the dye molecules do not have a pronounced effect on the surface coverage of the droplets. This is extremely important for the accuracy of the force measurements in Chapter 6 as the surface tension is employed for their calculation.

Since SDS is soluble in the continuous phase the transport of SDS molecules is facilitated through the emulsion, thus ensuring surfactant equilibrium conditions upon emulsification. We therefore deduce that the surface tension obtained for a macroscopic drop is equivalent to the value for the micron-sized droplets within the emulsion system.

3.7 Emulsion Component Selection

Having described the preparation and characterisation of the model emulsion system, a brief summary of the important properties of the components which lead to their compatibility and the formation of a stable system is given.

SDS makes a good choice for the surfactant because of its unusually high HLB value of 40, which ensures stabilisation of oil droplets, such as PDMS. It is an anionic surfactant, which ensures a stronger interfacial repulsion between the droplets. Furthermore, SDS has a high solubility in water and a low solubility in silicone oil, which are primary requirements for rapid adsorption at the interface between the phases to be emulsified.

If the emulsion is made at a very high volume fraction, this may also cause a phase reversal, which is why the emulsification procedure is performed at $\phi = 50\%$

at the most. Moreover, the preferred emulsion type may be altered by the sequence in which the components are added, the temperature and the shear regime. It is for this reason that the oil phase must be introduced dropwise (otherwise the emulsion is unstable or inverted), according to the procedure stated in Section 3.4.3.

Silicone oil is chosen because of its low refractive index ($n=1.403$) compared with other oils, making it easier to match with the water phase. Moreover, silicone oil can be obtained in a wide range of viscosities, which is a very useful parameter to be varied at the emulsification stage. The viscosity ratio achieved here, $p = \eta_d/\eta_c=10\text{cS}/5.3\text{cS}=0.53$, corresponds to the minimum in the critical capillary number, ensuring droplet breakup at relatively low shear, as shown in Fig. 3.5. It has been verified that if the viscosity of the continuous phase is significantly raised by using high levels of surfactant ($\approx 10\text{CMC}$), the silicone oil can be introduced manually with a spatula, producing the same size distribution of the parent emulsion with fewer small droplets (satellites).

3.8 Preliminary Experiments

As previously mentioned, the study of emulsion stabilisation is very complex because of the large number of parameters which influence the final product. In the process of searching for a stable system, we encountered numerous combinations which gave unsatisfactory results. Rather than presenting those in detail, we give specific examples of issues which arose in the process. A list of tested ingredients is presented in the table below.

Oil Phase	Additive	Surfactant
bromohexadecane (BHD)	polyethylene glycol 600	tween 60 ($n=60$) polyoxyethylene sorbitan monolaureate
heptane	hexylene glycol	tween 20 ($n=20$) polyoxyethylene sorbitan monolaureate
dodecane	lithium chloride	neodol (91-8) primary alcohol ethoxylate

Table 3.2: Examples of emulsion ingredients in the preliminary preparation.

3.8.1 Mixing Surfactants

The mixture of nonionic (Neodol 91-8) and ionic (SDS) surfactants resulted in a stable emulsion with a bimodal size distribution, shown in Fig. 3.11, visible in the xy plane image. The xz image additionally shows a size segregation with depth

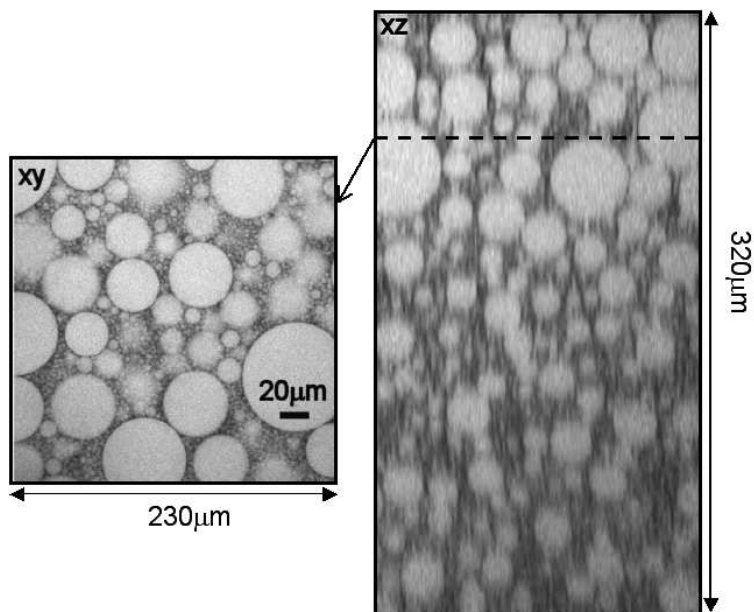


Figure 3.11: Bimodal distribution obtained by mixing surfactants (see Table 3.3). A very transparent sample is obtained by index matching with PEG 600, resulting in images of large depth ($20\times$ lens, NA 0.5, zoom 2).

due to buoyancy, as well as evidence of a very successful refractive index match which permits observation beyond $300\mu\text{m}$ into the sample.

Water Phase	Oil Phase	Surfactant	Shear
water (49%)	PDMS(10cS)	SDS (1%),	Silverson emulsifier
PEG 600 (48%)	nile red	Neodol (2%)	lowest setting (8mins)

Table 3.3: Mixed surfactant emulsion gives rise to a bimodal distribution in Fig. 3.11.

This emulsion remains stable over a period of several months, since the surfactant mixture ensures a stable elastic surfactant film. However, such a size distribution is not acceptable for the investigation of structural changes and stress transmission in this study.

3.8.2 Addition of Salt

Heptane alone does not form stable emulsions with the ingredients listed in the table. This is due to its slight solubility in water, leading to emulsion coarsening by Ostwald ripening, and eventual phase separation. The addition of a small amount of bromohexadecane (10%) which is insoluble in the continuous phase, renders the

Water Phase	Oil Phase	Surfactant	Shear
water (5ml)	heptane (90%)	tween 20(1%),	Silverson emulsifier
LiCl (1.74g)	BHD (10%)		lowest setting (3mins)

Table 3.4: Refractive index matching of the emulsion using monovalent LiCl salt. Mixing oils decreases the oil phase solubility in the water phase. The resulting emulsion is shown in Fig. 3.12.

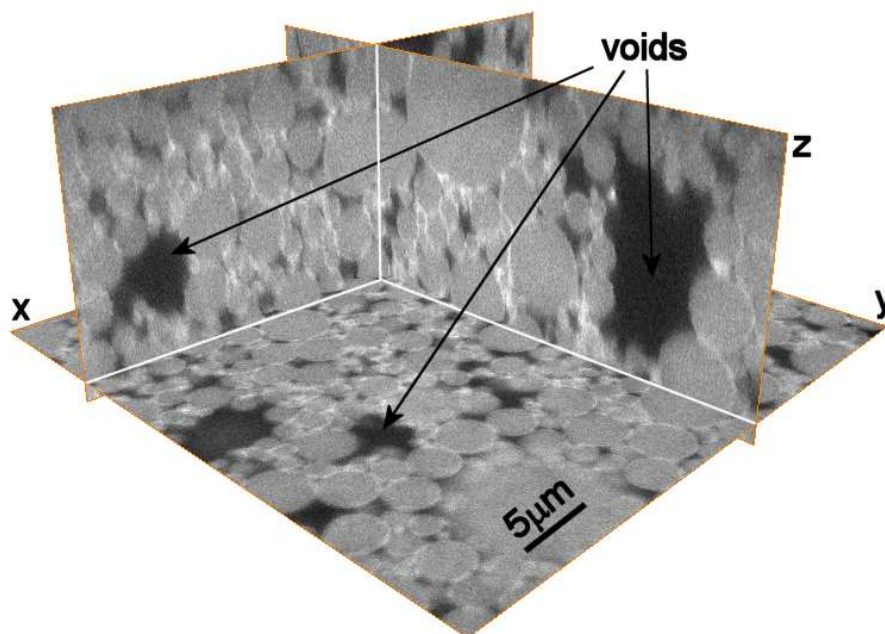


Figure 3.12: The addition of LiCl to achieve the refractive index match induces depletion flocculation, trapping the system into unstable configurations with unfilled voids (see Table 3.4). The same emulsion stabilised by glycerol is able to cream into a much more efficient packing (40× lens, NA 1.3, zoom 2).

emulsion stable in pure water.

The additives in the water phase also have a profound influence on the surfactant behaviour and can therefore destabilise the emulsion. If those additives, such as salts, introduce extra screening charges into the solution, they decrease the Debye screening length such that the droplets must get very close to one another before they ‘feel’ a force. This would not be disadvantageous to our experiments, however, the increase in electrical charges induces surfactant aggregation into micelles at much lower concentrations than usual. Therefore, even below the literature value of the CMC of tween 20 (0.06mM), the micellar aggregates induce a strong depletion flocculation.

In particular, upon addition of 1.754g LiCl into 5ml of water (saturation point) in order to refractive index match the emulsion phases, depletion attraction results

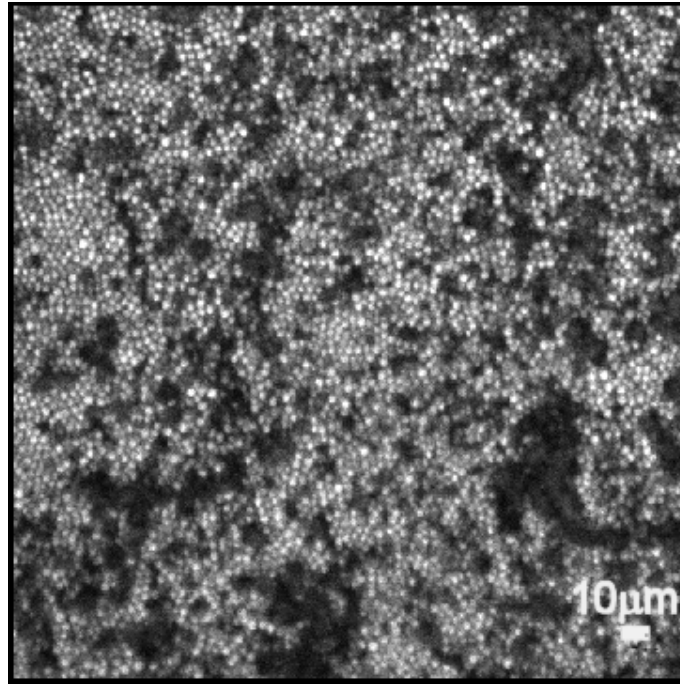


Figure 3.13: Colloidal PMMA dyed with Nile red observed using the $32\times$ lens, NA 0.4, below the sample surface. It shows the clusters formed by colloidal aggregation.

in bonds which are sufficiently strong to prevent further rearrangements. It is likely that adhesion also plays a role in this system owing to the presence of a monovalent salt, even though large contact angles were not observed in the images. The attraction gives rise to highly disordered structures, clusters separated by large voids, which have previously been described as fractal (Hagiwara et al., 1997). These are shown in Fig. 3.12. Although this study is mainly concerned with emulsions, it is interesting to note that colloidal poly(methyl-methacrylate) (PMMA) particles exhibit the same behaviour as they aggregate to form colloidal gels. The PMMA particles ($r=2\mu\text{m}$) (Antl et al., 1986), dyed with Nile red (Campbell and Bartlett, 2002), were also observed in confocal mode showing an even more prominent structure of clusters due to their monodispersity and smaller particle size. It is shown for comparison in Fig. 3.13.

However, if glycerol is added to the same emulsion system instead of LiCl, no such clustering is observed and the emulsion forms a randomly distributed droplet packing. On the other hand, glycerol has a destabilising effect on Tween 20 and Tween 60, the water soluble surfactants, making this emulsion unstable over longer timescales.

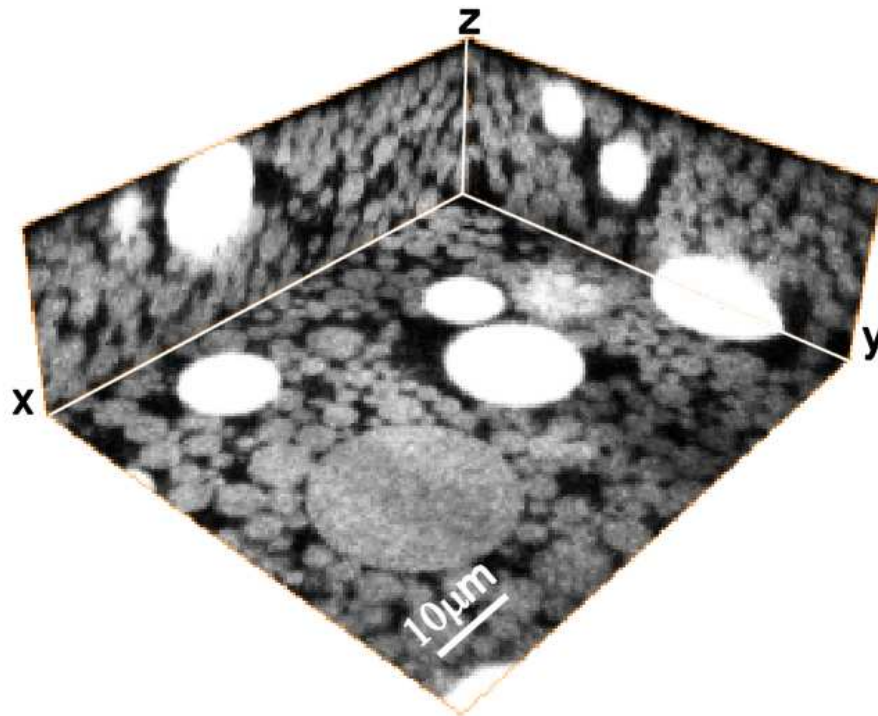


Figure 3.14: Dodecane ‘tracer’ droplets fluoresce more intensely than the ‘background’ silicone oil droplets. Both are stable and do not segregate upon creaming (32 \times lens, NA 0.4, zoom 2).

Property	Dodecane
Refractive index n	1.418
Viscosity η (cS)	1.53
Density ρ (g/cm ³)	0.753

Table 3.5: Properties of dodecane.

3.8.3 Dodecane Model Emulsion

The same emulsion preparation procedure as that in Section 3.4 works well with dodecane oil. The two emulsions cannot be simultaneously refractive index matched since dodecane has a higher refractive index. However, a higher proportion of glycerol (65%) in the water phase in the case of dodecane does not destabilise the emulsion. Interestingly, the fluorescence mechanism described in Chapter 4 is reproduced using dodecane, in that the Nile red dye partitions into the oil phase, the interfaces and less so into the aqueous phase. Nevertheless, the dye partitioning requires further quantitative investigation. This result is simply an indication that the fluorescence observed in the experiments is not specific to silicone oil, but is based on a more general mechanism of dye migration.

Introducing a small amount (1%) of the dodecane emulsion into a transparent

silicone oil emulsion reveals yet another interesting feature. Since Nile red is far more soluble in dodecane than in silicone oil, owing to its increased polarity, the tracers fluoresce much brighter than the silicone oil droplets. Thus, the two systems can be distinguished within an image, as shown in Fig. 3.14. This is a very useful tool for dynamic experiments, as one could use the dodecane emulsion as tracer particles for image analysis. In addition, the density difference between the two types of particles could be regarded as an additional external force acting on the tracers. This may lead to interesting investigations of the microrheology of the system (Makse and Kurchan, 2002).

3.9 Summary

A model emulsion system, mimicking the behaviour of compressible granular materials on a smaller length scale, has been successfully prepared. Even though the emulsion is ultimately only kinetically stable, efforts were made to choose components which would best reduce the interfacial tension, measured at $9.2\text{mN/m} \pm 0.5\text{mN/m}$, therefore improving the thermodynamic stability as well. The surfactant film surrounding the droplets was sufficiently elastic to keep the droplets intact under large compression forces. In order to ensure a purely repulsive potential, both adhesion and depletion attraction were avoided by the absence of monovalent salts in the aqueous phase and by working below the CMC, respectively. The droplets could be considered frictionless due to the lubrication by the continuous phase fluid.

A transparent sample was achieved by the addition of glycerol, with no destabilizing effect on the surfactant activity. The CMC of the transparent system was measured at 13mM SDS by conductivity. The high viscosity of the continuous phase improved the conditions for the emulsification procedure as lower shear rates could achieve small particle sizes (according to the capillary number). Several methods were employed to achieve narrow enough size distributions to simplify the image analysis procedure and support the analogy with grains, yet to avoid crystallisation. The control of particle size leads to the creation of a good statistical ensemble of droplets in one 3D image, with a manageable size distribution.

Finally, a hydrophobic dye of amphiphilic nature provided contrast in the images by fluorescently labeling the droplet phase and the interfaces, discussed in Chapter 4, facilitating the subsequent image analysis techniques. This completed the requirements of the model system, in that the emulsion could be regarded as a packing of deformable, frictionless, repulsive spheres suitable for observation.

Chapter 4

Fluorescence Techniques

Sometimes, with these cloudless evenings, the light
played a strange trick...At first glance you accepted the image.

Alex Garland,
The Beach.

4.1 Introduction

This Chapter introduces the fluorescence techniques used to investigate the model emulsion system, described in Chapter 3. The experiments were primarily performed using confocal microscopy, in which the spatially resolved droplet fluorescence is observed in a 3D image. A general introduction to confocal microscopy is provided, which is necessary for the understanding of the parameters governing image acquisition and therefore affecting the subsequent analysis (Paddock, 1999; Pawley, 1995). The experimental set-up and procedure are described in detail, as well as the resulting fluorescence images.

The images exhibit a very useful contrast between the sample regions due to a specific partitioning of the fluorescent dye molecules within the emulsion system. The differential bulk fluorescence of the dispersed and the continuous emulsion phases is investigated further using UV-Visible spectrophotometry. The fluorescence mechanism specific to our system is then inferred from the combined information from the two techniques.

4.2 What is Confocal Microscopy?

Confocal microscopy is widely used in the biological sciences, but is now seeing application to a wide range of problems in soft matter physics, including colloidal crystallisation (Gasser et al., 2001; van Blaaderen and Wiltzius, 1995), glassy dynamics (Weeks et al., 2000), 3D director orientation (Smalyukh et al., 2001), determination of the geometry of a particle ensemble (Bromley and Hopkinson, 2002) and interfacial structures in phase separated systems (Jinnai et al., 1997). Its invention was patented half a century ago (Minsky, 1957), but its use in the biological and physical sciences is a recent development.

The key feature of confocal microscopy is that only light from the focal plane is detected. The out-of-focus light is rejected by the use of an additional pinhole in the back focal plane of the objective lens, the size of which determines the thickness of the detected focal plane, see Fig. 4.3. Thus 3D images of translucent samples can be acquired by moving the sample through the focal plane of the objective (in the z direction) and acquiring a sequence of 2D images, as shown in Fig. 4.1. The ability to optically section the sample and subsequently reconstruct the 3D information (as shown by the vertical slices in the figure) is advantageous for any structural investigation as it does not involve the denaturing of the sample by physical sectioning. For example, in situations where boundary effects are important, it is possible to directly image the bulk of the sample and investigate the effects on the material structure of depth and proximity to the walls.

4.3 Principles of Fluorescence

Since the imaging process is based on the fluorescence of the sample, it is useful to consider the mechanism of fluorescence in detail (Lakowicz, 1999). Regions of interest within the sample can be detected by selectively targeting the desired molecular species with a fluorescent label. Fluorescence is only present in active species, fluorophores (Haugland, 2002). These are used to label specific components of the specimen to produce a contrast between phases. Contrast can arise either from labeling the phases with different fluorophores or from variations in the concentration (or the activity) of the same fluorophore. The preferred labeling method is specific to the system and depends on the adsorption of the dye molecules to the species in question.

To appreciate the mechanism of fluorescence, one should consider the transitions which occur within a molecule upon absorption of energy in the visible region.

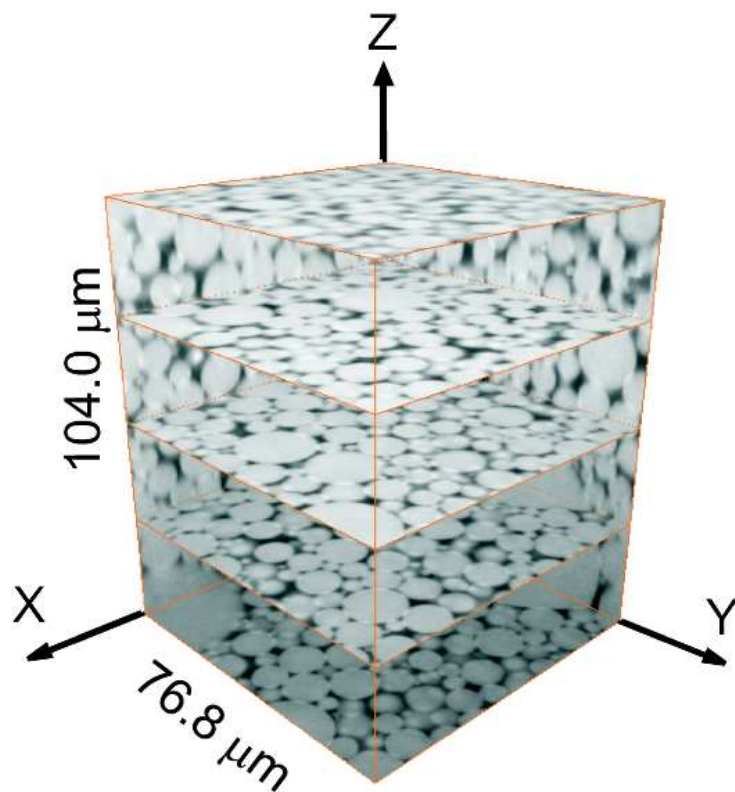


Figure 4.1: The horizontal xy 2D images are obtained by moving the transparent sample in the z direction. A stack of 185 2D images (5 are shown) allows for the image reconstruction in the third dimension, shown by the vertical 2D images in the xz and yz planes.

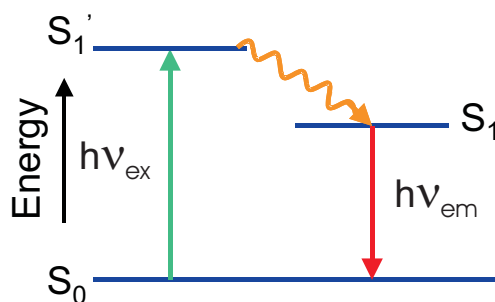


Figure 4.2: Jablonski diagram, illustrating the molecular processes resulting from optical absorption and the subsequent emission fluorescence.

At these wavelengths, molecules can absorb energy through electronic transitions, depicted in Fig. 4.2. The three stage process is summarized below:

1. The energy of the photons supplied to the system is determined by the laser wavelength used for excitation, $E = h\nu_{ex}$.
2. Upon illumination the molecule undergoes a transition from the ground state S_0 to the excited state S_1' whose lifetime is of the order of (10^{-8} s).
3. Subsequent conformational changes in the molecule lead to a relaxed excited state S_1 of a lower energy, from which the emission fluorescence originates. Thus, the emitted photon is of a longer wavelength.

Each fluorophore is characterised by an absorption and an emission spectrum which indicate the bandwidths at which the two processes occur. The emission intensity is proportional to the amplitude of the absorption spectrum at the specific excitation wavelength. It is the electronic configuration of the dye molecule which determines the absorption and emission wavelength bands, as well as the efficiency of the fluorescence. Since the electronic configuration depends on the molecular interactions with the surrounding environment, the fluorescence is also greatly affected by the solvent of the fluorophore. This effect can produce environment-sensitive spectral shifts in both amplitude and wavelength.

The excited state species S_1' are very reactive and can interact with other excited molecules such that the species is no longer fluorescently active. This effect is known as photobleaching and occurs at high levels of illumination. It must be avoided if good quality images are to be obtained.

The study of fluorescence and the mechanisms of photo-physical processes is a broad and much researched topic, but the simplified picture is sufficient for the purposes of this work.

4.4 Microscope Set-up

The microscope used in this study is the *Zeiss* LSM 510, which is a fluorescence laser scanning confocal microscope (LSCM). It is operated by proprietary *Zeiss* software, which also features post-acquisition image manipulation. It can be used in both the conventional transmission mode, which is useful for locating the sample, and epifluorescence modes for confocal imaging. The microscope is equipped with a wide range of dry and oil immersion lenses, ranging from $5\times$ to $100\times$ magnification. The parameters affecting the choice of the appropriate lens for our experiments are discussed in more detail in the following section. The sample can be illuminated at the wavelengths of light which are specific to the available laser-beams. In this case, there are four beam lines: two argon-ion lasers ($\lambda=458, 488\text{nm}$), and two helium-neon lasers ($\lambda=543, 633\text{nm}$). The intensity of the individual lasers can be accurately controlled (from the LSM software) using opto-acoustic filters.

Another important feature of the microscope is that the emitted light can be detected by three separate detection channels, according to the emission wavelength band which can be chosen by the filter set. The confocal scan head contains both the scanning optics and the detection channels. Since each of the channels has its own detector pinhole and photomultiplier tube (PMT), this gives an extra degree of freedom in adjusting the channel contributions to give the best resulting overlaid image. The technique of multiple-channel detection, either simultaneously (ie. in response to a single excitation) or independently, is extremely useful in deducing the variety of chemical environments present in the system, provided that they cause a shift in the emission spectrum of the dye.

4.5 Optics

The optics of the microscope assumes the fluorescent behaviour of the regions of interest within the sample (Born and Wolf, 1983), which are therefore fluorescently dyed prior to imaging. The fluorescence mechanism has been described in more detail in Section 4.3. The epifluorescence imaging process, depicted in Fig. 4.3, consists of several stages:

- Incident and collimated monochromatic laser light is reflected off the dichroic mirror and focused into the sample by the objective lens.
- The fluorescently active species in the region of sample illuminated by the laser emit incoherent fluorescent light, of a lower energy.

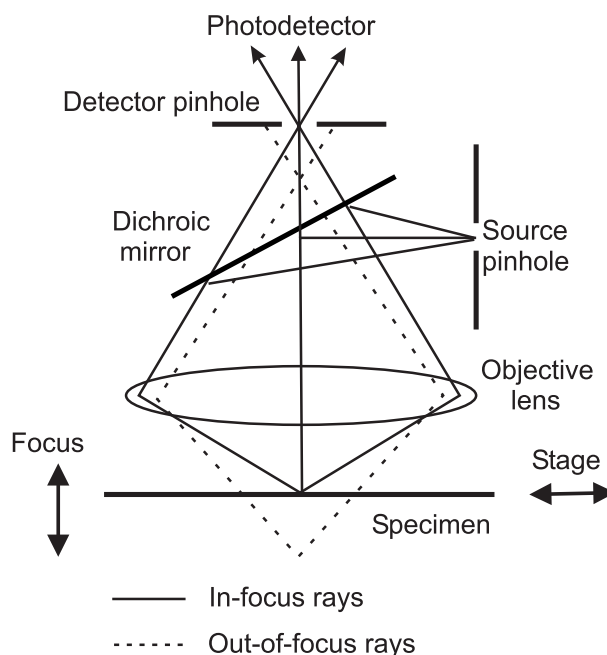


Figure 4.3: Schematic diagram of the light path in a stage scanning LSCM. It highlights the use of the detector pinhole in rejecting light originating from above or below the focal plane.

- The emitted fluorescence is collected by the objective lens and separated from the excitation light by an appropriate optical filter. The detector pinhole is placed such that only light from the focal plane is transmitted. Scanning produces a 2D image of small thickness determined by the pinhole size.
- The emitted signal can be split further into emission wavelength bands of interest using the different optical detection channels.
- A PMT detects the photons detected from each spatially resolved entity (voxel) and presents it in the available dynamic intensity range in the image.

4.5.1 Objective Lenses

The choice of the lens is extremely important since its numerical aperture (NA) determines the thickness of the optical sectioning and the final resolution of the image. The NA is defined as the sine of the maximum acceptance angle of light rays that can enter or leave the system, multiplied by the refractive index of the immersion medium,

$$NA = n_i \sin \Theta_{max} \quad (4.1)$$

The higher the NA, the thinner the optical section and the better the resolution. The lenses used are immersed in oil of the same refractive index as glass ($n_i=1.518$)

Magnification	Model	NA	WD(mm)	OSD ^a (μm)	FOV ^b (μm)
40	Plan-Neofluar	1.3	0.14	1.0	326
63	Plan-Apochromat	1.4	0.18	0.6	207
100	Plan Neofluor	1.3	0.12	0.6	187

Table 4.1: Properties of the lenses. [a] Optical slice depth for detector pinhole size of $74\mu\text{m}$ [b] The width of the maximum field of view (Myatt, 2002).

so that light rays are not refracted at the interface with the coverslip. The use of an immersion medium increases the maximum acceptance angle of the lens and improves the resolution as compared to air immersion lenses ($n_{air}=1$) according to Eq. (4.1).

Values of NA in air are therefore limited to 0.95, but are raised to 1.4 in the oil immersion medium with high magnification lenses, e.g. the $63\times$ lens. The disadvantage of using the oil immersion medium is that the lens is in physical contact with the sample cell. This may cause a relative motion during acquisition, resulting in skewed images unless the sample cell is infinitely rigid. Moreover, the working distance (WD) of the lens, i.e. the distance of the focal plane from the lens, decreases drastically with magnification, since it is determined by the NA and the diameter of the exit pupil of the lens. This limits the depth of the sample which can be imaged and must be taken into consideration when choosing the appropriate lens.

All the images presented in the Thesis were acquired using high magnification oil immersion lenses, namely 40 , 63 and $100\times$ lenses, the specifications of which are presented in Table 4.1. The working distance is compromised for the sake of a higher resolution in the z direction. Since the average particle size in our experiments is of the order of $5\mu\text{m}$, even low working distance lenses produce 3D images which are several particle diameters deep. These dimensions ensure a sufficiently large particle ensemble, such that a statistical analysis is appropriate.

It is important to note that the compressed droplets can be resolved by all the available lenses, including the $20\times$, NA 0.5, $32\times$, NA 0.6, and $50\times$, NA 0.7. The use of these air immersion lenses is particularly useful for dynamical measurements, such as shear or magneto-manipulation, which are not explored within this Thesis.

4.5.2 Image Degradation

Even though the above lenses were chosen to provide images of the highest possible resolution and magnification, several effects still play a role in degrading the image

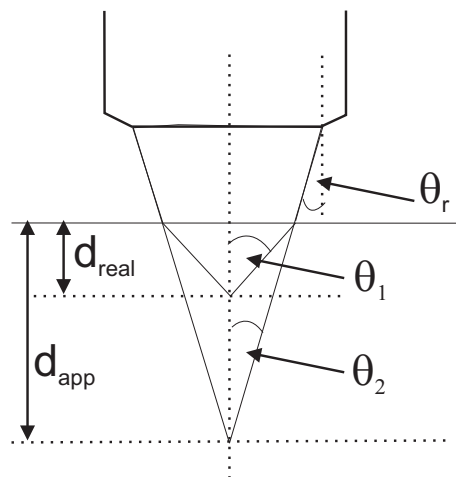


Figure 4.4: The discrepancy between the apparent depth and the actual depth of the sample arising from optically mismatched systems. The refractive index of the immersion oil coupled with the cover glass ($n_i = 1.518$) is higher than that of the specimen ($n_s = 1.40$), and the focus is therefore closer to the coverslip than under ideal conditions.

(Hell and Steltzer, 1995). Each of them is discussed in turn, in terms of their significance in our experiments.

Refractive Index Mismatch

Different species within the specimen may have different refractive indices, causing a loss of intensity with sample depth associated with the scattering of the incident and refracted light. Perhaps the most drastic degradation in the quality of our images arises from a mismatch in the refractive indices of the continuous and dispersed phases of the emulsion, as light crossing through the dense particulate pack faces many diverse sources of scattering.

Hence, particular care is taken to achieve diaphanous samples by matching the refractive indices to a high degree of accuracy, as described in Section 3.4.4. For a poorly matched high volume fraction sample, emulsion scattering at the interfaces leads to a rapid degradation of the image quality as a function of depth into the sample.

Refraction at the Sample Surface

The apparent depth and the real depth of the specimen differ due to the laser beam refraction at the specimen surface arising from a change in the refractive index as the light passes from the specimen to the immersion medium. The refraction at the interface between the two media is depicted in Fig.4.4.

The change in angle of light rays by refraction is governed by Snell's Law:

$$n_i \sin \Theta_1 = n_s \sin \Theta_2. \quad (4.2)$$

Using the small angle approximation and simple trigonometry we obtain

$$\frac{d_{real}}{d_{app}} = \frac{n_s}{n_i}, \quad (4.3)$$

which allows for the correction from the apparent depth to the actual depth given the refractive index mismatch. Since the refractive indices are similar in our experiments, the correction according to Snell's law is small ($d_{real} = 0.92 \times d_{app}$). The validity of using the small angle approximation in our set-up was tested using image analysis, to be presented in Section 5.5, and we found that it is justified. The necessity of checking the validity of this correction arises from the complexity of the light path through the emulsion system. Light can be deflected at the interfaces, and this can alter the true position of the focal point, as described below.

Spherical Aberration

If the change in refractive index between the immersion medium and the specimen is large, the rays passing through the periphery of the lens will have a different focus to those passing through the centre, thus blurring the image. This effect, known as spherical aberration, is a particularly pronounced problem in lenses with high NAs due to a large Θ_{max} . As mentioned above, the refractive index difference is relatively small in our case, nevertheless the images appear more smeared out and of a lower resolution close to the surface. Beyond the depth of $\approx 10\mu\text{m}$ the resolution and image quality improve. The regions close to the surface are therefore disregarded from further analysis of emulsion samples (physically, they are not useful because of possible wall effects (Sanchez et al., 2001)). This blurring effect is accompanied by a loss of intensity with depth, therefore requiring image intensity equalisation through the sample volume, as discussed in Section 5.2.3.

For such high resolution images as those achieved in the experiments, the amount of blur is minimal and can be removed by the readily available 'median filter' which attributes the median intensity value of a voxel and its nearest neighbours to the central voxel, thus smoothing the image.

Chromatic aberration

Chromatic aberration occurs when rays of different wavelengths of light are focused to different points. Thus, it affects the multi-channel images discussed in Section 4.8.1. Optical filters are applied to the detected light to separate the signal into particular wavelength bands. For instance, separating the detected emulsion signal into a band pass filter (BP505-550nm) and a long pass filter (LP560nm) with the same intensity gain and contrast settings, does not produce the same image clarity in the superimposed image as a single long pass filter at LP505nm, while they should in theory provide the same images. This effect can be attributed to the pinhole being correctly aligned for only one of the settings due to a variation in the back focal plane with wavelength. Nonetheless, the observed difference is negligible and both the multi-channel and single channel images can be used in the subsequent analysis.

Pinhole Misalignment

To maximise the LSCM performance, all the components along the optical path must be properly aligned. In a previous study, the performance of the current microscope was shown to be below the expected standards, which was attributed to a pinhole misalignment that could not be rectified (Myatt, 2002). For this reason, the field of view always exhibits an uneven intensity profile, which is particularly pronounced when using low magnification objectives. It is therefore necessary to use the zoom tool to magnify the field of view to a lengthscale over which this problem is minimised. It was found that a field of view of sidelength less than $100\mu\text{m}$ is sufficiently small to achieve a uniform intensity. Nevertheless, we perform a background intensity equalisation to ensure there are no such intensity fluctuations.

4.5.3 Image Resolution

One can expect 3D images which faithfully represent the sample once the necessary steps have been taken to:

- refractive index match the emulsion sample as much as possible,
- minimise the refractive index mismatch between the sample and the immersion oil,
- employ the highest available NA lenses with a high enough magnification as to eliminate the intensity variation across the field of view.

The spatial resolution of the microscope, influenced by all of the factors discussed in Section 4.5.2, determines the final image quality. The optical resolution of the microscope, i.e. the smallest distance between two separated features, is then determined by the NA and the wavelength of the illuminating light. The spatial resolution is quantified by the Point Spread Function (PSF), which is an empirical measure of the blurring of an image caused by resolution limitations.

An important feature of confocal microscopy is that the PSF suffers from an axial smearing of the order of the thickness of the optical slice, thus the axial resolution is lower. The intensity of a subresolution feature is therefore dependent on the orientation of the object. This effect has profound effects on the emulsion images, as will be shown in Section 4.8.2. Namely, the intensity of a flat object entirely contained within the xy plane will have a lower intensity in the image as its fluorescence contribution is smeared out over a larger distance in the z direction prior to digitisation. The same flat object in the xz plane (vertical in the image) will appear brighter as the subresolution dimension of the object is now detected by the higher, lateral microscope resolution.

Digitisation Process

The confocal image is comprised of voxels, the equivalent of pixels in 3D. The digitisation procedure converts the continuous image function into intensities of voxels of given dimensions. Assuming that the voxel resolution is finer than the optical resolution, there will be no information loss in the digitisation process.

The intensity of each voxel is proportional to the flux of fluorescent light entering the detector. By identifying the different fluorescent species in the image according to their emission wavelength bands, one can map the concentration of each species according to the relative intensities of the different regions within the sample. The image can then be regarded as a 3D map of the concentration of the fluorophores. In practice, the relation between image intensity and the local fluorophore concentration is not exact, as the PSF and fluorescence mechanisms such as quenching can alter the proportionality. However, a comparison of the relative intensity values in the image to deduce the fluorescence mechanisms present in the system was shown to be very useful in this study, as discussed in Section 4.9.5.

Most of the images shown in the Thesis were taken at $\approx 0.15\mu\text{m}$ lateral voxel resolution and $\approx 0.4\mu\text{m}$ axial resolution, which are almost a half of the theoretical optical resolutions for the lenses employed. These values were found to be a good compromise, ensuring no information loss from the continuous image yet avoiding oversampling issues.

4.6 Image Acquisition

The image acquisition stage is crucial for the efficiency of the subsequent image analysis. So far we have dealt with the parameters affecting the performance of the confocal microscope in general and the principles employed to achieve images of the highest resolution. Further details are now given in terms of the microscope settings chosen for our experiments and the degrees of freedom accessible to the instrument user, which can be optimised. All the values are quoted for the most frequently used $63\times$ oil-immersion objective lens.

Pinhole size The thickness of the optical slice, i.e. the resolution in the axial direction, strongly depends on the pinhole size. The smaller the pinhole the thinner the slice, but the less light gets through to the detector, thus reducing image brightness. The optimal size is found when the best compromise between the two effects is reached. The pinhole diameter is automatically set by the LSM software according to the NA, the objective lens and the filter sets employed, but it was found that setting the pinhole diameter corresponding to ≈ 1 Airy unit * gave the best results in the image. It corresponds to a pinhole diameter of $117\mu\text{m}$ and an optical thickness of $0.5\mu\text{m}$ for a $63\times$ lens.

Brightness and contrast The dynamic intensity range available is given by the grayscale intensities from 0 to 255. The amplifier gain and the base line settings of the photodetector amplifier should be set such that the full range is exploited, without saturating the signal. It is best to use the 'range indicator' palette as it identifies the regions of the image which are saturated below 0 as blue and those above 255 as red.

Voxel resolution The size of the voxels in the lateral plane is governed by the zoom setting, which determines the field of view, and the number of voxels in each section. Even though the size of the data set had to be compromised at the later stages for image analysis purposes, all the images were acquired at 512×512 voxel resolution. The resolution and the size of the axial direction were usually limited by the working distance of the objective lens or the loss of intensity with depth arising from slight mismatches in the refractive indices within the emulsion specimen.

The $63\times$ objective lens, set to zoom level 2.0, gives a field of view of $76.8\mu\text{m}$ with a voxel width of $0.15\mu\text{m}$, to yield a sufficiently large particle ensemble for analysis. These values were frequently altered to accommodate for different

*The Airy value depends on the numerical aperture of the lens and indicates the number of diffraction rings. For optimum resolution, Airy values should be small, around 1.

particle size distributions. The sample volume is typically acquired from regions several particle diameters below the upper surface of the sample. The z direction resolution is set to $\approx 0.5\mu\text{m}$, as it is the optimal resolution for the particular lens, suggested by the LSM software. The number of optical slices is set to 128 for image analysis purposes and approximately reaches the working distance of the lens. Beyond this distance, motion is observed within the sample volume as the coverslip begins to exert a pressure on the sample cell.

Acquisition time The capture time per voxel plays an important role in determining image brightness and resolution. The slower the scan the longer the illumination, resulting in a fluorescence of a higher intensity. However, it is often better to use an averaging technique in which the line is scanned faster several times and averaged, because the shorter exposure time avoids problems of photobleaching and heating of the sample. The signal to noise ratio is greatly improved in this way and sometimes allows for a decrease in the voxel resolution without a great compromise in image quality.

The most commonly used settings (for a 512×512 resolution) involve a scan time of 1.5s per 2D section, averaged 4 times, such that a typical 3D image is taken in ≈ 10 minutes. Since this project involves characterisation of the static structure, the acquisition time does not need to be compromised in most cases.

Laser intensity The Argon laser power is set to 75% of the maximum, as indicated in the LSCM manual, and the intensity illuminating the sample is set to $\approx 10\%$ for the silicone oil emulsion samples. Much above 20% laser power photobleaching occurs, resulting in permanent loss of the fluorophore. To avoid the necessity for high levels of illumination, the dispersed oil phase in the emulsion is saturated with Nile red dye. The fluorophore does not change the physical state of the specimen, as it often does in biological specimens, thus high dye concentrations were not a concern.

Filter sets The Nile red fluorescence is environment dependent and could therefore be observed using different filter settings, depending on which sample regions were of interest. The contrast in the image is important in distinguishing between regions of interest and can be fine-tuned using the multi-channel capabilities of the microscope, discussed in Section 4.8.1.

4.7 Experimental Methods

The experimental procedure consists of emulsion compression in the centrifuge and its subsequent transfer into a carefully designed sample cell, which avoids drying and particle motion while enabling the use of oil immersion lenses. The stages in the experimental procedure are described below.

4.7.1 Emulsion Compression

Once the emulsion has been prepared in the way described in Chapter 3, the sample is then compressed under varying pressures for observation of the droplet packings. The smallest pressure is applied by creaming under gravity, owing to a density difference between the phases, whilst further increasing the osmotic pressure is performed by centrifugation. The droplets are deformed according to the pressure. We explore a range of pressures which induce deformations detectable by the microscope, all the way up to the biliquid foam. In order to achieve an inter-droplet force which produces areas larger than the microscope resolution one needs pressures larger than 1/2kPa (depending on the droplet size and polydispersity), as discussed in Section 4.7.2.

As a result, the centrifugation rate is varied from 2000g up to 8000g, at which point the emulsion becomes a biliquid foam and cannot be compressed further. The height of the cream layer, or the volume fraction of the droplets, depends on the centrifugation rate. The samples are centrifuged for 20 minutes and the cream layer is then removed from the top of the centrifuge tube using a spatula. By isolating it from the continuous phase, volume is conserved, as the aqueous phase cannot seep back in between the droplets to relax the stresses.

Thus, the total stresses within the system are stored. However, the application of shear with the spatula may play a role in relaxing the stresses by allowing for an isotropic redistribution of the forces within the system. It is unreliable to consider the pressure applied in the centrifuge as the final pressure observed in the microscope images because the amount of relaxation is not known. Instead, the pressure is calculated directly from the density of forces in the images.

It is important to place the compressed emulsion directly into the cell described in Section 4.7.3, to avoid the drying of the sample. The samples are then left to equilibrate for several hours prior to measurements in the microscope.

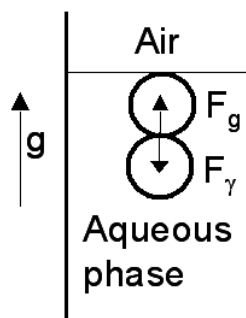


Figure 4.5: Schematic showing the forces acting between two vertically aligned emulsion droplets: surface tension counteracts the gravitational pull.

4.7.2 Centrifugal Forces

The centrifugation procedure introduces an osmotic pressure into the emulsion sample due to the density difference between the dispersed and the continuous phase, in response to which a force network develops. The application of an osmotic pressure implies an isotropic compression, acting on the whole volume through the suspending fluid. This results in isotropic compression rather than a uniaxial compressive force.

To get an estimate of the magnitude of the resulting interdroplet forces let us consider the force which would result between two adjacent particles, vertically aligned, as shown in Fig. 4.5. The forces acting on the particles are due to the earth's gravitational field and the surface tension holding the particle in a spherical shape. In mechanical equilibrium, these forces will be balanced. The related equation can then be used to deduce the area of deformation between the droplets, assuming a proportionality with the force.

The gravitational force F_g acting on the top droplet of volume V , given a density difference between them and the suspending medium, $\Delta\rho$, can be written as

$$F_g = \Delta\rho \times g \times V. \quad (4.4)$$

For silicone oil, $\rho_d=0.97\text{g/cm}^3$, and the continuous phase, $\rho_c=1.13\text{g/cm}^3$, giving rise to a density difference $\Delta\rho=0.16\text{g/cm}^3$. For particles of radius $R = 10\mu\text{m}$, gravity would produce a force of 1pN between the droplets, pointing vertically upwards as the droplets are lighter than the aqueous phase. The Laplace pressure of the droplet, $2\sigma/R$, where σ is the surface tension, governs the surface area A of droplet deformation in response to the force, as $p \propto F_g/A$. Since $\sigma = 9.2\text{mN/m}$ (see Section 3.6.3), the deformed area arising from the gravitational force, assuming a direct proportionality would be a circle of diameter 20nm .

Clearly, such an area cannot be resolved using a confocal microscope, hence

much larger external pressures need to be applied in order for the areas and therefore forces to be measurable quantities. According to the spatial resolution of the microscope, a patch which can be resolved accurately would have a diameter of $1\mu\text{m}$ (~ 5 voxels in the xy direction, ~ 3 voxels in the z), as indicated by the theoretical resolution stated in Table 4.1, which would need an acceleration of $2000g$ to be applied in the centrifuge, according to the above analysis. In practice, due to subresolution fluorescence enhancement mechanisms, the area of the patch must be larger than $4\mu\text{m}^2$ in order to be trustworthy (see Section 6.2.2), requiring an acceleration of at least $6000g$ which yields forces of the order of several nN.

These calculations are very rough estimates, as the collective nature of the system response will result in a complicated particulate structure, with much more complex force balance mechanics, where the total force on the system must be zero if the system is static. Nevertheless, this kind of an analysis leads to an understanding of the order of magnitude of the forces involved in the problem and the amount the forces need to be magnified in order to be accurately determined by confocal microscopy. The actual values of the forces will depend on the particle size distribution, system size and the geometry of the centrifuge tube with respect to the axis of rotation.

4.7.3 Sample Cell

The design of a sample cell which could satisfy all the experimental requirements was not a trivial task. It was necessary to ensure that the sample was unchanging during the imaging, which implied eliminating drying, the presence of air bubbles, drifts and sample relaxation of stress.

Drying has very adverse effects on the sample for several reasons. Since water evaporates preferentially to the other components, the refractive index match between the continuous and the dispersed phases is rapidly lost resulting in an optically impenetrable opaque sample. The volume fraction of the droplets is also increased due to the loss of the continuous phase, therefore increasing the osmotic pressure of the sample in an uncontrolled fashion. The presence of air bubbles in contact with the sample also induces slow drying of the surfaces in contact with it, giving rise to motion unrelated to sample relaxation of the stresses. In addition, if the sample cell is not sealed the air bubble grows inside the sample cell. All these effects can cause unwanted drifts in the sample volume which distort the images due to the comparatively slow image acquisition time.

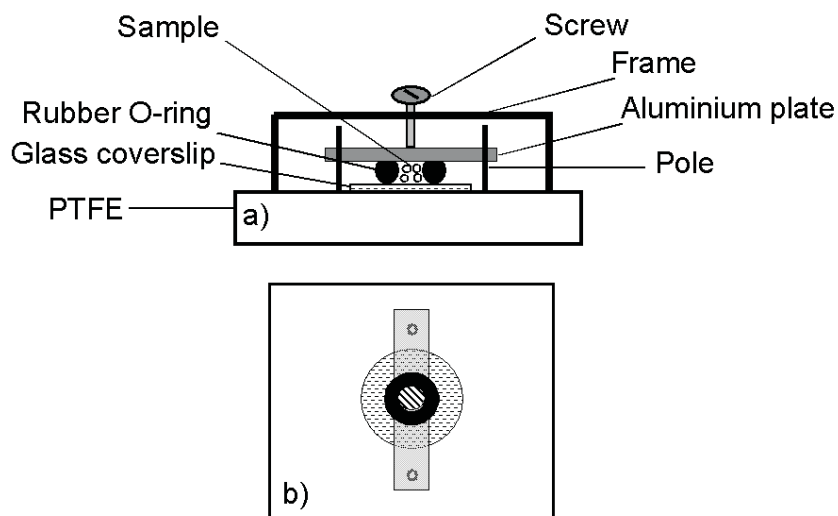


Figure 4.6: Schematic of the sample cell from a side view (a) and a head-on view (b), consisting of a mechanically sealed rubber o-ring in between a rectangular aluminium plate and a round cover slip.

After some experimentation, the set-up which succeeded in satisfying all of the above factors was found to be the one depicted in Fig. 4.6. It is achieved by placing a glass cover slip of 12mm diameter in a marked groove in the middle of a PTFE stand. A small spatula of the viscoelastic emulsion sample (capable of supporting its own weight) is then placed in the middle of the cover slip and a rubber o-ring (inner $d=2\text{mm}$) is placed on top, thus squeezing out excess emulsion from the sides of the o-ring. Excess emulsion ensures that the rubber o-ring is completely filled with sample. The two circular holes in the aluminium rectangular plate are then positioned above the poles surrounding the coverslip to ensure parallelism with the PTFE support and the plate is slid down to press onto the rubber o-ring. The parallelism prohibits the introduction of an air bubble. The screw is then carefully descended onto the metal plate (as illustrated), exerting enough pressure to compress the rubber, thus creating a mechanical seal. This stage prevents the sample from drying.

To ensure a sealed sample and no drift, the o-ring is then glued to the aluminium plate and the cover glass using Araldite epoxy resin and is left overnight to harden. It is necessary to remove the excess emulsion with an air gun prior to the gluing. Since the glue does not bind to the PTFE plate, once the cell is sealed and held together by the epoxy resin, it is possible to displace the sample cell by

simply unscrewing the top screw to release the pressure on the cell. It is then turned upside-down, such that the coverslip ends up underneath the microscope lens for imaging. This method ensures no motion of the sample for a very long period of time and is very important in aging experiments and micromanipulation.

If long periods of stability are not necessary, such as in ‘one-off’ measurements of pressure, a simpler method consists in placing a thin, flat, glass o-ring onto a microslide, introducing a slight excess of the emulsion with a spatula and closing the cell by placing a glass coverslip on top. The pieces are sealed together using nail-varnish, making sure that the o-ring is wide enough such that the sealant does not reach the emulsion sample. This method prevents drying for several hours.

4.8 Fluorescence in the Confocal Images

In the confocal images of the emulsion three environments are identified where the fluorescent dye has a different activity:

1. silicone oil inside the droplets,
2. interfaces, i.e. the droplet perimeters in a 2D slice,
3. aqueous continuous phase.

Moreover, due to the characteristics of the Nile red dye, as will be discussed in Section 4.9, the interfaces exhibit a spectral shift to higher wavelengths and an enhanced fluorescence which can be isolated using optical filters.

The automatic filter settings for Nile red dye use the excitation wavelength of 540nm and observe the fluorescence emission above 560nm using a long pass filter. Due to the blue shift in the absorption of the dye in silicone oil to much lower wavelengths (see Fig. 4.11a), it is more appropriate to use the excitation wavelength of 488nm in order to observe the contribution from the oil. At that excitation wavelength, the fluorescent species inside the oil and the species at the interface and in the continuous phase are simultaneously excited and the emitted signal can be observed using the LP 505nm filter. Using this single filter, one observes the joint emission from all the species, as seen in Fig. 4.8, and the resulting contrast between them is solely dependent on the dye partitioning within the sample.

Since this partitioning is:

1. dependent on the initial amount of dye in the system,
2. governed by the adsorption isotherm of Nile red,

3. affected by the SDS concentration in the continuous phase which alters the dye affinity towards the continuous phase, as discussed in Section 4.9.2,

it is difficult to adjust all those parameters to achieve the necessary contrast between regions. By splitting the emission signal into multiple detector channels, the same result is easier to obtain.

4.8.1 Multichannel Detection of Fluorescence

It is possible to split the emitted signal of the emulsion into channels of different wavelength bands, which forms the basis of the method for extracting the interdroplet forces. The different channels show the fluorescence of either the oil droplets or the interfaces alone, and the contributions of each channel can be tuned such that the areas of droplet contact fluoresce with a higher intensity in the resulting image, see Fig. 4.7.

The fluorescence in the resulting image is tuned by splitting the emitted signal using a band pass filter from 505nm to 550nm in the first channel and a long pass filter above 560nm or 585nm for the second channel. Channel 1 captures only the oil fluorescence intensity, shown in Fig. 4.7a, and channel 2 is able to isolate the rings around the droplets where the dye has migrated to the interface, shown in Fig. 4.7b. The intensity gain and contrast can be manipulated in the separate images such that the contribution from the oil and that of the rings are approximately equalised in the convoluted image, in Fig. 4.7c. The enhanced fluorescence at the areas of droplet contact is achieved when the droplet perimeters fluoresce with a slightly higher intensity than the bulk oil inside the droplets, such that when two interfaces are in contact (at a distance below the resolution of the microscope), their joint contribution gives rise to a significantly higher intensity of the voxels encompassing the contact areas.

The fluorescence enhancement mechanism at the interfaces is thus achieved for samples in which the dye partitioning initially does not provide the correct contrast. Moreover, this effect facilitates the recognition of the particle centres and radii from the information contained in image (a) and the particle deformation from the combined image (c) in the figure.

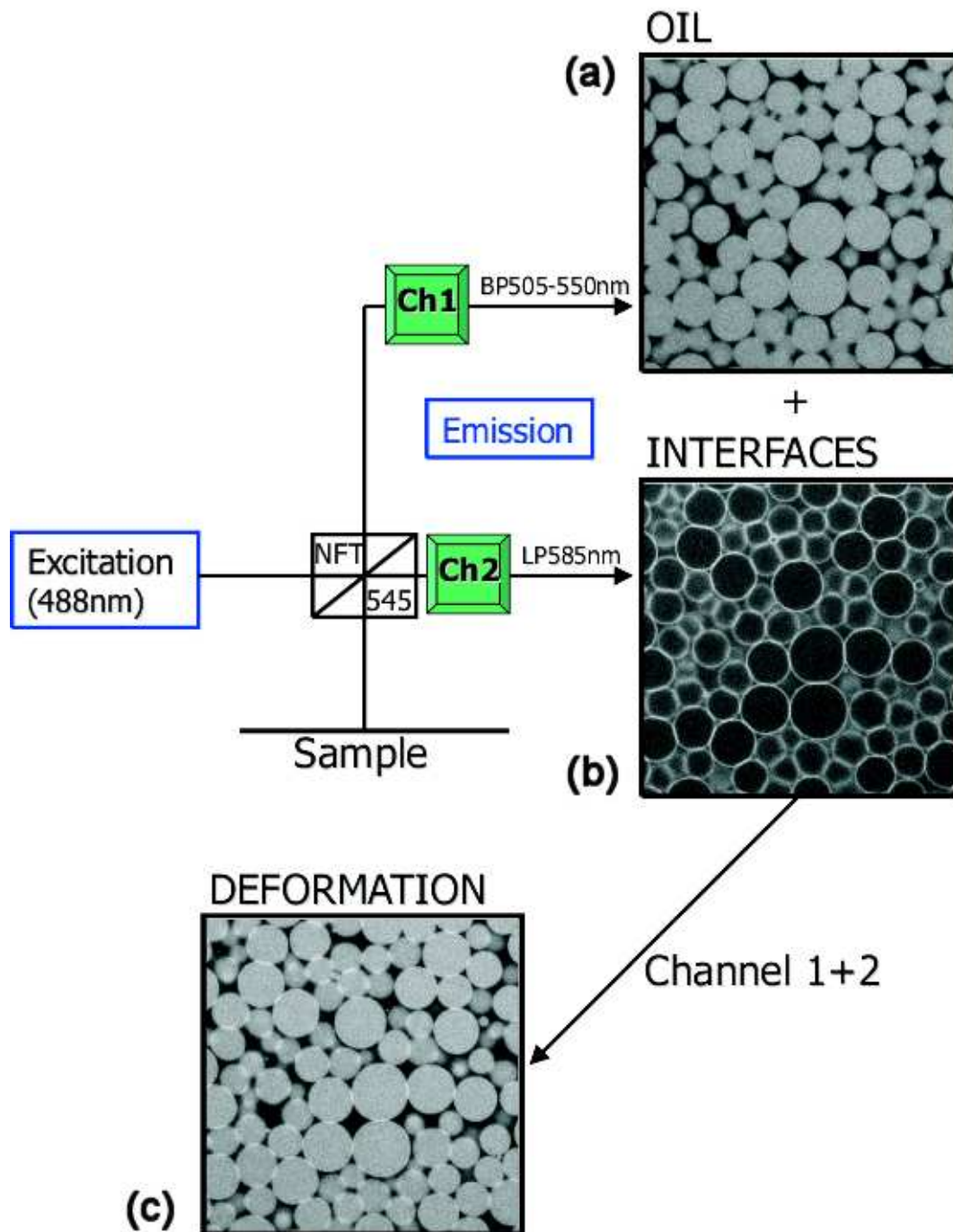


Figure 4.7: Confocal microscope images obtained by splitting the fluorescence using optical filters, (a) BP505-550nm and (b) LP585nm, and their subsequent superposition (c) providing the contrast necessary for image analysis, see Chapter 5.

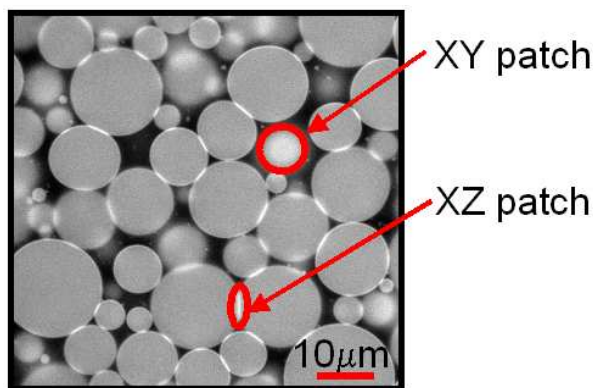


Figure 4.8: Confocal section of sidelength $73.1\mu\text{m}$ and optical thickness of $0.5\mu\text{m}$, obtained using a $63\times$, NA 1.4 Fluor lens with a detector pinhole size of $117\mu\text{m}$. The image shows the discrepancy in brightness of a deformation patch fully in the xy direction and a patch perpendicular to it. The intensity profiles relevant for thresholding issues are shown in Section 5.6.3.

4.8.2 Effects of the PSF on Experimental Data

The PSF anisotropy is an important feature of the microscope in that it affects the measurement of the surface areas of emulsion droplet deformation, as shown in Fig. 4.8. Under pressure, two droplets in contact deform one another proportionally to the force between them. It is very unlikely that they actually touch, due to the strong repulsive interaction potential, but remain separated by a subresolution distance of the order of 100\AA . The surfaces are stabilised by a monolayer of surfactants and are therefore of molecular thickness. Due to the affinity of the fluorescent dye for the interface, explained in Section 4.9, and the subresolution proximity of the two deformed surfaces, there is a higher density of the fluorophore per voxel in those regions as compared to the rest of the sample. Since the thickness of the flat areas is subresolution, the intensity variation of the areas according to orientation is a direct effect of the PSF anisotropy in the z direction. A further complication arises from the fact that the PSF varies with depth due to the image degradation methods described in the previous sections. As the PSF can be defined only locally, a global deconvolution to remove the undesirable effects is largely insufficient. Consequently, the intensity gain and contrast settings are adjusted such that the areas of deformation fluoresce more intensely than the rest of the sample even at the low resolution limit. This allows for a simple thresholding procedure for their identification, discussed in Section 5.6.3.

4.9 UV-Visible Fluorescence Experiments

The interesting fluorescence behaviour observed in the confocal microscope images is also detected and further investigated using a UV-Visible spectrometer, providing insight into the overall fluorescence from the bulk rather than a spatially resolved measurement. The following sections aim to investigate the properties of Nile red which lead to the observed behaviour as well as the fluorescence spectra of the emulsion components to rationalise the observed shifts in the images. The results are discussed in terms of the chemical properties of the species which govern the fluorescence.

All spectrophotometric experiments were performed using 1 cm pathlength quartz cuvettes with a Unicam 8700 series UV - Vis spectrophotometer. The emission spectra were taken at an excitation wavelength of 488nm, at $T = 25^{\circ}\text{C}$. The emulsion samples are separated by centrifugation, obtaining the pure aqueous phase as the supernatant liquid and the cream layer as the emulsion species. All the results presented here are obtained using emulsion samples which are observed in parallel in the confocal microscope, allowing for their direct comparison. This implies that the concentration of the surfactant is always below the CMC (unless otherwise stated), to ensure a repulsive interdroplet potential. The pure oil is recorded after the filtration of undissolved dye through $0.5\mu\text{m}$ pore size membrane.

4.9.1 Properties of Nile Red

Nile red, 9-diethylamino-5H-benzophenoxazine-5-one, is most commonly used for dyeing lipid droplets, due to its hydrophobicity. It belongs to a family of membrane probes with amphiphilic character, inserting the lipophilic portion of the molecule in the membrane and the polar fluorophore residing on the surface (Haugland, 2002). The molecular structure of Nile red, reveals that the molecule is surface active due to the polarity induced by electron conjugation, see Fig. 4.9. The aqueous interface of the hydrophobic droplet is therefore a favourable environment for the molecule.

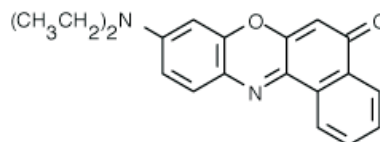


Figure 4.9: Nile Red dye.

Nile red is an uncharged molecule whose fluorescence is strongly influenced by the polarity of its environment. For instance, it is almost nonfluorescent in water but undergoes fluorescence enhancement and large spectral blue shifts in nonpolar environments (Sackett and Wolff, 1987). Hence it is very soluble and strongly

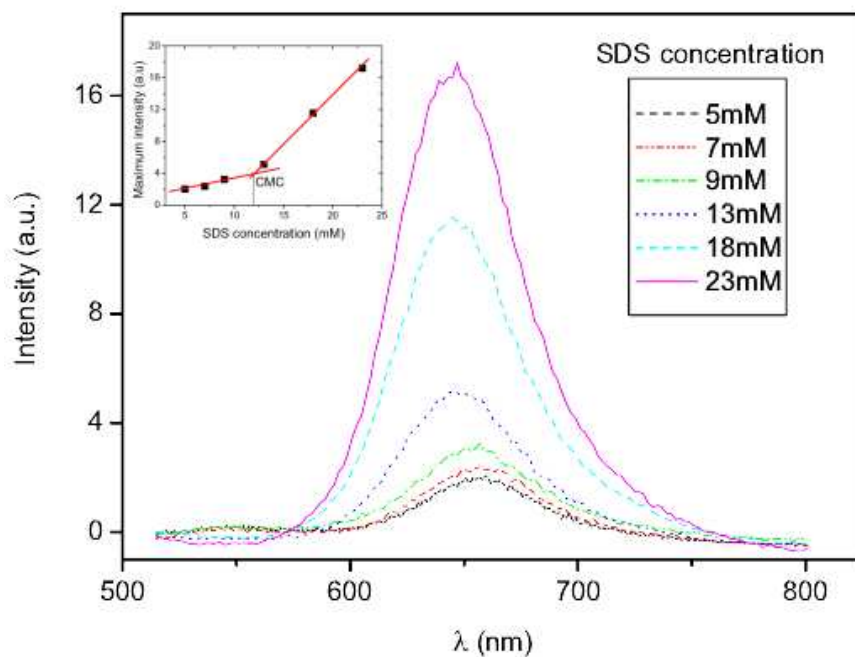


Figure 4.10: Emission spectra of the aqueous phase at a constant Nile Red concentration, but increasing SDS concentration. The maximum emission intensity is plotted against the SDS concentration in the inset, identifying the CMC.

fluorescent in organic solvents and the solubility increases with solvent polarity. For example, the shorter the alkane chain, the more soluble the dye is (Greenspan and Fowler, 1985).

Since both the absorption and the emission spectra of the molecule change according to the environment, it is possible to distinguish between sample regions with the use of only one fluorescently active species. Nile red is photostable, i.e. resistant to bleaching, and has a high quantum yield providing an intense signal in the confocal microscope image.

4.9.2 Amphiphilic Behaviour of Nile Red

The amphiphilic character of Nile red dye is investigated in our system by the addition of surfactant (SDS) into the aqueous solution and observing the changes in fluorescence. The dependence of the dye solubility on the surfactant concentration is shown in Fig. 4.10.

The fluorescence of Nile red is quenched in pure water. The emission is then blue shifted and of increasing intensity as the SDS concentration is raised. When surfactant molecules are incorporated in the aqueous medium, as is the case in the

continuous emulsion phase, they solubilise the dye by incorporating the molecules into the micellar surfactant formations, (Wagner et al., 2003). This observation is consistent with the blue shift associated with polarity, since the environment becomes progressively less polar. The more efficient fluorescence is explained by the greater solubility of the dye as more micelles are introduced. Therefore, the dye migration from the oil phase to other regions in the sample is indeed based on its surface active nature.

Additionally, this effect provides an alternative measure of the CMC, shown in the inset of Fig. 4.10 as a sudden increase in fluorescence intensity as micelles start to form. The cross-over behaviour takes place at $12\text{mM} \pm 1\text{mM}$ SDS concentration, in excellent agreement with the independent measurement of the CMC by conductivity, performed on the same system (see Section 3.6.2). The same change in the behaviour is observed in the absorption spectra as well.

Relevance to the Experiment

The effect of the increasing dye solubility with SDS concentration is relevant to the final contrast achieved for the force distribution experiments discussed in Chapter 6. The emulsion system in these experiments is used as a model for granular materials and therefore requires a purely repulsive interdoplet potential, see Section 3.3.2. Since micelles induce attraction between the droplets, the surfactant concentration is kept below the CMC.

In order to achieve monodisperse droplets emulsification must be performed in viscoelastic media (Mason and Bibette, 1996), where the surfactant concentration is typically of the order of $10\times$ the CMC and the effects of solubilisation are significant. This suggests that more Nile red molecules migrate from the oil phase into the aqueous phase during emulsification (at high SDS concentration), leading to insufficient dye quantities remaining in the oil to provide contrast. This difference can be seen by comparison of the relative intensity values of the oil and the aqueous peaks in the emission spectrum in Fig. 4.11b and those in Fig. 4.13. The latter was emulsified at a much higher SDS concentration (147mM), thus leaving very little fluorescence in the oil, whereas the former was emulsified in 20mM SDS (described in Section 3.4), leaving a much more prominent amount of dye inside the droplets. It is therefore better to lower the surfactant concentration to as low as possible when emulsifying, or alternatively dilute the sample with predyed aqueous phase to ensure the dye migration to the interfaces as well as the bulk droplets.

4.9.3 Environment-Sensitive Fluorescence Spectra

The absorption and emission spectra of the emulsion system, shown in Fig. 4.11, detect fluorescence from mixed species: the oil phase, the aqueous phase and the interfaces. Their overlapping absorption bands give rise to different fluorescent species at the same excitation wavelength.

The pure oil phase absorption is severely blue shifted and peaks at $\lambda = 488\text{nm}$, while the aqueous phase peaks at a much longer wavelength, $\lambda = 568\text{nm}$. This is consistent with the blue shift associated with a decrease in polarity. Since it is the droplets we are primarily interested in, it is necessary to excite the emulsion sample at a wavelength sufficiently low to allow comparison with the confocal microscope, i.e. 488nm . The resulting emission spectra experience the same spectral shifts with the oil peaking at 545nm and the aqueous solution at 645nm , although the aqueous solution fluorescence is much weaker because the excitation wavelength is not optimal for this species. The peaks are so well separated that it is possible to distinguish between them by introducing optical filters which decompose the emission signal into wavelength bands associated with each species. These results qualitatively agree with the observed fluorescence from the images, in that the oil fluorescence is clearly detected in the wavelength band between 505nm and 550nm in the images, whereas the relative signal intensity from the continuous phase is too weak to be detected.

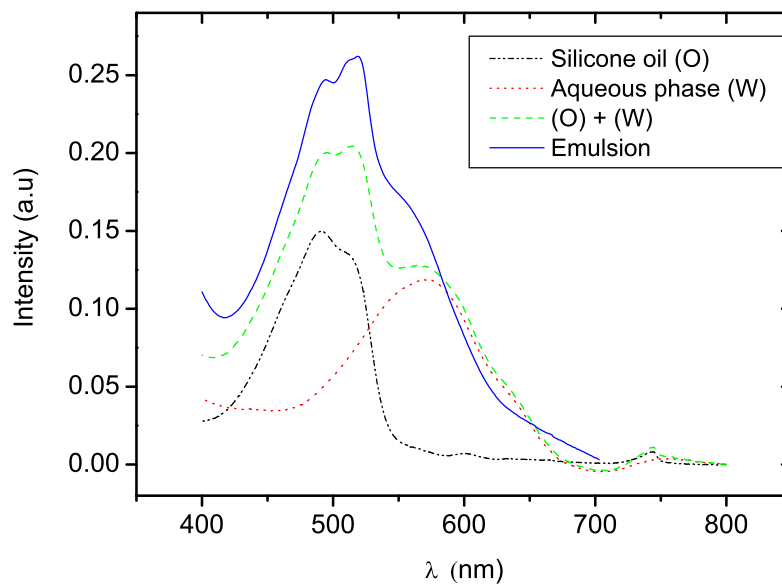
4.9.4 Interface Fluorescence

The droplet interfaces in the confocal image fluoresce with a higher intensity and are red shifted as compared to the fluorescence from the bulk of the droplet, as seen in Fig. 4.7b. A long pass filter at 585nm reveals a more efficient fluorescence localised at the interfaces in the images, whereas there is no obvious additional peak in the emulsion fluorescence spectrum to account for that.

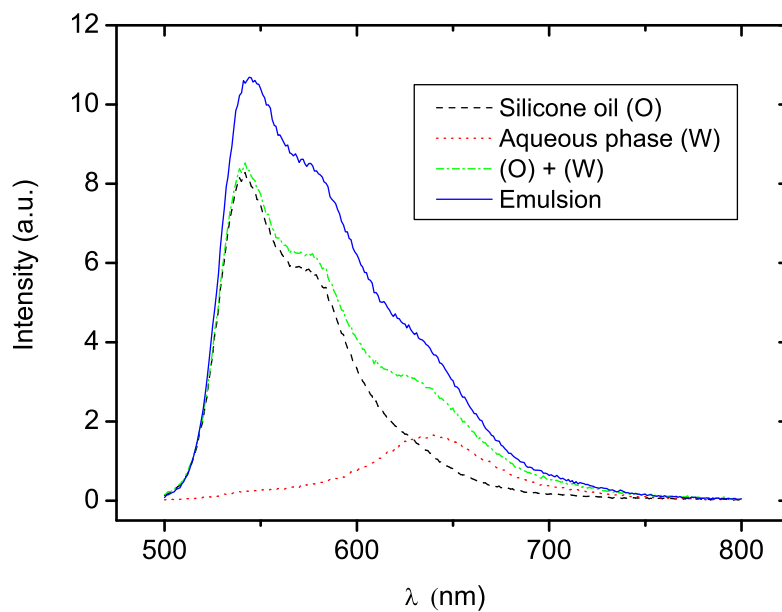
In order to investigate the contribution from the interface we first wish to quantify the difference between the oil and aqueous bulk phases taken separately, and the emulsion. The difference in the emission intensity in arbitrary units is influenced by many factors. At this point it should be noted that the fluorescence intensity is dependent on the same parameters as absorbance, defined by the Beer-Lambert law,

$$A = \epsilon \times l \times c_{dye}. \quad (4.5)$$

It is the product of the molar extinction coefficient, the path length and solute concentration and additionally depends on the efficiency of emission fluorescence



(a)



(b)

Figure 4.11: Environment sensitive absorption (a) and emission (b) spectra (excitation wavelength $\lambda=488\text{nm}$) of: 1) the separate emulsion components, 2) the sum of their contributions and 3) the emulsion sample. All the spectra arise from the differential fluorescence of Nile red dye.

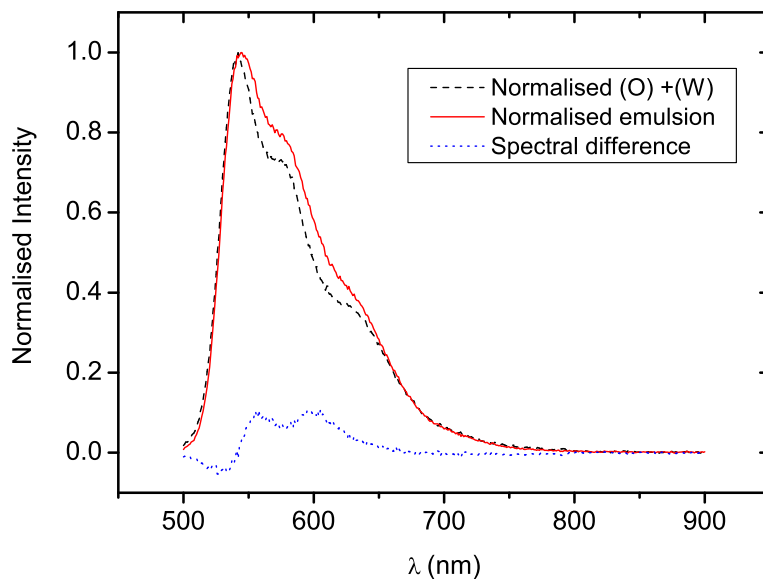
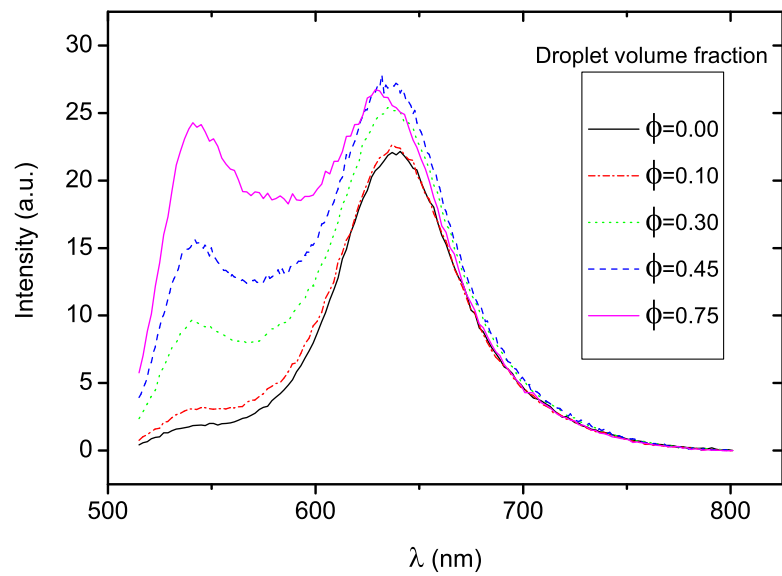


Figure 4.12: Normalised emission spectra of the emulsion and the added water and oil spectra, whose difference indicates the contribution of the interface.

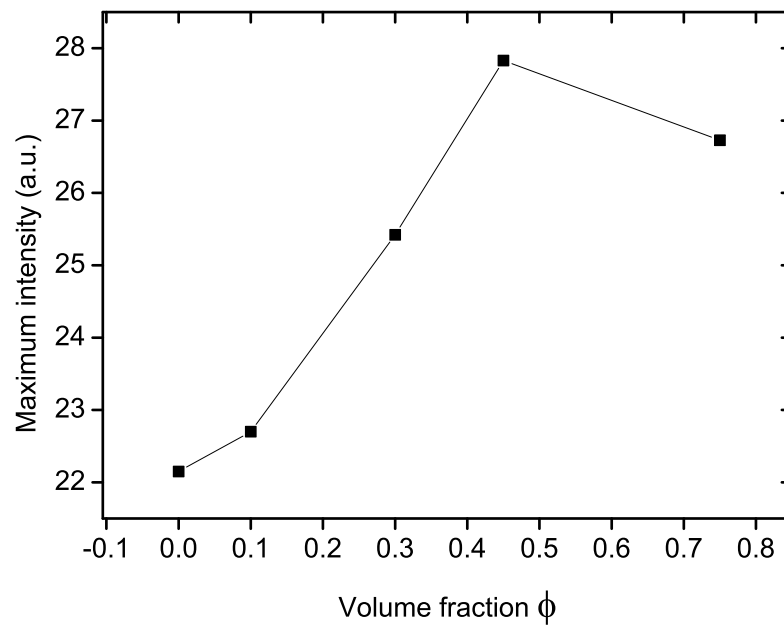
of the dye. Since an emulsion creams under gravity to form complex particulate structures of inhomogeneous particle density, it is difficult to draw conclusions from the intensity of the spectrum. In addition, scattering at the droplet interfaces is also possible if there is a slight mismatch in the refractive indices of the phases, also affecting the intensities of the absorption and emission spectra. However, spectral shifts can be detected by comparison of the normalised spectra of the sum of the different species present in the emulsion and the emulsion itself, shown in Fig. 4.12. The spectra are normalised to the maximum value of the intensity.

The spectral difference, also shown in the figure, reveals a small increase in fluorescence, giving rise to a small peak at the longer wavelength of 605nm. It is difficult to believe that such a small peak would give rise to such a significant fluorescence in the image, as it seems unlikely that it is a peak attributable to a new excited species. In addition, the aqueous phase peak in Fig. 4.11b, which is of a higher intensity, does not fluoresce in the confocal image intensity range. Thus, the origin of the interfacial fluorescence requires further investigation.

In order to further test the influence of the interfaces the spectral response is investigated as a function of the volume fraction of droplets, i.e. the number of interfaces, as shown in Fig. 4.13a. Increasing the volume fraction of droplets is



(a)



(b)

Figure 4.13: (a) Emulsion emission spectra as a function of the droplet volume fraction, showing the interfacial contribution. (b) Intensity maxima of the emission spectra (at $\lambda \sim 640\text{nm}$) as a function of the volume fraction.

achieved by the mixing of the pure continuous phase with a high volume fraction emulsion ($\phi = 0.75$). The recorded spectra are shown in Fig. 4.13. The oil peak (545nm) increases linearly with the volume fraction of oil and does not contribute to the interfacial fluorescence. The peak at longer wavelengths (aqueous peak) increases by only 22% between the two extreme situations: the pure aqueous phase and the maximum random close packed emulsion ($\phi = 0.75$) even though the maximum possible number of interfaces (without compression) are thus introduced.

This increase in the emission maximum at $\approx 640\text{nm}$ with increasing droplet volume fraction, as shown in Fig. 4.13b, can be attributed to the introduction of an increasing number of interfaces in the sample volume. A quantitative analysis is provided in Section 4.9.5. The increase seems to saturate above the droplet volume fraction $\phi = 0.45$, which may be due to a self quenching mechanism as the interfacial species are forced into contact with one another.

These results indicate that the actual number of dye molecules covering the interfaces is small compared to those in the bulk, but simply much more concentrated. These highly concentrated regions appear very bright in the images due to the increased number of emitted photons detected per voxel, thus dominating the signal from the bulk in the available intensity range. To avoid saturation at the interfaces, the aqueous phase now appears with a very low intensity on the grayscale, even though it is significantly fluorescent in the emission spectrum. The confocal microscope images are a *spatially* resolved measurement of fluorescence rather than an average. Such a spatial resolution is able to detect heterogeneities in the concentration of the same fluorescent species within the sample. Based on the emission wavelength band remaining unchanged, as well as the relatively small additional contribution to the fluorescence emission spectra by the interfaces, both the spectra and the images suggest that the interfacial dye species is the same as that in the bulk water. The analogous environments for Nile red, provided by the micelles in the water phase and the surfactant rich interface, are explained in Section 4.9.6.

4.9.5 Semi-Quantitative Analysis

The information from the confocal images and the fluorescence spectra are combined to provide a quantitative analysis of the fluorescence. We first measure the volume fraction of each of the components and the ratio of fluorescence intensity between the interfaces and the continuous phase (10mM SDS concentration) from the 3D images. We then calculate how much more concentrated the dye in the interfaces would have to be in order to account for the intensity increase observed

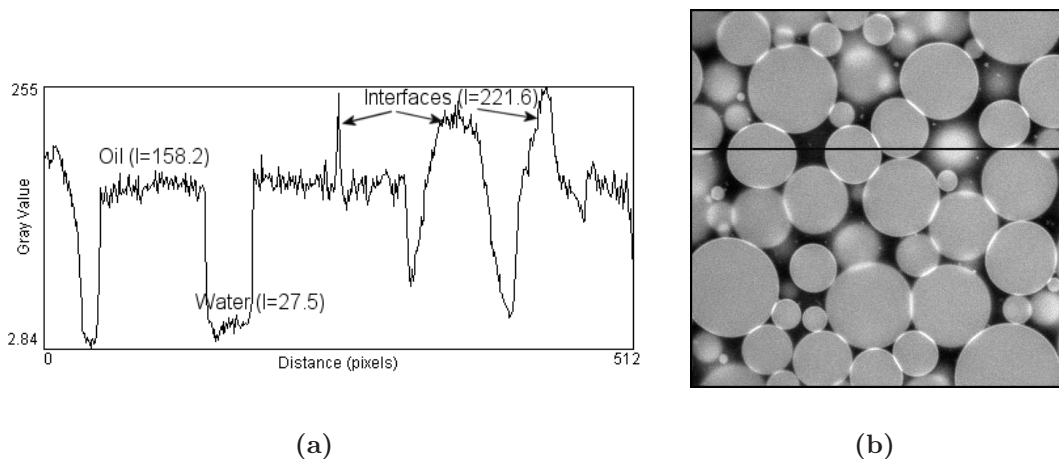


Figure 4.14: (a) Intensity profile across the field of view along the black line in image (b). The average gray scale intensity values, I , of each sample region are also indicated.

in the fluorescence spectra. We find that the fluorescence ratio measured from the image intensities coincides with the value predicted by the spectra, in support of the assumption that the interfacial dye species and those in the continuous phase are indeed the same.

Since the spectral peaks are dependent on the amount of fluorescent species present in the system, it is first necessary to quantify the volume fraction of each species. The emulsion volume fraction, previously defined in Eq. (4.13), is now defined more precisely as:

$$\phi = \frac{(V_d + V_i)}{V_{tot}}, \quad (4.6)$$

where subscripts d, i and tot refer to the volumes of droplets, interfaces and the whole system, respectively. The contribution of the interfaces to the system volume was previously omitted since it is usually negligible. Analysis of the confocal images of the random close packed emulsion revealed that the interfaces represent 12% of the sample volume, i.e. $V_{iRCP} = 0.12$ if the total volume is 1. This measure is simply achieved by applying a threshold to the images of the interfaces alone, such that the voxels belonging to the interfaces are attributed a value of 1, and the rest are 0. The proportion of the former in the whole image is then taken to be the volume fraction of the interfaces. Since the interfaces are subresolution (see Section 3.3.2) their volume is overestimated by the PSF smearing of their contribution. For that reason, it is only the apparent volume rather than the real volume. The same procedure applied to the droplet image alone reveals that the oil volume fraction is $V_{dRCP} = 0.63$ and that of the aqueous phase is therefore $V_{wRCP} = 0.25$.

The differential fluorescence intensity in the images is then quantified by the comparison of the voxel brightness, as measured by the intensity profile in Fig. 4.14a. According to the average gray scale values (0 – 255) corresponding to the interfaces and the surrounding aqueous phase, $I_i \approx 221.6$ and $I_w \approx 27.5$, respectively, in the image in Fig. 4.14b, the ratio $I_i/I_w=8.1$, meaning that the interfacial fluorescence is ≈ 8 times stronger than the contribution from the bulk aqueous phase.

The analogous analysis of the emission spectra showed that the overall increase in aqueous fluorescence peak between the pure aqueous phase and the random close packed emulsion was 22%, see Fig. 4.13. The emission peak intensity is in arbitrary units but is proportional to the fluorescence intensity arising from a given concentration of dye molecules in the sample volume. Therefore, the pure aqueous phase peak can be expressed as

$$P_0 \propto c_w V_0 \quad (4.7)$$

where c_w is the concentration of dye in the aqueous phase and V_0 is the volume of the pure water system - taken to be 1 in this analysis. The same peak at random close packing has an added interfacial contribution and a reduced volume of the bulk aqueous phase, and can be expressed as

$$P_{RCP} \propto c_w V_{wRCP} + c_i V_{iRCP}. \quad (4.8)$$

Then the measured ratio of the obtained peaks is deduced as

$$\frac{P_{RCP}}{P_0} = \frac{(c_w V_{wRCP} + c_i V_{iRCP})}{c_w V_0} = \frac{V_{wRCP}}{V_0} + \frac{c_i V_{iRCP}}{c_w V_0} = 1.22. \quad (4.9)$$

Since we know the volume fraction of each species as measured from the images, we can calculate the ratio of the dye concentration in the interfaces and the bulk water, c_i/c_w :

$$\frac{c_i}{c_w} = \frac{(1.22 - 0.25)}{0.12} = 8.1. \quad (4.10)$$

According to this approximate analysis, in order to see the increase in fluorescence intensity obtained from the emission spectra of the pure aqueous phase and the RCP emulsion, one would need an 8 times higher concentration of dye at the interfaces than in the bulk. This is in remarkably good agreement with the observed fluorescence intensity enhancement in the confocal images ($I_i/I_w = 8$) and gives support to the rationalisation of the spectra given the presence of the same excited species in both environments.

4.9.6 Postulated Mechanism of Dye Insertion

The structure of the surface active SDS molecule is shown in Fig. 4.15. From the results presented in this Chapter, we deduce that the Nile red molecules insert themselves in between the surfactant species at the interface, while they sit in the hydrophobic region of the SDS surfactant micelle, as shown in the diagram of Fig. 4.16. Micelles organise themselves in such a way as to keep hydrophobic residues together, separate from water, while the polar heads are in contact with the polar solvent. Both environments of the dye are primarily hydrophobic but ‘feel’ the surrounding aqueous phase, thus giving rise to the same excited species.

Influence of Compression

The question which remains to be answered is the direct effect of stretching the elastic surfactant film upon compression on the distribution of the dye. The brighter fluorescence at the interfaces coupled with the subresolution distance between two interfaces exerting a force on each other may well be sufficient in accounting for the intensity enhancement of the areas of deformation, however, an added effect of stretching the interface and therefore changing its curvature may also play a role.

It has been observed that the average intensity ratio between the interface and the droplet body increases in the same emulsion as the pressure is increased (see Fig. 3.1). This can be explained by the creation of more interfacial area to which the molecules can migrate from the bulk. The question of whether the concentration of dye per unit area of the interface increases as the SDS molecules are pushed apart by the stretch, or if the SDS molecules from the bulk preferentially diffuse to stabilise the stretched interface, requires further investigation of the adsorption kinetics of the two surfactants. One way of testing this effect would be to design an experiment in which two micro-manipulated droplets from this emulsion are brought in contact with one another under the confocal microscope (Bartlett et al., 2001), and the area of deformation is observed as a function of the force or the interdroplet separation. This would also allow for the derivation of the exact interdroplet potential excluding the effects of the system’s collective behaviour.

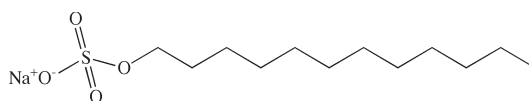


Figure 4.15: Sodium dodecyl sulfate surfactant molecule.

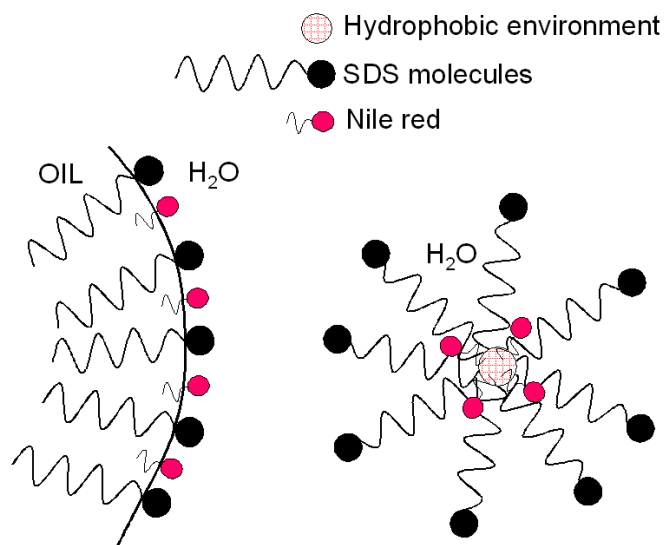


Figure 4.16: Mechanism of dye insertion into the (a) interface and (b) micelles. The interfacial environment is present in both cases, giving rise to the same excited species.

4.9.7 Limit of the Fluorescence Method

It is important to note that this differential fluorescence method is not valid for very low dye concentrations at which surface coverage is not achieved. The surface concentration versus the bulk concentration is known as the ‘adsorption isotherm’. The emulsion system is nominally stabilised by SDS surfactant species, hence there is a competitive adsorption between the SDS and the dye molecules at the interface. The adsorption isotherms for SDS on a hydrophobic surface are monotonic, but reach a plateau value at a low bulk concentration, approximately at 1/3 of the CMC (8mM for SDS), as measured by neutron reflection experiments (Lu, 2003). Below this concentration the amount of SDS at the surface decreases rapidly and the remainder of the molecules are found in the bulk. Assuming that the dye molecules undergo the same kind of adsorption mechanism at the surface, the fluorescence intensity at the interfaces will rapidly decrease below a critical concentration, but will remain fluorescent in the bulk, as before. There are at present no studies of the adsorption isotherms of surface active dye molecules, but the effect of Nile red adsorption presents a useful tool for the investigations undertaken in this research.

4.10 Summary

This Chapter has characterised the heterogeneous fluorescence of Nile red in the different regions within the emulsion system. The mechanism for this dye migration was explained by the amphiphilic nature of the dye molecule. This effect was investigated by increasing the surfactant concentration in the water phase above the CMC and observing the dye incorporation into the micelles. Moreover, the dye localised at the interface was shown to be the same fluorescent species as the dye incorporated into the micelles in the continuous aqueous phase, only at a concentration which is of the order of 8 times higher than in the bulk. On the other hand, the dye in the silicone oil was identified as a different fluorescent species, absorbing and emitting light at shifted wavelengths.

The environment-sensitive spectral shift, as well as the increased concentration of dye at the interface were found to be particularly useful in the confocal microscopy experiments. Splitting the detected light signal into channels of well-defined wavelength bands allowed for the separate detection of the different regions in the sample in separate images, and the subsequent fluorescence enhancement of the contact areas between the droplets in the superimposed image. As a result, we were able to identify the particle centers and radii using an algorithm described in Chapter 5, as well as the forces between them from the isolation of the areas of deformation arising from their compressibility.

Chapter 5

Characterisation of Compressed Emulsions

Although the pool's
reflection blurs before us often:
know the image.

Rainer Maria Rilke,
The Sonnets to Orpheus (IX)

5.1 Introduction

The characterisation of the compressed emulsion system is performed by the application of novel 3D image analysis algorithms to the confocal images with the aim of extracting the important physical features of the particle packings. Obtaining spatial and size distributions of the emulsion droplets is a very complex problem and can only be resolved by a combination of many elementary transformations.

This Chapter first provides a brief discussion of 3D image analysis methodologies in general. The novelty in their application to the problem of particle packings is then discussed in detail. We present the analysis routines applied to the images to extract the relevant quantities and illustrate every stage in the process.

While image analysis techniques in 2D have been developed to a sophisticated level by numerous commercially available software packages, the analysis in 3D is scarce and most of it is not generically in 3D. More often than not, this analysis simply reconstructs 3D information from the conventional 2D analysis methods characterising each slice in turn. Although this methodology can be qualitatively

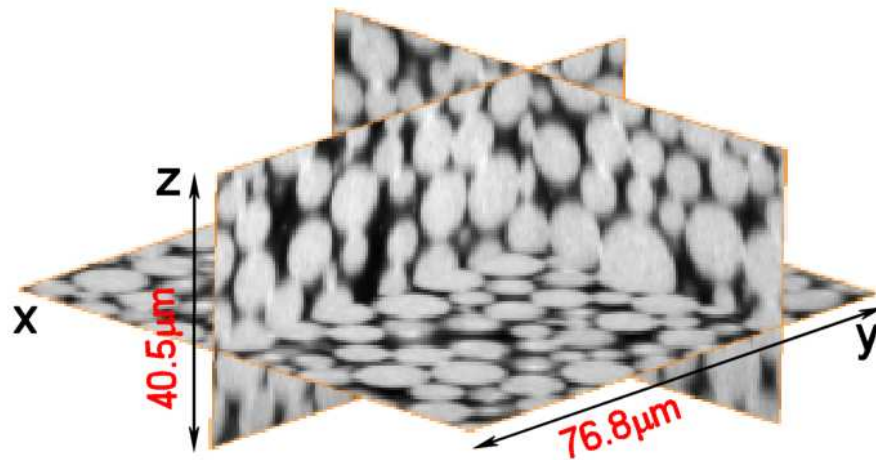


Figure 5.1: Confocal microscope image of a packing of droplets created under gravity. (40 \times lens, NA 1.3, zoom 3)

useful in some cases, it does not take into account the full spatial relation between the slices and without correlating the obtained information in the third dimension, one is not able to achieve optimum results in image reconstruction.

With the advent of a range of 3D imaging techniques, such as X-ray tomography, magnetic resonance imaging and ultrasonic imaging, there have been recent attempts to perform the analysis of these images using true 3D algorithms for features which are intrinsically three-dimensional. This area is certain to experience rapid growth since its importance spans from medical diagnosis, surgical planning, to robotics and visualisation of the natural world in its true dimension. The 3D image analysis methodology is covered in the literature, such as (Nikolaidis and Pitas, 2001; Luebke et al., 2003).

In our experiments the constituent particles of the compressed emulsions range from being entirely spherical at low confining pressures, as shown in Fig. 5.1, to forming a 3D honeycomb lattice at maximum compression. These two extreme cases require very different analysis methods. In the analysis presented in this Chapter, the approximation of sphericity, due to relatively low confining pressures, is considered adequate for the extraction of the relevant physical features. This assumption is very important as it allows for the determination of the sphere centres and radii using Fourier analysis (Lewis, 1995). The analysis of the biliquid foam structures are not within the scope of this Thesis.

The aim of the image analysis is to yield the spatial and size distributions of the emulsion droplets, and their surface areas of deformation, from which physical quantities, such as the forces on individual droplets, are later inferred. The sphere centres and radii are obtained from the 3D Fourier analysis of the data, by the recognition of their spherical shape. Furthermore, a morphological analysis of the areas of deformation, arising from the fluorescence mechanism described in Section 4.8, provides information about the true areas of droplet deformation, referred to as the ‘patches’. These areas are compared with the geometric sphere overlaps calculated from the identified droplet centres and radii, here referred to as ‘simulated overlaps’. The correlation between the ‘patches’ and the ‘simulated overlaps’ serves as a test for the validity of the experimental technique. Since the existing theoretical framework for determining the forces from the areas of deformation makes the assumption that the spheres are simply ‘cut off’ at the overlap, i.e. that there is no shape deformation upon compression, the validity of this assumption is also put to the test.

The output of the image analysis is a set of indexed contact areas, along with the undeformed radii and centres of the two droplets giving rise to each contact. This set of data enables the extraction of the normal force by means of existing interdroplet force models, discussed in Section 6.2.1.

To summarise, the characterisation of the compressed emulsions is a multi-step process, starting from the creation of the image in the microscope and leading to the force distribution data discussed in Chapter 6. The sequence of the steps leading to the full spatial information of the forces within the bulk is followed within this Chapter. Apart from the characterisation of the forces, this procedure provides a versatile platform for the extraction of configurational features such as the coordination number, the stress tensors and the spatial analysis, presented in Chapter 6.

5.2 3D Image Processing Methods

In the image analysis and reconstruction, numerous problems arise from either the noise contributions or the systematic imperfections of the imaging technique itself, as discussed in Section 4.5.2. It is of utmost importance to identify and remove them by filtration methods before venturing into the quantitative analysis of the physical features in the image. These filtering methods include noise level reduction, contrast and edge enhancements and the removal of outliers, covered in

the literature (Soille, 2003). The particular image filtration techniques which were employed in the preliminary image processing of each stack are presented in turn.

5.2.1 Image Segmentation

Segmentation is used in several stages of the analysis, not only in image pre-processing, but also the isolation of droplet centres in conjunction with the Fourier analysis (see Section 5.3.4) and in the construction of areas of deformation (see Section 5.6.3).

Image segmentation is the division of an image into different regions according to the properties of those regions. The simplest segmentation technique is thresholding: voxels whose intensity falls between two pre-defined threshold values are assigned to a corresponding region. The image is then partitioned into regions (objects) in which the thresholded voxels are connected. This is known as the connected component *labeling* of a binary image, and is a transformation directly associated with connectivity (Alnuweiri and Kumar, 1991). Once the objects have been labeled, the features of each object can be determined to give a quantitative interpretation of the image data. The features include the number of voxels in the region (object volume), object's centre of mass, its eccentricity, the density of voxels within the object etc. These quantities are useful for setting further object selection criteria. Specific examples are presented in the next section.

5.2.2 Removal of Outliers and Noise

In some cases, the samples contain bright, fluorescent impurities which can be interpreted as undissolved pieces of dye, or dust particles which have accumulated dye molecules on their surface. Within the image, they are considered as *outliers* since they do not belong to the experimental measurement range of interest and are few and far between. These objects are identified by the labeling technique, described in Section 5.2.1. They are easily removed as they are brighter than any other object in the image and their volume is larger than the maximum size of the relevant features in the image. This stage is important in that the presence of very bright large objects would cause problems in the particle-finding algorithm, described below.

Similarly, bright objects that contain less than 4 connected voxels were identified and subsequently removed, as they correspond to the true resolution of the microscope. This filtering reduces noise contributions to the data.

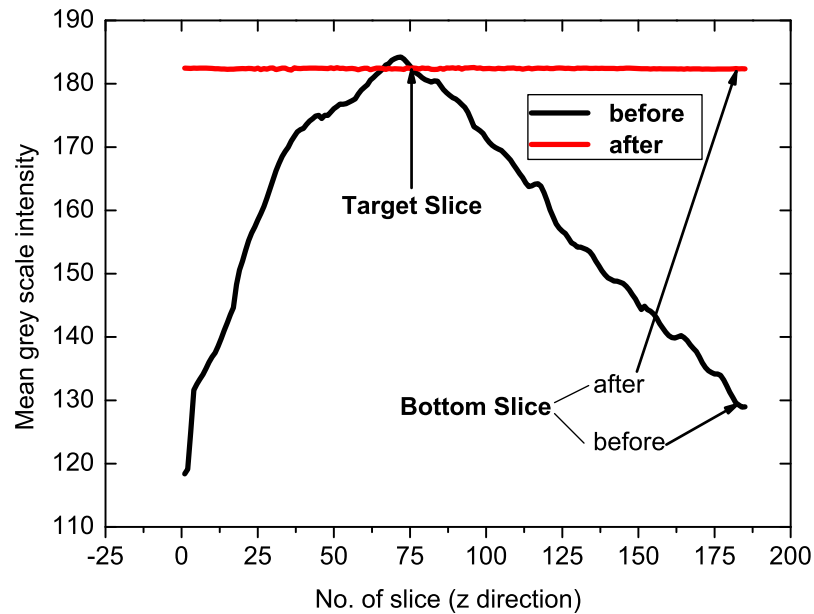


Figure 5.2: Mean intensity profiles from the surface to the bottom of the 3D image ($92\mu\text{m} = 184$ slices), before and after intensity equalisation. The slices indicated in the figure are shown in Fig. 5.3.

5.2.3 Intensity Histogram Equalisation

The loss of intensity with depth, arising from a refractive index mismatch and spherical aberration, has been discussed in section 4.5.2. Although the intensity of the beam can be increased manually with depth, it is better to provide a continuous correction to the image, post-acquisition, to achieve a uniform intensity variation through the sample. Of course, this is only possible if the intensity loss is relatively small, unaccompanied by the loss of object definition, such that the original features can be recovered by a simple intensity enhancement.

This filtration method concerns the correction of uneven illumination of an image through the sample and across the field of view. The output image should have an homogeneous background which eases all further treatments, such as global thresholds.

The contrast enhancement through the sample is performed using histogram equalisation. The basis of this function is to transform the intensity values in the original image such that the histogram of the output image approximately matches a specified, ‘target’ histogram. In this case, the target histogram is chosen to be that of a 2D slice close to the sample surface where the intensity loss is insignificant (see Fig. 5.3a). The intensity histograms of all the other slices in the image are equalised with the target, in practice resulting in the brightening of the slices deeper into the specimen, and the dimming of those closer to the

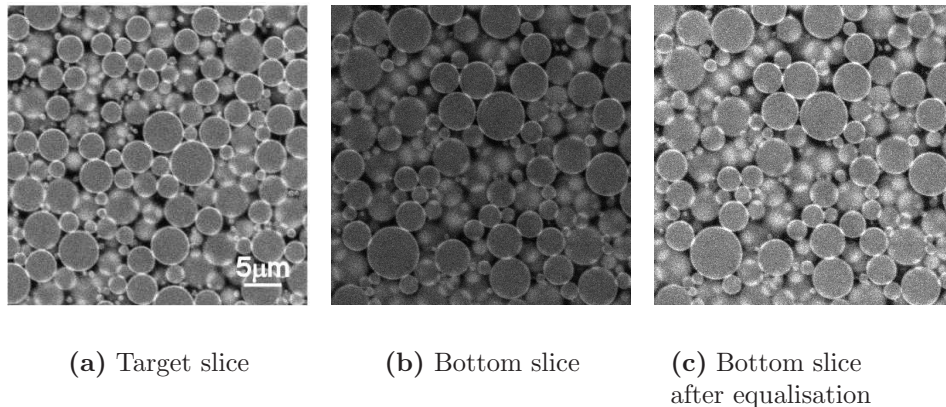


Figure 5.3: 2D slices showing: (a) the target histogram slice $z = 40\mu\text{m}$, (b) a slice near the bottom of the image stack $z = 90\mu\text{m}$ and (c) its intensity enhancement post-equalisation with the target.

surface. Surprisingly, it was found that the mean slice intensity reaches a peak some distance below the surface (I_{max} at $29.2\ \mu\text{m}$, slice 75 in the z direction), after which the aforementioned mechanism of degradation takes place, as seen in Fig. 5.2. This initial increase in intensity with depth is most probably due to the refraction at the interface which arises from the refractive index mismatch between the immersion oil and the emulsion, rather than between the emulsion phases.

An example of the image brightening, where the loss of intensity is much more significant than is usually the case in our images, is shown in Fig. 5.3c. It can be seen that the discrete nature of the digital image intensity in Fig. 5.3b causes a noise increase in Fig. 5.3c which can be detrimental to the analysis which follows. Performing a median filter (Paeth, 1990) on the 3D image, prior to equalisation, improves the output image, but was not always necessary for the relatively small loss of intensity in the samples used in this study.

Although the most pronounced variation in intensity occurs through the sample depth, the intensity variations across the field of view may also play a role. This is particularly true of the microscope used in this study since it is known to have a pinhole misalignment problem (Myatt, 2002). Using a high magnification lens and zooming into the region of interest greatly reduces this effect. As a precaution, a background function is calculated and subtracted from each two-dimensional image. A quadratic polynomial is used to approximate the background, in which the brightness is expressed as a function of the position in the following form (Russ, 1990):

$$I = a_o + a_1x + a_2x^2 + b_1y + b_2y^2 + c_1xy + c_2x^2y \quad (5.1)$$

and subtracted from each two dimensional image.

5.3 Droplet Reconstruction

The high volume fraction of particles present in the images, their polydispersity and their compression led to a complex network of deformed spheres in contact, which are difficult to divide into separate entities necessary for their identification. Significant noise contribution together with a large number of droplets being only partially present within the image also did not help in the morphological approach. Therefore, real space image analysis based on morphological operations were found to be inadequate for the analysis of such highly connected 3D objects (Haralick and Shapiro, 1992).

Another commonly used approach in the spatial domain is convolution, which involves shifting a kernel (in this case a sphere) to every location in the image and comparing it with all volume regions of voxels in search of best correlations. This is known as a template matching or correlation process (Dufour et al., 2002; Jurie and Dhome, 2001b). When the dimensions of the kernel and the space are large, such as in our case, this is a prohibitively slow and inefficient process (Jain et al., 2000; Russ, 1999).

On the other hand, the computational difficulties are reduced in Fourier space because the equivalent operation to a convolution in the spatial domain is a multiplication in the frequency domain. We can consider the emulsion image as a set of spheres of different sizes convolved with a set of delta functions defining their positions (Dufour et al., 2000b; Abu-Naser et al., 1998). The convolution theorem of Fourier transforms thus gives us a route to finding sphere centres of a particular size. The main attraction for using this method, apart from alleviating the computational difficulties encountered in the spatial domain, is the subvoxel accuracy with which it can determine the desired parameters.

This method is based on the identification of a particular feature in an image according to its structure, shape and geometry (Jurie and Dhome, 2001a; Dufour et al., 2000a). Since in the case of particulate packings the droplets are spherical such an analysis seems to be appropriate. On the basis of this approach, a novel image analysis procedure has been developed, tested and implemented in this study to analyse the compressed emulsion configuration using a sphere as a template. We have named this method the Sphere Matching Method (SMM). The novelty in our approach extends to the problems of polydispersity and the high level of connectivity in the particulate network.

The exploitation of 1D and 2D Fourier filtering is well established in the literature, but the equivalent 3D computation has not been extensively discussed. A very large amount of data in an image makes it almost impossible to use a 3D dis-

crete Fourier transform (DFT) due to the computational complexity of the method (Parker, 1997). However, Fast Fourier Transform (FFT) computation algorithms prove much more suitable in this respect and can be readily employed. Even so, this method of implementation required 1GB of RAM memory and careful memory allocation and deallocation.

5.3.1 Sphere Matching Method (SMM)

In the previous Sections, we have presented how to clean and enhance the confocal images and pointed out the advantages for using Fourier analysis to identify the particle centres and radii. In general terms, the Fourier transform converts features in the spatial domain into their equivalents in the frequency domain and provides a mathematical mechanism for building filters which remove or enhance features of a particular frequency in an image.

Perhaps the most famous application of this method in confocal microscopy is deblurring, which uses the point spread function (PSF), discussed in Section 4.8.2, as the template in the image and subsequently removes those frequencies corresponding to the blur introduced by the optical technique. This is known as the inverse filter (Berg and Malik, 2001; Russ, 1999).

5.3.2 Mathematical Basis for Using SMM

For simplicity, let us assume that there are N particles of the same radius in the system, each described by the function $S(\vec{x})$. Then the image function becomes the convolution (Abu-Naser et al., 1998)

$$I(\vec{x}) = \sum_{n=1}^N S(\vec{x}) \otimes \delta(\vec{x} - \vec{x}_n) \quad (5.2)$$

If the shape function S is given, it should be possible to find the positions \vec{x}_n from the image function. Since all the particles have the same radii the function S can be taken out of the sum, giving

$$I(\vec{x}) = S(\vec{x}) \otimes \sum_{n=1}^N \delta(\vec{x} - \vec{x}_n) \quad (5.3)$$

The Fourier transform of the image, \tilde{I} , is expressed as a product of the Fourier transform of the template sphere, $\tilde{S}(\vec{k})$ and the sphere positions:

$$\tilde{I}(\vec{k}) = \tilde{S}(\vec{k}) \sum_{n=1}^N \exp(i\vec{k} \cdot \vec{x}_n) \quad (5.4)$$

By division, the position information is extracted,

$$\tilde{I}(\vec{k})/\tilde{S}(\vec{k}) = \sum_{n=1}^N \exp(i\vec{k} \cdot \vec{x}_n) \quad (5.5)$$

The inverse Fourier transform of Eq. 5.5 yields the particle coordinates in real space,

$$\mathcal{F}^{-1}[\tilde{I}(\vec{k})/\tilde{S}(\vec{k})] = \sum_{n=1}^N \delta(\vec{x} - \vec{x}_n) \quad (5.6)$$

If the system were monodisperse, the particle-finding algorithm would end there. The problem arises due to the polydispersity of the system, since each particle size has its own shape function $S_n(\vec{x})$. The image function is then written as,

$$I(\vec{x}) = \sum_{n=1}^N S_n(\vec{x}) \delta(\vec{x} - \vec{x}_n) \quad (5.7)$$

and, in its Fourier transform, the shape function $\tilde{S}(\vec{k})$ cannot be taken out from the sum of the sphere positions and radii representation:

$$\tilde{I}(\vec{k}) = \sum_{n=1}^N \tilde{S}_n(\vec{k}) \exp(i\vec{k} \cdot \vec{x}_n) \quad (5.8)$$

making it more difficult to separate contributions from different sphere radii in the same image. Then, the identification of particles of a given radius, with the corresponding index, say, $n = 1$, would be obtained from:

$$\tilde{I}(\vec{k})/\tilde{S}_1(\vec{k}) = \exp(i\vec{k} \cdot \vec{x}_1) + \sum_{n=2}^N \exp(i\vec{k} \cdot \vec{x}_n) \tilde{S}_n(\vec{k})/\tilde{S}_1(\vec{k}) \quad (5.9)$$

yields their centres via the inverse Fourier transform,

$$\mathcal{F}^{-1}[\tilde{I}(\vec{k})/\tilde{S}_1(\vec{k})] = \delta(\vec{x} - \vec{x}_1) + \sum_{n=2}^N \mathcal{F}^{-1}(\tilde{S}_n(\vec{k})/\tilde{S}_1(\vec{k})) \delta(\vec{x} - \vec{x}_n). \quad (5.10)$$

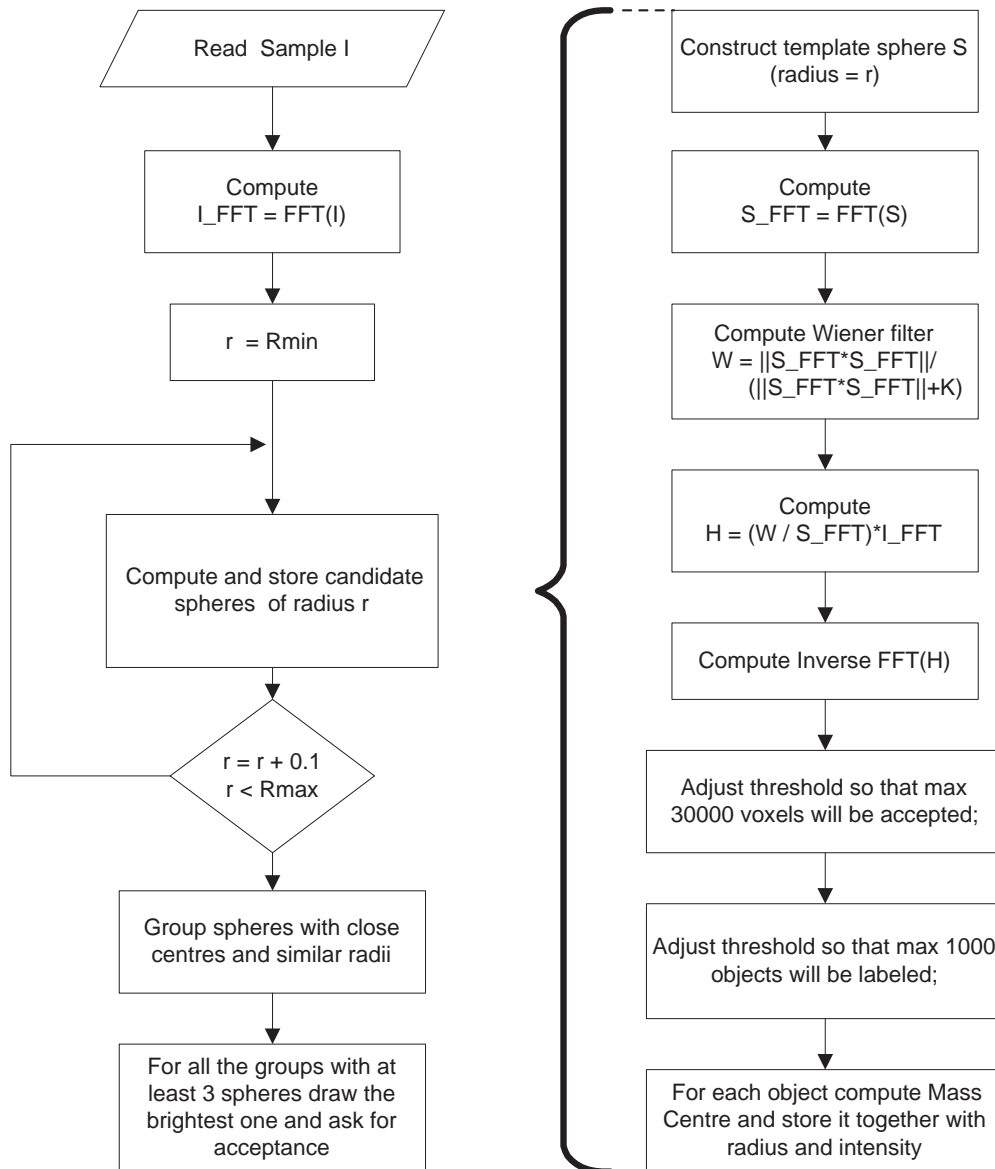


Figure 5.4: Image analysis procedure, starting from the confocal image to the identification of the droplet centres and their respective radii, is outlined in the flowchart. The stages in the Sphere Matching Method (SMM) for each template sphere radius are also presented.

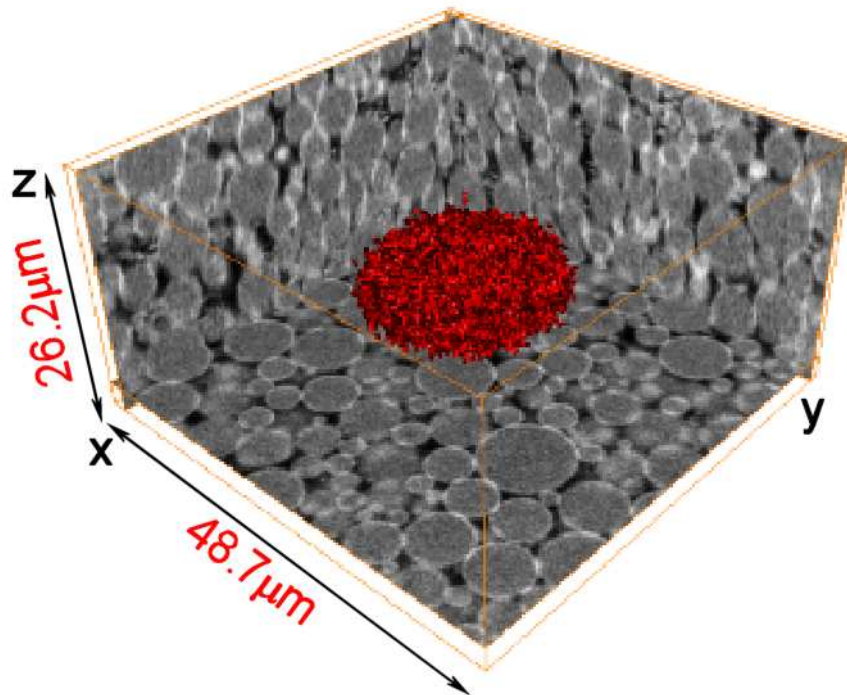


Figure 5.5: Fourier transform of the confocal image, \tilde{I} , depicted in red, with a background showing the original confocal image. No structure is detected in the Fourier image.

Most importantly, according to this mathematical derivation, the peaks of the highest intensity in the inverse Fourier transform represent the sphere centres in the original image. In addition to the centres of the spheres whose radius is equal to the template sphere radius, this function also gives the centres of spheres of all other radii, composed of delta functions smeared out by the factor S_n/S_1 . Thus, for the correct identification of all the radii and their respective centres it is necessary to perform further image analysis selection methods, described in Section 5.3.4. The details of the implementation of Sphere Matching Method are presented in the following Section.

5.3.3 Implementation of SMM

The image analysis methodology for reconstructing all the spheres within the confocal image is divided into two parts: the procedure for finding candidate spheres for each sample radius and the subsequent selection of those spheres which correctly reconstruct the original image. The methodology used to identify the spheres in the original 3D image is based on identifying the intensity peaks in the power spectra of the image. Those peaks correspond to the centres of the particles of a given sampling radius, R . The radius is changed incrementally, in steps of $0.1\mu\text{m}$

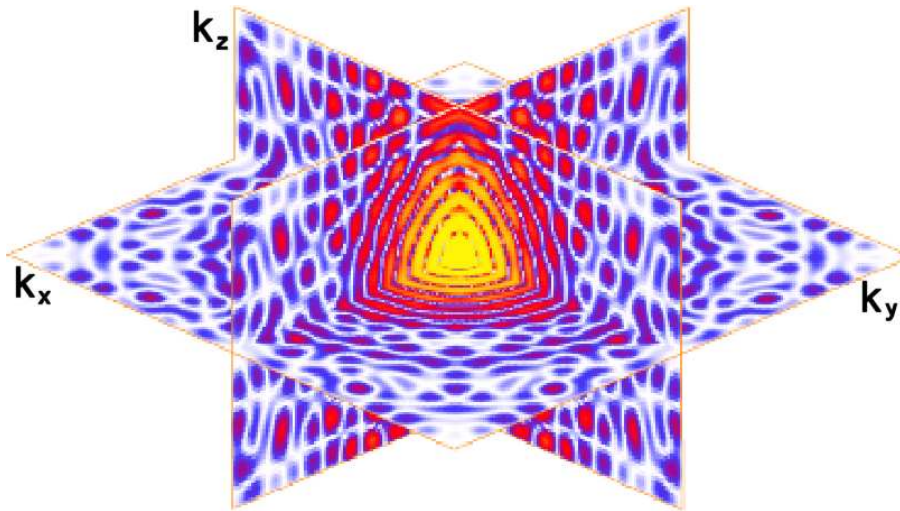


Figure 5.6: 3D Fourier transform of the template sphere, \tilde{S} . The intensity represented by the colour spectrum is the square of the magnitude of the Fourier transform. The values (in arbitrary units) increase in the following order: white, blue, red and yellow.

within the range corresponding to the realistic sphere sizes, and the procedure repeated for each value of R . The increment size is limited by the accuracy of this image analysis technique, which is $1/3$ of a pixel. Both procedures are outlined in the flowchart in Fig. 5.4, using the notation presented in the text which follows.

Even though the underlying mathematics is rather involved (see Section 5.3.2), the resulting Fourier filtering method can be described in simple algebraic terms. The following relation summarises the SMM, applied to our problem (Parker, 1997):

$$\tilde{I} = \tilde{S} \times \tilde{H} + Z \quad (5.11)$$

where \tilde{I} is the Fourier transform of the acquired 3D image, \tilde{S} is the Fourier transform of a perfect sphere of the radius R , \tilde{H} is the Fourier transform of the set of delta functions related to sphere positions and Z is the noise.

Prior to the implementation of SMM on the confocal images, it is necessary to perform a correction of the ‘apparent’ sample depth due to the refractive index mismatch between the sample and the cover glass. We show in Section 5.5 that SMM can be exploited to determine the actual sample depth by measuring the particle sphericity.

The first step in the algorithm involves taking the Fourier transform of the original image containing all the spheres, \tilde{I} , shown in Fig. 5.5, from which not much can be deciphered *per se*. The second stage generates the Fourier transform

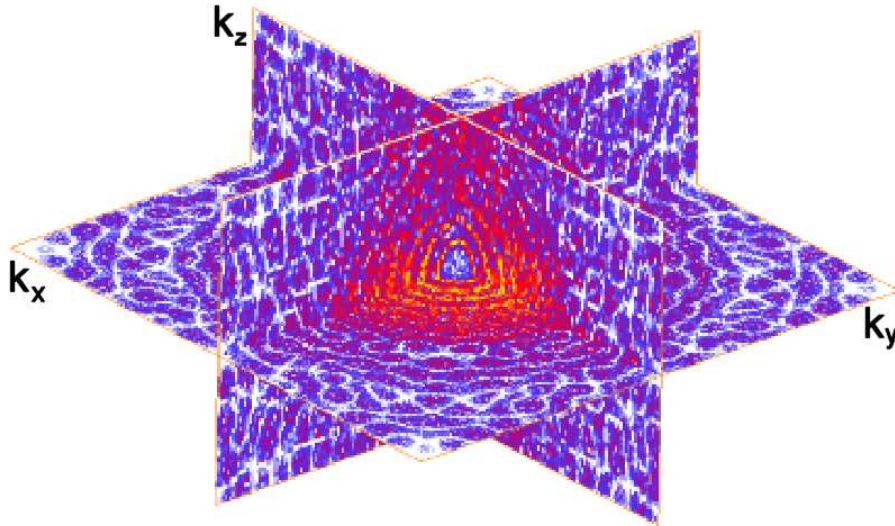


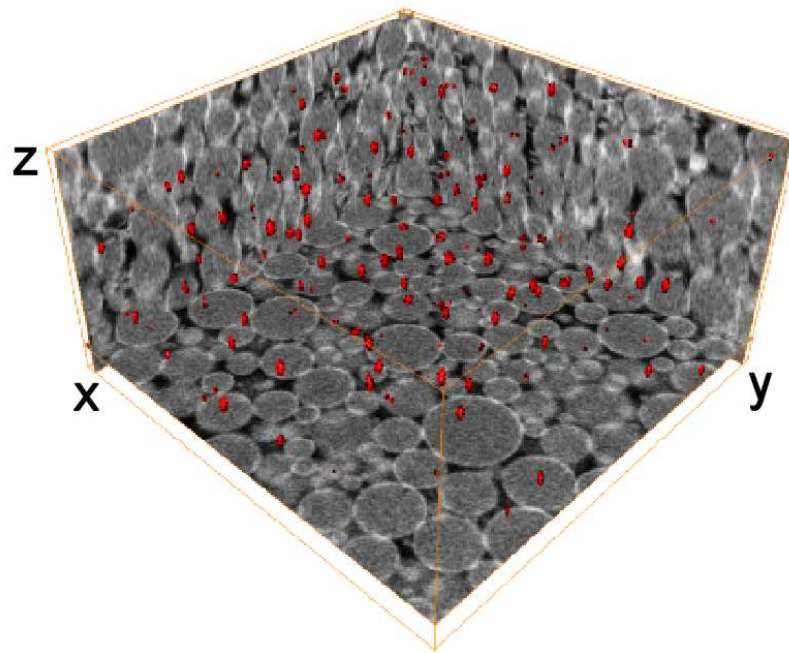
Figure 5.7: 3D Fourier transform of the set of delta function related to the sphere centres, $\tilde{H} = \tilde{I}/\tilde{S}$. No structural features are revealed.

of the template sphere, \tilde{S} , which is a well-defined function, as shown in Fig. 5.6. Ignoring noise contributions at this stage, it is possible to determine \tilde{H} from an algebraic manipulation: $\tilde{H} = \tilde{I}/\tilde{S}$, (Eq. 5.5), which constitutes the next stage. The division of the two Fourier transformed images is done by dividing the magnitude values and subtracting the phase values. In the Fourier space, the function \tilde{H} , however, does not reveal any structural features, as illustrated in Fig. 5.7. On the other hand, the inverse Fourier transform of the resultant array provides an image of blurred delta functions marking the centres of spheres of the radius R (Rericha et al., 2002), illustrated in Fig.5.8a. In the Fig.5.8b, the volume elements containing the respective sphere centres are shown zoomed in, while Fig.5.8c shows the convex hull of those elements, used to determine sphere centres with subvoxel accuracy, as discussed in Section 5.3.4.

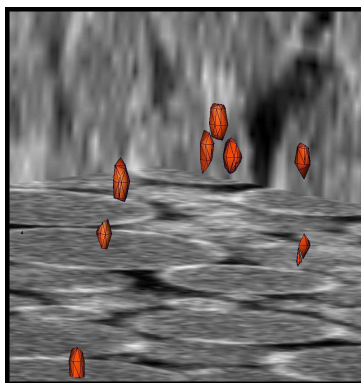
In order to visualise the Fourier transform of the image on the template sphere more intuitively, the zero-frequency component is shifted to the centre of the image by swapping the quadrants in the unshifted image (Russ, 1999), as illustrated in the Fourier transform of the template sphere in Fig. 5.9. This function forces all the edges of the image to be equidistant from the centre, thus eliminating discontinuities at the edges.

The Fourier transforms of the images into frequency space have complex values at each voxel. All the figures in Fourier space are therefore presented as the square of the magnitude, known as the image power spectra.

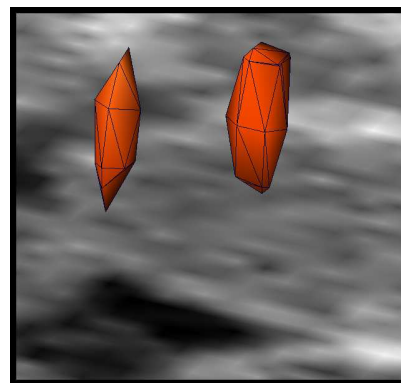
This summarises the basis of the method and its pictorial representation, but



(a) Inverse Fourier transform of the image in Fig. 5.7 marks the centres of spheres of size R by the thresholded delta peaks. The original image provides the background.



(b) Zoom of Fig. 5.8 showing the volume elements identifying the sphere centres.



(c) Convex hull of the volume elements, enabling subvoxel accuracy in the sphere centres.

Figure 5.8: Visualisation of the identified sphere centres in the spatial domain, depicted in orange, identified by the Sphere Matching Method for a given value of R . The original image and therefore the length scale is the same as that depicted in Fig. 5.5

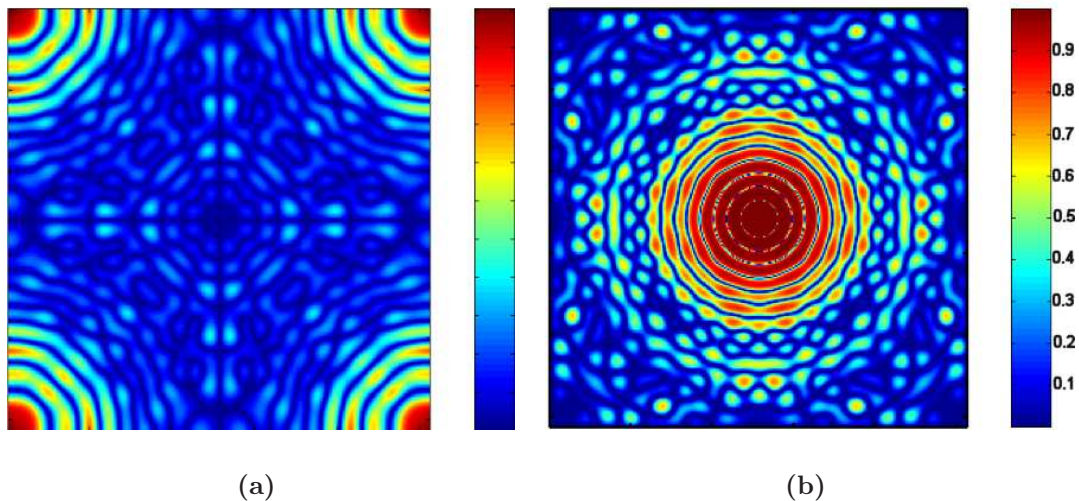


Figure 5.9: 2D slice through the middle of the 3D Fourier transform of the template sphere showing the importance of the zero frequency shift. It eliminates the discontinuities at the edges in the unshifted image in (a) by swapping the quadrants, as shown in (b).

the computational details necessary for implementation and further steps in achieving a better accuracy are discussed in the subsequent sections of this Chapter.

Template Construction

Since the procedure involves a point-by-point 3D matrix division, it is necessary to consider several issues that may arise. Firstly, the template and the image matrices must be of the same size, necessitating that the template sphere is centralised in the box of the same size. The sphere is created according to the equation,

$$(x - x_0)^2 + (y - y_0)^2 + (z - z_0)^2 < R^2 \quad (5.12)$$

identifying voxels encompassed by the sphere. The voxels belonging to the sphere acquire intensity values corresponding to the average intensity of the bulk of the droplets, discussed in Section 4.9.5, although it was found that mimicking the intensity profile of the original image in the template sphere did not add to the accuracy of the results.

The well known difficulty of division by small numbers may cause numeric overflow problems, resulting in the retransformation of the image such that it becomes dominated by noise (Russ, 1990). For that reason, a small (relative to the signal) random noise function, designed to mimic that of the noise in the original image, is introduced as the background of the template sphere.

Wiener Filter

As stated before, the whole process of image analysis is very susceptible to noise and the problem of eliminating the noise has to be addressed. In our case, a Wiener filter has been chosen to deal with the noise contribution to the image. The Wiener filter limits the effect of the small terms in the Fourier transform of the original image by reducing their contribution, either partially or to zero. An approximation of this filter can be expressed as follows (Russ, 1999):

$$\tilde{H} = \frac{\tilde{I}}{\tilde{S}} \times \left[\frac{\|\tilde{S}\|^2}{\|\tilde{S}\|^2 + K} \right] \quad (5.13)$$

where $\|\tilde{S}\|^2$ is the norm of the complex number \tilde{S} and K is a constant. The value of $K = 10^7$ was found by trial and error method until the restored image was considered satisfactory. This value corresponds to the maximum value obtained from the power spectrum of the Fourier transform of the template sphere image. In practice this filtering means that in the template image the important features, which are of high intensities, set the autocorrelation to 1 and therefore do not disturb the magnitude of the division term. On the other hand, for the lower intensity features the K term becomes significant (reducing the autocorrelation towards zero) and the contribution of those terms in the division becomes negligible. Since the lower intensity terms correspond to high frequencies, it is the high frequencies which are filtered out using this correlation function. Figure 5.9b shows the middle slice of the Fourier transform of the template sphere after the Wiener filter has been applied to it. The color map shows the achieved intensity range from 0 to 1, revealing the structural form of the transform. The Wiener filter is essential in extracting the sphere centres as it then sets the intensity range for the features found in the inverse FFT output of \tilde{H} .

5.3.4 Peak Location

For each radius, the original image is analysed using SMM with the Wiener filter to eliminate the contribution of high frequency terms and to make the desired peaks more pronounced. The resulting image also contains some lower, but significant peaks related to the centres of the spheres of similar radii and considerable noise contributions from all other features in the original image, as shown in Fig. 5.10. However, identifying the peaks is generally much easier than reconstructing the original structure of the whole image. In the sections that follow, other techniques that complement the peak identification will be introduced in order to identify each sphere in the original image by its centre and its radius, sufficiently accurately.

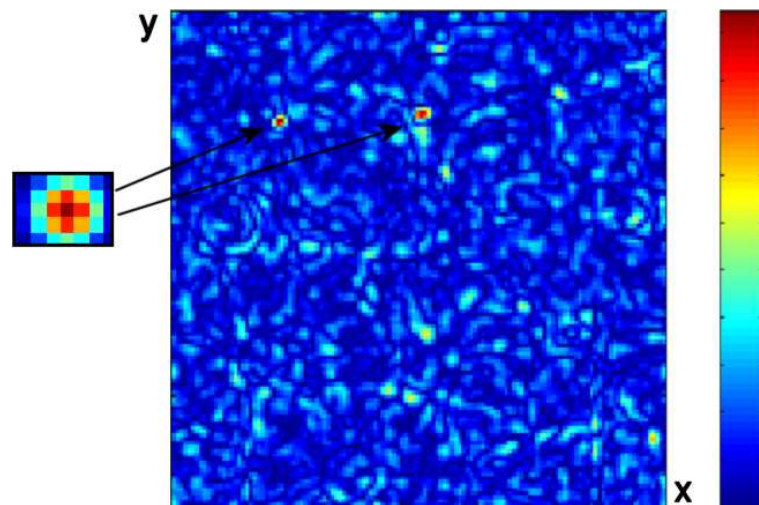


Figure 5.10: 2D slice of the 3D inverse Fourier transform. The zoom shows the blurred delta functions corresponding to the found sphere centres. The highest intensity (red) peaks are selected for further analysis.

Intensity Threshold

The procedure to test the significance of a particular feature requires further selection. The guiding principle is that the sought after peaks in the inverse FFT are narrow and rise prominently above the local background. More precisely, for each value of R , the contributions of the spheres of that radius appear as voxel clusters of high intensity. In order to extract the distinguished peaks a threshold intensity value is set, which is a fraction of the global maximum intensity across the whole of the 3D image. To reduce computation time, the value for the proportionality is chosen to be at the point when the number of accepted voxels is below a certain reasonable limit. Typically the value for the proportionality is around a half of the maximum intensity in the whole image. The image is then segmented, as explained in Section 5.2.1, into objects of maximum connectivity (26 in 3D) and the threshold is again raised until a realistic number of objects per radius is isolated. Since we know that there cannot be many more than 1000 spheres within the whole image, given the size of the box and the particle mean radius, setting such an upper limit for the number of highest intensity objects *per radius* reduces computation time and simplifies the task at hand.

Achieving Subvoxel Accuracy

Once the voxel clusters (objects) have been isolated for each radius (see Fig. 5.8b), the centre of each cluster is then determined as its centre of mass weighted by the

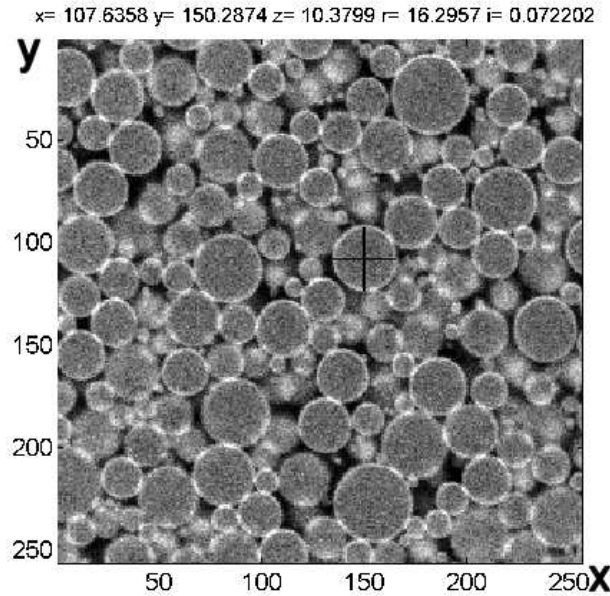


Figure 5.11: The user is asked to choose whether the sphere found by the algorithm (indicated by the white cross) should be accepted or declined. This precaution ensures a correctly reconstructed droplet packing.

intensity of each of its voxels:

$$C(x, y, z) = \frac{\sum_i x_i I_i + \sum_i y_i I_i + \sum_i z_i I_i}{\sum_i I_i} \quad (5.14)$$

This is the key feature in achieving subvoxel accuracy in the determination of the coordinates of the sphere centres. The maximum voxel intensity found in the object is then attributed to the calculated centre of mass, and together with the information of the centre coordinates and the sample radius, is stored for each object. These data are promising candidates to correspond to a real sphere in the bulk. These data are stored for each radius until the full range of radii have been tested. The number of spheres found in this way is still exaggerated as too many objects are considered through the thresholding procedure. Hence, the selection process continues.

Multiple Appearance of Significant Features

Sphere centres belonging to the same sphere in the original image are detected in more than one sample radius, as the discrepancy in the radii is not enough to significantly reduce the brightness of the intensity peak. These centres are identified by their proximity to one another and similarity in the value of the sample radius. In fact, if large intensities are observed in the same region of the sample volume for a number of different model values of R , it can be assured

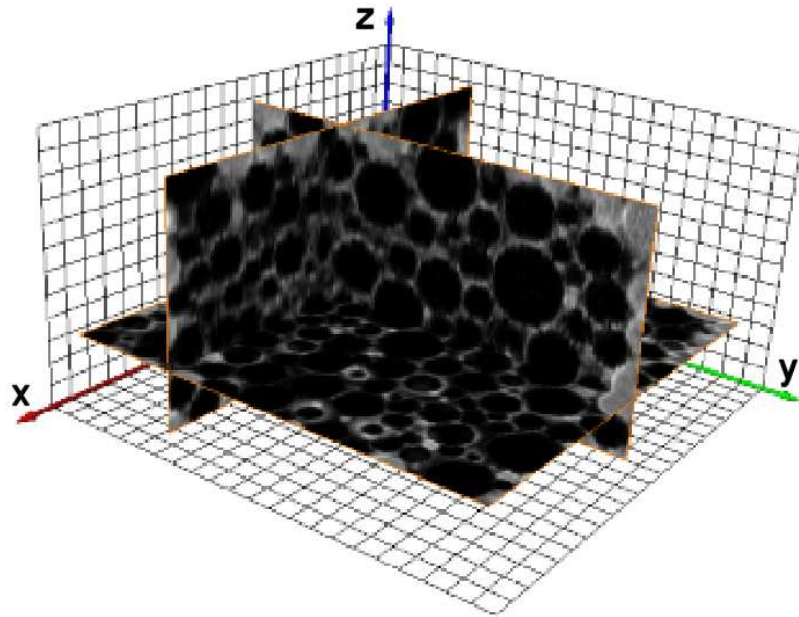


Figure 5.12: Superposition of the original image and the reconstructed image of spheres found using the SMM algorithm.

that the significant feature really exists (Law and Chung, 2001). The multiple appearance of features is a generally accepted tool for their recognition. Hence, only those intensities which appear for at least *three* sampling radii are finally accepted and the centre of the corresponding particle is taken to be at the position of the peak of the highest intensity in that particular region.

Interactive Sphere Selection

Using the methodology explained in the previous sections, we are able to obtain the sphere radii and their respective centre positions within the body of the 3D volume. The success rate of this automatic selection process is approximately 90%, which is a good result, but we still needed more accurate droplet identification. Each selected sphere is marked with a white cross of the length of the radius through the centre of the droplet, and the user is asked to choose whether the droplet is correctly estimated, as illustrated in Fig. 5.11. The procedure takes roughly half an hour for approximately 1000 droplets, typically found in the image. Once this final identification process is complete, a faithful reconstruction of the original image can be made from this, manually approved set of data, as shown in Fig. 5.12.

Once the correct set of sphere centres and radii have been identified, a sphere visualisation is used to make a final, on-screen comparison with the original image.

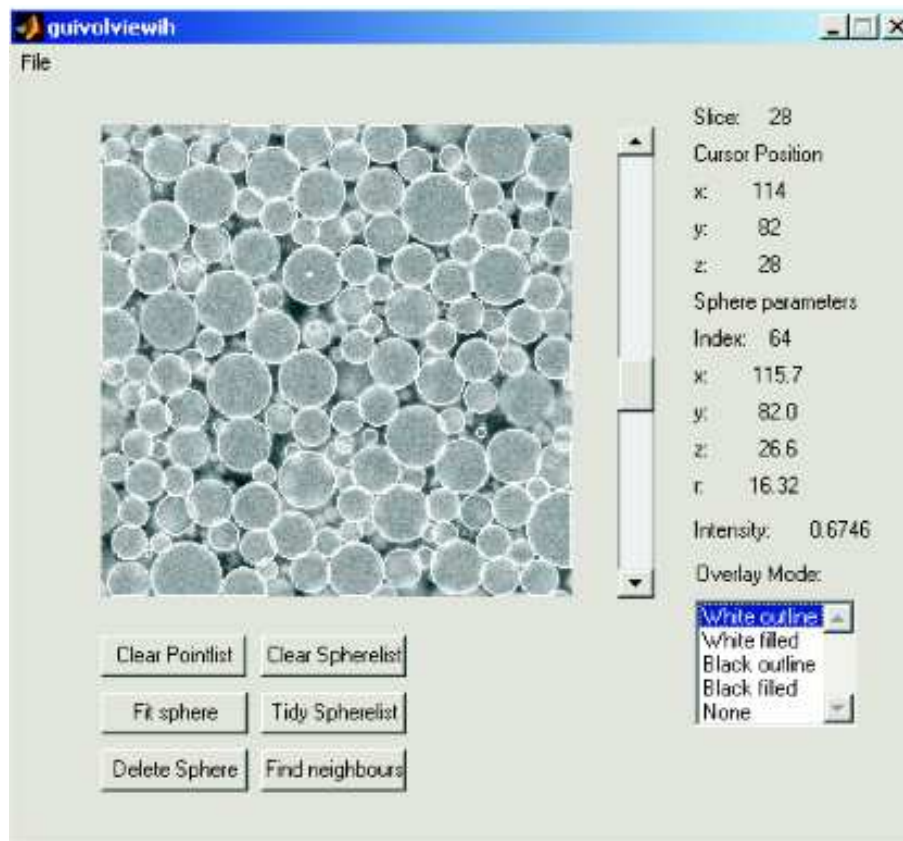


Figure 5.13: Visualisation program showing the original image superimposed with the circles drawn from the sphere data set. It indicates the possibilities to select, delete or add a sphere, as well as to identify its neighbours.

First, the original image is shown in the program window. Then the set of data is loaded, containing the information of the radii and centres of all found spheres and white circles or discs are drawn accordingly and overlaid on the original image. This allows an instant recognition of the spheres which have not been found in the identification process as well as the spheres which may have been erroneously selected.

To rectify those problems the user has the following tools to be able to:

- click on a given sphere and then delete it from the set,
- choose 4 points on the circumference of the sphere appearing in more than one 2D slice to represent the missed out particle manually,
- click on a sphere and identify all of its neighbours.

This final stage reassures the user that all the droplets have been accurately determined, adequately representing the entire packing.

5.3.5 Computation Requirements

The computation of the inverse Fourier transform function and the simultaneous manipulation of more than one 3D matrix, poses considerable demands on the processing power of the computer and limits the maximum amount of data that can be processed in reasonable time. The implementation of SMM was performed in Matlab (Version 6.5) and required the use of a powerful PC (Intel Pentium 4, 2.5 GHz processor and 1 GB of RAM).

The maximum size of the data set was constrained to a $256 \times 256 \times 128$ matrix. It is important that the box size lengths are powers of 2 to allow fast mathematical computation (involving bit shifting), implied by the Fast Fourier Transform algorithm. If the number of slices in z direction is limited to less than 64 by the working distance of the lens, the ‘missing’ slices are filled with zeros. Since the image acquisition resolution is set to 512×512 , it was subsequently ‘downsized’ using a bicubic interpolation.

5.4 Method Assessment

To measure the accuracy of the particle finding algorithm we apply the process, as explained, to a synthetic data set with known particle center positions and radii, and with the added noise. It was found that the algorithm is able to recover the particle positions with remarkable precision, with the mean error values of $0.02\mu\text{m}$ in the x, y coordinates and $0.06\mu\text{m}$ in the z coordinate. The accuracy is lower in the z direction due to the lower resolution along that coordinate. The standard deviation is found to be $\approx 0.001\mu\text{m}$ in all three directions, with the maximum mean value of the error being $\pm 0.06\mu\text{m}$ in the z direction. All these values correspond to a length which is almost an order of magnitude smaller than the size of one voxel.

	$x(\mu\text{m})$	$y(\mu\text{m})$	$z(\mu\text{m})$
mean error	0.0186	0.0168	0.0665
standard deviation	0.0013	0.0017	0.0035
maximum error	0.2971	0.1984	0.3113

Table 5.1: Error analysis.

An illustration of the accuracy in reconstructing the droplets is presented in Fig. 5.14. The error in determining the particle size is at the theoretical limit of $1/3$ of a pixel. Furthermore, the algorithm also finds particles cut by the boundaries of

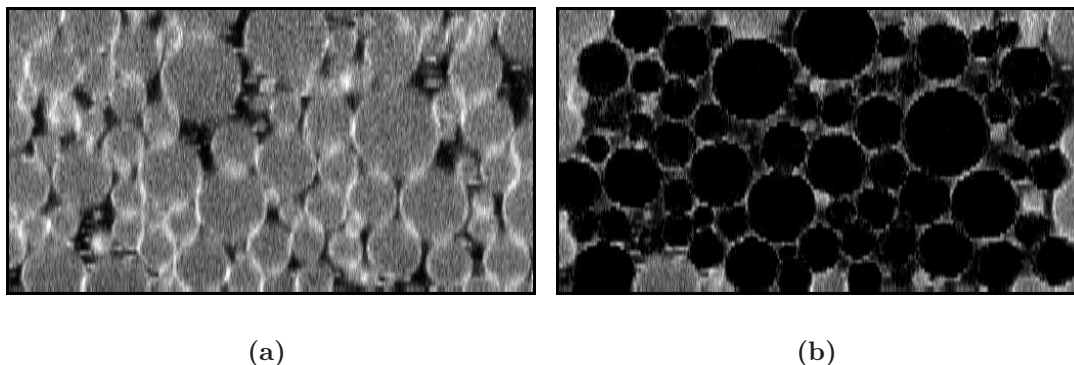


Figure 5.14: Comparison of the original 2D image in the xz direction (a) with the superimposed image of the simulated found spheres and the same original image (b).

the volume, suggesting a degree of tolerance to particle deformation. The obvious discrepancies between the two arise from more pronounced shape deformations of droplets in some cases and from the blurred contributions of features that are above or below the focal plane of interest. We find only a 2% lower volume fraction of the droplets in the image analysis reconstruction in Fig. 5.14b, as compared to the value obtained by a direct threshold of the original image in Fig. 5.14, which is a good indication of the information lost by the analysis methodology.

5.5 Test for the Validity of Snell's Law

Due to the refractive index mismatch between the immersion oil (R.I.=1.518) and the transparent emulsion (R.I.=1.400), the light path deviates from its original path and the sample appears further away in this case, thus lowering the resolution in the z direction. As a result, the spheres appear elongated along the z -axis. However, the discrepancy is too small to be detected and corrected by eye and a quantitative measure of sphericity needs to be introduced. As the droplet finding algorithm is based on the Sphere Matching Method it is also very useful for testing for the discrepancy between the real depth and the apparent depth of the sample, and comparing it to the predictions of Snell's law of refraction (see Section 4.5.2).

Given that the droplet finding algorithm yields a distinct peak each time a sphere is found, the intensity of which is proportional to the correlation between the feature found in the image and the set feature of interest, one can exploit this technique as a measure of sphericity as well. For a given sphere, the intensity value, as a function of the resolution in the z direction, peaks at the undistorted resolution which best describes the searched sphere. This method allows the true

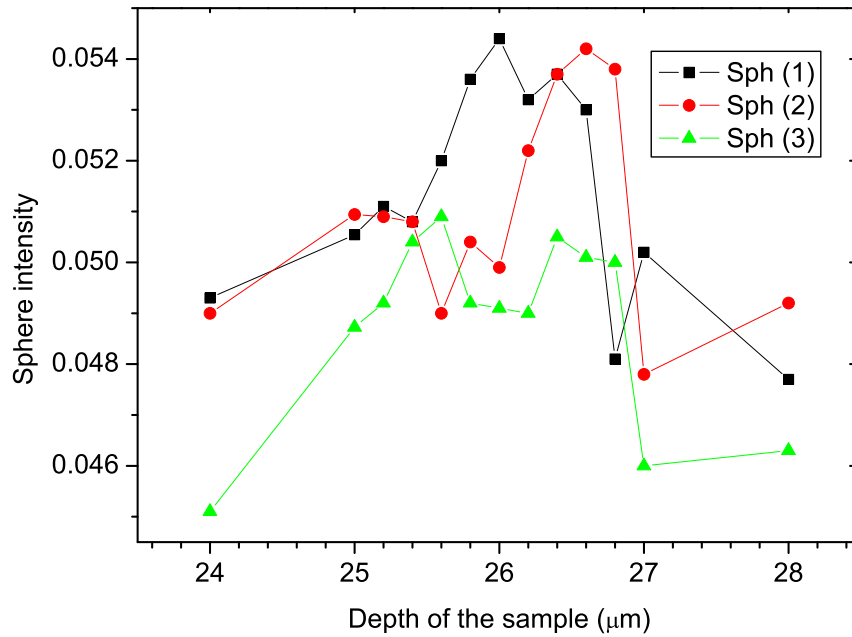


Figure 5.15: Intensity of the Inverse Fourier Transform image at the same sphere centre, from Eq. 5.14, for varying total depths of the sample, i. e. z resolutions. The results are shown for three different spheres of similar radius.

sample dimensions to be reconstructed from the images. The argument is visually supported by the superposition of the corresponding perfect circles in the xz plane with the circles in the image, shown in Fig. 5.14b. Of course, there are other factors influencing the correlation, such as the number of contacts the sphere has with other spheres as well as the more pronounced voxel distortion in artificially defining smaller spheres, but an approximate depth of the sample to within $0.1\mu\text{m}$ can be estimated. Indeed, the thus found ‘real depth’ coincides with that found using Snell’s law ($26.2\mu\text{m}$), as shown by the broad peak in Fig. 5.15, whereas the apparent sample depth measured in the microscope is $28.0\mu\text{m}$. The justification of the rescaling of the z direction according to Snell’s law is important in all further results, as it greatly influences the sphere overlaps. In other words, if the spheres were slightly elongated in one direction and still approximated as perfect spheres with coinciding centers, their ‘simulated’ contact areas in the plane perpendicular to that direction would be underestimated. Moreover, a small difference in the sphere deformation, gives rise to large discrepancies in the contact area.

5.6 Computation of Forces

In the second stage, once the particles have been found, two different methods are applied for isolating the areas of deformation, and therefore the forces. Particular care is taken to eliminate edge effects in the images, such that the force data would not be affected by them.

5.6.1 Eliminating Edge Effects

Spheres that are cut by the boundaries of the volume are not identified reliably and are therefore excluded from parts of the analysis. Therefore, the inner window selected for all further investigations is defined as the length of the maximum particle radius found in the system away from each edge of the original image. The use of such a “guard” region is common practice in image analysis.

This process ensures that every neighbour of every *whole* sphere inside that inner window has also been found in the original box size, enabling the calculation of the force acting between them. Thus, the coordination number and all the forces acting on any one of the spheres inside the inner window is known, allowing for a fully comprehensive investigation of the system configuration and stress propagation in that region. The statistical analysis is made more computationally efficient by such a measure (reducing the required data to approximately 1/4 of the total), but preserving the precision of the data, which is of paramount importance in drawing meaningful conclusions. It is also worth noting that even though the number of particles within the examined box is much smaller, the knowledge of the positions and radii of the remaining particles in the “guard” region is also used in the determination of the forces and is not redundant.

5.6.2 Geometrical Sphere Overlaps

The first method of measuring the size of the contact areas between the reconstructed spheres is by the application of simple geometric considerations, (Thompson, 1990). The radius of the circular overlap is calculated from the area A of the triangle formed by the two radii of the spheres in contact, R_1 and R_2 and the line d joining their centres, C_1 and C_2 (see Fig. 5.16):

$$A_t = \sqrt{S - (S - R_1) \times (S - R_2) \times (S - d)} \quad (5.15)$$

where $S = 1/2(R_1 + R_2 + d)$. Equating this area with $A_t = 1/2dr$, where r is the height of the same triangle, simultaneously yields the radius of the circular overlap. It calculates the circular plane of intersection of the spheres in contact

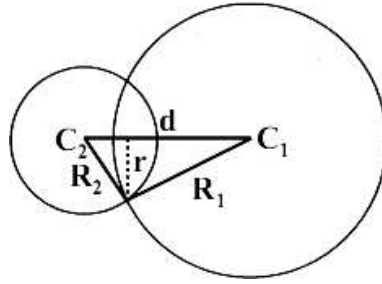


Figure 5.16: Schematic for the definition of ‘simulated’ sphere overlaps, $A_s = \pi r^2$, used throughout this work.

as $A_s = \pi r^2$, from which we determine the force assuming a linear order in the deformation and ignoring the changes in droplet shape, discussed in Section 6.2.1.

These predicted areas of contact serve as a test for the experimental technique of isolating areas of deformation as well as an indication of the relevant regions between droplets which should be investigated. It is a useful tool for justifying the obtained results.

5.6.3 Areas of Deformation-‘Patches’

In the second method, the highlighted contact patches shown in Fig. 5.17 are extracted based on an intensity threshold, since they are brighter than either the droplets or the aqueous background. The postulated mechanism for the enhanced intensity is described in Section 4.8 and is based on the distance between the droplets upon contact being sub-resolution. (The distance between them is determined by the electrostatic repulsion of their surfaces, which predicts a separation on the nanometer lengthscale.) Thus, there may be situations in which the droplets are not physically deforming one another, yet an apparent area of overlap is observed due to their proximity at the point of contact. Nevertheless, the sphere finding algorithm determines their centres and radii with such precision, that the prediction of their geometric overlap using the previous method ensures this is not the case. Hence we use the simulated overlaps from Eq. 5.15 to define the regions in the image in which there should be a highlighted area of deformation, referred to as the patch data. Searching for patches only in regions which are pre-defined by the sphere data greatly reduces computation time and therefore allows for thorough checks of the parameters involved in defining those areas correctly. It also permits the use of larger, higher resolution matrices ($512 \times 512 \times 128$) for better accuracy in the feature definition than previously employed in the SMM. The reconstructed spheres and their respective overlaps are shown in Fig. 5.18.

The determination of each patch in the image is described diagrammatically in

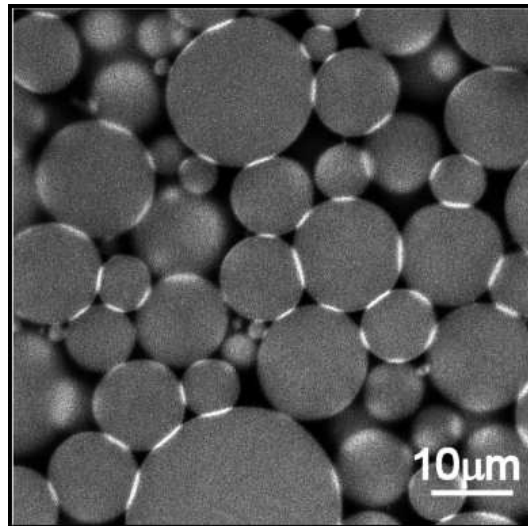


Figure 5.17: A high resolution 2D image clearly showing the highlighted areas of deformation, or patches, in a compressed emulsion.

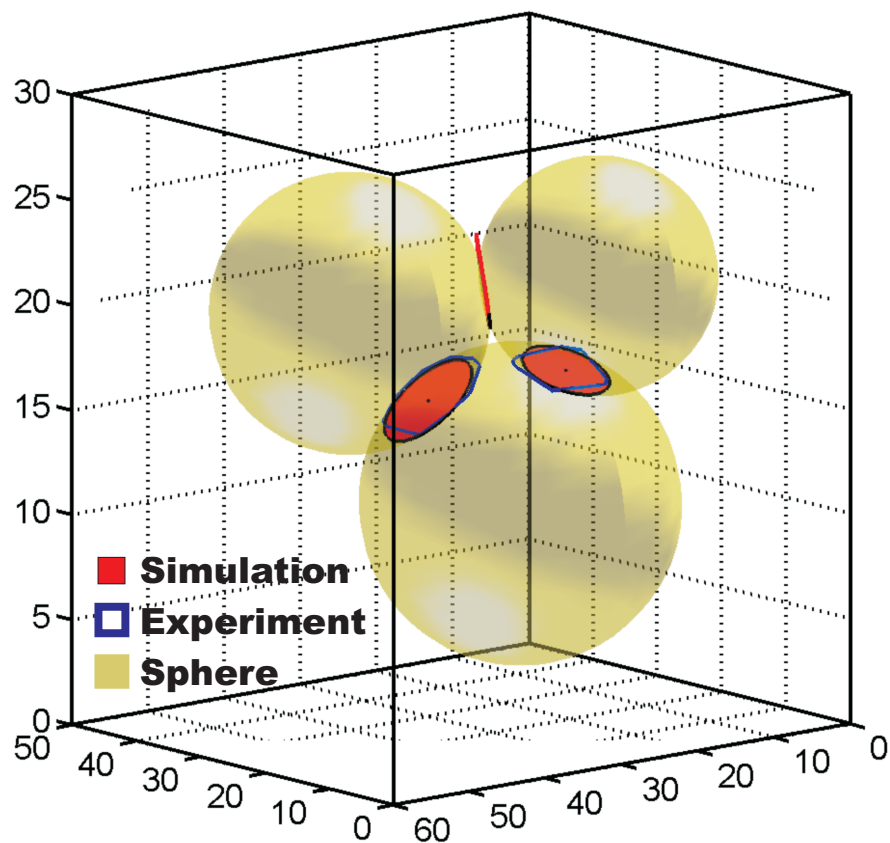


Figure 5.18: Reconstructed spheres in contact (yellow), their simulated overlaps (red) as well as the surface areas of deformation inferred from the regions of higher fluorescence from the original image (blue outline).

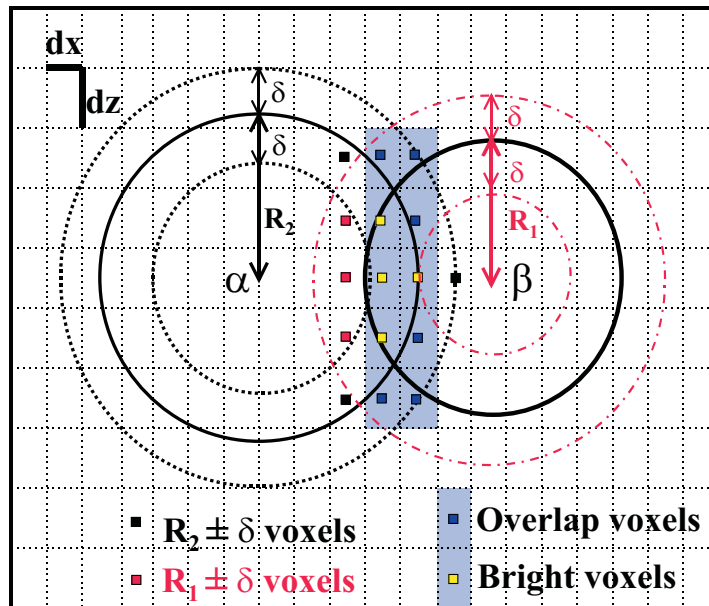


Figure 5.19: Schematic to show the method for finding bright areas of deformation between droplets. The region of overlap predicted by spheres α, β , found using the particle-finding algorithm, is redefined as the overlap of the voxels belonging to $R_1 \pm \delta$ (red squares) and $R_2 \pm \delta$ (black squares) and is depicted in light blue. The voxel centres belonging to this region are further selected according to an intensity threshold (yellow squares) and are then projected onto the plane of overlap to define the area of deformation.

Fig. 5.19. The features in the diagram are exaggerated for clarity, but show the principal idea of the methodology. The well-defined enlargement of the area under investigation is implemented because the smallest accessible lengthscale in the image is the distance between neighbouring voxel centres, represented by the grid in the figure. Since the voxel resolution does not define the thin region of overlap with sufficient precision as the voxel centres are not always encompassed into the curved sphere overlap, it is necessary to artificially search in a volume which is larger by a distance of up to one voxel side length to reproduce the ‘simulated’ areas which are not susceptible to this problem because they are calculated mathematically. As the voxel is anisotropic, this problem is even more prominent in the z direction due to its lower resolution and a compromise between the two resolutions in the increase in radii, i.e. δ , is found by careful comparison with the predicted data.

Physically, the region defined by the simulated overlap does not take into account the shape deformation effects upon compression, which may shift or alter the size of the patch. By contrast to the first method, these areas are calculated by measurement of an effect arising from actual contacts within the system, and hence take into account all non-linear effects in the droplet response to the applied stress. It is another reason why it is necessary to ‘inflate’ the investigated region

in which the bright pixels are sought, yet ensure that no neighbouring overlaps are included in the search. This condition is satisfied for the amount of enlargement employed to mimic a perfect sphere overlap.

For each contact obtained in Section 5.6.2, the information of the index numbers and the radii of spheres giving rise to it is used in the following algorithm, the principle of which is illustrated in Fig. 5.19. The algorithm first finds all voxel centres belonging to the region surrounding sphere α defined as $R_1 \pm \delta$ (only shown as black squares close to the overlap), followed by the same procedure for sphere β (red squares), and the common voxels of the two regions are then selected; their background is depicted in light blue. The voxels are further selected by the role of the threshold. Only those voxels with a higher intensity than the threshold value (yellow squares) are finally selected to define the true area of deformation. In the figure, the resulting area coincides with the area which would have been predicted by the simulated sphere overlap as all the voxel centres are incorporated into the region, however, in practice this is rarely the case.

Influence of the Threshold on Patches

The choice of an appropriate threshold is a non-trivial task due to intensity variations inherent to the technique. The decrease in intensity with depth is largely solved by the use of an equalisation histogram (see Section 5.2.3). However, as mentioned above, the increased fluorescence in the bright areas arising from a sub-resolution effect, is influenced by the digitisation of the point spread function and hence differs in the x or y and the z direction due to the difference in their resolutions. This introduces a dependence of the patch orientation on the intensity profile across it, shown in Fig. 5.20.

The intensity profiles of two patches exhibiting the two extreme orientations, i.e. completely contained within either the xy plane (triangles) or the xz plane (squares), are shown in the figure. These data correspond to patches which are similar to those presented in Fig. 5.22, purposefully illustrating the different volume element forms encountered for different orientations. For each orientation, both the intensity profile across the circular patch in the plane and the profile across the thickness of the same patch in the direction perpendicular to it confirm the resolution discrepancy. The patch in the xz direction fluoresces with a significantly higher intensity and the definition of its thickness is much finer and sharper due to the higher resolution in the xy plane of the voxel. The lower intensity of the xy patch comes from the fact that a subresolution physical feature looks much more diffuse in its representation in the z direction, in other words, the intensity attributed to each pixel is lower because the PSF is averaged over a larger region

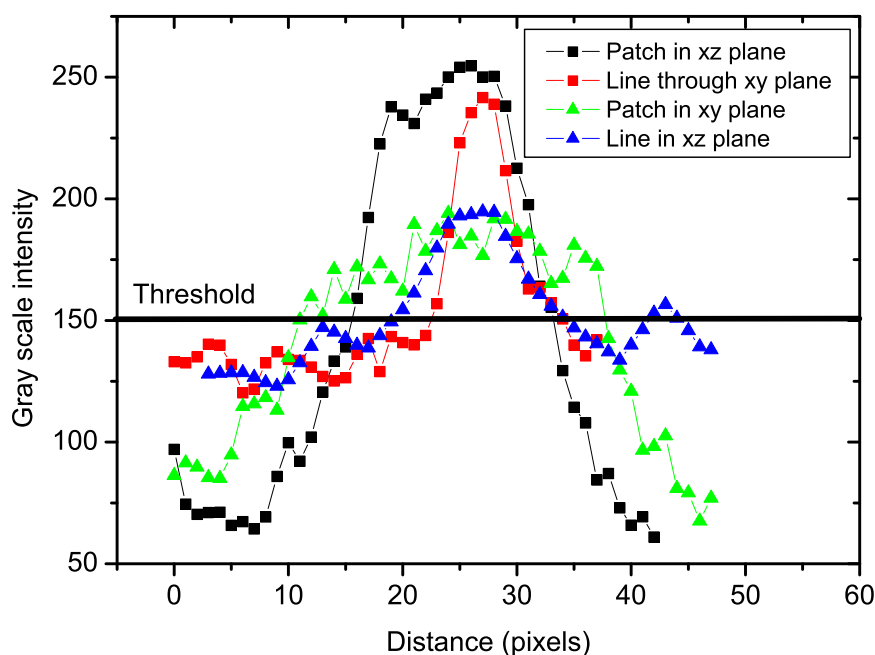


Figure 5.20: Intensity profiles across a patch fully in the xy direction and a patch perpendicular to it.

of voxels. Hence, even though the actual area is better defined in the xy direction, with finer voxels, the threshold must be lowered in order to accept *all* of them. The overestimation of the patch thickness does not introduce errors in the final results because all the voxels are projected onto a plane of overlap and do not add to the resulting area. The discrepancy in the intensity can be overcome by choosing a threshold which accepts all the highlighted voxels with respect to the background fluorescence, from the inside of the droplets, in both cases. In the example in Fig. 5.20, setting the threshold as indicated, allows all the voxels participating in the deformation through, as well as rejecting those which belong to the bulk. One could argue that the definition of the brighter patches is slightly overestimated at the edges, but this error is negligible with the large statistics of the experiment in mind. This relatively low threshold, employed to satisfy all the deformed surfaces, could in principle be incorporating noise from the bulk, but since the search only involves a small inflation of the relevant regions, these contributions are avoided. The baseline intensity is higher for the definition of the patch cross section than across the patch because they are found either between the bulk of two droplets or surrounded by the continuous phase, respectively. The areas of deformation isolated by the thresholding procedure are slightly smaller than those predicted by the geometrical overlap, on average.

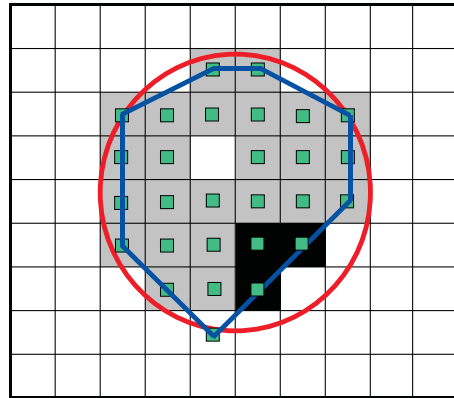


Figure 5.21: The convex hull (blue line), obtained from the bright voxels projected onto the plane of overlap (grey squares), includes the concavity region (black squares).

Area Calculation

The resulting regions of contact are overestimated because the original fluorescence gives the impression of volume elements rather than flat planes between droplets, due to the microscope resolution. In order to “flatten” the contacts into planar patches we perform a method which projects the voxel centres onto the plane normal to the line joining the corresponding droplet centres. The voxel is projected to the nearest point on the projection plane to the voxel itself. The plane coincides with that obtained via the first geometric method of defining the overlap. The resultant area of the set of projected points is obtained from the polygon defined by their convex hull (Barber et al., 1996). It is calculated as the sum of the triangles that the polygon is divided into by the selected voxel centres, as shown in Fig. 5.22. The points form a planar polygon with vertices P_0, \dots, P_n , where $P_{n+1} = P_0$, in an arbitrary plane perpendicular to a unit vector N . The area of the polygon from Stokes Theorem (Goldman, 1991) is calculated as

$$A_P = 1/2 |N \sum_k \{P_k \times P_{k+1}\}|. \quad (5.16)$$

There is a set difference between the convex hull of a shape and the shape itself, known as the concavity region. For a filled perfect circle, this concavity region is negligible, but more complex shapes will be ‘filled’ to make a convex region. In Fig. 5.21, an example of the planar patch constructed from the projected voxels is shown. Since the overlaps physically must be close to circular, this approximation works very well and improves the area estimation.

The patches shown in the figure are the same as those shown in Fig. 5.18 for clarity, this time additionally incorporating information of precisely those voxels

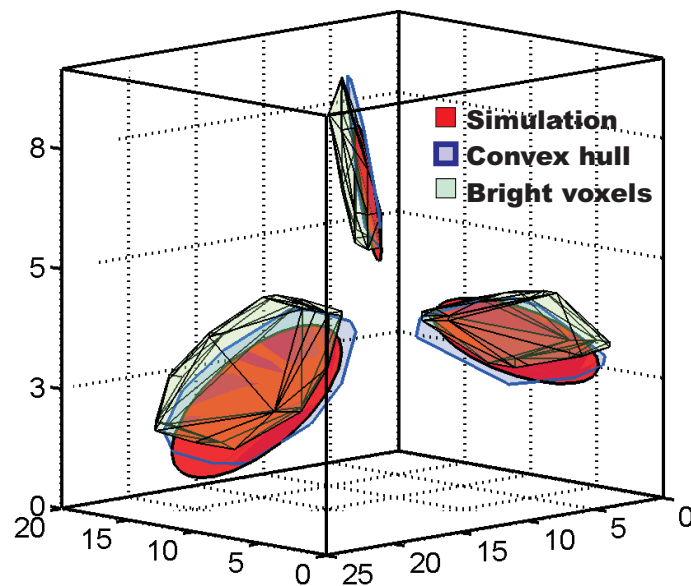


Figure 5.22: 3D representation of the ‘simulated’ overlaps (red), the triangulation of the bright voxels found in the region of overlap (black lines) and the convex hull of their projection (blue lines).

which contributed to their final area. It illustrates the negligible effect of the exaggerated width of the patch, the high correlation with the predicted circular areas and the capability of capturing the non-linear shifts and size discrepancies by the use of a well-chosen region and threshold.

The two methods of identifying the deformed areas resulting from the forces between the droplets are key to the results presented in Chapter 6. The forces can be determined from these areas by the Young-Laplace equation, using the surface tension measurement presented in Section 3.6.3 and the droplet radii (see Section 5.3). Their comparison provides an assessment of the methodology as well as a test for the correct force model, to be discussed in Section 6.2.1.

5.7 Summary

This novel image analysis methodology has enabled the three-dimensional identification of:

- *all* droplet centres and radii with subvoxel accuracy,
- contact areas arising from highlighted patches or geometrical overlaps,
- interdroplet forces in the bulk of the sample volume.

We have shown that the application of the Sphere Matching Method in 3D is a very fast, efficient and accurate way of identifying spheres within the sample volume, as compared to the available 2D morphological analysis. Moreover, the procedure of finding sphere centres according to the intensity weighted centre of mass of the selected voxels implies a subvoxel accuracy of the particle finding algorithm. The methodology was perfected using visualisation algorithms, such that the exact particulate configuration is reconstructed. Finally, the knowledge of the particulate packing facilitated the fast identification of bright patches corresponding to the areas of deformation in the predefined specific regions of geometric overlap.

Chapter 6

Statistical Mechanics of Jammed Matter: Results and Discussion

Now here, you see, it takes all the running you can do to stay in the same place; if you want to get somewhere else you have to run at least twice as fast as that.

Lewis Carroll,
Through the looking glass.

6.1 Introduction

A system of random close packed particles is fully described by the geometry of the system configuration and the distribution of forces and stresses in the particulate medium. For infinitely hard and rough bodies, such as grains, there is no internal energy and external forces have no effect on distribution functions. This means that if P is the probability distribution of configurations and of interparticle forces, it consists of two independent components P_f and P_c ,

$$P = P_f(\text{forces}) P_c(\text{configurations}) \quad (6.1)$$

which give the full description of the granular system.

The above statement has been presented in a theory context, but must be supported by experiment. In this Chapter, we present experimental results that test the basic granular theory and some of the assumptions within it by separately measuring the distribution of forces (Brujić et al., 2003b) and the distribution of configurations (Edwards et al., 2004). The influence of polydispersity, external pressure and microstructural features, such as the coordination number and force

chains, on the force distribution is also investigated experimentally and compared with the predictions of the theoretical model (Edwards and Grinev, 2003) and numerical simulation results. The latter were performed in parallel with the experiments by our collaborators at the City College of New York (Makse et al., 2000).

The experimental model system differs from the theoretical model in that the particles are neither rough nor rigid. The compressibility of the particles is a necessary requirement for the experimental measurement of the forces and the absence of friction can be accounted for in the theory. In the limit of small deformation, one can consider that the packing configuration has not been significantly altered, as compared to that of the rigid and rough grains, allowing for the comparison of the theoretical and experimental findings.

6.2 Probability Distribution of Forces, $P(f)$

It has been shown experimentally that the stress is transmitted inhomogeneously through granular matter, characterised by an exponential distribution of the interparticle forces (Liu et al., 1995). The mechanistic features giving rise to the distribution, postulated as force chains and arching, have yet to be given a proper theoretical basis and require further experimentation within the bulk of a 3D particle ensemble.

The form of the probability distribution of forces is predicted to be independent of the particle's material, provided it has well defined elastic properties. Therefore we can expect the micromechanics of an emulsion, consisting of very "soft" particles, to bear many similarities with a packing of granular materials, such as ball bearings or glass beads. Studies of $P(f)$ specifically devised for compressed emulsion systems do not appear to exist. We identify and examine $P(f)$ in compressed emulsion systems in this work, through which the universality of the thermodynamic approach is put to the test by comparison with granular materials. Several approaches have so far been employed, including 2D and 3D experimentation (Dantu, 1968; Liu et al., 1995; Erikson et al., 2002), numerical simulations (Radjai et al., 1996; Thornton, 1997; Makse et al., 2000; Antony, 2001; O'Hern et al., 2001) and statistical modeling (Coppersmith et al., 1996). Numerical simulations of the contact force distribution have extended the studies to systems such as supercooled liquids and foams (O'Hern et al., 2001). Previous experiments in 3D assemblies have been confined to measurements of the probability distribution of forces exerted at the boundaries with the container, thus reducing the dimensionality of the problem (Liu et al., 1995; Mueth et al., 1998; Lovoll et al., 1999;

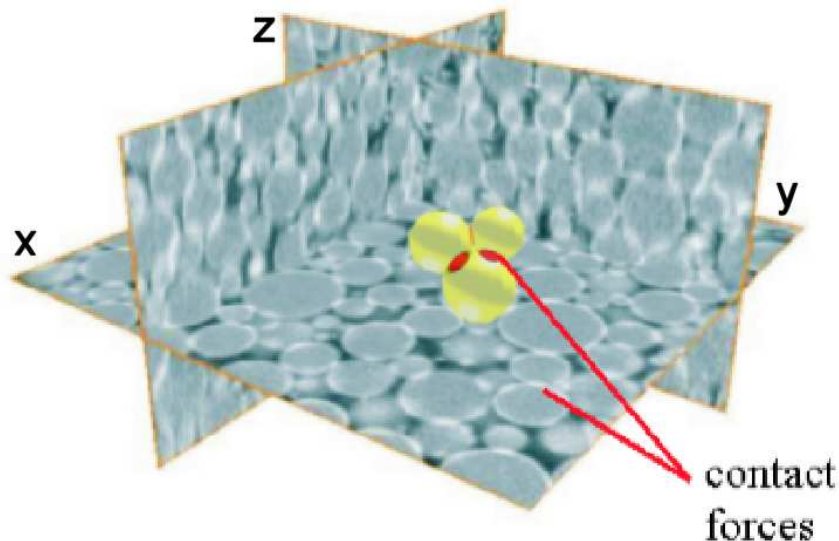


Figure 6.1: A typical image of the droplet packing at low compression, in which the bright regions lead to contact forces. Two reconstructed droplets in the bulk and their calculated geometric overlap are also shown.

Blair et al., 2001; Makse et al., 2000). These measurements provide a quantitative understanding of the inhomogeneity of stress transmission within the bulk. However, the method does not have access to the spatial arrangement of the contact force network and other structural features, such as force chains and arching, which have been postulated as the signature of jamming (O’Hern et al., 2001).

The quantitative agreement between $P(f)$ of a variety of systems has suggested a unifying microstructural behaviour governed by the jammed state. The salient feature of the probability distribution $P(f)$ of interparticle contact force f in jammed systems, obtained from the above methods, is an exponential decay above the mean value of the force. This feature of $P(f)$ seems very robust, with growing evidence that it is independent of particle rigidity (Radjai et al., 1996; Antony, 2001), crystallinity (Blair et al., 2001), tangential forces, construction history and friction (Makse et al., 2000). Nevertheless, there is no clear consensus on the general functional form of $P(f)$ as there are significant discrepancies in the literature particularly regarding the behaviour at small forces, both between experimental data and the theoretical model predictions. Moreover, the possibility of a crossover to a Gaussian-like distribution has been observed at large confining pressures (Thornton, 1997; Makse et al., 2000; Sexton et al., 1999). This is the context in which this Thesis contributes experimental data and discussions of the results.

6.2.1 Experimental Measurement of $P(f)$

In the previous chapters, we have described the confocal microscopy experiment which leads to the measurement of forces between compressed droplets in 3D. The particulate packing, characterised by image analysis, is illustrated in Fig. 6.1. The areas of deformation and the droplet radii are used to derive the interdroplet forces according to the force model presented below.

Force Model

While granular materials interact via normal and tangential forces (both contact and dissipative) (Makse et al., 1999), soft matter systems such as emulsions (Lacasse et al., 1996) and also foams (Durian, 1995) are considered to interact with normal forces only (repulsive and dissipative) at concentrations above the random close packing (RCP). The interdroplet forces are considered to be purely repulsive in this study, since the droplets do not aggregate in dilute solution and do not deform when in contact unless a sufficiently large external force compresses them beyond their random close packing configuration, i.e. their maximum density.

The determination of an accurate force model for the compression of two droplets is not trivial, but can be simplified within certain limits. For small deformations with respect to the droplet surface area, the Laplace pressure remains unchanged and all the energy of the applied stress is presumed to be stored in the deformation of the surface (Princen, 1983). Hence, at the microscopic level, two spherical droplets in contact with radii r_1 and r_2 interact with a normal force

$$f = \frac{\sigma}{\tilde{r}} A \quad (6.2)$$

where A is the area of deformation, σ is the interfacial tension of the droplets and \tilde{r} is the geometric mean of the radii of the undeformed droplets, $\tilde{r} = r_1 r_2 / (r_1 + r_2)$. The normal force acts only in compression, i.e. $f = 0$ when there is no overlap. The validity of using the simplified force law is investigated experimentally and discussed in Section 6.6.

The relation in Eq. (6.2) enables the calculation of the forces from the identified areas of deformation and corresponding particle radii in the images, as well as the measured surface tension value (9.2mN/m). This leads to the determination of the form of the probability distribution of forces, $P(f)$, and the spatial distribution of forces in the volume. We first present the results of this analysis and a critical appraisal.

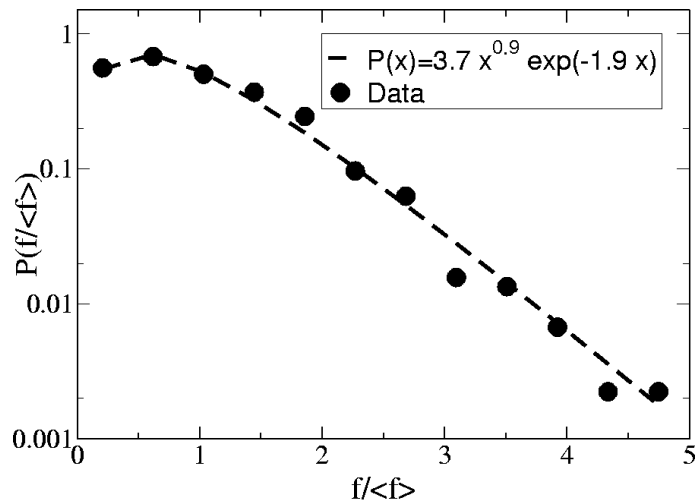


Figure 6.2: Probability distribution of the contact forces, $f/\langle f \rangle$, for the compressed emulsion system, normalised by the probability when $f = \langle f \rangle$. This curve is representative of 4 data sets at low compression. We also show a fit to the theory developed in Section 6.2.4.

Exponential Distribution of Forces

Figure 6.2 shows the probability distribution of interdroplet forces, $P(f)$, extracted from a 3D image which contains ~ 500 particles and over 1500 forces. The forces are calculated from the bright, fluorescent patches that highlight the contact areas between droplets. The droplets are only slightly deformed away from spherical at a pressure of $\langle p \rangle \sim 4.3$ Pa per droplet, calculated using Eq. (6.23) in Section 6.4. This indicates that the system is close to jamming, i.e. near RCP at $\phi \sim 0.64$ for monodisperse particles. The number of neighbouring particles exerting a force on each particle is known as the coordination number, discussed in detail in Section 6.3, and also gives an indication of the proximity of the system to the jamming transition (O’Hern et al., 2003). Since the average coordination number for this data set is $\langle Z \rangle = 6.48$, close to the minimal coordination value $\langle Z \rangle = 6$ for a static packing of particles interacting by normal forces only, this system is considered to be close to the jamming transition.

These data show an exponential distribution at large forces, consistent with the results of many previous experiments and simulations on granular matter, foams, and glasses. The behaviour in the low force regime indicates a small peak, although the power law decay tending towards zero is not well pronounced. The best fit to

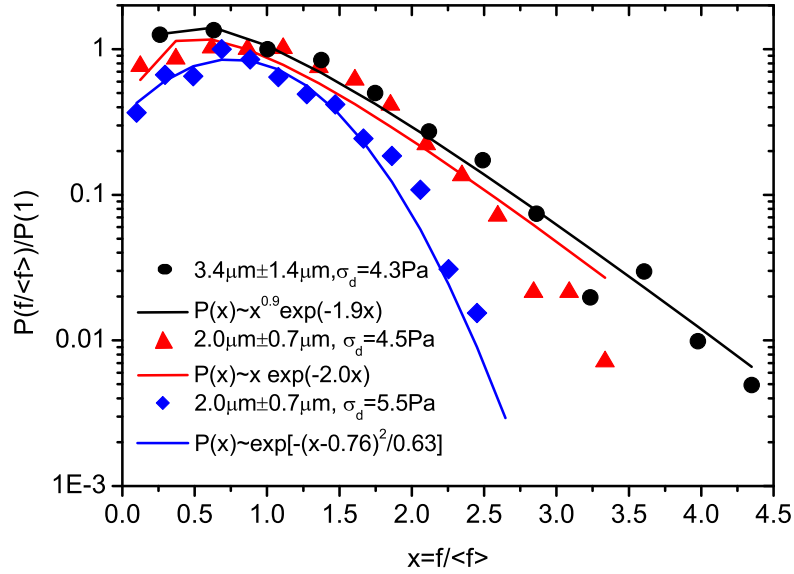


Figure 6.3: $P(f)$ for three data sets with two levels of polydispersity and at two osmotic pressures, normalised by the probability at the mean force, $P(x = 1)$. We show a fit to the theory for the low pressures and a deviation towards a Gaussian distribution as the pressure is increased.

the data gives a functional form of the distribution,

$$P(f) \propto f^n e^{-(n+1)f/\bar{f}} \quad (6.3)$$

consistent with the theoretical model to be proposed in Section 6.2.4 and the existing literature (Coppersmith et al., 1996). For the data set presented in the figure, the coefficient $n=0.9$ and the mean force $\bar{f}=20\text{nN}$. All other analysed data sets at low pressures are consistently fitted with n of the order of 1 (± 0.2). It is inappropriate to draw conclusions on the physical significance of the coefficient, since the geometry of the packing in the experiment is much more complicated than in the simple theoretical model. This coefficient is related to the average coordination number of the particles in the granular theory.

Effect of Polydispersity and Pressure on $P(f)$

Figure 6.3 is an extension to Fig. 6.2 in that it shows the $P(f)$ for two additional data sets, extracted from 3D images which contain ~ 1000 particles and over 5000 forces each. These data allow for the discussion of the effects of polydispersity and osmotic pressure on $P(f)$.

We obtain the pressure of the system from the images by calculating the trace of the stress tensor, which we obtain from the information of the interdroplet forces. Since the osmotic pressure applied in the centrifuge is dependent on many parameters, such as the height of the centrifuge tube, the initial volume fraction of the droplets, the waiting time between the centrifugation and sample observation, we do not include the exact experimental conditions which led to the measured pressures. All samples were centrifuged for 20 minutes at accelerations around $6000g$, which was sufficient to cause droplet deformation. The results in the figure show the following trends.

First, the agreement between the data for a narrower particle size distribution of $2\mu\text{m}\pm 0.7\mu\text{m}$ (triangles) and the previous data at $3.4\mu\text{m}\pm 1.4\mu\text{m}$ polydispersity (circles), indicated in the figure, shows that the level of polydispersity does not affect the exponential result. It should be noted, however, that the samples under investigation all have a relatively high level of polydispersity. Monodisperse particles are only investigated by simulations, and their force distributions, which are in excellent agreement with the polydisperse experiment, are presented in Fig. 6.5a of Section 6.2.3.

Polydispersity is reflected in the volume fraction of the droplets at which the particles achieve random close packing under gravity. The droplet volume fractions are calculated from the inner window of the reconstructed images, as defined in Section 5.6.1, in which one is certain to have identified all the particles. The two samples at the same pressure jam at different volume fractions; $\phi = 86\%$ for the more polydisperse case (circles), and $\phi = 74\%$ for the narrower size distribution (triangles). This is because the constituent particles are able to pack more efficiently for wider size distributions as the small droplets fill the interstices between the larger ones.

Second, at the larger pressure (diamonds), the probability distribution departs from the prediction of the theory and crosses over to a Gaussian distribution for the emulsion system with the narrower size distribution. This result is in qualitative agreement with the simulation results. However, the theoretical basis for this transition has not been investigated. At higher pressures, the forces begin to affect the distribution of configurations and the theory is therefore much more complex.

6.2.2 Limit of the Force Measurement

The results presented in Fig. 6.3 are obtained at osmotic pressures which are large enough to induce significant surface deformation. The magnitude of the interparticle force must be sufficient to deform the droplet surfaces to a degree which can

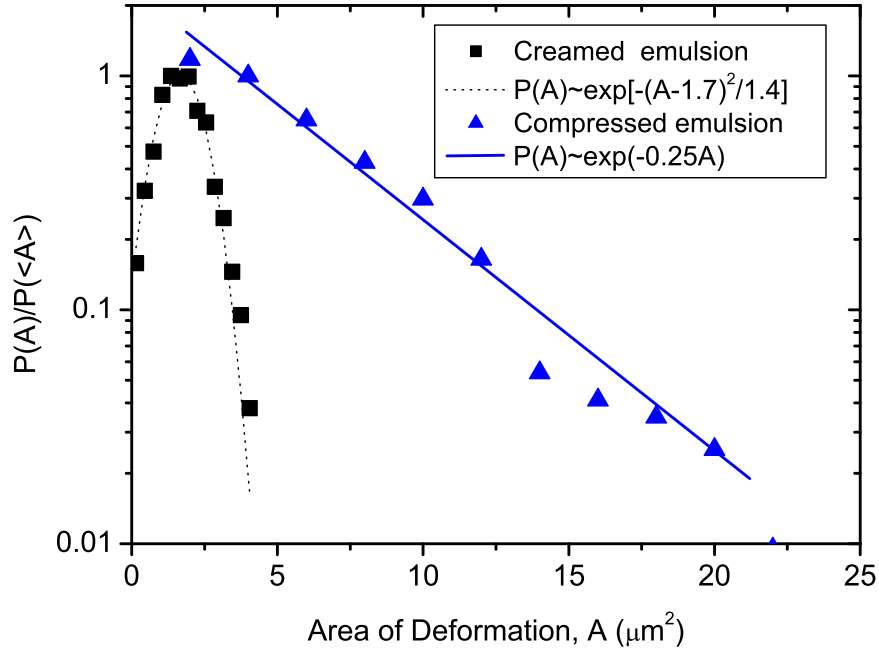


Figure 6.4: Probability distributions of areas, normalised by the probability at the mean area, arising from a subresolution fluorescence of touching droplets (creamed emulsion) and from droplet deformations (compressed emulsion).

be accurately identified in the microscope images. The lower limit of the pressure necessary for the characterisation of forces is determined by the microscope resolution. The calculation for the estimation of the minimum measurable area of deformation and the centrifugation force necessary to achieve such a deformation is given in Section 4.7.2. Acceleration of several thousand g is necessary to produce interdroplet forces of the order of 1 nN, which in turn deform the droplet surfaces by a few μm^2 . These estimated values are of the same order of magnitude as those found by experimentation, validating that the source of the measured deformed areas is indeed in response to the external pressure.

Under gravity, the forces are not large enough to induce surface deformation. However, since the fluorescence enhancement at the droplet contact arises from the subresolution proximity of the particles, the bright patches are observed even when the particles are simply touching, without the presence of deformation. Hence, the distribution of these ‘subresolution’ highlighted areas is investigated to determine the limitations of this method of measuring forces.

The probability distribution of the subresolution areas is compared with those arising from areas of deformation at higher pressures, as shown in Fig. 6.4. The two data sets are imaged at the same resolution of the microscope ($x,y=0.15\mu\text{m}$ and $z=0.4\mu\text{m}$) and both contain ~ 1100 areas. Creaming under gravity gives rise

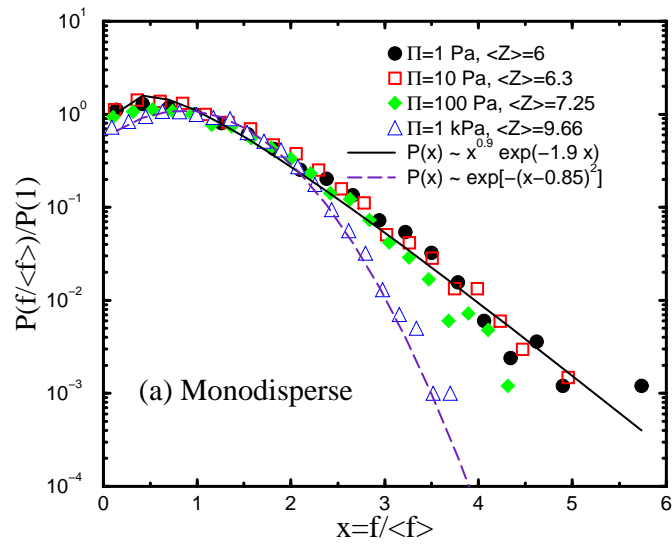
to much smaller contact areas with a maximum value of $4\mu\text{m}^2$, between the largest droplets. This value sets an upper limit to the error in the area measurement, but the results below this value are also presented in the force distributions measured at higher pressures. The value $4\mu\text{m}^2$ represents 5×5 voxels in the z -direction and is more than twice the theoretical resolution of the microscope, when using a high resolution lens. This maximum value for the areas observed in creamed emulsions depends on the global threshold intensity value, which is set to accept the bright voxels, as well as the contrast between the sample regions achieved in the image. Note that the contrast in the images between the deformed regions and the bulk droplet fluorescence improves as the compression is increased, thus reducing the subresolution areas in the images at higher compressions.

Another important observation is that the distribution of the subresolution areas is fitted with a Gaussian distribution, whereas the patch areas are clearly exponential. This difference in the distributions indicates that the areas in a creamed emulsion are measuring a quantity on which many independent random factors (such as area orientation and droplet curvature) act in an additive manner to create variability [in this sense, the central limit theorem implies a Gaussian distribution], whereas the exponential distribution of the areas is measuring a very different physical quantity. This result gives more confidence in the validity of the force measurements in the adequately compressed emulsions.

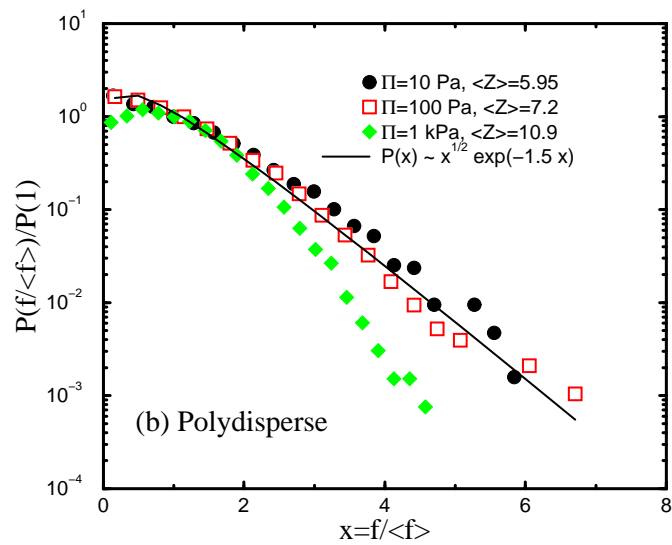
6.2.3 Simulations of Compressed Emulsions

Molecular dynamics (MD) simulations are performed to gain insight into the effects of osmotic pressure, polydispersity, and other microstructural features such as the coordination number and force chains on the probability distribution, $P(f)$. The numerical protocol is designed to mimic the experimental procedure used to prepare compressed emulsion systems at different osmotic pressures, described in Section 4.7. The numerical simulation result at low confining pressures and the same polydispersity as in the experiment, is in good agreement with that obtained from the experiment, showing that the form of the force distribution is indeed independent of the particle size distribution.

The model considers an assembly of deformable spherical droplets interacting via repulsive normal forces given by Eq. (6.2). The continuous liquid phase is modeled in its simplest form, as a viscous drag force acting on every droplet, proportional to its velocity. The dynamical evolution of the droplets is obtained by solving Newton's equation for an assembly constrained by a given osmotic pressure. This model is similar to the Discrete Element Method (DEM) (Makse et al., 2000) used in MD simulations of granular materials. However, the DEM for the system



(a)



(b)

Figure 6.5: Numerical results for $P(f)$ of (a) quasi-monodisperse and (b) polydisperse emulsions at different osmotic pressure, Π , and coordination number $\langle Z \rangle$.

of compressed emulsions is adjusted by exclusion of transversal forces (tangential elasticity and Coulomb friction) and by computation of interparticle forces using the principles of interfacial mechanics described by the emulsion model.

The simulations begin with a set of non-overlapping 2000 spherical particles located at random positions in a periodically repeated cubic cell of side L . Generating a mechanically stable packing is not an easy task. At the outset, a series of strain-controlled isotropic compressions and expansions are simulated until a volume fraction slightly below the critical density of jamming is reached (Makse et al., 2000). The system is then compressed and extended slowly until a specified value of the stress and volume fraction is achieved at static equilibrium. The distribution of forces within the static structure is calculated and then directly compared to that obtained from experiments and theory.

A perfectly monodisperse system exhibits crystalline regions under pressure, which are not considered in the granular theory presented in Chapter 2. Therefore, a quasi-monodisperse system is considered first, composed of 1000 droplets of radius $1.05 \mu\text{m}$ and 1000 droplets of radius $0.95 \mu\text{m}$. Then, the effect of polydispersity is investigated by consideration of the radii distribution obtained from our experiments presented in Fig. 6.2, characterized by a Gaussian distribution with a mean value $\langle R \rangle = 3.4 \mu\text{m}$ and standard deviation $1.44 \mu\text{m}$, and a distribution range between $1 \mu\text{m}$ and $6.6 \mu\text{m}$. The osmotic pressure, Π , is varied between 1 Pa and 1 kPa.

Figure 6.5 shows the results of the simulations. We see that the simulated data for monodisperse and polydisperse systems at low osmotic pressure agrees with the experiments and the theory: the salient feature of the distributions close to the jamming transition is the exponential. Increasing the pressure such that the coordination number significantly departs from its minimal value results in a Gaussian distribution in the case of the monodisperse system. In the case of the polydisperse system, the distribution at large pressures departs from the exponential decay at large forces, but its form cannot be fitted by a Gaussian-like distribution.

The experimental data for the polydisperse system at the lowest measurable compression was fitted with a function of the form $P(f) \propto f^{0.9} e^{-1.9f/\bar{f}}$. The numerical simulation performed under the same conditions as in the experiment yields a $P(f)$ of the same functional form for the appropriate polydispersity (Fig. 6.5b), although the fitting coefficients obtained numerically do not correspond to those obtained experimentally. Moreover, the monodisperse system shows similar results as long as the system is at low osmotic pressure. These results indicate that the significant feature is not the detail of the system, but its proximity to the jamming transition.

6.2.4 Theory of Force Distributions

Although the experimental system consists of polydisperse particles which are deformable, in order to get a tractable theory, we simply consider rough, rigid grains with coordination number greater than or equal to four in 3-D, excluding ‘rattlers’, as illustrated in Fig. 6.6. Even though this is a gross simplification we believe that a theory that can be carried through to an analytic solution is worthwhile. The geometric constraints are appropriate for comparison with the experimental system in that these coordination numbers imply a jammed state for grains in 3D, which we believe is the unifying concept in this study (Edwards and Grinev, 1999; Moukarzel, 1998). Since the particles in the experiment are frictionless, the condition for a jammed state is satisfied when the coordination number is six. It has already been postulated by O’Hern *et. al.* (2001) that the functional form of the probability distribution of the forces which unifies the behaviour of many systems far from equilibrium arises at the point at which these systems experience a structural arrest. There exist more comprehensive theories such as the q-model (Coppersmith *et al.*, 1996) or force-splitting models (Bouchaud *et al.*, 2001) for more detailed theoretical analysis, which are correspondingly more difficult to solve.

The Simplest Model

By Newton’s laws, in mechanical equilibrium the sum of all the forces exerted on a particle by its nearest neighbours is zero. In two dimensions the average shape of a particle is a circular disc, and the co-ordination number N of random close packing is three (Moukarzel, 1998). Consequently the force \vec{f} exerted by a particle on one of its neighbours will equal the sum of the forces $\vec{f}_1 + \vec{f}_2$ of the other neighbours in contact with it. To simplify, we consider the scalar $f = |\vec{f}|$ since it will have a very similar distribution on every grain. The distribution of the vector \vec{f} will differ even on adjacent grains, therefore we calculate $P(f)$, not $P(\vec{f})$. It is important to note that only those forces which are pushing on each particle are taken into account in the calculation of $P(f)$, a fact which will appear in the range of integration.

First we look at the simplest possible model. The average force \vec{f}_1 in the direction of \vec{f} is $\frac{1}{2}|\vec{f}_1|$ and similarly for \vec{f}_2 . We now have

$$f = \frac{1}{2}f_1 + \frac{1}{2}f_2. \quad (6.4)$$

This gives rise to an equation of Boltzmann form

$$P(f) = \int_0^\infty \int_0^\infty df_1 df_2 \delta(f - \frac{1}{2}f_1 - \frac{1}{2}f_2) P(f_1) P(f_2). \quad (6.5)$$

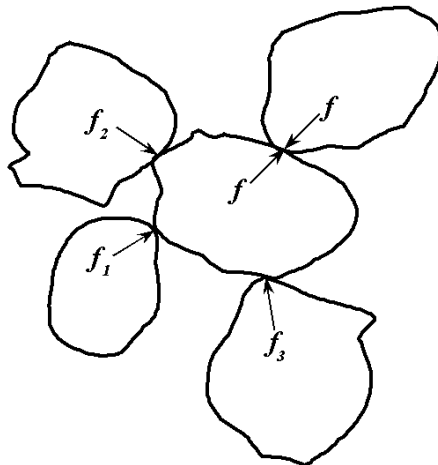


Figure 6.6: 3D Schematic of contact forces between grains.

It is convenient to work with the Fourier transform of the probability distribution $\mathcal{P}(k) = \int_{-\infty}^{\infty} e^{ikf} P(f) df$ which gives

$$\mathcal{P}(k) = \mathcal{P}^2(k/2). \quad (6.6)$$

The integral of the probability distribution is normalised to unity and so $\mathcal{P}(0) = 1$. The general solution of the above equation is

$$e^{i\bar{f}k - \beta|k|} \quad (6.7)$$

giving a probability distribution

$$P(f) = \frac{\gamma\beta}{(f - \bar{f})^2 + \beta^2}, \quad (6.8)$$

where γ is a constant of integration. The contribution to $P(f)$ for $f < 0$ vanishes. This leads to $\beta = 0$ as the only possible solution, and we reach the solution $P(f) = \delta(f - \bar{f})$.

A more accurate model would take into account the direction cosines of each of the forces. By taking the “averaged” particle to be a circular disc, we have implicitly assumed the forces are normal to it. Excluded volume is also an important factor as particles 1 and 2 cannot overlap and the four particle force correlation function should be included. All these effects can be crudely modeled by blurring the contribution from each of the pushing forces by a factor $\lambda_i \in [0, 1](i = 1, 2)$, which plays the role of the direction cosine and the other correlation factors.

The ‘‘Boltzmann’’ equation now becomes

$$P(f) = \int_0^\infty \int_0^\infty df_1 df_2 \int_0^1 \int_0^1 d\lambda_1 d\lambda_2 \delta(f - \lambda_1 f_1 - \lambda_2 f_2) P(f_1) P(f_2). \quad (6.9)$$

Proceeding as before

$$\mathcal{P}(k) = \left(\int_0^1 d\lambda \mathcal{P}(\lambda k) \right)^2, \quad (6.10)$$

having the solution

$$P(f) = \frac{f}{p^2} e^{-f/p}, \quad (6.11)$$

which has been normalised and $p = \bar{f}/2$, where \bar{f} corresponds to the mean force. Note that since f is the sum of positive terms, whose value starts at zero, the distribution $P(f)$ must be zero at $f = 0$.

The 3-D model

In 3-D the co-ordination number of random close packing is greater than or equal to four (see Fig. 6.6). In this case the angular effects can be represented by three ‘‘direction cosines’’ λ_i and we find a force balance equation which is capable of analytic solution to be

$$f = \lambda_1^2 f_1 + \lambda_2^2 f_2 + \lambda_3^2 f_3. \quad (6.12)$$

Averaging the resulting force over the angles $\int_0^1 \lambda^2 d\lambda = \frac{1}{3}$ gives $f = \frac{1}{3}(f_1 + f_2 + f_3)$ representing equal weighting to each of the contact forces. This gives rise to an equation of the Boltzmann form:

$$P(f) = \int_0^\infty df_1 df_2 df_3 \int_0^1 d\lambda_1 d\lambda_2 d\lambda_3 \delta(f - \lambda_1^2 f_1 - \lambda_2^2 f_2 - \lambda_3^2 f_3) P(f_1) P(f_2) P(f_3) \quad (6.13)$$

Proceeding as before, the Fourier transform of the probability distribution satisfies

$$\mathcal{P}(k) = \left(\int_0^1 d\lambda \mathcal{P}(\lambda^2 k) \right)^3, \quad (6.14)$$

which can be solved to give the normalised distribution

$$P(f) = \frac{2}{\sqrt{\pi}} \frac{f^{1/2}}{p^{3/2}} e^{-f/p}, \quad (6.15)$$

where $p \propto \bar{f}$ and the proportionality constant depends on the exponent of the power law rise at low forces. More generally, if there are N contacts arising from

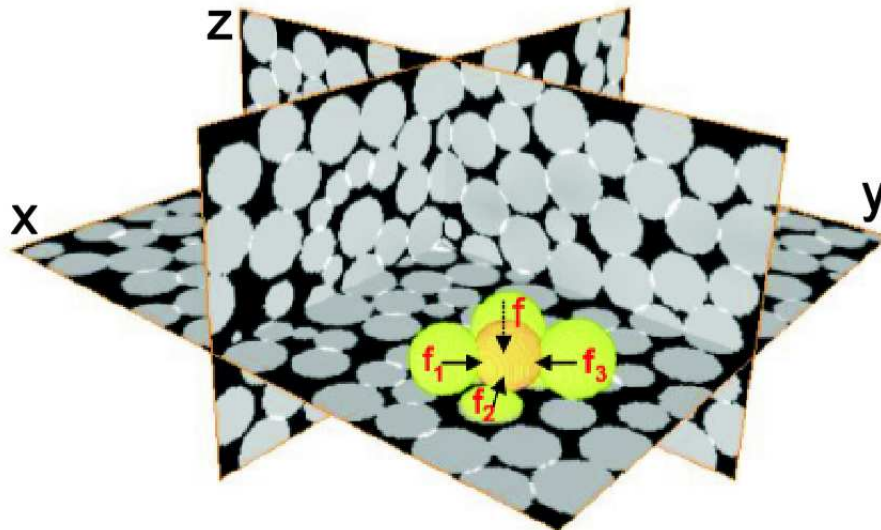


Figure 6.7: The background image is the reconstructed confocal microscopy image using the droplet centres and radii found by the image analysis algorithm. First coordination shell of particles exerting forces on the centre particle are depicted in colour. The force data for each particle in the image are used to calculate the vector sum of forces on each particle, the pressure per particle, the coordination number distribution and indirectly the volume function W .

differing geometric configurations, similar calculations give

$$P(f) \propto f^{1/(N-2)} e^{-f/p}. \quad (6.16)$$

The coefficients of proportionality are determined by normalisation. The functional form which fits the experimental result, $P(f) \propto f^n e^{-(n+1)f/\bar{f}}$, where n is 0.9, is the same as the normalised distribution proposed by the theory. There are many improvements which are essential for belief in coefficients and the significance of the number of contacts N , but the functional form, starting at zero and ending with an exponential decay, seems well founded.

6.3 Coordination Number, Z

The theory of the force distribution is fully dependent on the configurations. Since the configurations can be most complicated, the theory is simplified by the assumption that all particles within the system have the same coordination number, as illustrated in Fig. 6.7. However, physically, if some grains have more than the theoretically determined number of contacts, others must have less, giving rise to a distribution of coordination numbers which is theoretically daunting. Therefore,

this study aims to test whether the average coordination number coincides with the theoretical prediction. The assumption of a single coordination number, rather than a distribution, is also investigated.

Consider the static packing of particles under an external force f_{ext} . The overall force balance equation is

$$\partial_i \sigma_{ij} + f_{j\text{ext}} = 0. \quad (6.17)$$

where σ_{ij} is the macroscopic stress tensor. Since there are 3 equations (in 3-D) for 6 independent stress components (the stress tensor is symmetric), then the system is indeterminate, and the equations must be augmented by additional constitutive equations. The conventional elastic approach is then to consider the deformability of the packing which is described by the strain field. Linear constitutive relations are introduced to relate the strain to the stress via the elastic constants of the material (Hooke's law). For an isotropic elastic body only two elastic constants (for instance, the shear modulus and the Poisson ratio) are sufficient to fully describe the stress transmission in an elastic packing (Landau and Lifshitz, 1986).

In the limit of infinitely rigid grains the absence of the strain field questions the validity of elasticity theory. In this case, it has been argued that it is possible to solve the stress distribution, based on Newton's equations alone without resorting to the existence of the strain, only when the system is at a particular *minimal coordination number* (Edwards and Grinev, 1999; Bouchaud et al., 1995; Ball and Blumenfeld, 2002). The granular indeterminacy is then solved by resorting to the configurational information alone. Such approaches are intimately related to the thermodynamics of jamming (Blumenfeld and Edwards, 2003).

The minimal coordination number can be understood in terms of simple constraint arguments for a system of N rigid spherical grains in D dimensions (Alexander, 1998; Moukarzel, 1998; Edwards and Grinev, 1999). In the case of frictionless grains, $ZN/2$ normal forces have to be determined with DN equations of force balance. The critical coordination number for which the equations of force balance are soluble is found to be $Z_c = 2D$, i.e. $Z_c = 6$ in three dimensions. Similar arguments lead to a minimal coordination of $Z_c = D + 1$, i.e. 4 in 3D, for infinitely rough spherical grains, i.e. grains with finite tangential forces, f_t , but with an infinitely large friction coefficient ($\mu \rightarrow \infty$).

Below Z_c the system cannot be jammed and it exists only in suspensions. Above Z_c the system is underconstrained and elasticity theory may give the correct approach to describe such a packing of deformable grains. At the minimal coordination number the system is in a state of marginal rigidity, otherwise known as the isostatic limit.

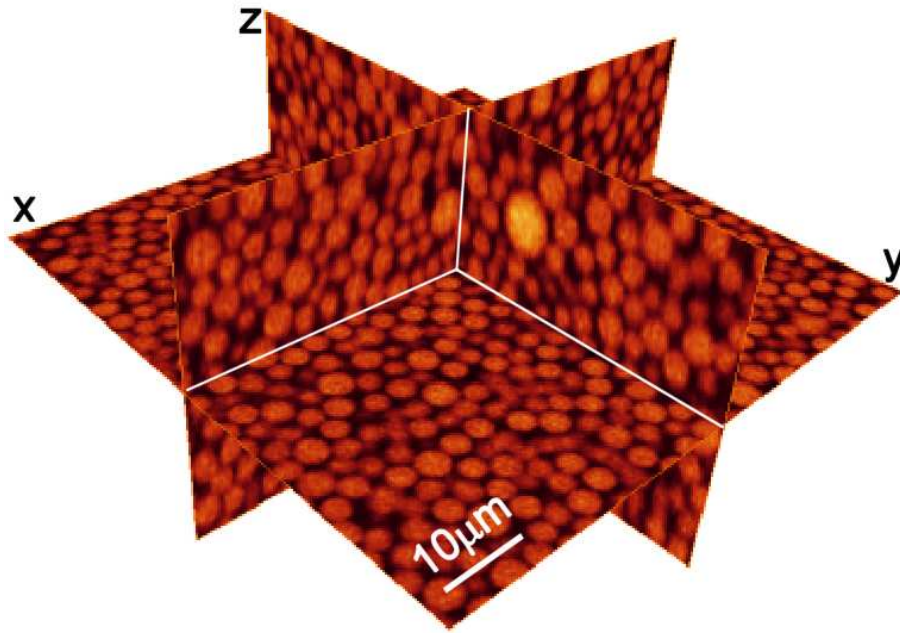
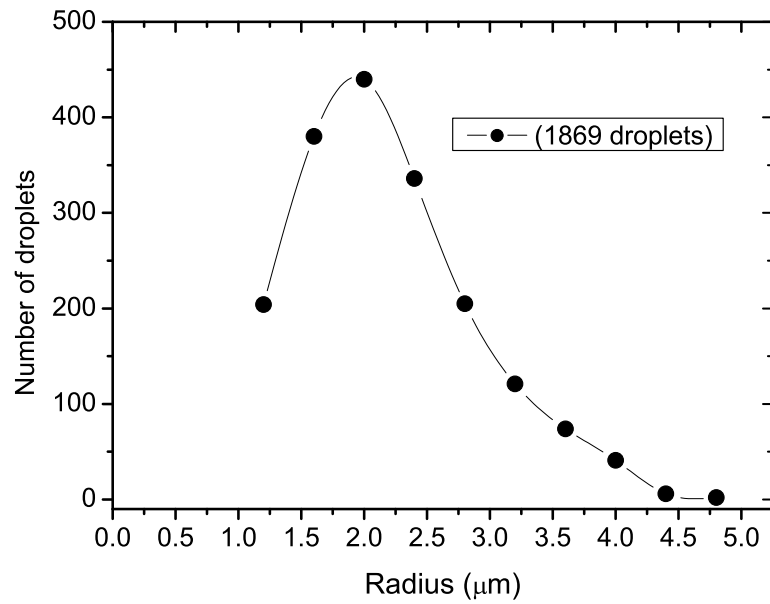


Figure 6.8: 3D representation of the colloidal packing of PMMA particles with a purely repulsive interaction potential. The particles cream under gravity over a period of ≈ 1 hour.

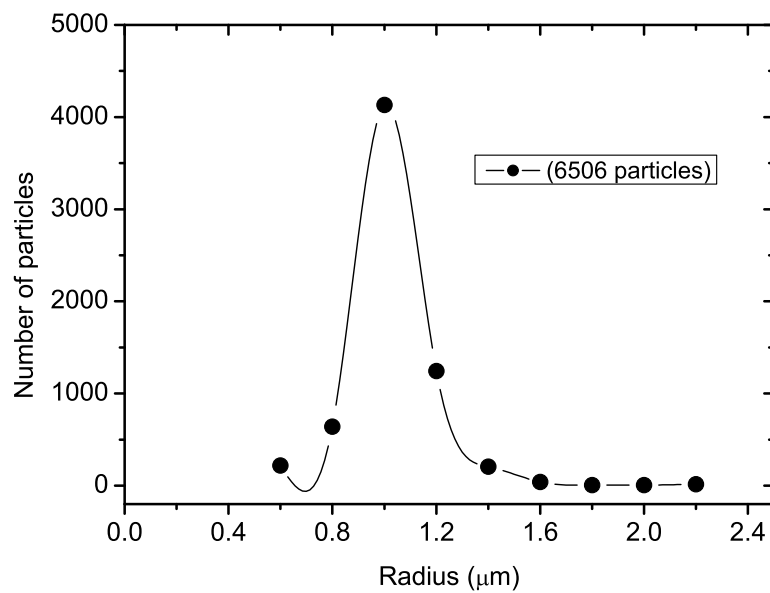
6.3.1 Determination of the Coordination Number

In order to test the existence of the isostatic limit we study the coordination number for two frictionless systems: a packing of emulsion droplets and a packing of poly(methyl-methacrylate) (PMMA) particles. The packings are investigated at the isostatic limit, i.e. at the lowest pressure. Both types of particles are lighter than the suspending fluid and therefore cream rather than sediment under gravity to form a static configuration. Since friction is eliminated by the lubrication of the continuous phase liquid, the particles achieve a jammed state, as defined in Section 1.2.2, without the need for external perturbations. Moreover, the structure does not evolve significantly with time (see Section 6.7), suggesting that an efficient random close packed structure is reached with relative ease.

It should be noted that the theoretical coordination number assumes that there are forces being exerted at each contact point. Since the forces due to gravity cannot be resolved in the confocal microscope, we rely on the accuracy of the particle finding algorithm to determine whether the particles are truly touching. Thus, only the geometrical sphere overlaps are sought, rather than the increased brightness at the contacts. The assumption of particle sphericity is valid in both emulsions and colloids at low pressures, meaning that the sphere centres and their



(a)



(b)

Figure 6.9: Distribution of radii obtained from image analysis for (a) the emulsion system and (b) the colloidal system of PMMA particles. The line through the data serves as a guide to the eye.

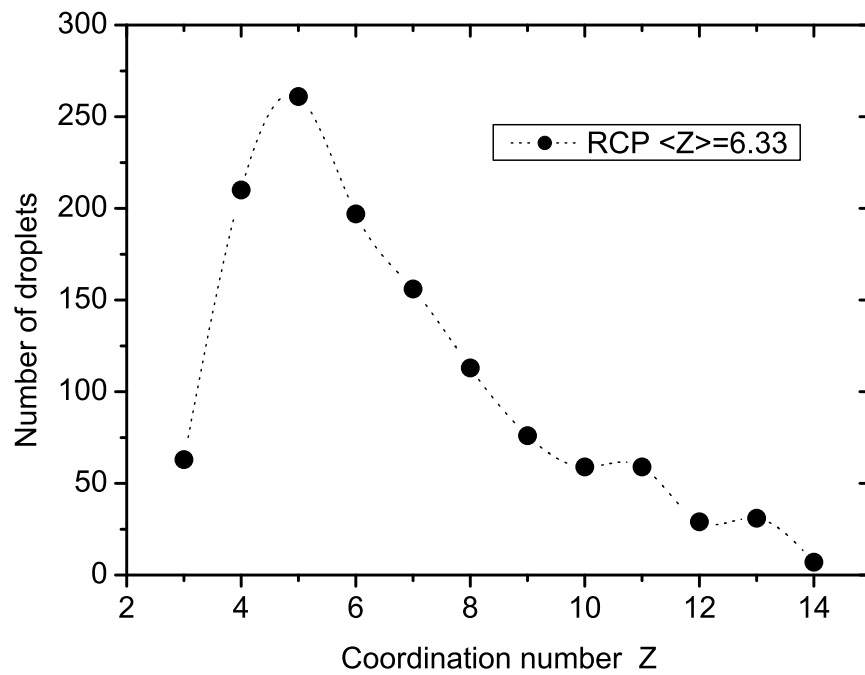
respective radii are identified with subvoxel accuracy. Unlike in the case of the force measurements, there is no minimum overlap required in order to define the contacts as long as the distance between the sphere centres, R^α and R^β , is smaller than the sum of their radii, $d < r_\alpha + r_\beta$. The agreement with the theory and the high accuracy of the sphere reconstruction gives validity to the method.

We first consider the variation in polydispersity between the two systems, as obtained from image analysis. The emulsion radii distribution is characterized by a Gaussian distribution with a mean value $\langle r \rangle = 2.0\mu\text{m}$ and standard deviation $0.7\mu\text{m}$, with a distribution range between $1\mu\text{m}$ and $4.8\mu\text{m}$. The PMMA particles have a much narrower size distribution with a mean value $\langle r \rangle = 1.0\mu\text{m}$ and standard deviation of $0.1\mu\text{m}$. Both are shown in Fig. 6.9.

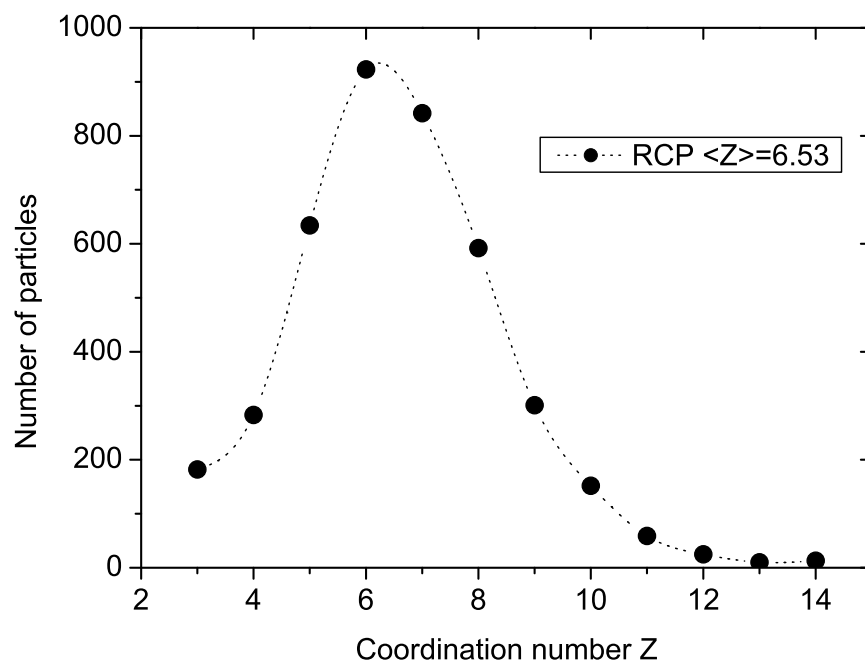
Next, we show the coordination number distribution within the inner window of the emulsion packing in Fig. 6.10a. The statistical analysis is derived from a set of 6 image stacks, in total containing 1344 droplets with a reliable coordination number. At low pressures compared to the Laplace pressure of the droplets, the emulsion system behaves most like a pack of rigid balls, thus approaching the isostatic limit (Silbert et al., 2002). Therefore, for the coordination number determination, the emulsions were left to cream under gravity and the packing configuration was observed after a period of several hours. We find that the average coordination number of the packings is $Z = 6.33 \pm 0.5$ at $p \approx 0$. This value is in approximate agreement with the theoretical value for frictionless particles in 3D, as $Z_c = 2D$. The peak of the distribution is shifted towards $Z = 5$ and there is a proportionally larger number of droplets with exceptionally high coordination numbers. The wide distribution ranging up to 14 contact points per sphere, is explained by the polydispersity, which implies a more efficient packing.

The colloidal packing contains a much larger statistical ensemble with 6506 particles in one 3D image, shown in Fig. 6.8, due to the narrow size distribution and small average particle size. Hence, the statistics presented in Fig. 6.10b is performed on the 4178 particles in the inner window of that image. The peak of the distribution is close to the mean coordination number value at $Z = 6.53$, yet again in agreement with the prediction of the theoretical isostatic limit. The volume fraction of the colloidal sample was measured to be 58% by image analysis, in good agreement with previous measurements of the random close packing limit of suspensions of nearly hard colloidal spheres (Pusey and van Meegen, 1986). The coordination number distribution is much narrower than in the case of emulsions, indicating a more uniform packing configuration.

It is difficult to achieve a large statistical ensemble of droplets for which one



(a)



(b)

Figure 6.10: Coordination number distribution within the particulate packing of (a) emulsion droplets and (b) colloidal (PMMA) particles at $p \rightarrow 0$.

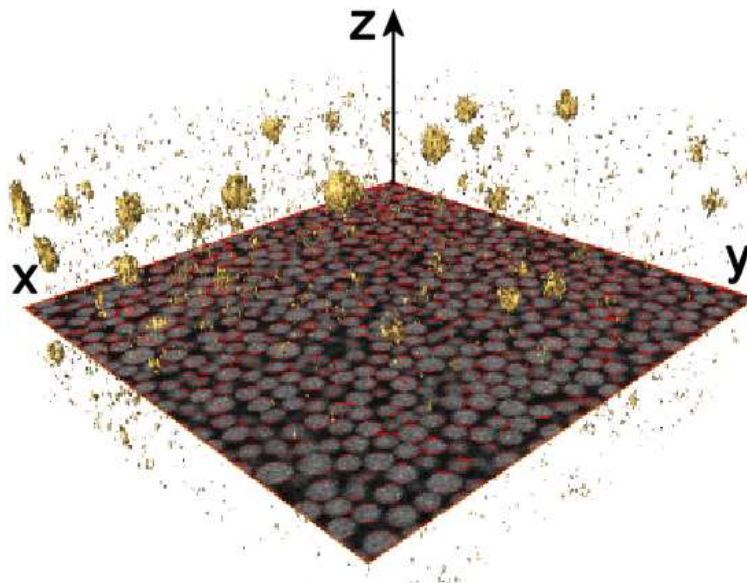


Figure 6.11: 3D representation of the particles which have not been found by the image analysis algorithm. Note that they are a small fraction of the identified 6506 particles, mostly situated at the edges of the box. Several stages led to this image: 1) The reconstructed spheres are subtracted from the original image to create image (A). 2) Drawing an isosurface at the intensity 137 in image (A) isolates the remaining particles. 3) A slice of the original image and isolines highlighting the particulate structure are also shown for clarity.

is certain to have incorporated all the contact points. For instance, a packing of ≈ 1000 reconstructed droplets will only contain ≈ 250 whole spheres in the inner window of the image (depending on the polydispersity) once the spheres at the edges are eliminated. Note that the requirement for an accurate coordination number is not only that the sphere is whole in the image, but also that all its neighbours have been identified, in order to be able to derive whether the droplets are actually touching. If some spheres are not identified in the image, the coordination number determination will be underestimated. It is for that reason that we have gone to great lengths to reconstruct the original image to within 1% of the total number of droplets. Such a small error would not play a significant role in this analysis. The success of the image analysis algorithm in finding all the spheres in the image is illustrated in Fig. 6.11 for the packing of PMMA particles. The few unfound spheres are clearly shown and are situated mostly at the edges which are eliminated from the coordination number analysis.

In conclusion, the critical coordination number for a jammed state of frictionless spheres is shown to be close to the theoretical value of 6 in two different

particulate systems. The agreement between the two systems suggests that the particle elasticity does not affect the average coordination number of the packing, since it is governed by the balance of forces. Furthermore, the distribution of the coordination number is dependent on the particle size distribution and much larger coordination numbers than Z_c can be observed in the packing, even in the absence of particle deformation. The observation that the coordination number fluctuates through the packing does not dismiss the theory. The theory deals with such arbitrary packings by making the assumption that the major force is transmitted through Z_c number of contacts. These contacts are considered to be active, and the rest of the contacts transmit only an infinitesimal stress, and can therefore be assumed as passive. This assumption implies the existence of stress-bearing paths within the packing, which are investigated experimentally by the spatial distribution of the forces, presented in Section 6.5.

6.4 Structure and Force Correlations

The second important assumption which the force distribution theory makes is that the forces are uncorrelated. This assumption allows one to base the theory on the analysis of a first coordination shell of particles. In reality, it is thought that higher order correlations do exist, which would demand for a more complicated theoretical analysis.

First, we test this assumption by investigating the ‘fabric tensors’ constructed according to the geometrical definitions of the packing. The stress tensors are calculated for the same data as that used to determine the $P(f)$ curves in Fig. 6.3. The configurational tensors are additionally calculated for the uncompressed emulsions investigated in Section 6.3. Then, we calculate the radial distribution function and the force correlation function within the droplet packing in search of structure-force correlations. Since the results are reproducible for all the data sets, a representative set is presented here.

The configuration of the droplet packing can be described by the geometric specification illustrated in Fig. 6.12. This diagram is oversimplified, in that it includes all the approximations made in the analysis of the experiment. The justification for using the approximations is explained below. The first coordination shell of a grain is defined in terms of a number of contact points, $m^{\alpha\beta}$, and the particle centroids, R^α . Since the droplets only exert normal forces on one another and are spherical to a good approximation, the centroids are considered to be the sphere centres, as determined by image analysis, rather than the geometric mean of the contact point vectors. The contact points, $m^{\alpha\beta}$, are taken to be the centres

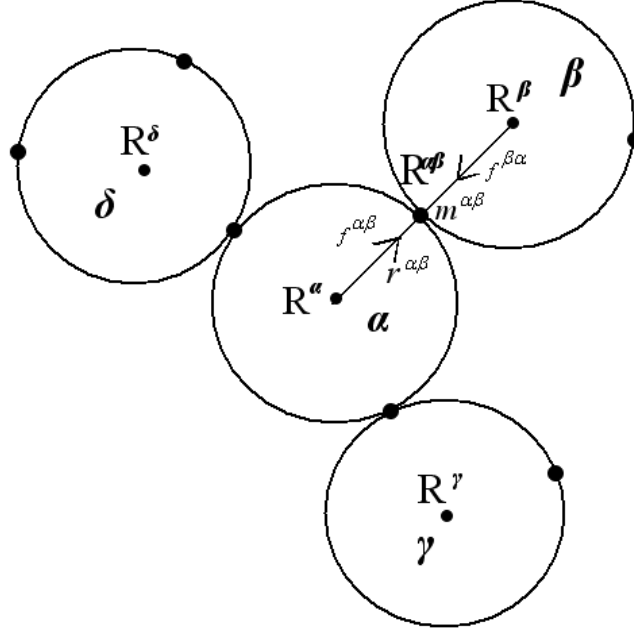


Figure 6.12: 2D Schematic of configuration tensors in an assembly of droplets.

of the circular areas of deformation, since the emulsion droplets are compressible. The vector joining the centroid of contact with the contact point is

$$r^{\alpha\beta} = m^{\alpha\beta} - R^{\alpha} \quad (6.18)$$

and can be assumed to be the magnitude of the particle radius if the deformation is small. The distance between particles α and β is defined as the distance between their centroids of contacts

$$R^{\alpha\beta} = R^{\beta} - R^{\alpha} = r^{\alpha\beta} - r^{\beta\alpha}. \quad (6.19)$$

The forces act along the vectors $R^{\alpha\beta}$, since there is no tangential component to the force. Hence, R^{α} and $r^{\alpha\beta}$ are the geometrical properties chosen for consideration, while other terms accounting for non-sphericity are not included. Several useful tensors can be constructed to describe the particulate system, and much of the granular theories are expressed in terms of those tensors.

We introduce the configuration tensor $\mathcal{C}_{ij}^{\alpha}$ per particle

$$\mathcal{C}_{ij}^{\alpha} = \sum_{\beta} (R_i^{\alpha} - R_i^{\beta})(R_j^{\alpha} - R_j^{\beta}), \quad (6.20)$$

with β being the nearest neighbours. One can see from Fig. 6.12 that vector $R^{\alpha\beta}$ joins the centroids of contact of grains α and β . The isotropy of the configuration

in the whole sample volume is investigated by the construction of the macroscopic tensorial matrix. The resulting tensor \mathcal{C}_{ij} , summed over all the particles in the system, is a 3×3 matrix in three dimensions, which has 3 Euler angles of orientation and 3 eigenvalues, expressed in μm^2 . They are divided by the system volume and presented in units of μm^{-1} . A typical set of values obtained for a packing of droplets is given:

$$\begin{pmatrix} 80.13 & 1.01 & 0.61 \\ 0.74 & 79.45 & 0.74 \\ 0.61 & 1.01 & 84.64 \end{pmatrix} = \begin{pmatrix} \mathcal{C} & \delta & \delta \\ \delta & \mathcal{C} & \delta \\ \delta & \delta & \mathcal{C} \end{pmatrix} \quad (6.21)$$

where \mathcal{C} and δ are labels for the diagonal and offdiagonal terms in the matrix. The configurational tensor is symmetric, with 6 independent terms. The diagonal terms are approximately equal ($\pm 5\mu\text{m}^{-1}$), whereas the off-diagonal terms are two orders of magnitude smaller, $\mathcal{C} = \delta \times 10^2$, indicating isotropy.

Since tensor \mathcal{C}_{ij}^α describes the configuration of the first coordination shell of a reference grain α , its invariants play a special role in the thermodynamics formalism discussed in Chapter 2. The experimental analysis of the packing in this context is presented in Section 6.9 of this Chapter.

Another important tensor is the force moment tensor, σ_{ij}^α of particle α , which is the microscopic analogue of the stress tensor,

$$\sigma_{ij}^\alpha = \frac{1}{2} \left(\sum_{\beta} f_i^{\alpha\beta} r_j^{\alpha\beta} + f_j^{\alpha\beta} r_i^{\alpha\beta} \right). \quad (6.22)$$

This tensor is calculated for each particle in the inner window of the image. Moreover, the trace of the tensorial matrix, calculated from experimental data, gives a quantitative measure of the pressure on the particle as

$$p = \frac{1}{3V_\alpha} (\sigma_{xx}^\alpha + \sigma_{yy}^\alpha + \sigma_{zz}^\alpha). \quad (6.23)$$

This method of determining the pressure of the system comes directly from the measurement of density of forces within the volume. By comparison of the components of the stress tensor of the whole particulate packing the isotropy of stress transmission is investigated. The stress tensor matrix obtained from the data set giving rise to $P(f)$ in Fig. 6.2 is presented as the pressure per droplet in Pa, with the following values:

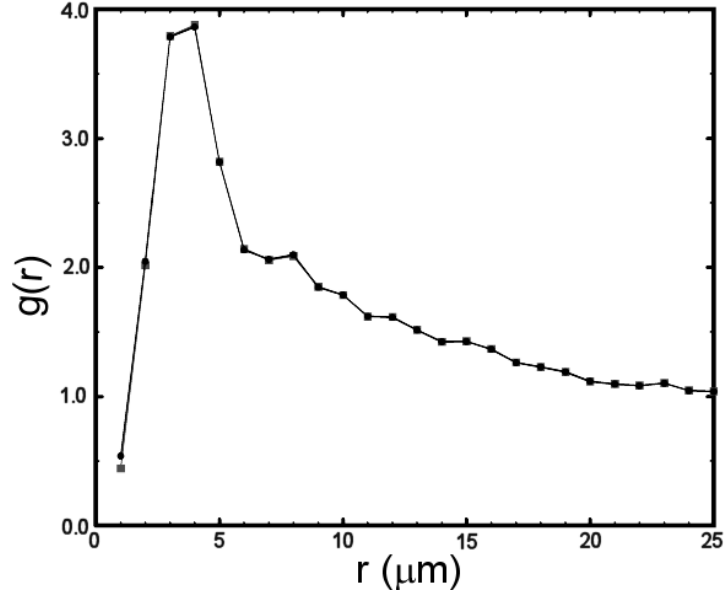


Figure 6.13: Radial distribution function: Experimental result for 369 droplets inside the inner window of the image showing one broad peak.

$$\begin{pmatrix} 3.98 & -0.24 & -0.02 \\ -0.62 & 4.14 & -0.62 \\ -0.02 & -0.24 & 4.72 \end{pmatrix} = \begin{pmatrix} p & \epsilon & \epsilon^{-1} \\ \epsilon & p & \epsilon \\ \epsilon^{-1} & \epsilon & p \end{pmatrix} \quad (6.24)$$

where p and ϵ are labels for the terms in the matrix. Even though one of the off-diagonal terms in the matrix is an order of magnitude smaller than the rest, i.e. ϵ^{-1} , the pressure can be considered to be isotropic in the specified directions since the mean system pressure is $4.28\text{Pa} \pm 0.45\text{Pa}$. The off-diagonal terms are an order of magnitude smaller, thus indicating isotropic stress transmission.

To further probe the uniformity of the packing, we proceed to calculate the radial distribution function, defined as

$$g(r) = \frac{V}{N^2} \langle \delta(r - r_{ij}) \rangle. \quad (6.25)$$

In practice, a spherical shell of a radius between r and $r + \Delta r$ is created around each sphere and the number of spheres inside the shell are counted and divided by $2\pi N^2 r^2 \Delta r / V$, where N is the number of particles and V is the total volume. $g(r)$ is shown in Fig. 6.13 exhibiting one very broad peak because the system is polydisperse. The absence of other peaks indicates that the system is very uniform, again due to the polydispersity.

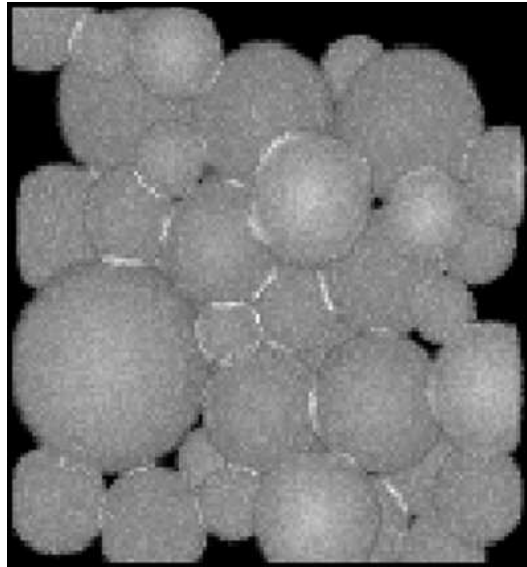


Figure 6.14: 3D projection of the reconstructed droplets from the identified centres and radii in the confocal image. The areas of deformation, from which the interdroplet forces are calculated, are shown with a higher intensity than the droplets. The forces provide the full spatial distribution in the sample volume.

Similarly, the force correlation is defined as,

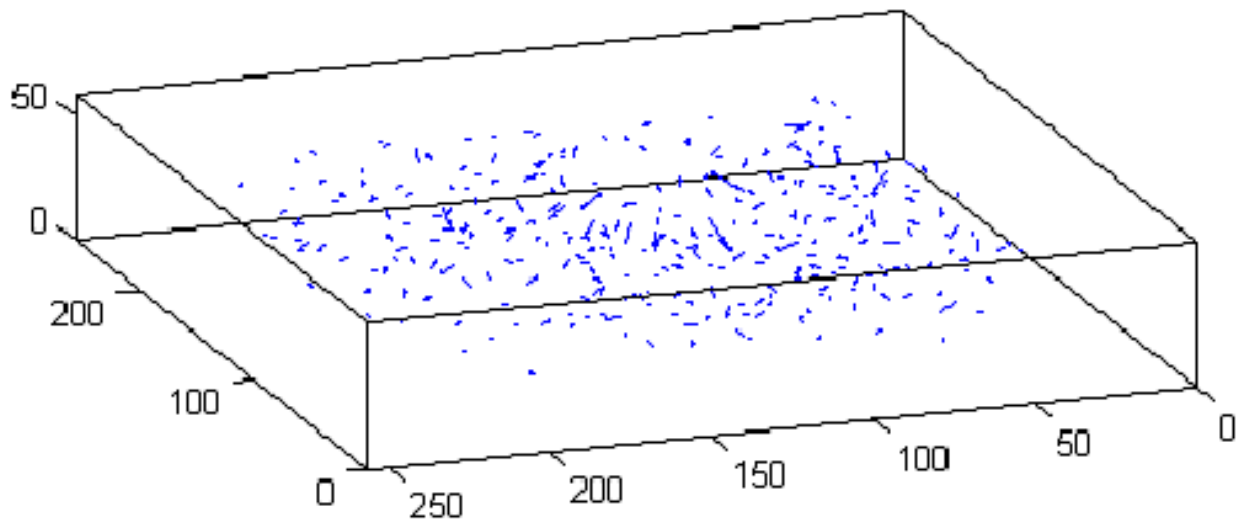
$$F(r) = \langle \delta(r - r_{ij}) f_i f_j \rangle / \langle \delta(r - r_{ij}) \rangle, \quad (6.26)$$

but shows no correlation peaks in the investigated data set. Since the function $F(r)$ is flat, it is not included here. It indicates that there are no correlations between the forces, in agreement with the theoretical assumption in Section 6.2.4.

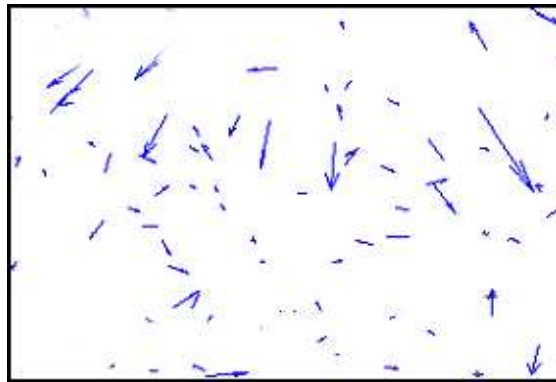
6.5 Spatial Distribution of Forces

The structural features which arise in the stress transmission through granular packings have been investigated extensively (Liu et al., 1995; Vanel et al., 1999). The idea that most of the stress is transmitted through well-defined paths, named force chains and arches, has been postulated in the literature (Hidalgo et al., 2002). The assumption that the major forces are transmitted through 6 contacts of each grain, while the others are bearing very little stress, also implies structural features in the distribution.

The experimental data allows us to examine the spatial distribution of the forces in the compressed emulsion, since the 3D image reconstruction contains all the spatial information of droplet deformation, illustrated in Fig. 6.14. This leads to the spatial representation of the forces as arrows in the direction of the force

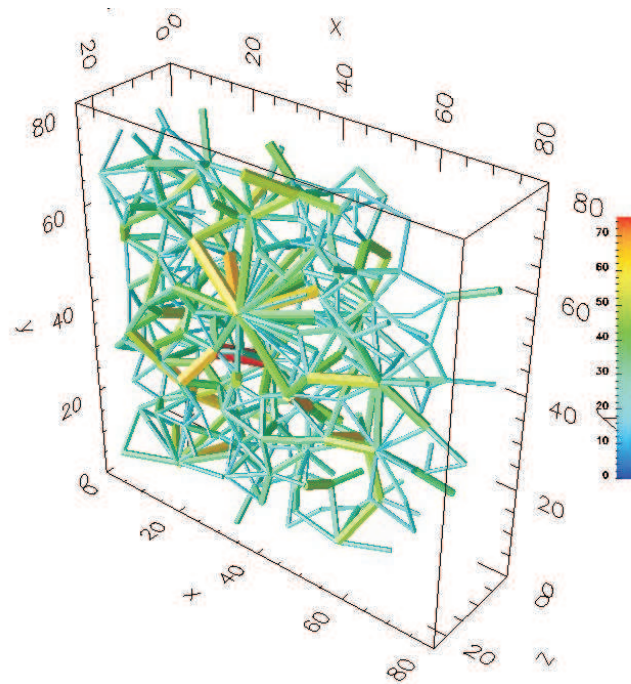


(a)

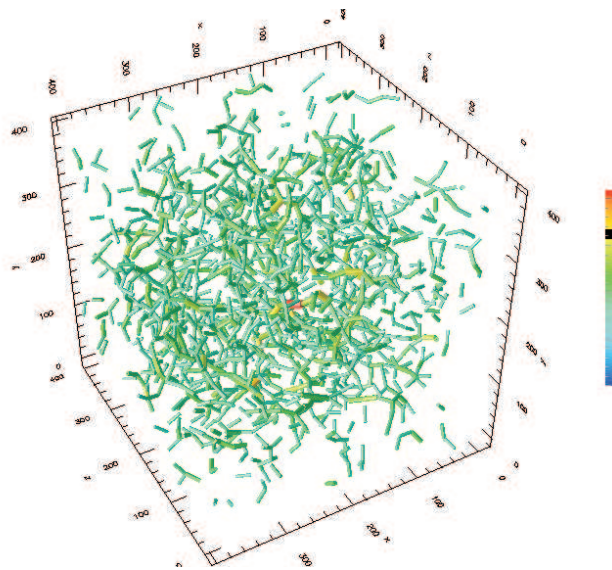


(b)

Figure 6.15: (a) Forces in the middle of the sample volume (acting on whole spheres only) are represented as arrows in the direction of the force, the length of which is proportional to their magnitude. The box size is $76.8 \times 76.8 \times 16.8 \mu\text{m}$. (b) Zoom inside the volume shown for clarity.



(a) Experiment



(b) Simulation

Figure 6.16: Force chains: (a) Plot of the interdroplet forces inside the packing of droplets obtained in the compressed emulsion experiment at 4.3Pa. The box axes are labelled in pixels and correspond to the dimensions in Fig. 6.15. (b) Frictionless isotropic granular system at $p = 100$ kPa in 3D from simulations of Hertzian spheres, not discussed in the Thesis. Force chains are tenuous and not well defined.

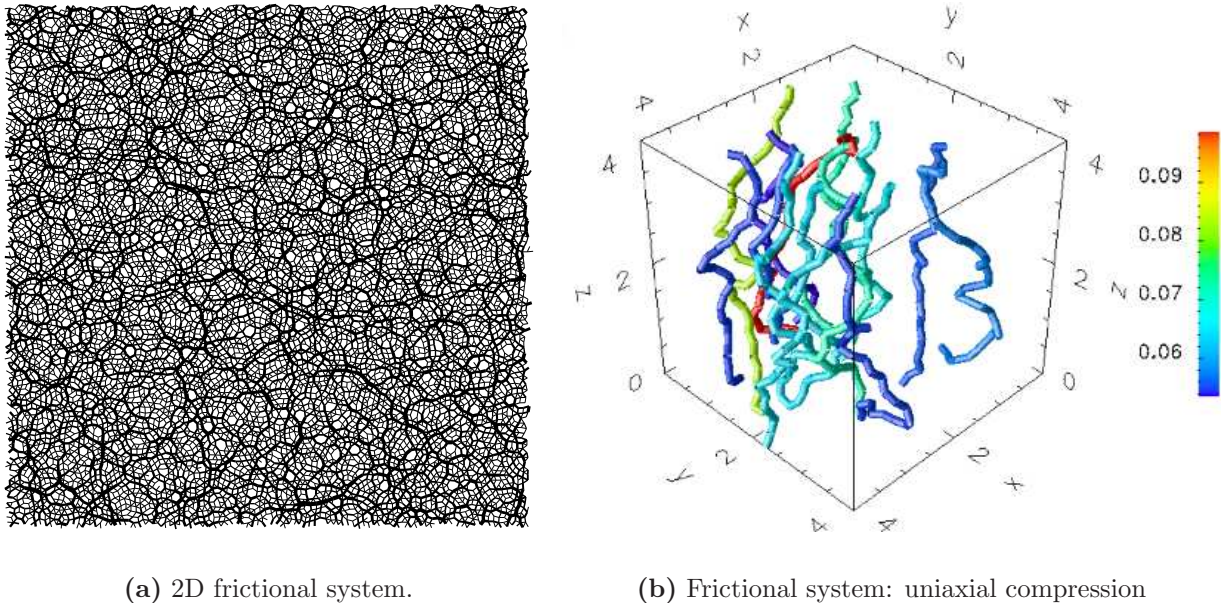


Figure 6.17: Force chains:(a) Clearly visible force chains in a 2D frictional system from simulations (Radjai et al., 1996), (b) Frictional system under uniaxial compression from simulations. Percolating force chains are seen in this case, provided by H. Makse at CCNY, for comparison.

(from the contact points towards the particle centres) within the 3D volume, as shown in Fig. 6.15.

In search of structural features carrying the largest proportion of the stress, we plot only the forces larger than the average, shown in Fig. 6.16a. For better visualisation, the forces are represented as rods joining the centers of pairs of droplets in contact. The thickness and the colour of the rod is proportional to the magnitude of the force. In this sample volume, the forces appear to be uniformly distributed in space and do not show evidence of localisation of forces within the structure, in support of the theoretical assumptions.

For comparison, we also show computer simulation results for isotropic packings of Hertz-Mindlin spherical particles in Fig. 6.16b where force chains are not observed either. On the other hand 2D packings clearly show the existence of force chains under isotropic pressure, shown in Fig. 6.17a (Radjai et al., 1996), indicating that their existence may be related to the dimensionality of the problem. Furthermore, force chains can be obtained in 3D by uniaxially compressing an isotropic packing, as shown in Fig. 6.17b. It should be noted that in the case of Fig. 6.17b, an algorithm which *looks* for force chains is applied by starting from a sphere at the top of the system, and following the path of maximum contact force at every grain. Only the paths which percolate are plotted, i.e., the stress paths spanning the sample from the top to the bottom.

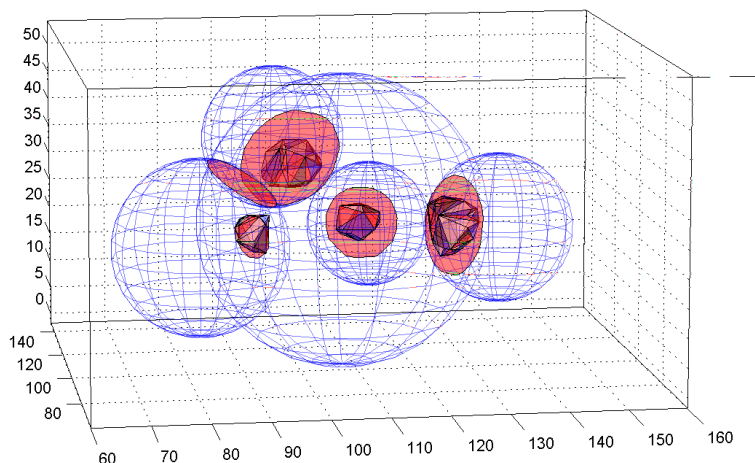


Figure 6.18: Circular planes of intersection of the spheres in contact obtained from their geometric overlap and those from highlighted patches in the original images, from which we determine the force. The geometric overlaps are enlarged for clarity.

Interestingly, the salient feature of all the particulate packings shown in Figs. 6.16 and 6.17, irrespective of their spatial characteristics, is an exponential distribution of forces. This indicates that force chains are not necessary to obtain such a distribution. The rationalization of this observation has been exploited in the theory developed in Section 6.2.4, which is based on the assumption of uncorrelated force transmission through the packing.

6.6 Experimental Validation of the Force Model

The force model used in this study corresponds to an energy of deformation which is quadratic in the area of deformation, analogous to a harmonic oscillator potential that describes a spring satisfying Hooke's law (Princen and Kiss, 1986). There have been several more detailed calculations (Morse and Witten, 1993) and numerical simulations (Lacasse et al., 1996; Lacasse et al., 1994) to improve on this model and allow for anharmonicity in the droplet response by also taking into consideration the number of contacts by which the droplet is confined. Typically these improved models lead to a force law for small deformations of the form $f \propto A^\alpha$, where A is the area of deformation and α is a coordination number dependent exponent ranging from 1 ('Linear' Model) to 3/2 (Hertz model).

In our experiment, the discrepancy of the areas observed as the highlighted regions of the images and those calculated from a geometric overlap which ignores the response of the droplet shape to the deformation and the number of surfaces the droplet is confined by, provides a direct measure of the effects of anharmonic-

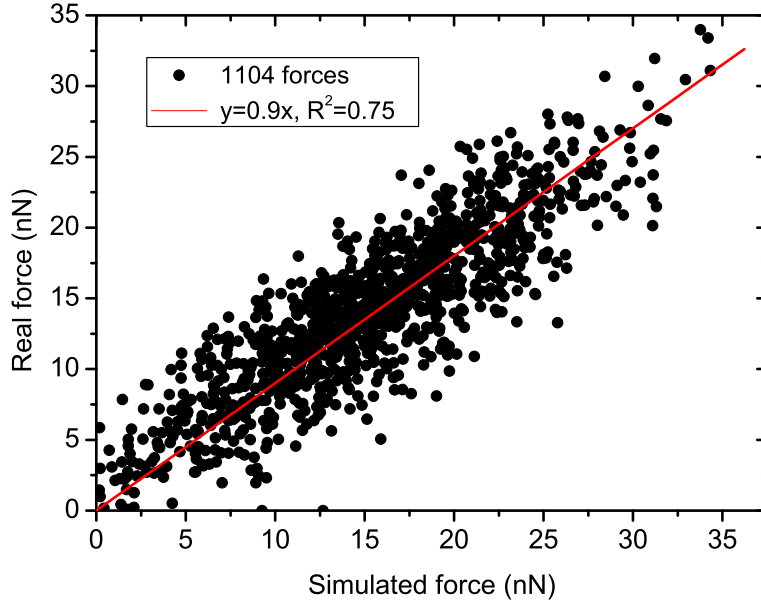


Figure 6.19: Correlation of the forces calculated from areas of deformation extracted from the highlighted regions in the image, i.e. the ‘patch forces’, and those from the geometrical overlaps, referred to as the ‘simulated forces’.

ity of the interaction between the droplet surfaces (Fig. 6.18). Calculating the geometrical sphere overlaps effectively makes the same assumptions as the simple model in Eq. (6.2). The areas arising from both methods are strongly correlated, as shown in Fig. 6.19, with an approximately linear relationship between the two. Moreover, we find that the form of the probability distribution $P(f)$ is not strongly dependent on α in the predicted range, and therefore assume the model where $\alpha = 1$ throughout this study.

A further test of this model is whether the vector sum of forces on each droplet is zero in a packing which is in mechanical equilibrium. For each sphere in the inner window of the image, the vector sum of forces acting is calculated as

$$\sum_{\alpha} \vec{f}_{\alpha} \quad (6.27)$$

and compared with the sum of the magnitudes of the same forces,

$$\sum_{\alpha} |\vec{f}_{\alpha}| \quad (6.28)$$

as shown in Fig. 6.20. Overall, the error is within 15% of the total force, calculated

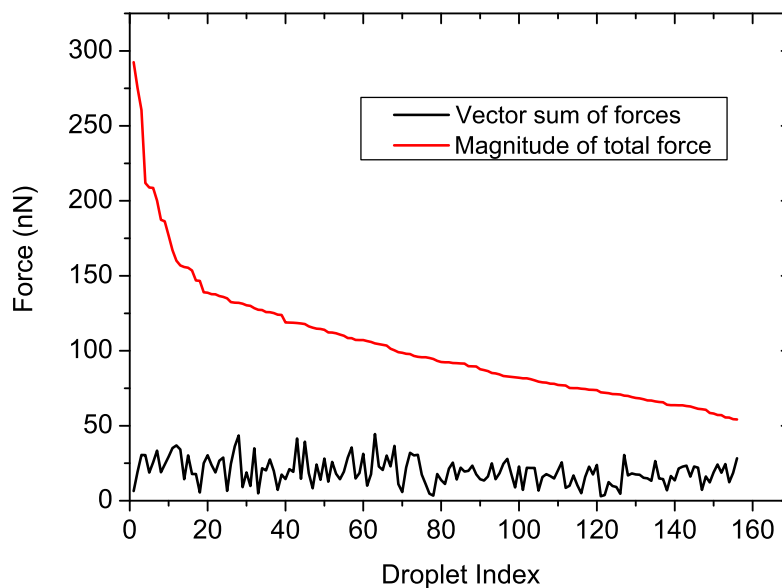


Figure 6.20: The sum of the magnitudes of the forces acting on each particle in the inner window of the packing is compared to the vector sum of those forces, which must be zero if the sample is in mechanical equilibrium.

for 10 data sets. The important observation is that the error is independent of the total magnitude of the force on the particle and the number of forces acting on the particle. This suggests that the error is not related to an incorrect estimation of the force, but points to systematic inaccuracies in the technique. Interestingly, the vector sum in the z direction is twice as large as the x, y and the residual force is always pointing upwards. By visualisation of the spheres with the largest residual force, it was revealed that the increase in error arises from the sample depth being only several particles thick. Removal of the edges only leaves ≈ 4 particle layers, with some unidentified neighbours vertically above the inner window of the image. This causes the anisotropy in the error fluctuations.

6.7 Aging in Emulsions

The slow relaxation below the glass transition in thermal systems, introduced in Section 1.1, can be applied to athermal systems as well. The aging phenomenon in macroemulsions has been postulated theoretically (Sollich et al., 1997) and reported experimentally (Cipelletti and Ramos, 2002). The idea is that over long periods of time (many hours) the frictional thresholds are overcome by thermal fluctuations, such that very few particles within the system can actually ‘spontaneously’ rearrange. Since the particulate packing has a complex, interconnected

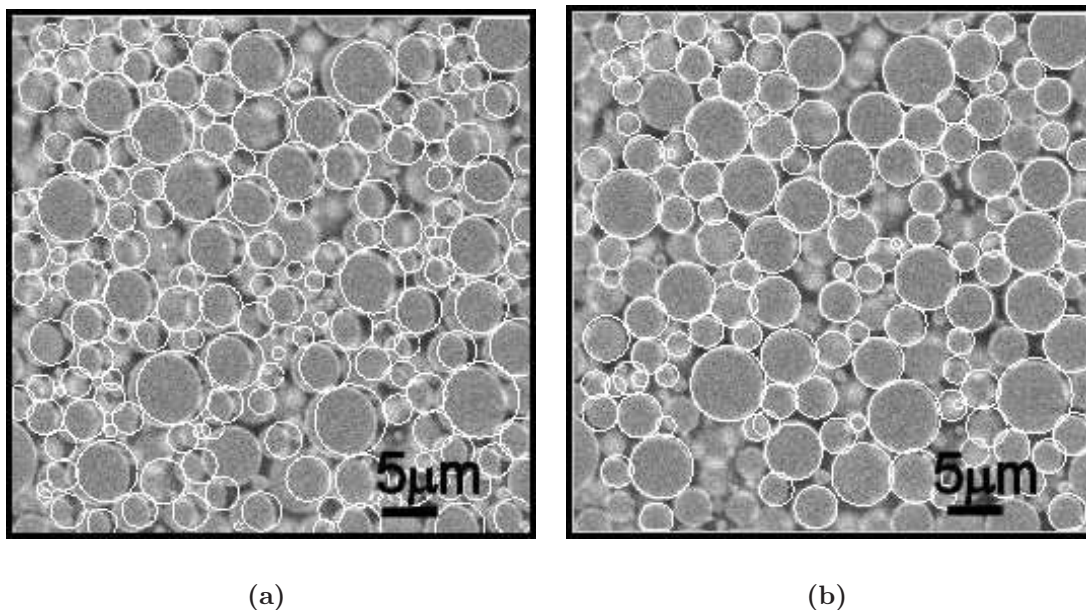


Figure 6.21: (a) A slice from the first image in the sequence, overlaid with the reconstructed droplets for the subsequent image, showing the bulk shift. (b) The same slice overlaid with droplets after the bulk shift correction. No relative droplet motion can be detected by eye.

structure, the motion of only one particle which slips from its jammed configuration may result in a collective rearrangement of the surrounding particles, thus causing a structural relaxation. This kind of behaviour has been characterised using diffusing wave spectroscopy, which measures an average motion over the whole particle assembly (Cipelletti et al., 2003).

In order to check for a microscopic origin of the structural evolution over time, we performed experiments in which all other sources of motion, such as drying and system expansion, were eliminated to the best of our abilities, as described in Section 4.7.3. We imaged the packing of creamed droplets at 1 hour intervals over a period of 4 hours. The imaging was performed using the $63\times$ oil-immersion lens, such that the glass coverslip was in contact with the oil. For that reason, a slight bulk shift was detected between images, which could be attributed to the vertical motion of the sample with respect to the lens.

We eliminated this bulk shift assuming a rigid-body transformation, as shown in Fig. 6.21, while any droplet rearrangements or structural changes would become apparent in the subsequent analysis. The method involved the computation of the centre of mass of all the droplet centers in the inner window for the sequence of images. The translation between the centres of mass of two consecutive images was then applied to each of the droplets in the original packing with the aim of bringing them closer to those in the subsequent image. This shift is of the order of $1\mu\text{m}$.

Then, the corresponding droplets were identified according to their proximity and similar radius, $\pm 0.1\mu\text{m}$. The square of the distance between each corresponding pair was then calculated and summed for all the droplet ‘pairs’ found in the system.

After the bulk shift we found that the four analysed images, each with 800 identified droplets, experienced an average displacement of $0.17\mu\text{m}$ per droplet, which is of the order of the microscope resolution in the xy plane, i.e. ~ 1 pixel. We did not detect a random event which would impose significant rearrangements, instead, we found an evenly distributed small particle displacement. Such a small displacement is most likely due to the error in the particle finding algorithm combined with the error in determining the bulk shift. It cannot be attributed to the aging of the sample, given the accuracy of this method.

Since there is no significant aging detected by our analysis method, we propose that the observed relaxation in previous experiments of macroemulsions (Cipelletti et al., 2003) is attributable to the submicron particles, known as rattlers, which could not be detected by our imaging technique.

6.8 Summary

We have presented experimental data showing the force distribution in three dimensions of a lightly compressed emulsion, close to the jamming transition. These data show an exponential distribution of interdroplet forces $P(f)$ at large f . At low f , a peak in the distribution function is observed. We have fitted the experimental data with a function of the form $P(f) \propto f^{0.9}e^{-1.9f/\bar{f}}$, suggested by the simple theoretical model proposed for such a system.

Furthermore, we have investigated the effects of polydispersity and osmotic pressure on the force distribution function, both experimentally and using numerical simulations. The results are in good qualitative agreement with one another and show that the exponential distribution is independent of the particle size distribution. Moreover, a Gaussian-like distribution was observed at larger pressures, indicating that the exponential $P(f)$ is characteristic of the distributions close to ‘jamming’, at low confining pressures.

The theoretical model predicts a general distribution of the form $P(f) \propto f^n e^{-(n+1)f/\bar{f}}$, where the power law coefficient n is determined by the packing geometry of the system. It is too crude a model to account for the complexity of the emulsion system, and it is therefore inappropriate to draw conclusions from direct comparisons of the coefficients obtained from theory with those arising from experimental and simulation data. Nevertheless, the agreement in the functional form for all three methods is an important result.

In order to test the assumptions of the theoretical model, we have measured the coordination number in the bulk of the sample, investigated structure-force correlations and probed the micromechanical features within the sample volume. We found that the average coordination number for two particulate systems, emulsions and PMMA particles, is approximately six, as predicted by the theory of marginal rigidity. In addition, the coordination number distribution was found to depend on the polydispersity of the system. The assumption of no force correlations was also put to the test and justified in our experiment. The stress distribution was found to be isotropic and no structural features were detected within the packing. This result is also supported by the theoretical model.

The investigations of the interdroplet force model led to the justification for using the linear model, but the question of the influence of non-linear terms still remains open. Finally, the aging experiment did not reveal any significant structural changes, suggesting that the energy barriers are too high for the athermal emulsion system to rearrange.

6.9 Probability Distribution of Configurations, $P(W)$

Having investigated the probability distribution of forces within the system, we now consider the distribution of the configurations of the packing. We first calculate the probability distribution of the volume function defined in Chapter 2 and find an exponential behaviour, characteristic of the canonical ensemble. Then, we calculate the volume and entropy per particle of the system as a function of the compactivity under a single particle approximation. The obtained result for the entropy is compared with the entropy calculation which takes into account higher coordination shells of particles. The two estimates of the entropy are in reasonable agreement. These results provide the first experimental measurement of the compactivity in particular matter and provide the basis for further studies of this nature. We emphasize that the result is preliminary since it has only been applied to one emulsion and one colloidal data set.

6.9.1 Partitioning into volumes W_i

In Chapter 2, we have justified the application of statistical mechanics to jammed conditions, as defined in Chapter 1, provided there is a mechanism for changing the configurations by tapping or external vibrations. The probability distribution of the configurations is governed by Eq. 2.19.

For a given number of rigid grains of well-defined shape, it is argued that the statistics of the system would be defined by the volume function W , a function which gives the volume of the system in terms of the specification of its grains. This volume function is approximated from geometrical considerations to be

$$W = \sum W^\alpha = \sum 2\sqrt{\text{Det } \mathcal{C}^\alpha}. \quad (6.29)$$

W^α is the volume produced by grain α with its nearest neighbours, but it does not accommodate complex topologies.

Using an extension to the same image analysis method as that used in the determination of the force distributions, the 3D images of the densely packed emulsion now allow for the characterisation of the volume function \mathcal{W} . This is performed by the partitioning of the images into first coordination shells of each particle, described in Section 2.3.1. For this study we use the emulsion system compressed under gravity, previously employed in the coordination number investigation in Section 6.3.

The images are partitioned into volumes of the first coordination shell of each particle. This partitioning is performed in two ways: by an image analysis algo-

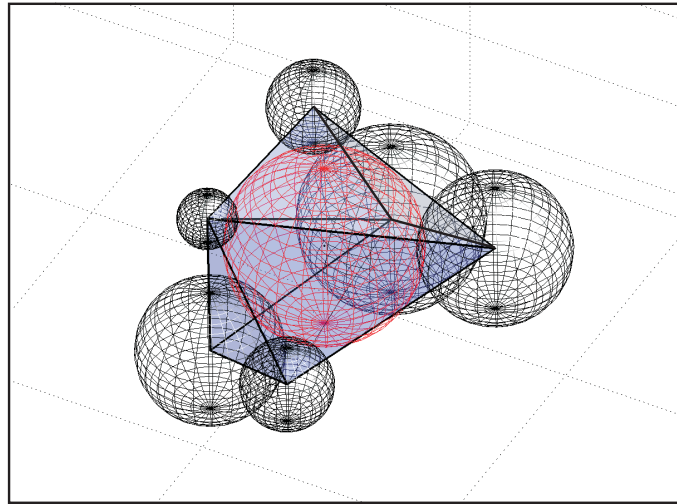


Figure 6.22: An example of a volume \mathcal{W} as the polyhedron constructed from the 3D images. The centre grain (red) has 6 grains in contact (black), the centres of which are joined to form the polyhedron.

rithm which calculates the actual volume of the coordination shell of each particle, shown in Fig. 6.22, and by the geometric approximation of the same volume from the configuration tensor of each particle defined in Eq. (6.20).

We first test how the approximation in Eq. (6.29) for the volume compares with the actual volume measured from the image for each grain. Their correlation is shown in Fig. 6.23. Interestingly, this approximation (which has been shown to be exact for coordination number 3 in 2D) works well for other coordination numbers and even in 3D. Since the obtained polyhedra are constructed from triangles/pyramids connecting each neighbour to the central particle and subsequently summing over them, symmetry is preserved, ensuring the success of the method. It is clear that very large volumes, belonging to grains with high coordination numbers, do stray from the theoretical value due to the complex geometries involved.

However, this definition is clearly only an approximation of the space available to each grain since there is an overlap of \mathcal{W}^α for grains belonging to the same coordination shell. Thus, it overestimates the total volume of the system: $\sum \mathcal{W}^\alpha > V$. The experimentally measured \mathcal{W} for all the particles in the inner window of the packing are summed together and compared with the known total system volume - i.e. the volume of the inner window. The total volume of the system was found to be overestimated only by $\approx 5\%$.

Next we calculate the probability distribution of the volume per particle, \mathcal{W} , in the whole image and find an exponential behaviour:

$$P(\mathcal{W}) \propto e^{-\mathcal{W}/\lambda X}, \quad (6.30)$$

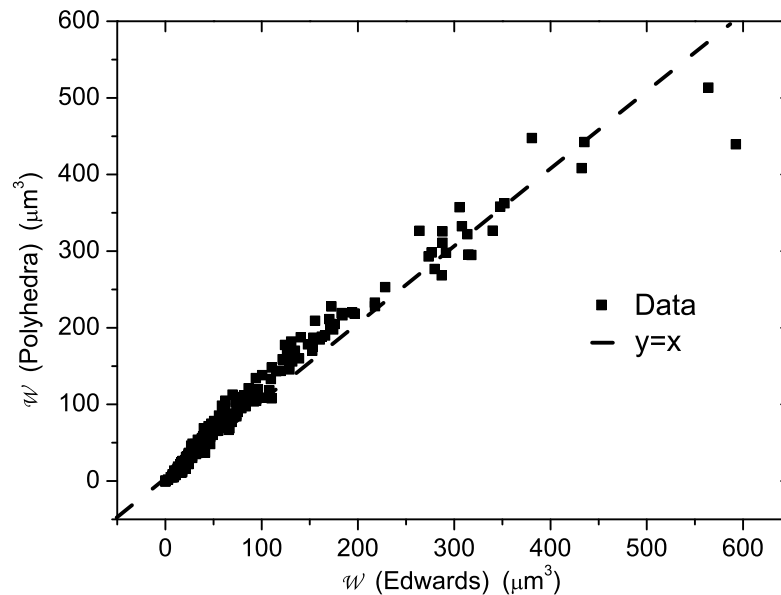


Figure 6.23: \mathcal{W} functions obtained from the configuration tensor \mathcal{C} are plotted against the polyhedra constructed from the images.

which enables the measurement of the compactivity. The value obtained in this way is $X = 79.4\mu\text{m}^3/\lambda$, shown in Fig. 6.24. The conversion of this measurement of the compactivity into a measurement of the analogue of temperature requires a new temperature scale for granular matter. In other words, λ is the analogue of the Boltzmann constant in thermal systems, and needs to be determined for jammed matter. This would require a separate experiment in which the equivalent of ‘heat flow’ would be quantified. For that reason, we also measure the entropy in units of lambda in the next section.

6.9.2 Calculation of the Entropy

The ability to measure the distribution function of \mathcal{W} and therefore its fluctuations in a given particle ensemble, enables the calculations of the macroscopic variables such as the entropy.

Consider a single particle approximation, then the partition function for N particles can be expressed as

$$Z = \left[\sum_n e^{-\mathcal{W}_n/\lambda X} \right]^N, \quad (6.31)$$

from which the mean volume per particle, v , can be calculated as

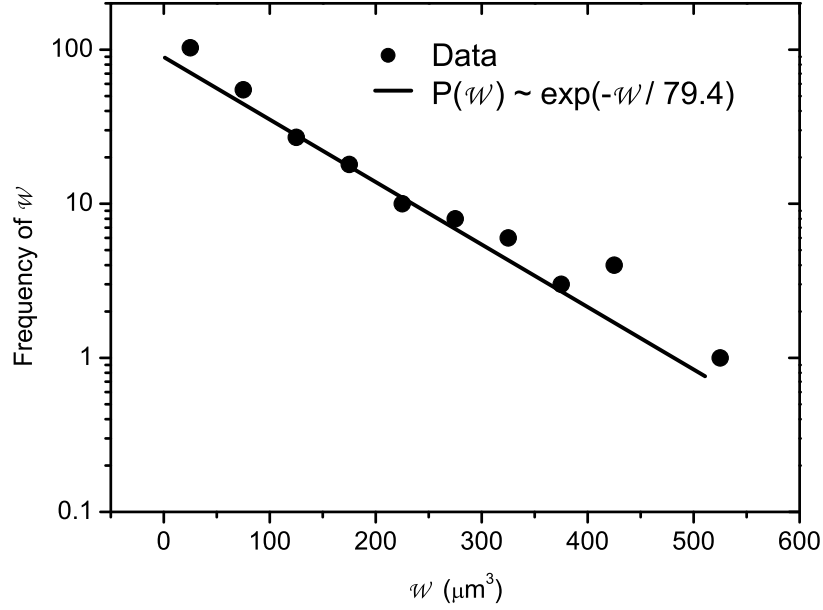


Figure 6.24: Frequency distribution of \mathcal{W} for the emulsion system. The decay constant is the compactivity, $X = 79.4\mu\text{m}^3/\lambda$.

$$v = \frac{\partial \ln Z}{\partial(-1/\lambda X)}. \quad (6.32)$$

Using the experimental values of \mathcal{W}_n we calculate the mean value of the volume per particle for the emulsion data as a function of the compactivity, which is arbitrarily chosen between 0 and $100\mu\text{m}^3$. The results are shown in Fig. 6.25a, showing a monotonic increase of v with compactivity, as expected. This represents the equation of state for the particulate packing.

Using

$$\frac{\partial s}{\partial v} = \frac{1}{X}, \quad (6.33)$$

we obtain the entropy density, s , by integration of the data shown in Fig. 6.25a:

$$s(X) - s(0) = \int_0^X \frac{dv}{X}. \quad (6.34)$$

The results are shown in Fig. 6.25b indicating that the entropy increases approximately logarithmically with compactivity. Since we know the compactivity of the packing under investigation from the fit of $P(\mathcal{W})$, we find that for $X = 79.4\mu\text{m}^3$ the entropy is 1.39 [in units of λ , see Eq. (6.31)]. This result is the first experimental attempt at measuring the entropy of a particulate ensemble from the microscopic variables. The logarithmic increase is analogous to that of the entropy

vs. temperature in an ideal gas. According to this analogy, the volume dependence on compactivity should be linear with some corrections in the high compactivity regime.

The speculative nature of this approach comes from the assumption of the first coordination shell of each particle in the system describing the system behaviour as a whole. In order to test this approximation, in the next section we develop a protocol to calculate the entropy as a function of the shell-size based on information theory concepts.

6.9.3 Coordination Shell Approximation

We present a method based on information theory (Shannon, 1948) and related to recent work by Vink and Balkema (Vink and Barkema, 2002) who determined the configurational entropy of amorphous silicon and vitreous silica.

The method is based on the Shannon entropy $H(n)$ defined as

$$H(n) = - \sum_i p(i) \ln p(i), \quad (6.35)$$

where the index i runs over all possible clusters of size n and $p(i)$ is the probability of the cluster i to occur. The Shannon entropy is identical to Boltzmann's definition in this case, only applied to a network of points in space. The actual Shannon entropy is defined with \log_2 , however, we use \ln for comparison with the experimental data shown above. The entropy density is then obtained as

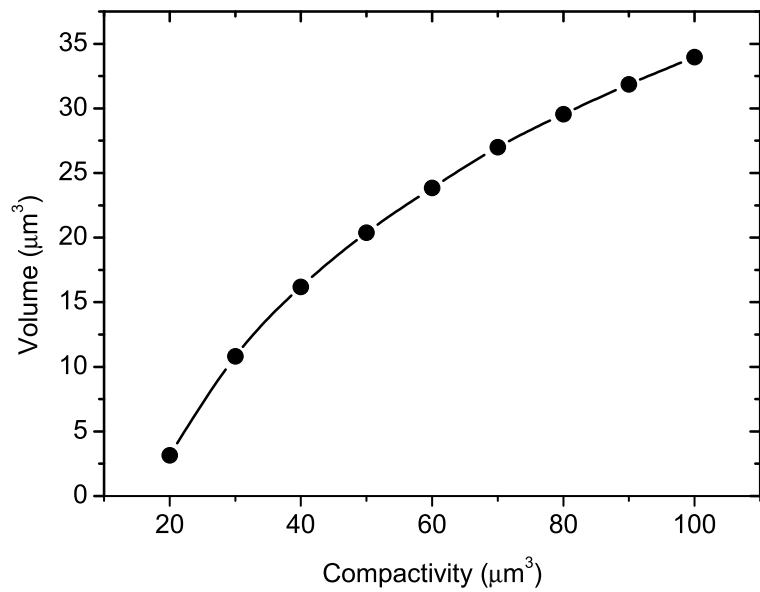
$$s = \lim_{n \rightarrow \infty} [H(n+1) - H(n)]. \quad (6.36)$$

A practical way to estimate s is to extract a large number of m clusters of size n from the system and obtain an estimate of the probability $p(i)$ as

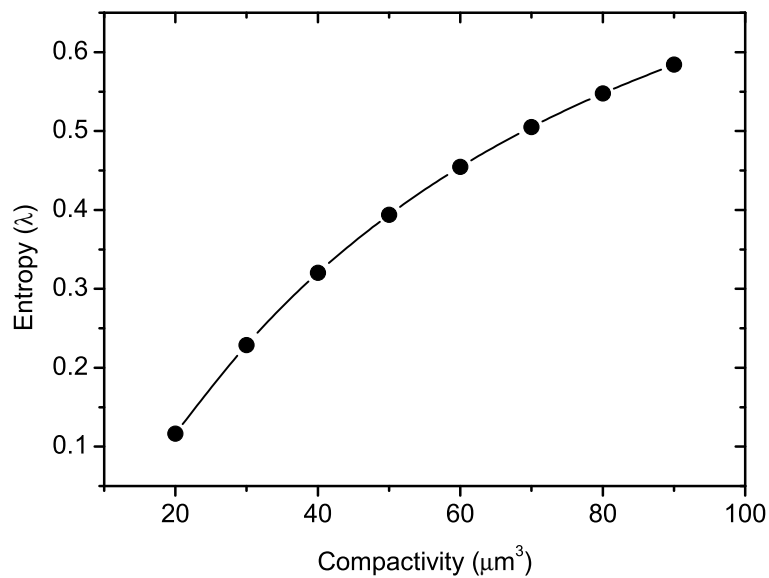
$$p(i) \approx \frac{f_i}{m} \quad (6.37)$$

where f_i is the number of times a cluster i is observed. The estimates of $p(i)$ in combination with Eqs. (6.35) gives $H(n)$. The entropy density is then obtained from Eq. (6.36). Usually, s converges rapidly and even moderate values of the cluster size n are enough to predict s .

For systems in equilibrium, i.e. systems having a compactivity, the Shannon entropy and the thermodynamic entropy are equivalent, apart from a factor of k_b . Here we use Eq. (6.36) to obtain the configuration entropy of the packing studied in the previous section by analysing the configuration as a function of the cluster



(a)



(b)

Figure 6.25: (a) Volume per particle as a function of the compactivity for the emulsion system. (b) Entropy density in units of λ as a function of compactivity.

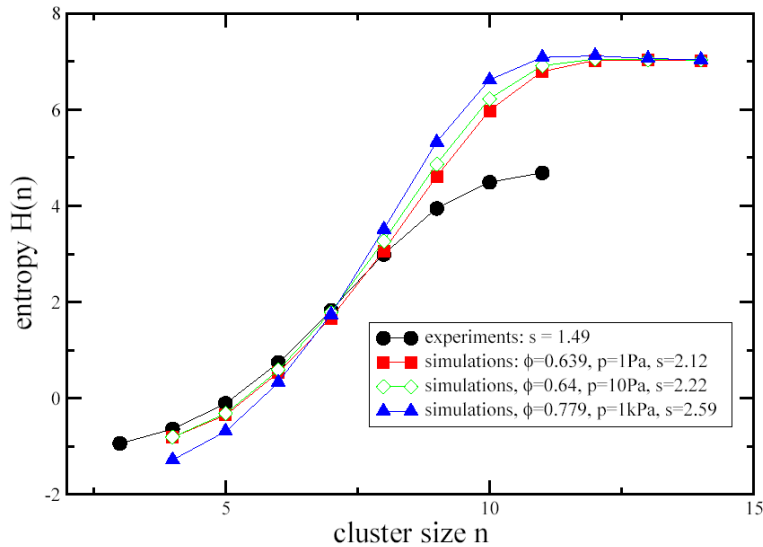


Figure 6.26: Entropy $H(n)$ for the packings obtained in the experiments and simulations. Simulation data is shown for different volume fractions and pressures. Entropy density, s , is calculated from the slope of this graph.

size. It will be shown that a cluster size of the order of the first coordination shell is enough to obtain an accurate estimate of the entropy of the packing, thus validating the use of the volume function \mathcal{W} discussed above. The analysis is applied to the experimental data of emulsion systems and also to simulation data of soft droplets to validate the approach.

We choose a large number m of random positions in the system. For each position we identify the nearest n droplets and identify the graph formed by the bonds connecting the droplets. We consider the topology of the graph thus obtained which is defined in terms of only the bonds. We use a graph automorphism (McKay, 1990) to transform a given list of bonds into a standard form such that two topologically equivalent graphs yield identical lists. We then count the number of times a given graph is observed and use Eq. (6.37) to estimate the probability of occurrence of the given configuration. The probabilities are then used in Eq. (6.35) to obtain the entropy and then in (6.36) to obtain the density.

In Fig. 6.26 we show the behavior of the entropy $H(n)$ as a function of the cluster size n for the experimental data of emulsion droplets. We also plot the entropy of the simulated data obtained for a system of 2000 droplets with a monodisperse size distribution and at different osmotic pressures, p , and therefore volume fractions ϕ as indicated in the figure. The rapid convergence of the limit Eq. (6.36) is demonstrated by the linear behaviour of $H(n)$ for intermediate values of n . The entropy per particle is the gradient of the linear part of this graph. The behavior

of $H(n)$ for large n clearly shows a finite size effect which appears in both simulations and the experiment. However, the important feature of the results is that the linear regime exists for clusters of $n \approx 6 - 8$ droplets which is in good agreement with the number of droplets in the first coordination shell, as investigated in Fig. 6.10(a). The same behaviour is validated with the simulated data which confirms the span of the linear regime. This provides support for the estimation of the entropy based on the \mathcal{W} function proposed in the previous sections.

The entropy obtained for the experimental data is $s = 1.49\lambda$. Simulated data provide entropy densities between $s = 2.12\lambda$ and $s = 2.59\lambda$ according to the volume fraction and pressures. For the same experimental data set we have obtained $s = 1.39\lambda$ using the statistical distribution of the volumes. The two entirely different methods for the entropy calculation give values in good agreement with one another, further supporting the use of entropy as a valid concept for the description of jammed matter.

Chapter 7

Conclusions

We have made the first experimental attempt at characterising and testing the statistical mechanics of jammed matter in the bulk of a 3D particle ensemble. It is the geometry of the configuration of the densely packed grains as well as the transmission of stress through the system which fully define the problem. Hence, we designed an experiment which could probe the probability distribution of configurations and forces within the bulk of a 3D particulate packing.

More specifically, we used confocal microscopy to study the 3D static packings of compressed emulsion droplets by directly imaging the sample bulk. Owing to an interesting fluorescence mechanism we were able to extract the interdroplet forces from the bright areas of droplet deformation at the contacts. The information of the particle configurations was extracted using sophisticated image analysis algorithms in 3D and coupled with the force data to provide the full characterisation of the particle ensemble. The achievements leading to the realisation of this experiment and the main results concerning the physics of jammed matter are summarised below.

7.1 Experimental Method

The main experimental achievements include the design of a model system, the discovery of an interesting fluorescence mechanism within the emulsion phases, and the development of a 3D image analysis methodology to enable a quantitative analysis of the system.

7.1.1 Development of a Model System

We designed a novel system to model granular materials, suitable for a 3D investigation. This was achieved by a dense packing of emulsion droplets, with a

sufficiently elastic surfactant stabilising layer to mimic solid particle behaviour, suspended in a continuous phase fluid. The model emulsion consisted of silicone oil droplets dispersed in a continuous phase solution of water and glycerol, stabilised by sodium dodecyl sulfate. The constituent emulsion particles could be regarded as frictionless, compressible spheres, deforming at the droplet contacts in response to external pressure. The conditions which were satisfied by this system to allow for the subsequent analysis are:

- transparency, enabling the 3D confocal imaging of the sample,
- elasticity, allowing for the extraction of the forces from the deformation of the surfactant stabilised interfaces,
- sufficiently narrow size distribution for a good statistical ensemble,
- stability against phase separation over a period of years,
- an alternative medium to rigid grains, suitable for the test of the universality in the behaviour of systems united by jamming.

7.1.2 Environment-Sensitive Fluorescence of Nile Red

The identification of the features in the confocal images, such as the particle centres, radii and areas of deformation at the contacts, was facilitated by a novel application of Nile Red fluorescent dye. Its fluorescence was investigated using UV-Visible spectrophotometry and compared with the observations from the confocal images.

The dye provided contrast between the sample regions owing to its environment-sensitive spectral shifts. It was found that the solubility and the emission wavelength band of the dye depend on the solvent polarity. This enabled the separation of the emulsion signal into specific wavelength bands representing the different sample regions: the pure oil phase, the interfaces and the continuous phase.

Moreover, the images were found to exhibit a fluorescence enhancement at the regions of droplet deformation due to the subresolution proximity of the droplet interfaces, allowing for their isolation, independent of other features in the image. Since the area of deformation is related to the force, this effect is an extremely important discovery for this and future studies of micromechanics.

The interesting behaviour of the dye presents a very useful tool for studying emulsion packings in general, as the mechanism of the differential fluorescence is based on the surface active nature of the dye molecule itself rather than the specific components used in the experiment.

7.1.3 Novel Image Analysis Technique in 3D

The obtained image stacks of the compressed particulate packings presented a challenge in terms of the identification of the physical features of interest owing to the complexity of the 3D particulate structure. The interconnected, polydisperse droplets were found based on their approximate sphericity.

We developed a new application of the Fourier analysis method for template matching which identified spheres in the 3D images with subvoxel accuracy. This analysis procedure provided a pathway to the full reconstruction of the original image by isolating all the sphere centres and their respective radii in the complex particulate packing. These data formed the basis of all subsequent analysis, including the fast recognition of the highlighted patches of deformation corresponding to the interdroplet forces, the fabric tensors, the spatial analysis and the first coordination shell analysis of the system.

7.2 Physics of Jammed Matter

We separated the study of the statistical mechanics of jamming into the study of the probability distribution of forces and the probability distribution of configurations, characterised by the volume function. These distributions are investigated independently, although future work may well find that the forces and the particle geometry are intimately related.

7.2.1 Force Distributions, $P(f)$

Using the model emulsion system we first characterised the probability distribution of forces. We found a small peak at low forces and an exponential decay at forces above the mean value, in excellent agreement with previous numerical studies on foams and structural glasses as well as experiments on granular materials measured at the walls. Moreover, the distribution is well described by the functional form derived from a simple theoretical model for rigid grains. The form of the probability distribution of forces seems to be independent of the material of the particle provided it has well defined elastic properties. Therefore, the micromechanics of an emulsion, comprised of very “soft” particles bears many similarities with other jammed systems, thus supporting the hypothesis of a common behaviour for all such matter.

7.2.2 Microstructure

This is the first experimental 3D study of the distribution of forces, enabling structural examination. The packings were not only investigated in terms of the distributions, but also the coordination number of each particle, the pair distribution function, force correlations, the spatial distribution and the visualisation of stress transmission through the packing.

Coordination Number. The study of the coordination number revealed that emulsion systems at low pressures are an example of isostatic packings, which arise when $\langle Z \rangle = 6$. This is a theoretically important result because it allows for the investigation of stress transmission in packings without the use of elasticity theory. Thus, the present system can be used further to investigate the theory of marginal rigidity which has been proposed recently as an alternative theory to elasticity to describe particulate packings. Moreover, a system of sedimented colloidal particles shows a similar coordination number indicating that this is a general result. The distribution of the coordination number seems to be dependent on the particle size distribution, in that a higher polydispersity implies a broader range of coordination numbers.

Spatial Analysis. The spatial analysis showed an uniform packing, indicated by one broad peak in the pair distribution function. Moreover, the packings were isotropic as indicated by the configurational and stress tensors. The assumption in the theory for the force distribution of uncorrelated forces was shown to be valid, as well.

Force Chains. The visualisation of the forces in the packing allowed for the conclusion that force chains are not prominent in our system, although they can be seen in uniaxially compressed 3D granular packings and in 2D systems of compressible grains. Since these systems and our system all exhibit an exponential distribution of forces, the existence of force chains is not a necessary requirement for the exponential result. Rather, it is the proximity to the jammed state which is the determining factor.

7.2.3 Configuration Distributions, $P(\mathcal{W})$

The thermodynamics of jammed matter is introduced in terms of the probability distribution of configurations, which is characterised by the fluctuations of the volume function, \mathcal{W} . The entropy and the compactivity, which is the derivative of the entropy with respect to the volume, are then extracted from the knowledge of the probability of configurations.

The complete 3D information of our packing allowed for the microscopic determination of all these quantities, providing us with a microscopic test for the thermodynamics of jammed matter.

- The volume function was first obtained from the images as the geometrical measurement of the volume of the coordination shell of each particle and compared with the value obtained by the theoretical approximation expressed in terms of invariants of configuration tensors of each particle. The two separate measurements were found to agree very well.
- We then calculated $P(\mathcal{W})$ and found an exponential distribution, as expected for a canonical ensemble. This information was then used to calculate the entropy and the mean volume as a function of the compactivity (via the partition function), arriving at an equation of state for jammed systems.
- The thermodynamics calculations were carried out under the first coordination shell approximation for \mathcal{W} , as proposed by the theory. This assumption was tested using a different clustering method to describe the configurations based on information theory. Preliminary calculations indicate that the assumption is approximately valid.

7.3 Final Conclusion

We have designed a unique experiment capable of testing and improving a range of theories in the field of granular matter and more generally, soft condensed matter physics. This study involves the design of a model system consisting of a packing of emulsion droplets under compression. The ability to measure the forces inside a 3D particulate packing, owing to a fluorescence enhancement mechanism, is a novel, powerful and non-invasive tool for investigating the micromechanics of the system. It opens the path for numerous microrheological studies, which have been much sought after in the literature.

Moreover, we have developed a methodology for quantifying the data from the confocal images, such that the important physical quantities can be directly derived. The statistical concepts presented here are thus given a microscopic foundation. The results presented in this Thesis clearly indicate that statistical mechanics for jammed matter is a successful way to describe the particulate system.

7.4 Future Work

The experimental method has been exploited only in static structures so far, but can be readily expanded to dynamic situations. Continuing in the same framework as the current research, the capabilities of the established confocal technique can be expanded to a more quantitative measurement of the elasticity of the material. In contrast to the conventional rheology experiments which extract the elastic modulus of the system by applying macroscopic shear, one can probe the microscopic response by the application of a localised perturbation to the system. This method would involve the observation of the response visually, by following the changes in the force network. The response of the system can theoretically be predicted by the Green function, which could be measured using sophisticated micro-manipulation within the confocal microscope. Experimentally, the local external force could be provided by a magnetic field gradient, acting on magnetic tracer particles embedded in the particulate packing.

This experiment would provide a test for the validity of elasticity theory to describe the stress propagation through a particulate system, which is a much debated topic. A more complete analysis of the force propagation would lead to detailed information on the frictional thresholds which need to be overcome to induce particle motion, the yield stress of the material and the collective behaviour of the cooperative motion of particles in such a medium. If one particle is moved, how do its neighbours respond. The answers may well apply to other types of particulate systems, such as the colloidal suspensions of poly(methyl-methacrylate) (PMMA) particles, leading to more profound unifications of existing theoretical concepts.

Bibliography

- Abu-Naser, A., Galatsanos, N. P., Wernick, M., and Schonfeld, D. (1998). Object recognition based on impulse restoration using the expectation maximisation algorithm. *J. Opt. Soc. Am. A*, **15**, 2327.
- Alexander, S. (1998). Amorphous solids: Their structure, lattice dynamics and elasticity. *Phys. Rep.*, **296**, 65.
- Alnuweiri, H. and Kumar, V. (1991). Fast image labels using local operators on meshconnected computers. *IEEE Trans. on Patt. An. and Machine Intelligence*, **13**, 202.
- Antl, L., Goodwin, J. W., Hill, R. D., Ottewill, R. H., Owens, S. M., Papworth, S., and Waters, J. A. (1986). The preparation of poly(methyl methacrylate) lattices in nonaqueous media. *Colloid. Surface.*, **17**, 67.
- Antony, S. J. (2001). Evolution of force distribution in three-dimensional granular media. *Phys. Rev. E*, **63**, 011302.
- Aronson, M. P. (1989). The role of free surfactant in destabilizing oil-in-water emulsions. *Langmuir*, **5**, 494.
- Aronson, M. P. and Princen, H. M. (1982). Contact angles in oil-in-water emulsions stabilised by ionic surfactants. *Colloids Surf.*, **4**, 173.
- Ball, R. C. and Blumenfeld, R. (2002). Stress field in granular systems: Loop forces and potential formulation. *Phys. Rev. Lett.*, **88**, 115505–1.
- Barber, C. B., Dobkin, D. P., and Huhdanpaa, H. (1996). The quickhull algorithm for convex hulls. *ACM T. Math. Software*, **22**, 469.
- Barrat, A., Kurchan, J., Loreto, V., and Sellitto, M. (2000). Edwards measures for powders and glasses. *Phys. Rev. Lett.*, **85**, 5034.
- Bartlett, P., Henderson, S. I., and Mitchell, S. J. (2001). Measurement of the hydrodynamic forces between two polymer-coated spheres. *Phil. Trans. R. Soc. Lond. A*, **359**, 883.

- Becher, P., editor (1983). *Encyclopedia of Emulsion Technology*, volume 2, New York. Dekker.
- Behringer, R. P. and Jenkins, J. T. (1997). *Powders & Grains 97*. Balkema, Rotterdam.
- Berg, A. and Malik, J. (2001). Geometric blur for template matching. In *Computer Vision and Pattern Recognition*, page I:791.
- Bernal, J. D. (1960). Coordination of randomly packed spheres. *Nature*, **188**, 910.
- Bibette, J. (1991). Depletion interactions and fractionated crystallisation for poly-disperse emulsion purification. *J. Colloid. Interface Sci.*, **147**, 474.
- Bibette, J., Leal-Calderon, F., and Poulin, P. (1999). Emulsions: basic principles. *Reg. Prog. Phys.*, **62**, 969.
- Bibette, J., Leal-Calderon, F., Schmitt, V., and Poulin, P. (2002). *Emulsion Science: Basic Principles, An Overview*. Springer-Verlag, Heidelberg.
- Bibette, J., Morse, D. C., Witten, T. A., and Weitz, D. A. (1992). Stability-criteria for emulsions. *Phys. Rev. Lett.*, **69**, 2439.
- Blair, D. L., Mueggenburg, N. W., Marshall, A. H., Jaeger, H. M., and Nagel, S. R. (2001). Force distributions in three-dimensional granular assemblies: Effects of packing order and interparticle friction. *Phys. Rev. E*, **63**, 041304.
- Blumenfeld, R. and Edwards, S. F. (2003). Granular entropy: Explicit calculations for planar assemblies. *Phys. Rev. Lett.*, **90**, 114303.
- Born, M. and Wolf, E. (1983). *Principles of Optics*. Pergamon Press, Oxford.
- Bouchaud, J.-P., Cates, M., and Claudin, P. (1995). Stress-distribution in granular media and nonlinear-wave equation. *JOURNAL DE PHYSIQUE I*, **639**, 5.
- Bouchaud, J.-P., Levine, D., and Otto, M. (2001). Force chain splitting in granular materials: A mechanism for large-scale pseudo-elastic behaviour. *Eur. J. Phys. E*, **4**, 451.
- Bromley, E. H. C. and Hopkinson, I. (2002). Confocal microscopy of a dense particle system. *J. Colloid Interface Sci.*, **75**, 245.
- Brujić, J., Edwards, S. F., and Grinev, D. (2003a). Jammed systems in slow flow need a new statistical mechanics. *Phil. Trans. R. Soc. Lond. A*, **361**, 741.

- Brujić, J., Edwards, S. F., Grinev, D., Hopkinson, I., Brujić, D., and Makse, H. A. (2003b). 3d bulk measurements of the force distribution in a compressed emulsion system. *Faraday Disc.*, **123**, 207.
- Brujić, J., Johnson, D. L., Sindt, O., and Makse, H. A. (2003c). Stress relaxation in granular matter. to be published.
- Campbell, A. I. and Bartlett, P. (2002). Fluorescent hard-sphere polymer colloids for confocal microscopy. *J. Coll. Interface Sci.*, **256**, 325.
- Cates, M. E., Wittmer, P., Bouchaud, J. P., and Claudin, P. (1998). Jamming, force chains, and fragile matter. *Phys. Rev. Lett.*, **81**, 1841.
- Chakravarty, A., Edwards, S. F., Grinev, D. V., Mann, M., Phillipson, T. E., and Walton, A. J. (2002). Density fluctuations in vibrated granular materials. to be published in the proceedings of the workshop on ‘Quasi-static deformations of particulate materials’.
- Cipelletti, L. and Ramos, L. (2002). Slow dynamics in glasses, gels and foams. *Curr. Opinion in Colloid and Interface Sci.*, **7**, 228.
- Cipelletti, L., Ramos, L., Manley, S., Pitard, E., Weitz, D. A., Pashkovski, E. E., and Johansson, M. (2003). Universal non-diffusive slow dynamics in aging soft matter. *Faraday Disc.*, **123**, 237.
- Coluzzi, B., Parisi, G., and Verrocchio, P. (2000). Thermodynamical liquid-glass transition in a lennard-jones binary mixture. *Phys. Rev. Lett.*, **84**, 306.
- Coppersmith, S. N., Liu, C., Majumdar, S., Narayan, O., and Witten, T. A. (1996). Model for force fluctuations in bead packs. *Phys. Rev. E*, **53**, 4673.
- Cugliandolo, L. F., Kurchan, J., and Peliti, L. (1997). Energy flow, partial equilibration, and effective temperatures in systems with slow dynamics. *Phys. Rev. E*, **55**, 3898.
- D’Anna, G. and Gremaud, G. (2001). The jamming route to the glass state in weakly perturbed granular media. *Nature*, **413**, 407.
- Dantu, P. (1968). *Géotechnique*, **18**, 50.
- Debenedetti, P. G. and Stillinger, F. H. (2001). Supercooled liquids and the glass transition. *Nature*, **410**, 259.

- Deminere, B., Colin, A., Leal-Calderon, F., Muzy, J. F., and Bibette, J. (1999). Cell growth in a 3d cellular system undergoing coalescence. *Phys. Rev. Lett.*, **82**, 229.
- Dinsmore, A. D., Hsu, M. F., Nikolaides, M. G., Marquez, M., Bausch, A. R., and Weitz, D. A. (2002). Colloidosomes: Selectively permeable vapsules composed of colloidal particles. *Science*, **298**, 1006.
- Dufour, R. M., Miller, E., and Galatsanos, N. P. (2000a). Geometric parameter estimation with a multiscale template library. In *Automatic Target Recognition X*.
- Dufour, R. M., Miller, E., and Galatsanos, N. P. (2000b). Impulse restoration template matching under geometric uncertainties. In *International Conference on Image Processing (ICIP 2000)*, page TP12.07.
- Dufour, R. M., Miller, E., and Galatsanos, N. P. (2002). Template matching based object recognition with unknown geometric parameters. *IEEE T. Image Process*, **11**, 1385.
- Durian, D. J. (1995). Foam mechanics at the bubble scale. *Phys. Rev. Lett.*, **75**, 4780.
- Edwards, S. F. (1991). The aging of glass forming liquids. In Blackman, J. and Taguena, J., editors, *Disorder in Condensed Matter Physics*, Oxford. Oxford University Press.
- Edwards, S. F. (1994). The role of entropy in the specification of a powder. In Mehta, A., editor, *Granular Matter: An Interdisciplinary Approach*, New York. Springer-Verlag.
- Edwards, S. F., Brujić, J., and Makse, H. A. (2004). New statistical mechanics for granular matter. to be published in the proceedings of the workshop on ‘Unifying concepts in granular matter and glasses’.
- Edwards, S. F. and Grinev, D. V. (1999). Statistical mechanics of stress transmission in disordered granular arrays. *Phys. Rev. Lett.*, **82**, 5397.
- Edwards, S. F. and Grinev, D. V. (2003). Statistical mechanics of granular materials: stress propagation and distribution of contact forces. *Granular Matter*, **4**, 147.
- Edwards, S. F., Grinev, D. V., and Brujić, J. (2003). Fundamental problems in statistical physics of jammed packings. *Physica A*, **330**, 61.

- Edwards, S. F. and Oakeshott, R. B. S. (1989). Theory of powders. *Physica A*, **157**, 1080.
- Erikson, J. M., Mueggenburg, N. W., Jaeger, H. M., and Nagel, S. R. (2002). Force distributions in three-dimensional compressible granular packs. *Phys. Rev. E*, **66**, 040301.
- Fierro, A., Nicodemi, M., and Coniglio, A. (2002). Equilibrium distribution of the inherent states and their dynamics in glassy systems and granular media. *Europhys. Lett.*, **59**, 642.
- Ganan-Calvo, A. and Gordillo, J. M. (2001). Perfectly monodisperse microbubbling by capillary flow focussing. *J. Coll. Interf. Sci.*, **87**.
- Gang, H., Krall, A. H., and Weitz, D. A. (1995). Thermal fluctuations of the shapes of droplets in dense and compressed emulsions. *Phys. Rev. E*, **52**, 6289.
- Gasser, U., Weeks, E. R., Schofield, A., and Weitz, D. A. (2001). Real-space imaging of nucleation and growth in colloidal crystallization. *Science*, **292**, 258.
- Goldman, R. N. (1991). Area of planar polygons and volume polyhedra. In Arvo, J., editor, *Graphics Gems II*, San Diego. Academic Press.
- Goldstein, M. (1969). Viscous liquids and the glass transition: A potential energy barrier picture. *J. Chem. Phys.*, **51**, 3728.
- Greenspan, P. and Fowler, S. D. (1985). Spectrofluorometric studies of the lipid probe, Nile red. *J. Lipid Res.*, **26**, 781.
- Hagiwara, T., Kumagai, H., and Nakumara, K. (1997). Fractal analysis of aggregates in heat-induced BSA gels. *J. Opt. Soc. Am. A*, **14**, 139.
- Haralick, R. M. and Shapiro, L. G. (1992). *Computer and robot Vision*, volume 3. Addison-Wesley, New York.
- Haugland, R. P. (2002). *Handbook of Fluorescent Probes and Research Products*. www.probes.com/handbook.
- Hell, S. W. and Steltzer, E. H. K. (1995). Lens aberrations in confocal fluorescence microscopy. In Pawley, J. R., editor, *Handbook of Biological Confocal Microscopy*, New York. Academic Press.

- Herrmann, H. J., Hovi, J. P., and Luding, S., editors (1998). *Physics of Dry Granular Matter*, Dordrecht. Kluwer.
- Heusch, R. (2002). Emulsions. In *Ullman's Encyclopedia of Industrial Chemistry*, Germany. Wiley-VCH.
- Hidalgo, R. C., Grosse, C. U., Kun, F., Reinhardt, H. W., and Herrmann, H. J. (2002). Evolution of percolating force chains in compressed granular media. *Phys. Rev. Lett.*, **89**, 205501.
- Hinch, E. J. and Acrivos, A. (1980). Long slender drops in a simple shear flow. *J. Fluid. Mech.*, **98**, 305.
- Huang, Q. R., Wang, C. H., and Deng, N. J. (2000). Emergence of macroscopic temperatures in systems that are not thermodynamical microscopically: towards a thermodynamical description of slow granular rheology. *J. Phys. Condensed Matter*, **29**, 6611.
- Huibers, P. D. T. (1996). *Surfactant self-assembly, kinetics and thermodynamics in micellar and microemulsion systems*. PhD thesis, University of Florida.
- Jain, A. K., Duin, R. P. W., and Mao, J. (2000). Statistical pattern recognition: a review. *IEEE T. Pattern Anal.*, **22**, 4.
- Jenkins, J. T. and Savage, S. B. (1983). A theory for the rapid flow of identical, smooth, nearly elastic, spherical particles. *J. Fluid Mech.*, **130**, 187.
- Jinnai, H., Koga, T., Nishikawa, Y., Hashimoto, T., and Hyde, S. T. (1997). Curvature determination of spinodal interface in a condensed matter system. *Phys. Rev. Lett.*, **78**, 2248.
- Josserand, C., Tkachenko, A. V., Mueth, D. M., and Jaeger, H. M. (2000). Memory effects in granular materials. *Phys. Rev. Lett.*, **85**, 3632.
- Jurie, F. and Dhome, M. (2001a). Real time 3d template matching. In *Computer Vision and Pattern Recognition*, pages I:791–796.
- Jurie, F. and Dhome, M. (2001b). A simple and efficient template matching algorithm. In *IEEE International Conference on Computer Vision 2001*, pages II: 544–549.
- Kirkpatrick, T. R. and Thirumalai, D. (1987). P-spin-interaction spin-glass models - connections with the structural glass problem. *Phys. Rev. B*, **36**, 5388.

- Knight, J. B., Ehrichs, E. E., Kuperman, V. Y., Flint, J. K., Jaeger, H. M., and Nagel, S. R. (2001). Experimental study of granular convection. *Phys. Rev. E*, **54**, 5726.
- Kob, W., Sciortino, F., and Tartaglia, P. (2000). Aging as dynamics in configuration space. *Europhys. Lett.*, **49**, 590.
- Kurchan, J. (2001). Rheology and how to stop aging. In Liu, A. and Nagel, S. R., editors, *Jamming and Rheology: Constrained Dynamics on Microscopic Scales*, London. Taylor & Francis.
- Lacasse, M., Grest, G. S., Levine, D., Mason, T. G., and Weitz, D. A. (1994). Uniaxial elastic-modulus of concentrated emulsions. *Langmuir*, **10**, 4503.
- Lacasse, M., Grest, G. S., Levine, D., Mason, T. G., and Weitz, D. A. (1996). Model for the elasticity of compressed emulsions. *Phys. Rev. Lett.*, **76**, 3448.
- Lakowicz, R. L. (1999). *Principles of Fluorescence Spectroscopy*. Plenum Press, New York.
- Landau, L. D. and Lifshitz, E. M. (1970). *Statistical Physics*. Pergamon, New York.
- Landau, L. D. and Lifshitz, E. M. (1986). *Theory of Elasticity*. Pergamon, New York.
- Law, N. F. and Chung, R. (2001). Multiresolution discontinuity-preserving surface reconstruction. *Pattern Recognition*, **34**, 2133.
- Leal-Calderon, F., Stora, T., Mondain-Monval, O., Poulin, P., and Bibette, J. (1994). Direct measurement of colloidal forces. *Phys. Rev. Lett.*, **72**, 2959.
- Lewis, J. P. (1995). Fast template matching. *Vision Interface*, page 120.
- Liu, A. and Nagel, S. R. (2001). Jamming and rheology: An introduction. In Liu, A. and Nagel, S. R., editors, *Jamming and Rheology: Constrained Dynamics on Microscopic Scales*, London. Taylor & Francis.
- Liu, A. J. and Nagel, S. R. (1998). Nonlinear dynamics - jamming is not just cool any more. *Nature*, **396**, 21.
- Liu, C. H., Nagel, S. R., Schechter, D. A., Coppersmith, S. N., Majumdar, S., Narayan, O., and Witten, T. A. (1995). Force fluctuations in bead packs. *Science*, **269**, 513.

- Lovoll, G., Maloy, K. N., and Flekkoy, E. G. (1999). Force measurements on static granular materials. *Phys. Rev. E*, **60**, 5872.
- Lu, J. (2003). private communication.
- Luebke, D., Reddy, M., Cohen, J., Varshney, A., Watson, B., and Huebner, R. (2003). *Level of Details for 3D Graphics*. Elsevier Science, San Francisco.
- Mabille, C., Leal-Calderon, L., Bibette, J., and Schmitt, V. (2003). Monodisperse fragmentation in emulsions: Mechanisms and kinetics. *Europhys. Lett.*, **61**, 708.
- Mabille, C., Schmitt, V., Gorria, P., Leal-Calderon, F., Faye, V., Deminiere, B., and Bibette, J. (2000). Rheological and shearing conditions for the preparation of monodisperse emulsions. *Langmuir*, **16**, 422.
- Makse, H. A., Gland, N., Johnson, D. L., and Schwartz, L. M. (1999). Why effective medium theory fails in granular materials. *Phys. Rev. Lett.*, **83**, 5070.
- Makse, H. A., Johnson, D. L., and Schwartz, L. M. (2000). Packing of compressible granular materials. *Phys. Rev. Lett.*, **84**, 4160.
- Makse, H. A. and Kurchan, J. (2002). Testing the thermodynamic approach to granular matter with a numerical model of a decisive experiment. *Nature*, **415**, 614.
- Manoj, P., Fillery-Travis, A. J., Watson, A. D., Hibberd, D. J., and Robins, M. R. (1998). Characterization of a polydisperse depletion-flocculated emulsion. *J. Coll. Interface Sci.*, **207**, 283.
- Mason, T. G. and Bibette, J. (1996). Emulsification in viscoelastic media. *Phys. Rev. Lett.*, **77**, 3481.
- Mason, T. G., Bibette, J., and Weitz, D. A. (1995). Elasticity of compressed emulsions. *Phys. Rev. Lett.*, **75**, 2051.
- Mason, T. G., Gang, H., and weitz, D. A. (1997a). Diffusing-wave-spectroscopy measurements of viscoelasticity of complex fluids. *J. Opt. Soc. Am. A*, **14**, 139.
- Mason, T. G., Lacasse, M. D., Grest, G. S., Levine, D., Bibette, J., and weitz, D. A. (1997b). Osmotic pressure and viscoelastic shear moduli of concentrated emulsions. *Phys. Rev. E*, **56**, 3150.

- McKay, B. D. (1990). Nauty user's guide (version 1.5). Tech. Rep. TR-CS-90-02, Australian National University, Department of Computer Science.
- Mehta, A. and Edwards, S. F. (1989). Statistical mechanics of powder mixtures. *J. Stat. Phys.*, **157**, 1091.
- Minsky, M. (1957). Microscopy apparatus. *US Patent No. 3013467*.
- Mondain-Monval, O., Leal-Calderon, F., Phillip, J., and Bibette, J. (1995). Depletion forces in the presence of electrostatic double-layer repulsion. *Phys. Rev. Lett.*, **75**, 3364.
- Morse, D. C. and Witten, T. A. (1993). Droplet elasticity in weakly compressed emulsions. *Europhys. Lett.*, **22**, 549.
- Moukarzel, C. F. (1998). Isostatic phase transition and instability in stiff granular materials. *Phys. Rev. Lett.*, **81**, 1634.
- Mueth, D. M., Debregeas, G. F., Karczmar, G. S., Eng, P. J., Nagel, S. R., and Jaeger, H. M. (2000). Signatures of granular microstructures in dense shear flows. *Nature*, **406**, 385.
- Mueth, D. M., Jaeger, H. M., and Nagel, S. R. (1998). Force distribution in a granular medium. *Phys. Rev. E*, **57**, 3164.
- Myatt, M. J. (2002). *Confocal microscopy of a ternary polymer system undergoing phase separation due to solvent loss*. PhD thesis, University of Cambridge.
- Nicodemi, M. (1999). Dynamical response functions in models of vibrated granular media. *Phys. Rev. Lett.*, **82**, 3734.
- Nikolaidis, N. and Pitas, I. (2001). *3-D Image Processing Algorithms*. Wiley, New York.
- Nowak, E. R., Knight, J. B., Jaeger, E. B. H. M., and Nagel, S. R. (1998). Density fluctuations in vibrated granular materials. *Phys. Rev. E*, **1971**, 57.
- Nowak, E. R., Knight, J. B., Povinelli, M. L., Jaeger, H. M., and Nagel, S. R. (1997). Reversibility and irreversibility in the packing of vibrated granular material. *Powder Technology*, **94**, 79.
- O'Hern, C. S., Langer, S. A., Liu, A. J., and Nagel, S. R. (2001). Force distributions near jamming and glass transitions. *Phys. Rev. Lett.*, **86**, 111.

- O'Hern, C. S., Silbert, L. E., Liu, A. J., and Nagel, S. R. (2003). Jamming at zero temperature and zero applied stress: The epitome of disorder. *Phys. Rev. E*, **68**, 011306.
- Orsi, T. H., Anderson, A. L., and Lyons, A. P. (1996). X-ray tomographic analysis of sediment microstructure in eckernforde bay, western baltic sea. *Geo-Mar. Lett.*, **16**, 232.
- Paddock, S. W. (1999). *Confocal Microscopy, Methods and Protocols*. Humana Press, New Jersey.
- Paeth, A. (1990). Median finding on a 3×3 grid. In Glassner, A. S., editor, *Graphics Gems*, San Diego. Academic Press.
- Parker, J. R. (1997). *Algorithms for Image Processing and Computer Vision*. Wiley, New York.
- Pawley, J. R. (1995). *Handbook of Biological Confocal Microscopy*. Plenum Press, New York.
- Perrin, P. (2000). A one step method to create and immobilise the ordered structures of fluid dispersions. *Langmuir*, **16**, 4774.
- Perrin, P., Devaux, N., Sergot, P., and Lequeux, F. (2001). Shear-induced formation of ordered monodisperse emulsions stabilized by an associating amphiphilic polyelectrolyte. *Langmuir*, **17**, 2656.
- Philippe, P. and Bideau, D. (2002). Compaction dynamics of a granular medium under vertical tapping. *Europhys. Lett.*, **60**, 677.
- Porion, P., Sommier, N., and Evesque, P. (2000). Dynamics of mixing and segregation processes in a 3d blender by nmr imaging investigation. *Europhys. Lett.*, **50**, 319.
- Princen, H. M. (1980). Highly concentrated emulsions, i. cylindrical systems. *J. Colloid Interface Sci.*, **128**, 176.
- Princen, H. M. (1983). Rheology of foams and highly concentrated emulsions. elastic properties and yield stress of a cylindrical model system. *J. Colloid Interface Sci.*, **91**, 160.
- Princen, H. M. and Kiss, A. D. (1986). Rheology of foams and highly concentrated emulsions. 3. static shear modulus. *J. Coll. Interface Sci.*, **112**, 427.

- Pusey, P. N., Pirie, A. D., and Poon, W. C. K. (1993). Dynamics of colloid polymer mixtures. *Physica A*, **201**, 322.
- Pusey, P. N. and van Megen, W. (1986). Phase behaviour in concentrated suspensions of nearly hard colloidal spheres. *Nature*, **320**, 340.
- Radjai, F., Jean, M., Moreau, J., and Roux, S. (1996). Force distributions in dense two-dimensional granular systems. *Phys. Rev. Lett.*, **77**, 274.
- Rericha, E. C., Bizon, C., Shattuck, M. D., and Swinney, H. L. (2002). Shocks in supersonic sand. *Phys. Rev. Lett.*, **88**, 014302.
- Richetti, P. and Kekicheff, P. (1992). Direct measurement of depletion and structural forces in a micellar system. *Phys. Rev. Lett.*, **68**, 1992.
- Russ, J. C. (1990). *Computer-Assisted Microscopy: The Measurement and Analysis of Images*. Plenum Press, New York.
- Russ, J. C. (1999). *The Image Processing Handbook*. Springer, Heidelberg.
- Sackett, D. L. and Wolff, J. (1987). Nile red as a polarity-sensitive fluorescent-probe of hydrophobic protein surfaces. *Anal. Biochem.*, **167**, 228.
- Sanchez, M. C., Valencia, C., Franco, J. M., and Gallegos, C. (2001). Wall slip phenomena in oil-in-water emulsions: Effect of some structural parameters. *J. Coll. Interface Sci.*, **241**, 226.
- Sastry, S., Debenedetti, P. G., and Stillinger, F. H. (1998). Signatures of distinct dynamical regimes in the energy landscape of a glass-forming liquid. *Nature*, **393**, 554.
- Savage, S. B. (1984). The mechanics of rapid granular flows. *Adv. Appl. Mech.*, **24**, 289.
- Scott, G. D. (1960). Packing of equal spheres. *Nature*, **188**, 908.
- Sexton, M. G., Socolar, J. E. S., and Schaeffer, D. G. (1999). Force distribution in a scalar model for noncohesive granular material. *Phys. Rev. E*, **60**, 3164.
- Shannon, C. E. (1948). Prediction and entropy of printed english. *Bell Sys. Tech. J.*, **27**, 1948.
- Silbert, L. E., Ertas, D., Grest, G. S., Halsey, T. C., and Levine, D. (2002). Geometry of frictionless and frictional sphere packings. *Phys. Rev. E*, **65**, 031304.

- Smalyukh, I. I., Shiyonovskii, S. V., and Lavrentovich, O. D. (2001). Three-dimensional imaging of orientational order by fluorescence confocal polarizing microscopy. *Chem. Phys. Lett.*, **88**, 336.
- Soille, P. (2003). *Morphological Image Analysis*. Springer-Verlag, Berlin.
- Sollich, P., Lequeux, F., Hébraud, P., and Cates, M. E. (1997). Rheology of soft glassy materials. *Phys. Rev. Lett.*, **78**, 2020.
- Stillinger, F. H. and Weber, T. A. (1984). Hidden structure in liquids. *Phys. Rev. A*, **25**, 978.
- Struik, L. C. E. (1978). *Physical Aging in Amorphous Polymers and other Materials*. Elsevier, Houston.
- Taylor, G. I. (1934). The formation of emulsions in definable fields of flow. *Proc. R. Soc. London A*, **14**, 225.
- Thompson, K. (1990). Area of intersection: two circles. In Glassner, A. S., editor, *Graphics Gems*, San Diego. Academic Press.
- Thornton, C. (1997). *KONA Powder and Particle*, **15**, 81.
- Trappe, V., Prasad, V., Cipelletti, L., Segre, P. N., and Weitz, D. A. (2001). Jamming phase diagram for attractive particles. *Nature*, **411**, 772.
- Umbanhowar (2000). Monodisperse emulsion generation via drop break off in a coflowing stream. *Langmuir*, **16**, 347.
- van Blaaderen, A. and Wiltzius, P. (1995). Real-space structure of colloidal hard-sphere glasses. *Science*, **270**, 1177.
- Vanel, L., Howell, D., Clark, D., Behringer, R. P., and Clement, E. (1999). Memories in sand: Experimental tests of construction history on stress distributions under sand piles. *Phys. Rev. E*, **60**, 5040.
- Vink, R. L. C. and Barkema, G. T. (2002). Configurational entropy of network-forming materials. *Phys. Rev. Lett.*, **89**, 076405.
- Wagner, B. D., Stojanovic, N., Leclair, G., and Jankowski, C. K. (2003). A spectroscopic and molecular modelling study of the nature of the association complexes of Nile red with cyclodextrins. *J. Incl. Phenom. Macro.*, **45**, 275.

- Weeks, E. R., Crocker, J. C., Levitt, A. C., Schofield, A., and Weitz, D. A. (2000). Three-dimensional direct imaging of structural relaxation near the colloidal glass transition. *Science*, **287**, 627.